Computer Simulations of Block Copolymer Nanocomposite Systems

UNIVERSITY OF
LINCOLN

Javier Díaz Brañas

A thesis submitted in partial fulfilment of the requirements of the University of Lincoln for the degree of

Doctor of Philosophy

School of Mathematics and Physics
College of Science
University of Lincoln
United Kingdom
July 2019

Supervisory team

First Supervisor: Prof. Andrei Zvelindovsky, University of Lincoln, UK
Second Supervisor: Dr. Marco Pinna, University of Lincoln, UK

Declaration

I declare that this thesis and the work presented in it has been planned and generated by myself and my supervisors. This work has not been reported in any previous thesis.

Javier Diaz

Acknowledgements

Firstly, I would like to express my utmost gratitude to my supervisors Prof. Andrei Zvelindovsky and Dr Marco Pinna, who have not only helped me throughout my PhD, but also provided me with support and guidance, both academically and personally. This has been an incredible opportunity for which I am hugely grateful

I would like to thank Prof. Ignacio Pagonabarraga, who has helped me immensely with this research. I am extremely grateful for his dedication and effort.

I feel extremely lucky to have spent these years at the School of Mathematics and Physics at the University of Lincoln, being able to learn from such a great group of researchers. This PhD would have been much harder without the help of Dr Manuela Mura, whose help on every aspect of my studies has been immense. I want to thank Dr Bart Vorselaars for the useful comments and the chance to assist him on lectures and gain experience. I would like to thank all the postgraduate students at the School of Maths and Physics. I want to thank Sergey Chulkov for his help with the School's cluster and help with HPC questions.

I want to thank my BSc final year thesis supervisor Dr Alvaro Domínguez for his interest and continuous collaboration during these years.

I want to thank Prof Roy Shenhar for his collaboration and discussions.

I want to thank the HCP Europa 3 scheme for financial support and access to Mare Nostrum. In particular, I thank Guillermo Oyarzún for his help with the parallelisation of the CDS code.

I thank the BritishSpanish Society and Plastic Energy for their financial support.

I owe so much to my family for their support and help.

To Li, because thanks to you Lincoln has truly been a home.

I would like to thank my friends from Spain, specially those who have shared the same journey through PhD and research.

Abstract

Block copolymers and nanoparticles are elements of the soft matter family which includes deformable materials and is increasingly part of industry and biological applications. Block copolymer melts can self-assemble into well-ordered, periodic structures in the mesoscale. Furthermore, block copolymers are perfect scaffolds to locate colloidal nanoparticles and, when applicable, control their orientation. Nonetheless, the co-assembly of colloids within block copolymers is not that of simple passive fillers. Instead, the presence of particles can greatly disturb the original block copolymer structure leading to a true collective behaviour where several length scales compete, along with entropic and enthalpic mechanism of assembly. To study such a complex problem, computer programs are used. Cell Dynamic Simulation provide an efficient method to study hybrid block copolymer/nanoparticle systems in the mesoscale, combining a continuous approach to the phase separation of block copolymers with colloids, which are individually treated following Brownian Dynamics. Using this method, a series of experimental results have been reproduced. Moreover, it has been used to study otherwise complex open questions such as the full phase diagram of block copolymer morphologies in the presence of an arbitrary number of particles with arbitrary chemical characteristic. Colloids have been found to segregate within the block copolymer structures dictated by their chemical properties, size, shape and concentration in the system. At high concentrations nanoparticles can greatly disturb the polymeric morphology and interesting cases of aggregation and phase-separation have been found. Neutral nanoparticles can macro-phase separate into elongated clusters along the lamellar direction. Non-spherical particles such as nanorods or square-like particles have been studied in detail, finding highly ordered configurations of nanoparticles in accordance with recent experiments. Highly anisotropic nanoparticles have been found to display higher occupancy rate of the block copolymer interface, which makes them ideal to segregate in layers at block copolymer interfaces. Chemically inhomogeneous nanoparticles have been also found to assemble into complex configurations when mixed with block copolymers. In order to achieve relevant box sizes, an efficient CDS scheme is used. Furthermore, a parallel scheme using FORTRAN Coarrays has been used, which allows to simulate up to tens of μm sized systems, which is considerably larger than previously reported simulations of block copolymer nanocomposite systems.

Contents

Overview of this Thesis

Aim of the Investigation

This thesis has been devoted to the study of block copolymer (BCP) systems in the presence of nanoparticles (NPs), using computational tools. Block copolymers are ideal matrices to host and order nanoparticles[1, 2]. Due to the intrinsic periodicity of block copolymers, arrays [3] or sheets of colloids can be created by segregating nanoparticles within block copolymers. The resulting block copolymer nanocomposite material, for instance, can act as a photonic gap material[4]. Furthermore, it has been shown that the presence of nanoparticles can reduce the critical elecric field needed to induce orientation in lamellar block copolymers [5].

While the behaviour of pure block copolymer materials is considerably well studied, the presence of nanoparticles in block copolymers leads to phenomena which are less understood. For instance, nanoparticles have been shown to induce changes in the hosting block copolymer matrix. In this sense, colloidal particles do not act as mere passive fillers. Instead, nanoparticles can change the morphology of the block copolymer[6] or induce orientational changes, for example, in thin films[7] . In extreme cases, the block copolymer can undergo an order-disorder transition if the nanoparticle loading is high enough[8]. These experimental examples motivate us to use computer simulations to explain the complex behaviour of block copolymer nanocomposites.

The combination of interesting and useful applications, along with the complexity of its behaviour, motivates us to study block copolymer nanocomposite systems. Because the colloids do not act as mere passive fillers, non-trivial behaviour emerges. Even processes which are well understood can be hardly stufdied in detail, due to the limitation to perform experiments, with a very large parameter space at play: block copolymer properties, colloidal size and their number, polydispersity, etc. For instance, phase transitions induced by nanoparticles have been reported experimentally [6, 9], yet there is room to assert the exact phase diagram of a general BCP/NP system for a variety of parameters, such as block copolymer configuration, chemical composition of the NP, etc.

In recent years, non-spherical colloidal particles have been used, both in solution and mixed with block copolymers[10]. Shape-anisotropic nanoparticles such as nanorods or nanoplates introduce an additional degree of freedom per colloidal particle, which translates into a more complex assembly. The co-assembly of non-spherical particles with block copolymers results in extremely interesting materials, where colloids can be found to achieve high orientational[11]

and translational ordering [12].

Spherical particles with chemical anisotropy in its surface (patchy particle, for instance) have been created and studied in recent years. Janus nanoparticles have been found to segregate to interfaces in binary mixtures and self-assemble into interesting morphologies in solvents. The co-assembly of Janus nanoparticles in block copolymers is a promising way to achieve interface-segregated arrays of nanoparticles and substancial experimental effort has been made in that direction[13].

While other theoretical and computational methods have focused on the molecular details of the block copolymer, the intrinsically mesoscopic length scale of the BCP phases (lamella, cylinders, gyroid, etc) can be addressed with a coarse grained model that ignores many of the details of the polymer chain -strictly speaking, introduces such details through an effective model-, while focusing on the collective properties of the system.

A mesoscopic model that follows the Landau-Ginzburg free energy description of the system can be used to study block copolymer/nanoparticle systems. Furthermore, an efficient computer implementation allows us to address large systems. The need to simulate large systems is crucial, as many properties of the block copolymer nanocomsposite systems require several lattices periods to be studied. For example, Bockstaller et al[2] reported the aggregation of considerably large nanoparticles in domains of several micrometers. This length scale is much larger than a lamellar period and larger than the typical simulation length scale that can be achieved using, for instance, Self Consistent Field Theory[14] or Molecular Dynamics methods[15]. The model that will be presented here serves as a precursor to more detailed, microscopic models.

Outline of this work

Chapter 1 introduces the main elements of this research (colloids and block copolymers), their definitions, modelling and computer simulations. A general review of previous works on block copolymer nanocomposites is presented, while more specific references and be found in each chapter.

In **Chapter** 2 we describe the general model that will be used throughout this thesis. The computer simulation scheme is also described and put in context with alternative approaches to the study of block copolymer and colloids. In later chapters the model will be extended to simulate more complex systems, for which an specific model section will be included when necessary.

Chapter 3 constitutes a description of the parallel scheme that extends the previous serial code as explained in Chapter 2. This chapter contains an introduction to FORTRAN Coarrays to obtain an efficient parallel CDS code which can be compared with a previous version using MPI. Furthermore, a parallel complete CDS/Brownian Dynamic scheme is presented, validated and studied.

In **Chapter** 4 we compare several simulation results with experimental works involving spherical (circular in 2 dimensions) colloids in block copolymers. This serves as an introduction to the ability of our model to reproduce physical problems and a motivation for the rest of this thesis.

In **Chapter** 5 we perform a quantitative study of the morphology of block copolymers in the presence of colloidal particles. This is motivated by previous experiments and simulations and results in a complete study of the phase behaviour of block copolymers in the presence of nanoparticles. This is done by tuning the fraction of particles in the system, their chemical composition and the relative length scales relevant to the system.

Chapter 6 is devoted to the assembly of colloids in block copolymers. In this chapter we concentrate on the colloidal ordering while on Chapter 5 the morphology of the BCP was the main subject. Several instances of aggregation and phase-separation of colloids are tacked here.

In **Chapter** 7 we consider chemically inhomogeneous nanoparticles possessing two hemispheres of arbitrary different affinity. The amphiphilic-like properties of such particles are studied and compared with homogeneous NPs, mainly as they segregate to the interface between domains.

In **Chapter** 8 we consider the simplest case of anisotropic nanoparticles, motivated by experimental results involving nanorods. A model for ellipsoidal nanoparticles is presented and compared with experimental results, focusing on the formation of ordered colloidal configurations within one BCP domain.

In **Chapter** 9 we extend the anisotropic model to include a range of non-spherical shapes including rhomboids, squares and rectangles. Instances of colloidal assembly within one domain or within the interface are studied.

Chapter 10 is dedicated to three dimensional simulations of block copolymer nanocomposite systems. Here, we consider physical aspects which are intrinsically three dimensional, or where a two dimensional approach missed interesting aspects to study. Three dimensional organisation of colloids in ordered layers or kinetic pathways of colloid-induced phase transition in the BCP are studied here.

While each chapter contains a dedicated conclusion section, in **Chapter** 11 we present the main overall conclusions to this thesis as well as brief explanation on future perspectives.

In **Appendix** A we present the dimensionless version of the main dynamical equation used in this thesis. While this is relevant to the whole document, it is not an essential feature.

In **Appendix** B we derive and present several instances of nanoparticle distortion in the block copolymer profile. This is done using analytical approximations and numerical tools. This appendix can help understand some essential effective effects of the block copolymer in the presence of NPs.

In **Appendix** C we provide supporting information to Chapter 5 of the role of nanoparticle size on phase diagrams.

In **Appendix** D we provide supporting information to Chapter 9 on the derivation of a fitted potential.

CHAPTER 1

Background: Block Copolymers and Colloids

1.1 Introduction to soft matter

Polymers and colloids are part of a large group of materials called *soft matter*, along with liquid crystals, gels and surfactants, among others, as coined by Pierre-Gilles de Gennes in his Nobel Prize lecture in 1991. Soft materials are all easily deformable, meaning that relatively small external fields can lead to large responses. This is a consequence of the size of its building units. A typical gold nanoparticle, for instance, has a diameter in the realm of a few nanometers, much larger than the size of an atom[16]. These fascinating materials have attracted a lot of attention in the last few decades for, among other reasons, their role in biological materials. Lipids, for example, form the bilayer separating the inside of cells, creating a membrane.

Polymers and colloids will be the two main ingredients in this thesis. Nonetheless, features from other soft materials will be present in this work, such as the analysis of the orientational order in nematic-like liquid crystals in Chapter 8. Moreover, the assembly of particles with two chemically distinct faces will be studied in Chapter 7, which resembles the behaviour of amphiphilic surfactant particles at interfaces between liquids.

Polymers are chain-like macromolecules made of several repeated units called monomers [16]. The number of monomers in a chain can be considerably large, ranging from thousands up to tens of millions[17]. Polymers are extremely important in a vast range of materials, from plastics, rubbers textiles to biological macromolecules such as proteins. In the last-mentioned, amino acids are sequenced to form the protein chain. Their role in modern industry cannot be overestimated and a huge amount of research has been devoted to polymeric materials.

Polymers can exhibit extremely complex structures, originated, for instance, by chain branching. Different constituent units (chemical composition of the repeated units) and their number (molecular weight) add a further level of complexity into the polymer chain and results in a diverse and rich assembly behaviour. The branching and monomer arrangement is usually referred to as configuration of the chain. The conformation, instead, refers to the spatial arrangement of monomers. In this work we will restrict to linear (no branching) polymers with rich chemical properties due to the grafting of different (co)polymer chains into a single one.

The other ingredient of this research -along with polymers- are colloids. In particular, we will focus on colloidal nanoparticles (NPs), that is, relatively large (larger than ~ 1 nm) particles dispersed in a fluid. Colloidal particles can be found everywhere, for instance, used as dyers to colour water or in the case of milk, as globules of fat particles dispersed in water. More generally, a colloidal particle can be defined as a small solid particle or fluid droplet which is large enough to behave classically. This constitutes a lower bound to the typical length scale of colloids. Thus, the colloidal diameter must be above the atomic scale ($d > 10^{-9}m$). A colloidal particle suspended on a solution is additionally characterized by a dominance of random motion over sedimentation, which limits the upper bound of the colloidal particle length scale.

1.2 Block copolymers

A subfamily of polymers are called block copolymers (BCP). In such systems, monomers are grouped in blocks, which are joined covalently forming larger structures. Each block is a copolymer, and the overall structure of the block copolymer chain can range from simple A-*b*-B diblock copolymers [1] to virtually any complicated linked structures made of many different

[1] Throughout this thesis we will use indistinctly A-*b*-B, A-B BCP when referring to an arbitrary BCP, specially when BCP is symmetric and A or B monomers are exchangeable. When referring to a particular simulation, we may refer to the different blocks or domains as majority/minority, when applicable. To facilitate visualisation, we will also refer to them by the colouring when considering an specific snapshot.

copolymers. In this sense, the resulting macromolecule can be made of many different copolymer chains linked one onto the other, each one being made of a different monomer type. In Fig. 1.1 two simple schemes are shown for a diblock copolymer chain (top) and triblock copolymer (bottom).

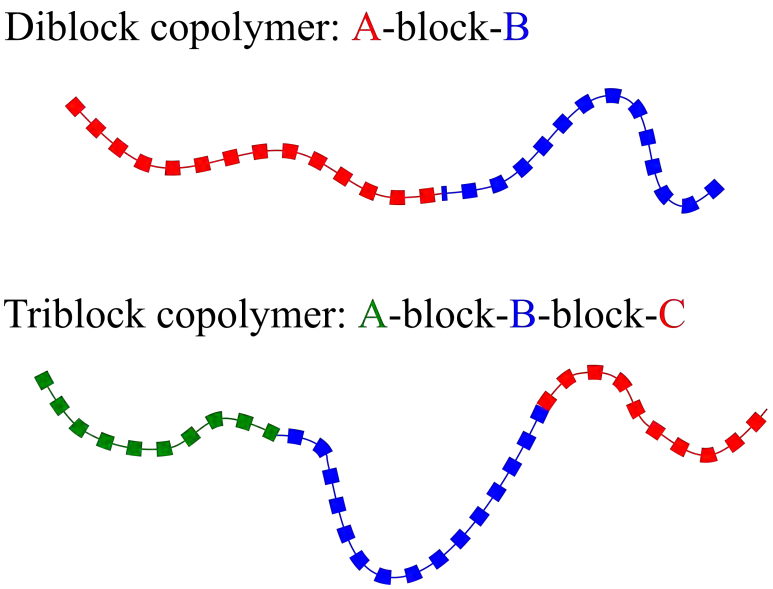

Figure 1.1: Simplified scheme of two kinds of (co)polymer chains: diblock copopolymer and triblock copolymer on top and bottom, respectively.

Block copolymer self-assembly can be used, for instance, in the creation of porous materials[18]. At high temperature block copolymer systems tend to appear in a disordered state. Below a certain order-disorder transition (ODT) temperature block copolymer display ordered mesophases, which arise from the tendency of dissimilar blocks to demix. At even lower temperatures we can find glassy structures, although these are not part of the scope of this work. When mixed in solution, block copolymers can appear forming micellar structures[19]. Similarly, block copolymers can be used as surfactants due to their inherent amphiphilic nature, serving as perfect compatibilizers at interfaces[20]. Apart from an homopolymer - a polymer chain made of simply one type of monomer- the simplest possible block copolymer is called an A-*b*-B diblock copolymer , in which an A-monomer chain and a B-monomer chain are joined together, as in Fig. 1.1, top. Typical examples of diblock copolymers are PMMA-*b*-PS or PS-*b*-PI. More complex architectures include triblock copolymers such as PS-*b*-PB-*b*-PI. A diblock copolymer in a selective solvent, for instance, will expose the most compatible block to the solvent while a core of insolvable monomers will be protected.

Enthalpic incompatibilities between dissimilar monomers can lead to the formation of phase separation in melts of polymers. However, macrophase separation (ie, as in oil and water mixtures) is prevented by the structural constraint imposed by the covalent link between chains in a BCP. This leads to a wide variety of ordered structures which are periodic in space, depending on the chemical incompatibility and the configuration of the individual chains. Restricting to diblock copolymers, the simplest mesoscale structure is originated by a near-symmetric chain in which the number of A and B monomers is similar. This lamellar morphology consists of alternating layers of A and B monomers. In equilibrium, a flat interface with a single director appears separating A-rich or B-rich domains. In simulations and experiments, often we can observe grains of cohesive orientations and defects in the boundaries between grains. An external field such as a electric field can help achieve a global orientation[21]. In Figure 1.2

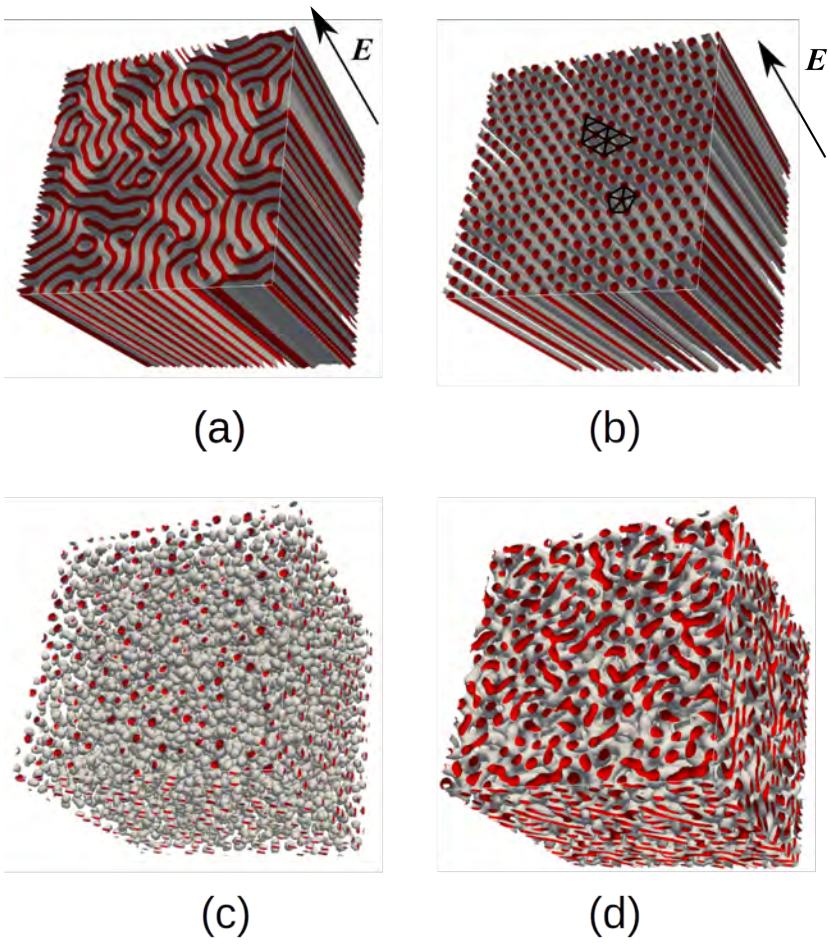

Figure 1.2: Snapshots of representative BCP morphologies. In order to assist visualisation, we show lamellae (a) and cylindrical phase (b), both under electric field. Spheres (c) and bi-continuous phase (d) are shown in the lower row.

(a) we can observe a typical layered lamellae structure. In other cases, the asymmetry in the monomer concentration of A and B can lead to the formation of hexagonally packed cylinders containing the minority phase, as in Fig. 1.2 (b) or spheres (c), also containing the rarest block in the melt. In both cases, the majority block forms a single continuous phase while minority blocks are confined into isolated domains [2] . Furthermore, more complex structures such as bi continuous can be found in the boundaries between phases. Using Self Consistent Field Theory (SCFT) it was possible to determine the phase diagram of a block copolymer melt [22, 23, 14] , as reproduced in Fig. 1.3.

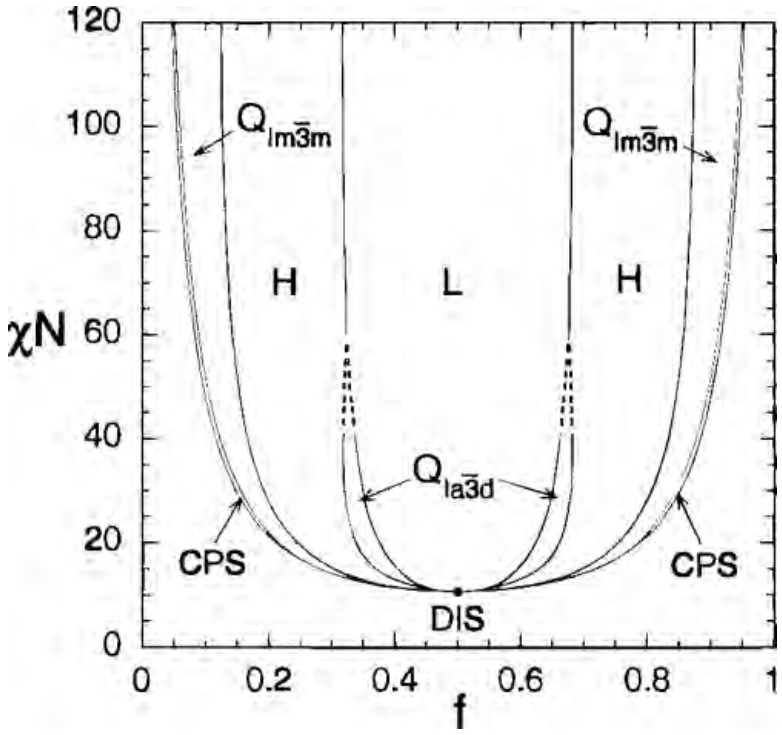

Figure 1.3: Phase diagram for a linear AB diblock copolymer using Self Consistent Field Theory (SCFT), depending on f_A, composition fraction of A monomers and χN, χ being the Flory-Huggins parameter-related to the incompatibility of A and B monomers- and N the degree of polymerization. Reprinted with permission from Matsen, M. W., and Bates, F. S., (1996) Macromolecules, 29(4), 1091-1098 Copyright 1996 American Chemical Society

Flory[24] and Huggins[25] developed a theory for the behaviour of polymer chains in a solvent, where an universal dimensionless parameter was derived. The Flory-Huggins segment-segment interaction parameter χ energy cost per contact

$$\chi = \frac{z}{k_B T}\left[u_{AB} - \frac{1}{2}\left(u_{AA} + u_{BB}\right)\right] \tag{1.1}$$

where z is the lattice coordination number and u_{ij} is the energy of contact between a segment i and j. A positive value of χ indicates a repulsion between two species. The ordered mesophases that block copolymer exhibit are largely the result of the competition between entropic and enthalpic interactions. As shown in equation 1.1, the Flory-Huggins parameter is inversely proportional to the temperature, meaning that high temperatures can lead to a order-disorder transition for a given block copolymer morphology. Similarly, the degree of polymerisation N plays a role in the assembly of block copolymer chains, as the number of contacts between

[2] In many experiments and simulations involving cylindrical phase, the system can be trapped in a disordered phase where cylinders are highly connected. This can also appear in early stages of the phase separation.

segments grows with N. A useful distinction is made between strong and weak segregation limits: for low incompatibilities -ie, low χN- the spatial variation of the composition profile is approximately sinusoidal in the direction normal to the lamellar plane. At higher values of χN, instead, a sharp profile separates the domains of purely A or purely B chains.

1.3 Block copolymer nanocomposites

The introduction of nanoparticles (NPs) into polymeric matrices has proved to result in better performing materials, such as the well-known case of carbon-black[26]. In the case of block-copolymer/ nanoparticle mixtures, adding colloids can reduce the critical electric field needed to induce alignment of the domains with the external electric field[5]. Block copolymer (BCP) materials are strongly periodic, serving as perfect templates for controlled placement of colloids[27, 28], resulting in highly ordered materials. In order to achieve a detailed control of the NP assembly within the BCP matrix it is necessary to be able to predict the phase behaviour of the overall system once nanoparticles are added, as the distribution of nanoparticles critically depends on the morphology of the BCP, and the morphology itself is modified by the presence of NPs.

Modifying the surface of the nanoparticles to make them compatible with one of the blocks can lead to a control of the localization of the NPs within BCP domains [1, 29, 30] or the interface between them [28, 31]. A precise control of the localisation can sometimes be problematic. For instance, Thomas et al demonstrated that the NP size plays an additional role in its localisation within the BCP domains[32]. Since the presence of nanoparticles can induce a phase transition of the BCP, it is crucial to determine the overall morphology of the polymer nanocomposite system.

1.4 Mesoscale modelling of block copolymers

During the 1980's several authors [33, 34, 35] derived the free energy functional of a BCP melt in terms of the local difference in volume fraction of the block copolymer. Ohta and Kawasaki used this result to obtain the 2/3 power law for the dependence of the domain dimension with the polarization index, N, the number of repeated units in the copolymer chain. In this description the diblock copolymer is treated like an incompressible fluid mixture, thus a single local order parameter describes the composition of the system completely. The global free energy is then a functional of this order parameter and its gradient. This is, in essence, a Ginzburg-Landau free energy with an additional long-range term accounting for the connectivity of the block copolymer chain. Therefore, taking the limit of an infinity long chain is equivalent to modelling binary mixtures [36]. This will become clear when the parameters of the model are explicitly shown in Chapter 2. In fact, the dynamic equation that will be used in this thesis was originally proposed for alloys melts. Using Self Consistent Field Theory (SCFT) other authors [14, 37, 23] constructed the phase diagram of a pure A-B diblock copolymer system, as can be found in Figure 1.3. Several ordered phases can be distinguished: (L) lamella, (G) gyroid, (C) cylindrical and (S) spherical, depending on the relative fraction of one type of monomer and the strength of their interactions. [3]

Oono and Puri applied a Cell Dynamic Simulation procedure to the phase separation of two components [38, 39] , while Oono and Bahiana later used this technique to study the

[3] More complex, often metaestable structures have been found in theory and experiments, but will not be part of this study.

phase separation of a block copolymer system [40, 41]. Ren and Hamley[42] later performed 3D simulations to completely reproduce the phase diagram of a BCP system.

The CDS method has been recently proved to be an efficient and versatile scheme to study large BCP systems, for example, under external fields such as electric or shear [43, 44, 45, 46, 47, 48, 49, 21] . In these cases the microscopic details of the system are of less importance compared to the target properties such as ordering, phase behaviour, global orientation, presence of defects, etc.

1.5 Simulations of BCP nanocomposites

BCP/NP systems have been widely studied with theoretical and computational techniques. Strong segregation theory have been used to analytically study the viscoelastic propeties of polymer nanocomposites [50, 51, 52] , finding a reduction of the lamella thickness when non-selective nanoparticles are present in the interface. A lamellar to bicontinuous transition was also reported, given by the vanishing of the bending modulus of the diblock copolymer, which is in accordance with experimental findings [31].

Simulation techniques such as Monte Carlo have been used [53, 54] to assert the assembly of BCP/NP systems on chemically nanopatterned substrates. In close resemblance with experiments, this method allowed to obtain well-ordered assembled nanoparticles. Furthermore, Huh et al[55] reported the changes in the diblock copolymer morphologies due to the presence of A-compatible nanoparticles in a diblock copolymer of arbitrary morphology (that is, exploring the composition ratio) using 3D simulations. This provided a phase diagram with only a few points. Molecular Dynamics [15] was used to study the phase behavior of BCP/NP systems for different Flory–Huggins parameter values using fixed symmetric diblock copolymers. It was also reported that nanoparticle localisation is increased with nanoparticle size, as was experimentally found by Bockstaller et al [32].

The aggregation of two kinds of nanoparticles within diblock copolymer was examined using Dissipative Particle Dynamics [56, 57, 58, 59], finding NP-assembly dependence on the lamella morphology, resulting in a transition to a complex phase. These simulation methods often require considerable computational time, thus limiting the simulation box to less than three or four periodic domains.

Self Consistent Field Theory [60, 61, 62, 63] has been widely used to study the segregation of nanoparticles within the diblock copolymer domains, again reporting the size-selectivity of NP localisation found in experiments[32]. Using SCFT Ginzburg et al [63, 64] explored the order-disorder transition of a binary polymer blend in the presence of A-compatible nanoparticles. While Lee et al[9] provided phase diagrams of the diblock copolymer morphology in terms of the composition ratio and the affinity of the nanoparticle, the volume fraction of nanoparticles was not explored.

The Cahn-Hillard equation [65, 66, 67] has been used to study the dynamical evolution of the phase separation, which is found to be slowed down by the presence of nanoparticles in the polymer blend. In these cases, a moderate volume fraction of nanoparticles that do not interact with each other is considered. A complete description of the interparticle interaction and the BCP/NP coupling was introduced by Pinna et al [68] and simulations were compared with experiments using the same model [69].

CHAPTER 2

Model: Hybrid Cell Dynamic/Brownian Dynamics Simulations

Abstract

Computational tools can be used to numerically solve the equations that describe a particular model for a system of block copolymers. While in Chapter 1 a multitude of approaches have been mentioned, here we provide a thorough description of the Cell Dynamic Simulation method. This is a fast, time-dependent mesoscopic numerical method that have successfully reproduced a large number of physical processes, namely, the phase separation of binary mixtures. Furthermore, its extension to block copolymer systems have provided insight over the equilibrium and dynamical properties of such systems. We present a further extension to model hybrid block copolymer/nanoparticle systems by means of Brownian dynamics. Although simple, this coupled method has proved to be computationally fast, thus, considerably large systems can be simulated, compared to other methods such as Molecular Dynamics or Self Consistent Field Theory.

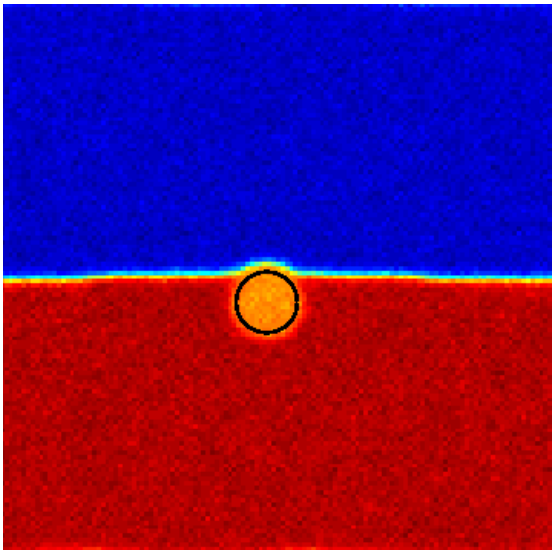

2.1 Introduction

In chapter 1 we have largely covered the historical context of polymer and block copolymer research.

2.2 Cell Dynamic Simulations

The evolution of the BCP/colloids system is determined by the excess free energy which can be separated as

$$\mathcal{F}_{tot} = \mathcal{F}_{pol} + \mathcal{F}_{cc} + \mathcal{F}_{cpl} \tag{2.1}$$

with $\mathcal{F}_{pol}$ being the free energy functional of the BCP melt, $\mathcal{F}_{cc}$ the colloid-colloid interaction and the last contribution being the coupling term between the block copolymer and the colloids.

2.2.1 Polymer Dynamics: Cell Dynamics Simulations

The diblock copolymer is characterized by the order parameter $\psi(\mathbf{r}, t)$ which represents the differences in the local volume fraction for the copolymer A and B with respect to the relative volume fraction of A monomers in the diblock, $f_0 = N_A/(N_A + N_B)$

$$\psi(\mathbf{r}, t) = \phi_A(\mathbf{r}, t) - \phi_B(\mathbf{r}, t) + (1 - 2f_0) \tag{2.2}$$

where $\phi_A(\mathbf{r}, t)$ and $\phi_B(\mathbf{r}, t)$ stand for the local volume fraction of A and B monomers, respectively

The order parameter must follow the continuity equation in order to satisfy the mass conservation of the polymer:

$$\frac{\partial \psi(\mathbf{r}, t)}{\partial t} = -\nabla \cdot \mathbf{j}(\mathbf{r}, t) \tag{2.3}$$

If the polymer relaxes diffusely towards equilibrium, the order parameter flux can be expressed in the form

$$\mathbf{j}(\mathbf{r}, t) = -M \ \nabla \mu(\mathbf{r}, t) \tag{2.4}$$

as a linear function of the order chemical potential

$$\mu(\mathbf{r}, t) = \frac{\delta \mathcal{F}_{tot}[\psi]}{\delta \psi} \tag{2.5}$$

Introducing these equations into the continuity equation and taking into account the thermal fluctuations we obtain the Cahn-Hilliard-Cook equation (CHC) [70, 71]

$$\frac{\partial \psi(\mathbf{r}, t)}{\partial t} = M \ \nabla^2 \left[\frac{\delta \mathcal{F}_{tot}[\psi]}{\delta \psi} \right] + \xi(\mathbf{r}, t) \tag{2.6}$$

where M is a phenomenological mobility constant and ξ is a white Gaussian random noise which satisfies the fluctuation-dissipation theorem[72], which can be expressed as

$$\langle \xi(\mathbf{r}, t) \xi(\mathbf{r}', t') \rangle = -k_B T M \nabla^2 \delta(\mathbf{r} - \mathbf{r}') \delta(t - t') \tag{2.7}$$

with a zero mean value $\langle \xi(\mathbf{r}, t) \rangle = 0$.

The copolymer free energy is a functional of the local order parameter which can be expressed

in units of the thermal energy k_BT as[33]

$$\mathcal{F}_{pol}[\psi(\mathbf{r})] = \int d\mathbf{r} \left[H(\psi) + \frac{1}{2}D|\nabla\psi|^2 \right] + \frac{1}{2}B \int d\mathbf{r} \int d\mathbf{r}' \; G(\mathbf{r}-\mathbf{r}')\psi(\mathbf{r})\psi(\mathbf{r}') \tag{2.8}$$

where the first and second terms are the short and the long-range interaction terms respectively, the coefficient D is a positive constant that accounts for the cost of local polymer concentration inhomogeneities, the Green function $G(\mathbf{r}-\mathbf{r}')$ for the laplace Equation satisfies $\nabla^2 G(\mathbf{r}-\mathbf{r}') = -\delta(\mathbf{r}-\mathbf{r}')$, B is a parameter that introduces a chain-length dependence to the free energy[73] and $H(\psi)$ is the local free energy [73, 74] ,

$$H(\psi) = \frac{1}{2}\left[-\tau_0 + A(1-2f_0)^2\right]\psi^2 + \frac{1}{3}v(1-2f_0)\psi^3 + \frac{1}{4}\psi^4 \tag{2.9}$$

where τ_0, A, v, u are phenomenological parameters[42] which can be related to the block-copolymer molecular specificity. Previous works[68, 42, 33] describe the connection of these effective parameters to the BCP molecular composition. $\tau' = -\tau_0 + A(1-2f_0)^2$, D and B can be expressed[33] in terms of degree of polymerization N, the segment length b and the Flory-Huggins parameter χ(inversely proportional to temperature). Parameters D and B -respectively governing lamella interface thickness and domain size- are written in dimensionless form by defining $\tilde{D} = D/(\delta x)^2$ and $\tilde{B} = B\ (\delta x)^2$ (for simplicity we will drop this notation), δx being the lattice spacing. Subsequently, we will consider u and v constants[35], which define all the parameters identifying the BCP local free energy $H(\psi)$. As previously shown [75, 21] , CDS can be used along with more detailed approaches like dynamics self-consistent field theory (DSCFT), using CDS as a precursor in exploring parameter space due to the computationally inexpensiveness nature of CDS.

The dynamic equations are numerically solved in a square lattice. We can express the time evolution of ψ , Equation 2.6, using CDS as

$$\psi(\mathbf{r}_i, t+1) = \psi(\mathbf{r}_i, t) - \delta t[\langle\langle\Gamma(\mathbf{r}_i, t)\rangle\rangle - \Gamma(\mathbf{r}_i, t) + B[1 - P(\mathbf{r}_i, t)\psi(\mathbf{r}_i, t)] - \eta\xi(\mathbf{r}_i, t)]] \tag{2.10}$$

$\mathbf{r}_i$ being the position of the node i at a time $t\delta t$, and the isotropic discrete laplacian for a quantity X is given by [40] $\frac{1}{a_0^2}[\langle\langle X\rangle\rangle - X]$. In two dimensions, we will use

$$\langle\langle\psi\rangle\rangle = \frac{1}{6}\sum_{NN}\psi + \frac{1}{12}\sum_{NNN}\psi \tag{2.11}$$

while in three dimensions ,

$$\langle\langle\psi\rangle\rangle = \frac{6}{80}\sum_{NN}\psi + \frac{3}{80}\sum_{NNN}\psi + \frac{1}{80}\sum_{NNNN}\psi \tag{2.12}$$

NN, NNN, NNNN meaning nearest neighbors, next-nearest neighbors, and next-next-nearest neighbors, respectively.

In Equation 2.10 we have introduced the auxiliary function

$$\Gamma(\mathbf{r}, t) = g(\psi(\mathbf{r}, t)) - \psi(\mathbf{r}, t) + D\left[\langle\langle\psi(\mathbf{r}, t)\rangle\rangle - \psi(\mathbf{r}, t)\right] \tag{2.13}$$

and also, the map function [41, 42]

$$g(\psi) = -\tau'\psi - v(1-2f_0)\psi^2 - u\psi^3 \tag{2.14}$$

Contrary to previous CDS models [76, 74] , in Equation 2.10 we have introduced a function $P(\mathbf{r},t)$ that takes into account the volume excluded by the colloid particle, with values $P=0$ in a unbound medium and $P=1$ inside a solid particle.

The CDS model for block copolymer melts has been extended to include external electric fields and shear flow [77]. In this thesis there will be brief mentions to an external electric field, even though it is used mainly to produce simulations with high global ordering, mainly for visualisation purposes. [1] In such a case, we follow Refs [76, 79] to introduce a generalised dynamic equation

$$\frac{\partial\psi(\mathbf{r},t)}{\partial t} = M\ \nabla^2\left[\frac{\delta\mathcal{F}_{tot}[\psi]}{\delta\psi}\right] + \xi(\mathbf{r},t) + \tilde{\alpha}\nabla_x^2\psi \tag{2.15}$$

where

$$\tilde{\alpha} = \frac{\epsilon_0 v_0 E_0}{k_B T}\frac{(\epsilon_A-\epsilon_B)^2}{\epsilon_A f+\epsilon_B(1-f_0)} \tag{2.16}$$

with ϵ_0 the vacuum permittivity,v_0 is the volume of one polymer chain, ϵ_A and ϵ_B are the dielectric constant of blocks A and B, respectively. Finally, E_0 is the strength of the applied electric field.

2.2.2 Colloid Dynamics: Brownian Motion

In addition to the described continuous description of the polymer melt we want to model the individual motion of a suspension of N particles in a block copolymer. In order to facilitate the polymer/colloid coupling description, we assign a continuous field that represents the particles[80] : an undeformable tagged field $\psi_{c,i}$ for a particle i centered around the position $\mathbf{R}_i$ (not restricted to lattice nodes) that changes continuously in space while moving rigidly around particle i. For computer efficiency it is convenient to introduce a field that is compact. In addition, in order to avoid non-finite values for the derivative of $\psi_{c,i}$, we select a form

$$\psi_{c,i} = \exp\left[1-\frac{1}{1-\left(\frac{|\mathbf{r}-\mathbf{R}_i|}{R_i^{\text{eff}}}\right)^{\alpha}}\right] \tag{2.17}$$

which allows for a cutoff distance at R_i^{eff}, which is defined in terms of the hard-core radius as $R_i^{\text{eff}} = R_i^0\,(1+1/\ln 2)^{1/\alpha}$, meaning that the tagged field has decreased to $1/2$ at R_0^i. The parameter α can be tuned to modify the sharpness of the field as we can see in Figure 2.1. Continuity of both ψ_i^0 and its derivative holds if we use Equation 2.17.

Summarizing, the overall colloidal suspension is described through the superposition of all the contributions by each particles as in

$$\psi_c(\mathbf{r},t) = \sum_{i=1}^{N}\psi_{c,i}(\mathbf{r},t) \tag{2.18}$$

For the colloid/colloid interaction we propose a pairwise interaction derived from a Yukawa potential,

$$V(\mathbf{R}_i,\mathbf{R}_j) = U_0\left\{\frac{\exp\left[-\alpha_0\left(\frac{R_{ij}}{R_{ij}^0}-1\right)\right]}{\frac{R_{ij}}{R_{ij}^0}+\beta_0} - \frac{e^{-\eta_1}}{\frac{\eta_1}{\alpha_0}+1+\beta_0}\right\} \tag{2.19}$$

where $R_{ij} = |\mathbf{R}_i-\mathbf{R}_j|$ is the distance between the center of mass of the colloids and $R_{ij}^0 = R_i^0+R_j^0$ is the distance between two particles when they touch as hard spheres. Parameter α_0

[1] The reader is referred to Ref [78] for a complete study of electric field in a block copolymer nanocomposite.

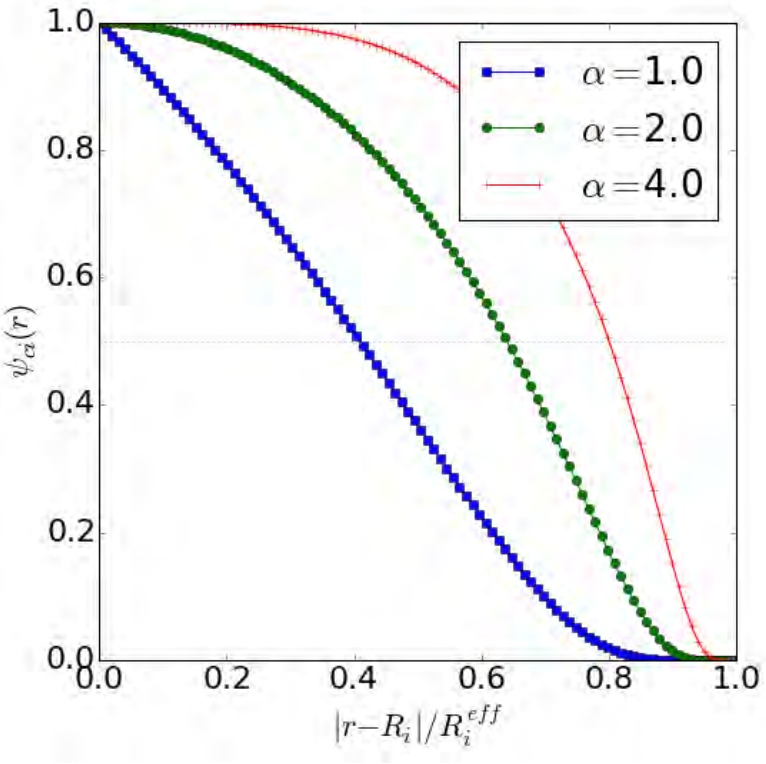

Figure 2.1: Tagged field ψ_{ci} of one particle for several values of α. The horizontal line cuts ψ_{ci} at the distance we consider the hard-core radius of the colloid R_i^0 .

determines the steepness of the potential while β_0 prevents the potential from divergence for complete overlap. A cut-off is introduced for computer efficiency at R_c^*, written in terms of η_1 as

$$\frac{R_c^*}{R_{ij}^0} = 1 + \frac{\eta_1}{\alpha_0} \tag{2.20}$$

Given this potential the pairwise colloidal force can be derived as $\mathbf{F}_i^{cc} = -\frac{\partial}{\partial \mathbf{R}_i}\mathcal{F}_{cc}$ and thus the Equation of motion in a Langevin dynamics scheme would be

$$m_i \frac{d\mathbf{v}_i}{dt} = -\gamma_i \mathbf{v}_i + \mathbf{F}_i^{tot} + \sqrt{2k_B T \gamma_i}\xi \tag{2.21}$$

with m_i as the particle's mass, $\mathbf{F}_i^{tot}$ is the total force done both by the surrounding polymer as by the rest of the colloids, while γ_i stands for the friction exerted by the polymer melt. The thermal motion of the colloids is determined by the temperature through the random term ξ_i, with correlations $< \xi_i(t) >= 0$ and $< \xi_i(t), \xi_j(t') >= \delta_{ij}\delta(t-t')$. If we neglect inertia, the Langevin equation reduces, in this overdamped regime, to the Brownian dynamic equation that governs the colloidal dynamics

$$\mathbf{v}_i = \frac{1}{\gamma_i}\left(\mathbf{F}_i^{cc} + \mathbf{F}_i^{cpl} + \sqrt{2k_B T \gamma_i}\xi\right) \tag{2.22}$$

2.2.3 Polymer/Colloid interaction

The interaction between the polymer and colloids is included through a contribution to the free energy $\mathcal{F}_{cpl}$, which must take into account the fact that colloids may have a preference for

one of the components of the block copolymer. The simplest free energy that satisfies that is

$$\mathcal{F}_{cpl} = \sum_{i=1}^{N} \sigma \int d\mathbf{r}\ \psi_{c,i}(\mathbf{r}) \left[\psi(\mathbf{r}) - \psi_0^i\right]^2 \tag{2.23}$$

where σ defines the strength of the interaction between polymer and colloids, and ψ_0^i describes the affinity of particle i with one of the copolymer blocks. The value of ψ_0^i stands for the preferred order parameter value for the NP, thus minimising the coupling free energy. $\psi_0^i = 0$ will result in neutral NP's while positive or negative values of the affinity means a preference for one of the blocks in the BCP. The affinity is associated with the chemical compatibility of the NP with the monomers.

Associated with this term in the free energy there is a corresponding additional force acting on each colloid. For particle i, the force felt due to the nearby polymer inhomogeneities is

$$\mathbf{F}_i^{cpl} = -\sigma \int d\mathbf{r}\ \left[\psi(\mathbf{r}) - \psi_0^i\right]^2 \frac{\psi_{c,i}(\mathbf{r})}{\left[1 - \left(\frac{|\mathbf{r}-\mathbf{R}_i|}{R_i^{\text{eff}}}\right)^{\alpha}\right]^2} \frac{\alpha}{R_i^{\text{eff}\alpha}} |\mathbf{r} - \mathbf{R}_i|^{\alpha-1} \frac{\mathbf{r} - \mathbf{R}_i}{\mathbf{r} - \mathbf{R}_i|} \tag{2.24}$$

and the corresponding term in the copolymer chemical potential that colloids induce in the copolymer dynamics is

$$\mu_{cpl} = \frac{\delta \mathcal{F}_{cpl}}{\delta \psi} = 2\sigma \sum_{i=1}^{N}\ \psi_{c,i}(\mathbf{r}) \left[\psi(\mathbf{r}) - \psi_0^i\right] \tag{2.25}$$

As opposed to previous approaches[65, 66, 67] , we treat individual colloids through a soft interaction which allows for a simpler computational treatment and a more straight-forward interpretation of the interactions both between colloids as with the copolymer medium.

Two characteristic time scales appear in our model. BCP diffusive time scale is given by[81] $\delta x^2/M$ while the colloidal diffusion constant $D = k_B T/\gamma$ sets the NP's diffusive time scale as R_0^2/D. Periodic boundary conditions will be used throughout this thesis, both in two and three dimensional simulations.

Throughout this thesis lengths will be presented in grid points units, unless explicitly expressed. The block copolymer period can be derived from parameter B, as shown in Appendix A. Typical values $B = 0.002$ and $B = 0.02$ result in BCP periods $H \approx 16$ and $H \approx 8$, respectively. The colloid-colloid interaction parameters will be fixed as $\alpha_0 = 1$, $\beta_0 = 0$ and $\eta_1 = 0$ unless otherwise specified.

2.3 Conclusions and overview

A basic model that will be used throughout this thesis has been presented. In the following chapters we will make use of this model -Chapters 4, 5 and 6 - to study 2D BCP/NP systems. On top of that, we will extend the current serial code into a three-dimensional parallel scheme in chapter 3 to study three dimensional systems in Chapter 10. After that, the model will be modified to extend the analysis to more complex nanoparticles in Chapters 8, 9 and 7.

Serving as a starting point, the presented hybrid CDS/BD scheme is a relatively fast model that can achieve large system sizes at reasonable simulation times. The mesoscale nature of this scheme makes it perfect to study the dynamical and equilibrium properties of a BCP/NP mixture over large length scales and long time scales. This model is nonetheless unsuitable to assert microscopic properties below the nanometer scale.

CHAPTER 3

Parallel Cell Dynamics/Brownian Dynamics

Abstract

Computer simulations of realistic system sizes often require considerable elapsed times. The use of several CPUs can reduce the needed time, ideally by a factor of the number of processors. We present a parallel computation method using FORTRAN Coarrays. It has been implemented and tested both for purely block copolymer systems and more complex hybrid block copolymer/-nanoparticle systems. The scaling of the parallel CDS displays no drawbacks over MPI and provides an example of the simplicity of the Coarray approach. The code has been tested on several architectures and compilers. The hybrid block copolymer nanocomposite parallel scheme can achieve -to our knowledge- the largest system sizes in the literature, in terms of BCP periods.

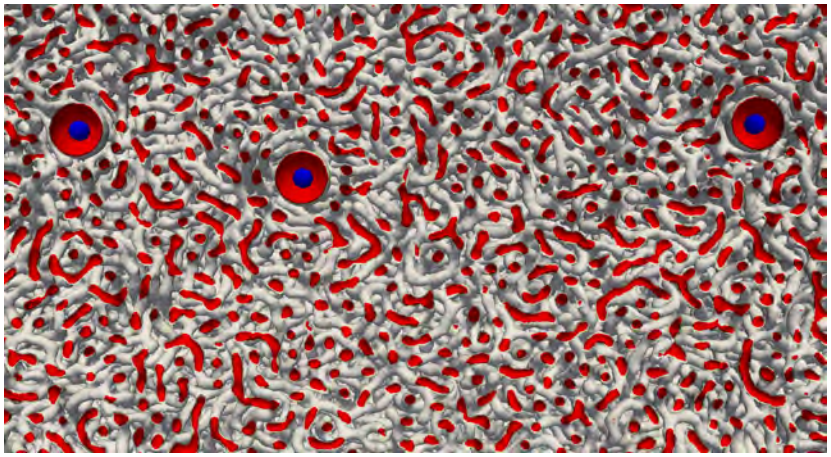

3.1 Introduction

The field of High Performance Computing (HPC) has dedicated enormous research into the efficient solution of differential equations, which are ubiquitous in the description of most systems. In Soft Matter physics there has been a considerable effort to develop simulation techniques that allow to mimic experimental length and time scales, particularly when making use of mesoscopic coarse grained methods.

Simulations of BCP/NP composite systems generally involve up to less than 5 BCP periods, while typical experimental images can span up to several hundreds. Moreover, many physically relevant mechanisms require taking into account large length scales, such as the ordering of BCP in the presence of NPs. In order to address such problems, larger box sizes are crucial and efficient programs are needed.

Parallelisation -use of two or more computer CPUs- has become a standard way to reduce the computational time needed to perform a simulation. By sharing the workload between several processing units, the overall time required to perform a job can be considerably reduced. A program can be divided into serial and a parallel part. Ideally, the parallel part of a computer program can be efficiently speed-up as many times as the number of processors involved. In most cases, communications between processors introduce latencies in the parallel scheme. An efficient parallel code should make use of an adequate communication mechanism between processors. Moreover, the distribution of tasks among processors are balanced in order to avoid some processors waiting for others to finish their tasks.

Coarray Fortran (CAF) is a parallelisation technique introduced in recent versions of the Fortran standard, which allow to perform parallel computing requiring minimal changes in a serial code[86]. CAF is an abstraction of Message Passing Interface (MPI) that simplifies the treatment of scalars or multidimensional arrays by creating several images which execute a program asynchronously[87] . Moreover, CAF uses distributed memory, meaning that each image or processor has its own workspace and communications between processors should be explicitly called. In fact, FORTRAN Coarrays belongs to the parallel model called partitioned global address space (PGAS). In CAF, a standard variable is purely local to the current image (processor), while a coarray can be accessed from remote images. In recent years there has been a growing number of programs using CAF due to the simplicity of its approach and the popularity of Fortran in the field of HPC. The OpenCoarrays project, for instance has introduced wrapper compiler and executable launchers among other utilities[87]. CAF performance has been compared with MPI, finding no drawback in the use of CAF over MPI [88].

3.2 Model

3.2.1 Parallel CDS scheme

Fortran coarrays provides an efficient abstraction of the MPI parallelisation scheme. It naturally allows for a partition of a large system into smaller parts, which are divided into images. Each image performs a copy of the whole program, except from user-specified conditions (see if condition below). While each image has its own workspace, codimensions can be used to share values across images. For instance, the next example shows a simple communication across processors. While all images execute the program, only image 1 prints to the screen.

```
implicit none ! Requires all variables to be explicitly defined
integer :: I  ! integer variable which is exclusive to each image
```

```
real :: x[*]  ! defines a real variable x which can be shared
! this co-scalar has a single codimension, which is
! automatically assigned to the number of images at runtime
! There will be N_{images} number copies of x
I = this_image() ! this is an index of the processor.
                              ! It is an intrinsic CAF function
sync all        ! all images must be synchronized at this point
x=x[1] + I ! Cross-image communication. We read from image 1
if (this_image().eq.1) then
  do k=1,num_images() ! looping over all images.
     ! From Image 1, we loop over all images to print the value
     ! of x, reading from image 1
     print*, 'Image=',k,'x(k)=',x[k]
  enddo
endif
```

A more complex partition of the system involves a three-dimensional partition of the system into N_x, N_y, N_z images, which can be performed as

```
! ...
! we declare the order parameter array psi as a 3D allocatable array
 real, dimension(:,:,:),codimension[:,:,:], allocatable :: psi
!....
! ... we partition the system and create appropriate variables
! DeltaX,DeltaY,DeltaZ
allocate(psi(DeltaX+2,DeltaY+2,DeltaZ+2)[nx,ny,*])
! +2 extra grid points are allocated to copy information
! from neighboring images
! [Nx,Ny,*] describes the partition of images.
```

Thanks to this partition utility, we break-up the system size $V = L_x \times L_y \times L_z$ into $n_{images} = N_x \times N_y \times N_z$ images with one processor per image. Images are accordingly distributed such that each partition spans a region of system space $V_{partition} = \Delta_x \Delta_y \Delta_z$ with $\Delta_\alpha = L_\alpha / N_\alpha$ and $\alpha = x, y$ and z. Computationally, each image possess a local $\psi_{i,j,k}$ version of the order parameter scalar field. This local image is allocated a size $(\Delta_x + 2) \times (\Delta_y + 2) \times (\Delta_z + 2)$, in order to allow space to read from neighbouring processors. Ghost points are indeed needed only in the exchange of information required to calculate the Laplacian in the Cahn-Hilliard equation. These communications are only done across neighbouring images. Because the CDS scheme is strongly short range, we do not require any long range communication as in Fast Fourier Transforms [81].

Figure 3.1 shows a simple two dimensional scheme of the communication between images. Image 2 reads the boundary points of the rest of images into its ghost points, taking into account periodic boundary conditions. Non-square partitions are equally valid while a generalised three-dimensional communication scheme involves reading of boundary corners, edges and sides of the surrounding partitions.

By partitioning the system in this way and having each image allocating only their local nodes plus ghost points, we are optimising the memory usage during simulations. Information is not repeated across images except for ghost points. In summary, we have presented a paralelisation scheme requiring a minimal change of the original serial code, thanks to the CAF

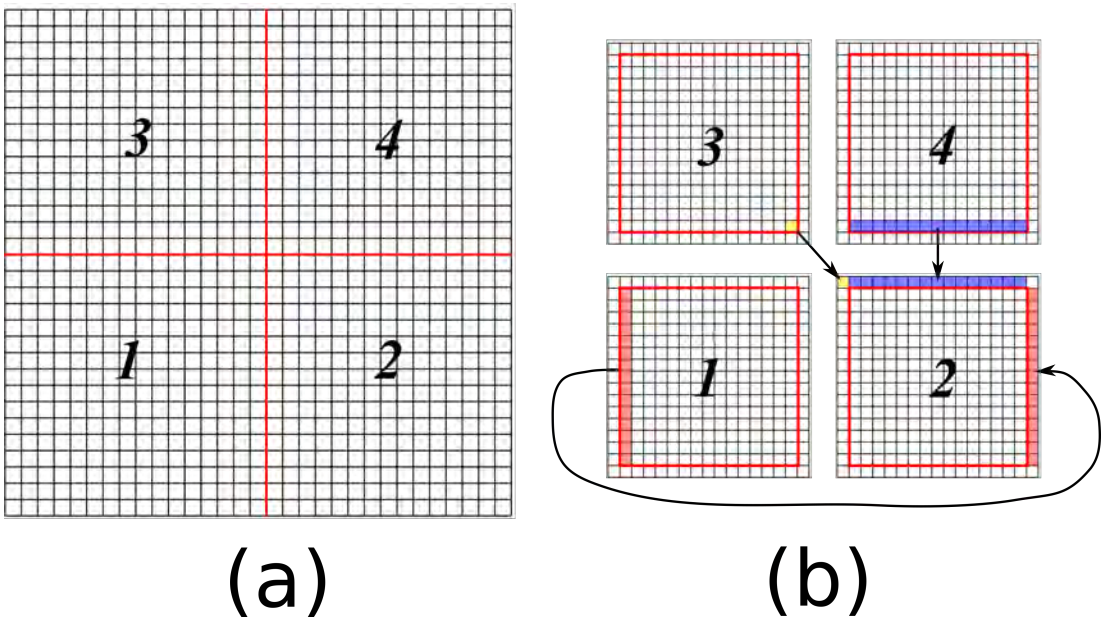

Figure 3.1: Example of a 64^2 2D spatial decomposition. In (a) we show the serial equivalent of the system, with the four processor subregions in red. In (b) we include the ghost points, and for processor $P = 2$ we show the mechanism of read and copy from surrounding processors.

utility in Fortran.

3.2.2 Parallel hybrid CDS/Brownian Dynamics code

Adding NPs into a parallel CDS simulation model requires an efficient parallelisation of the calculation of the BCP/NP coupling (forces and chemical potential) along with the interparticle forces. Using CAF, it is essential to have an spatial decomposition of the system. We choose to respect the same spatial decomposition into N_x, N_y, N_z processors, respectively assigned to $\Delta_x, \Delta_y, \Delta_z$ subregion of the system, as described in the previous section. To this end it is desirable to use a Cell List method [89], in which the system size is divided into cells and particles are sorted into linked list. We use a number $N_{cells} = M_x^c M_y^c M_z^c$ number of cells. Therefore, each processor is dedicated to particles in the region occupied by their respective cells.

Firstly, the calculation of the BCP/NP coupling requires N_p summations (triple loops) around the centre of each particle. In order to minimise the number of processor communications, processor s performs the summation only for particles that are within the subregion assigned to it. In order to avoid later double counting of forces and chemical potential, we perform the summation strictly within that region. Furthermore, a neighbouring particle whose centre of mass is not within the processor's region can overlap within it. For this reason, each processor performs a search throughout neighbouring cells (ie, closest cells within neighbouring processors). Once that list is made, we need to again check which of those particles are indeed overlapping the processor's partition.

The interparticle forces are also calculated making use of the Cell List algorithm as described by Allen[89]. In order to make an efficient use of the CPU resources each processor performs NP-NP force calculation only for the particles within its partition.

3.2.3 Analysing parallelisation

In this section we have presented a parallel implementation of the CDS scheme. In order to analyse the efficiency of parallel programs, it is common to test the scaling of the code with the number of processors for a fixed system size (strong scaling) or for a fixed amount of elements per processor (weak scaling). The speed-up and the efficiency are defined as

$$S(m, n_p) = \frac{T(m, 1)}{T(m, n_p)} \tag{3.1a}$$

$$E(m, n_p) = \frac{T(m, 1)}{PT(m, n_p)} \tag{3.1b}$$

where m represents the scale of the problem. In the case of CDS, it can refer to the number of grid points.

3.3 Results

For clarity, we display the available resources along with technical information which can be useful to compare with other parallel implementations.

- **Archer**, UK supercomputer. Cray XC30 MPP supercomputer. Each node has two 12-core Intel Ivy Bridge. Each node has a total of 64 GB of memory. [1]
- **Mare Nostrum** BarcelonaSuperComputer, Spain. 2 sockets Intel Xeon Platinum 8160 CPU with 24 cores each @ 2.10GHz for a total of 48 cores per node . [2]
- **Lincoln2-UoL**. Centre for Computational Physics (U. of Lincoln) Cluster. 4 nodes with AMD Opteron 6348, 48 CPU cores per node. 126 GB RAM.

3.3.1 Scaling of CDS model

In the previous section we have presented a parallel implementation of the Cell Dynamic Simulation scheme using FORTRAN Coarrays. Furthermore, we have extended the purely polymeric parallel scheme into a CDS/Brownian Dynamic code. Firstly, we need to study the scalability of this code. An appropriate parallel implementation should ideally reduce the required time with the number of processors involved. In order to test this, we can explore the effect of parallelisation of a system with size $V = L_x L_y L_z$ into $n_p = N_x N_y N_z$ processors.

In Fig 3.2 we plot the strong scaling of elapsed time for three different machines: University of Lincoln cluster, Archer Supercomputer and Mare Nostrum for (a), (b) and (c), respectively. We also consider three system sizes $V = 128^3, 256^3$ and 512^3. We aim to observe how linear (ideal) is the scaling with a fixed system size. In dotted lines, we plot the ideal scaling. In all cases we are considering only one computer node which may contain a different number of cores. In all machines used, the scaling is fairly linear, specially as the system size grows ($V = 512^3$). This is expected, as larger systems means that the communications are less relevant over the total computational time.

In Fig 3.2 (a) the OpenCoarrays wrapper is used [87] with gfortran. The scaling here can be found to be relatively poor compared to other machines, which can be related to a lower quality communications between processors as compared to national supercomputers Archer (UK) and

[1] The author is grateful to Archer Supercomputer which allowed 1 year and 1200 kAUs access through the ARCHER Driving Test.
[2] The author is grateful to the HPC Europa 3 scheme for allowing access to BSC for 50000 hrs

Mare Nostrum (Spain). Indeed, the scaling drops to $S \sim 12$ for 32 processors and $V = 128^3$, as compared to $S \sim 20$ using Mare Nostrum. In this machine (UoL cluster), communications play a heavier role in the overall time. Fig. 3.2 (b) shows a good scaling using Archer with the CRAY compiler, even though restricting to one single node means we cannot check beyond $n_p = 24$ processors. On the contrary, using Mare Nostrum in Fig. 3.2 we can observe a considerably good scaling even at $n_p = 32$ processors. We observe instances of scaling above the ideal. This can be explained as follows: even though we allow the $n_p = 1$ case to use 8 memory cores, spanning over 32 processors permits each processor to use a lower amount of memory. In conclusion, we can observe a reasonably good scaling behaviour. In fact, the scaling is closer to idea than in previous MPI parallel implementations [81].

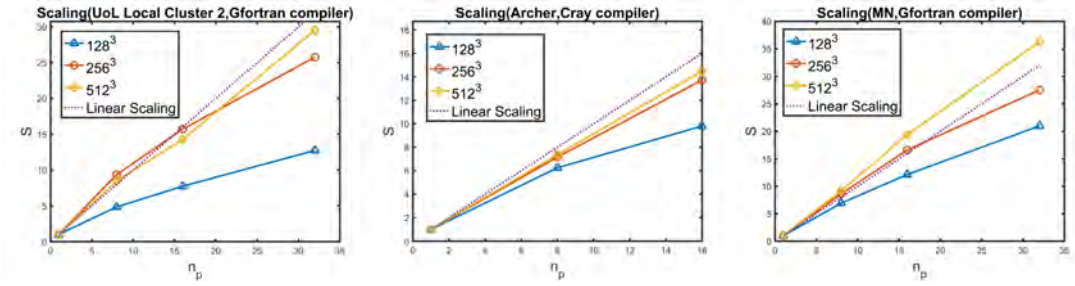

Figure 3.2: Strong scaling for the purely polymeric CDS parallel scheme in three supercomputers (see top titles) and a number n_p of processors for three system sizes (see legends). These simulations were performed in a single node.

In Fig. 3.3 we display the efficiency as defined in Eq. 3.1b for several distributions of processors $n_p = N_x N_y N_z$ along X,Y and Z, respectively. Although changes in the relative elapsed time are not extreme, an optimal speed-up can be achieved using a non-square partition (ie different from $N_x = N_y = N_z$). In particular, we can observe that a highly efficient arrangement can be found in $1, 4, 2$. FORTRAN access to arrays in memory privileges a minimal jump in the Z direction. For this reason, it generally recommended to perform DO loops in the order Z-Y-X. This can explain the hierarchy of elapsed time for $S(118 > S(181) > S(811)$. Further understanding of the more complex arrangements require knowledge over the particular architecture of the BSC nodes.

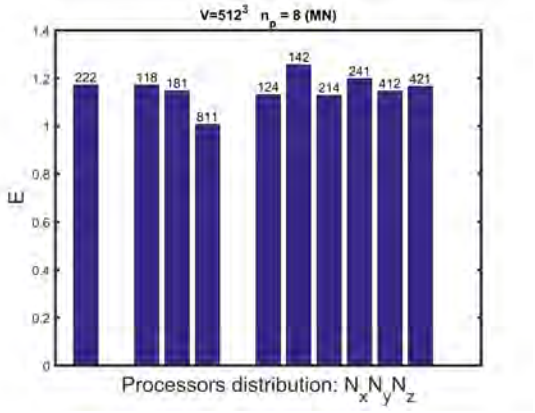

Figure 3.3: Comparison of the efficiency of several processor distributions in a 512^3 system using $n_p = 8$ processors in different ways along the X,Y and Z axis.

Modern parallel implementations can span over thousands of computer cores. In such a

case, the communications between different nodes are crucial as they are performed through a network, which generally introduce a higher penalty on exchanges of information. In Fig. 3.4 we plot the elapsed time for several number of processors using Mare Nostrum and the intel compiler[3] . Here, we are testing the weak scaling of the code, ie. the elapsed time for a fixed amount of elements per processor. In this sense, the system size is tuned to lead to an equal amount of grid points per processor. We can observe an initial grow in the elapsed time as we increase the number of processors from 8 up to 64. For higher number of processors the elapsed time remains approximately constant. Thus, the parallel implementation shows an initial decrease in the quality of the performance, but it is kept constant for higher number of processors. It must be noted that the elapsed time is heavily dependent on the distribution of processors for multi-node calculations. Changes of up to 55% can be observed. For multi-node calculations, the most efficient calculation involved a parallelisation along a single dimension, as it minimised the number of communications along different nodes.

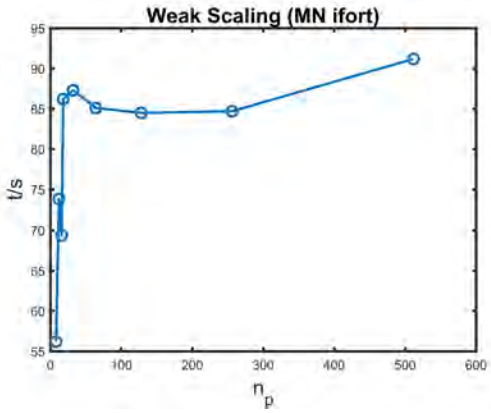

Figure 3.4: Weak scaling of the CDS parallel code at Mare Nostrum. The number of grid points per processors is kept constant and equal to 256^3. Processors are spanned from single node to multi-node.

The cylindrical morphology under a vertical electric field found in Figure 3.5 is obtained using parameters found in reference [76]: $\tilde{\alpha} = 0.2, B = 0.02, A = 1.5, D = 0.5, \tau = 0.3, f = 0.40, u = 0.5, v = 1.5$ in a $V = 128^3$ box. Cylinders are formed along then applied electric field, while a hexagonal organisation of cylinders can be roughly observed. This is in accordance with Figure 4c in Reference [76] and serves as a validation of our parallel model.

3.3.2 Scaling of hybrid CDS/BD

The scaling of the hybrid CDS/Brownian Dynamics scheme is more complex than the purely polymeric program. For this reason, it is useful to separately explore many of the important contributions to the total elapsed time. Firstly, we can study the scaling of the program with the number of particles in the system. Figure 3.6 shows the elapsed time in function of the number of particles in the system for a considerably large system $V = 128^3$ and 8 processors. The scaling is seen to be strongly linear with the number of particles. This is expected, as the two main colloid-dependent contributions to the time of the program are: colloid-colloid interaction and coupling between BCP/NP. The colloid-colloid calculation of forces naively scale with N_p^2,

[3]The OpenCoarrays wrapper with GNU FORTRAN showed an unexpected drop in the speed-up for calculations involving two or more nodes. A related issue had been reported before `https://github.com/sourceryinstitute/OpenCoarrays/issues/560`. Meanwhile, the single-node GNU OpenCoarrays wrapper has shown better performance over Intel compiler, which motivates us to use GNU OpenCoarrays wrapper for simple, one-node calculations while Intel compiler for large, multi-node simulations.

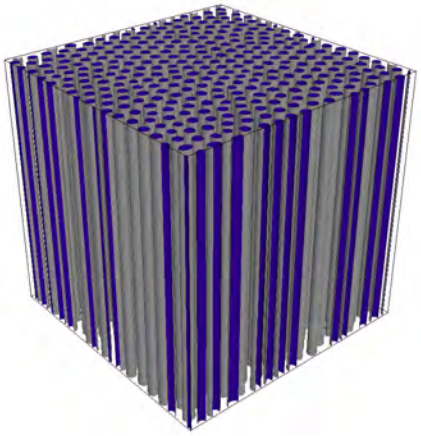

Figure 3.5: Cylinder-forming BCP under an electric field. Variables are obtained from Ref [76]. This Figure can be compared with Fig. 4 (b) in Ref [81] and Fig. 4 (c) in Ref [76] to validate our parallel implementation.

but can be reduced to a N_p^1 scaling by using a cell list scheme [89]. The coupling contribution is linear with N_p -by definition-as it consists of a sum of each particle's contribution.

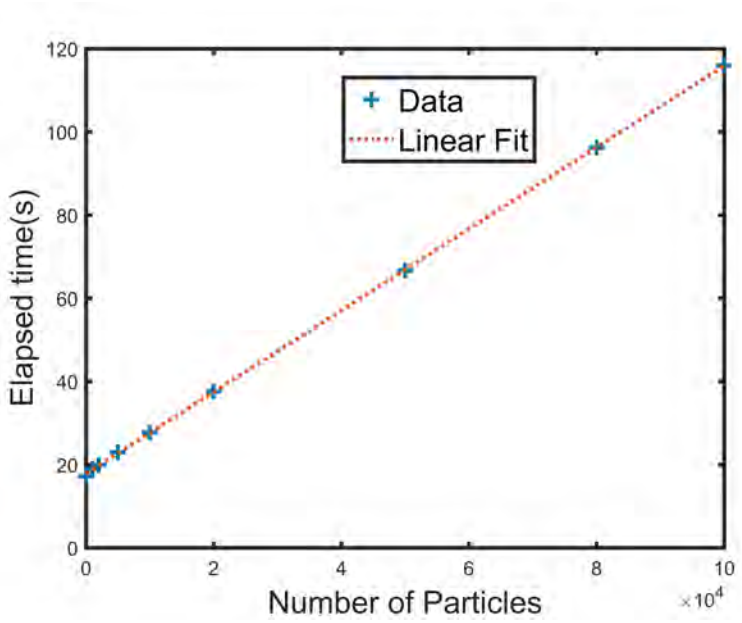

Figure 3.6: Scaling of the elapsed time with respect to the number of particles N_p. The number of processors and system sizes is fixed: $n_p = 8$,$V = 128^3$. Particles are sized $R_0 = 1.0$. This simulations are performed in Archer.

One of the conclusions from Figure 3.6 is that the NP contribution to the program time is comparable with the BCP part, when high concentrations of particles are chosen. For this reason, it is essential to have an efficient NP part of the program. In a second step, we can differentiate between the coupling and the colloid-colloid interaction time. Figure 3.7 shows the elapsed time with respect to N_p with $\sigma = 1$ and 0. The present program skips the coupling calculations if σ is set to zero. Therefore, it is an easy way to separate different contributions. We can observe that both the total and the colloid-colloid runs strongly depend linearly with N_p, while the coupling is clearly the most important contribution. This suggests

that the cell-list scheme that we use is considerably efficient as it is sub-dominant over the more computationally-heavy coupling calculations. It also motivates a more detailed exploration of the coupling parallelisation.

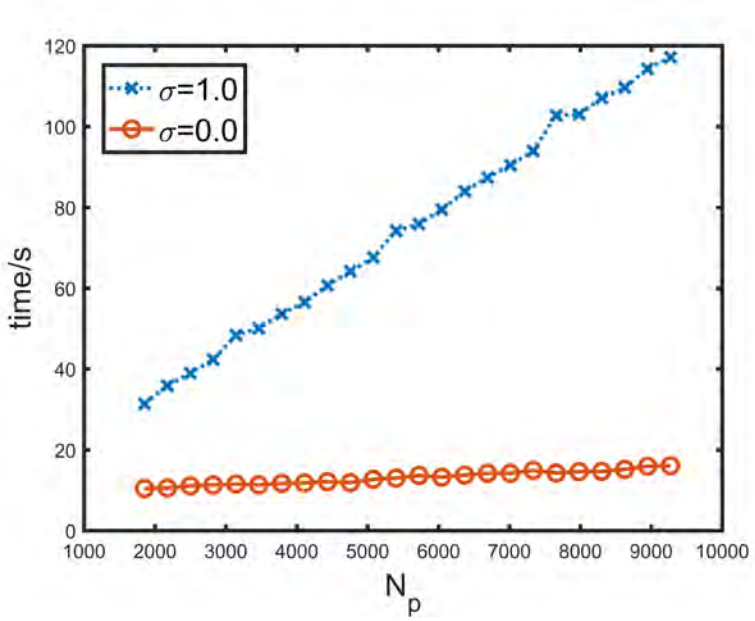

Figure 3.7: Simulation time a parallalised code ($n_p = 8$, Lincoln 2) with the number of NPs N_p for colloids with a size $R_0 = 1.5$. Two sets are produced: for $\sigma = 1$ and $\sigma = 0$. In the latest the coupling calculations are ignored, which can be seen to lead to a considerable reduction in the elapsed time.

We can separate the different contributions to the coupling calculation as follows: firstly, each processor explores all the particles within its subregion (only those with the center of mass within it). Then, we perform a search for all particles in the processor's neighbour. Finally, the list of neighbours is used to calculate the coupling of these particles. Manually profiling these three contributions allow us to eliminate the second step (searching) as a negligible contribution. We are therefore left with the bulk (the interior) and surface (the boundary) contributions. As expected, the bulk scales as the volume of the subregion while the boundary scales as the surface of the cuboid. This suggests that it is crucial to use a parallelisation scheme such that the volume and the surface of the partitions are considerably different. This can be achieved with a cell size that is as small as possible.

In Fig. 3.8 the strong scaling for a system sized $V = 512^3$ with $N_p = 10^6$ nanoparticles is shown, in Mare Nostrum. The scaling is reasonably good within one node ($n_p < 64$) and shows only a slight drop in efficiency as compared with Fig. 3.2. It must be noted that the number of particles is considerably large as compared to previous CDS/Brownian Dynamic schemes in serial.

Finally, in Fig. 3.9 we show two snapshots of moderate volume size $V = 128^3$ with a low concentration of NPs sizes $R_0 = 1.0$. The number of processors used were 8 and 16 for (a) and (b) respectively. The lack of artefacts suggests that the parallelisation scheme communicates correctly. Furthermore, colloidal NPs are found to segregate to the interior of the gray phase, as dictated by the affinity $\psi_0 = -1$.

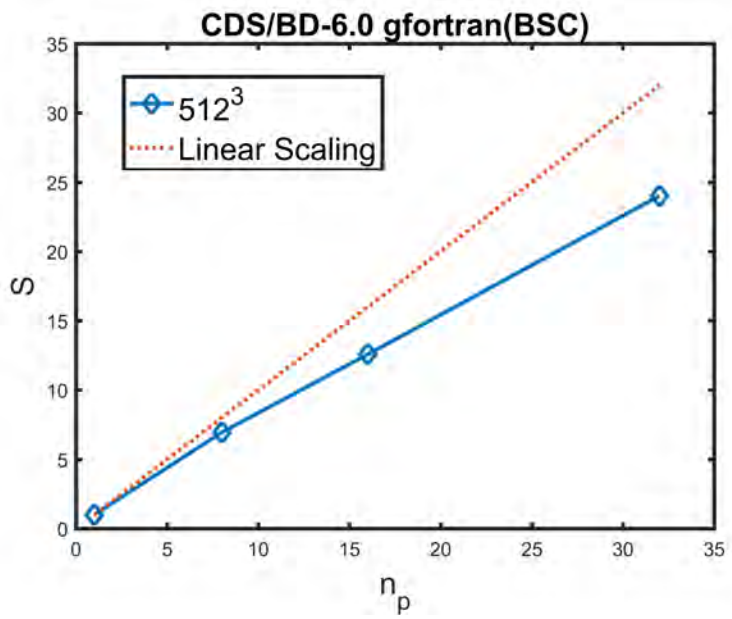

Figure 3.8: Strong scaling of the hybrid BCP/NP code vs the number of processors n_p in one node. The speed-up S is compared with the ideal, linear scaling(dotted line). The number of particles is $N_p = 10^6$ and simulations were performed in Mare Nostrum.

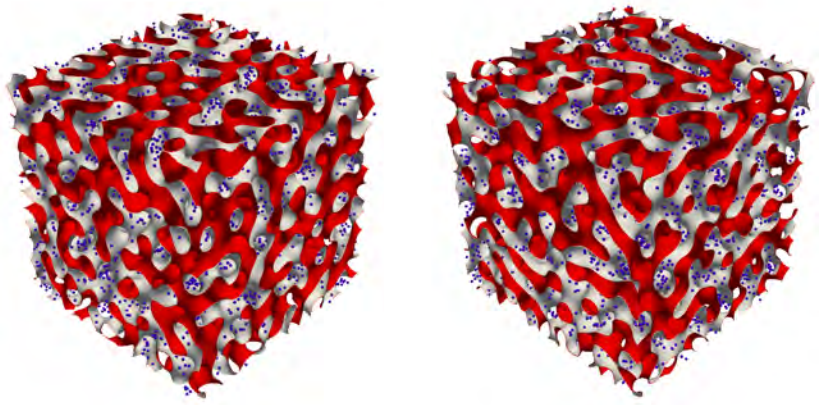

Figure 3.9: A-compatible $\phi_p = 0.01$ concentration of small $R_0 = 1.0$ NPs with symmetric lamellar forming BCP. Number of processors is set to 8 and 16 for (a) and (b), respectively.

3.4 Future work

In this Chapter we have presented a parallel CDS/Brownian Dynamic scheme using CAF. This work has been possible thanks to the HPC Europa 3 scheme that allowed computer time in BSC, from February to April 2019. This is, nonetheless, a work in progress. Even though the bulk of the parallelisation has been achieved (scaling and validation), many aspects of this scheme can be polished. In the following lines I provide some comments on further work that could be performed.

For considerably large systems, initialisation can take a considerable time. At the time of writing this thesis, this is performed by a single processor which later broadcasts it. A detailed work on this aspect could result in the ability to initialise from a random distribution or from a specified file, for restarting purposes, for example. This could be done in parallel.

Similarly, writing files is performed serially by a single image into a simple text file. This is unrealistic when considering extremely large systems. Work could be devoted to an efficient parallel saving scheme.

Finally, the update of the colloidal positions is performed serially. This is not a largely time consuming step, but its parallel implementation could assure that a larger fraction of the code is indeed correctly parallel.

3.5 Conclusions

FORTRAN Coarrays have been used to develop a parallel code of the CDS scheme. This is a relatively simple approach based on spatial decomposition and shows no drawbacks when compared with a more elaborate approach using MPI [81]. The scaling of the pure CDS code is highly linear for relatively large system sizes and improves the previous implementation using MPI. It allows to scale large system sizes while maintaining reasonable computational times.

The CDS parallel code has been tested both on single-node and multi-node calculations, both exhibiting a linear scaling behaviour. Furthermore, we have made use of Coarrays Fortran in two relevant national supercomputer facilities: Archer (UK) and BSC (Spain). The ability of our code to scale to a large number of computer nodes allow us to reach previously unavailable system sizes. For instance, we have used 10 computer nodes (512 CPUs) to study a $V = 1024^3$ grid points box. A $N_{steps} = 10^5$ steps simulation would take a moderate time of $t \sim 8$ hrs. Considering a typical lamellar period size, we can estimate our box size as having 50^3 periods which for a typical lamellar period [8] could result into 2 μm lateral size, which is comparable to experimental images.

Secondly, a scheme for a parallel hybrid BCP/Nanoparticle mesoscopic model has been presented. Similarly as the purely polymeric CAF implementation, this code has the ability to scale linearly with the number of processors in play. The actual scaling of the code depends heavily on colloidal size -due to its influence in the cell size- but the code has been found to perform efficiently over a wide range of parameters. This parallel code opens the possibility to study more complex systems involving block copolymer nanocomposites at considerably large length scales.

CHAPTER 4

Diblock Copolymer Nanocomposites: Comparing Simulations and Experiments

Abstract

The presence of nanoparticles in a diblock copolymer leads to changes in the morphology and properties of the matrix and can produce highly organized hybrid materials. The resulting material properties depend not only on the polymer composition, but also on the size, shape and surface properties of the colloids. We study the dynamics of this kind of systems using a hybrid mesoscopic approach. A continuum description for the polymer is used, while colloids are individually resolved. The method allows for a variable preference of the colloids, which can have different sizes, to the different components the block copolymer is made of. We can analyze the impact that the nanoparticle preference for either, both or none of the blocks have on the collective properties of nanoparticle-block copolymer composites. Several experimental results are reproduced covering colloid-induced phase transition, particles' placement within the matrix and the role of incompatibilities between colloids and monomers. [1]

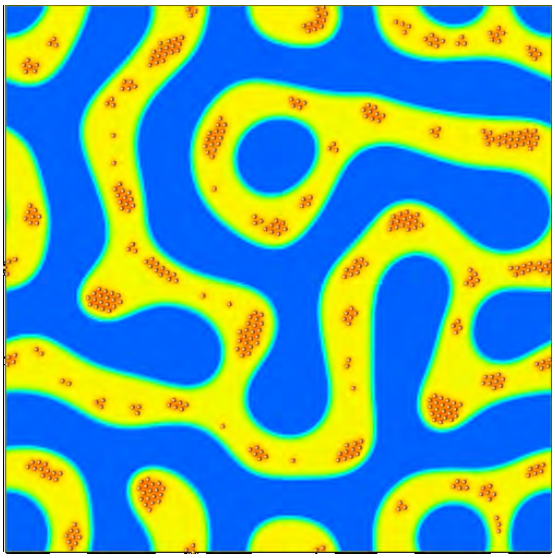

[1] The content of this chapter has appeared in the publication Diaz, J., Pinna, M., Zvelindovsky, A.V., Asta, A. and Pagonabarraga, I., **2017**. Cell dynamic simulations of diblock copolymer/colloid systems. *Macromolecular Theory and Simulations*, 26(1), p.1600050.

4.1 Introduction

The addition of nanoparticles (NPs) to Block Copolymers (BCP) results in a nanomaterial whose properties are significantly different from the one without NPs (e.g. changes in the BCP morphology[90]). The resulting hybrid material can be used as a catalyst in separation processes or as photonic-gap materials[91, 92, 4] . The nonlinear optical properties of BCP are enhanced with the inclusion of selective NPs [84] . Following a previous Cell Dynamic Simulations/Brownian Dynamics work [68], we study colloidal particles of the size of the order of magnitude of the BCP domain which in our case is in the range of a few nanometers. In this regime, both NPs and BCP evolve in a similar time scale.

In this chapter we aim to improve our understanding of the role of NPs in a BCP matrix and their assembly and placement within their soluble block. We will use the model described in Chapter 2 to study BCP nanocomposite and compare the simulation results with experimental results. This can serve as a way to validate our model against experiments and justify the use of the CDS/BD scheme. While previous previous works mentioned in section 1.4 have studied block copolymer nanocomposite systems, the complexity of the simulations of these hybrid systems results in computationally expensive numerical calculations. From a mesoscopic point of view we can reduce the complexity, thus allowing us to perform a considerable number of simulations exploring a particular parameter. The volume fraction of NPs and their affinity will be carefully studied in order to analyse its role in the morphology of the BCP as well as the assembly and placement of the NPs within the matrix.

4.2 Model

This chapter introduces no new elements to the model described in Chapter 2

4.3 Results

In this section we present the results of the simulations of our model. Unless otherwise specified, we will set the polymer and colloid parameters to $A = 1,\ D = 0.5,\ v = 1.5,\ u = 0.5,\ \tau_0 = 0.3,\ k_BT = 1,\ \alpha = 2,\ \eta = 0,\ \beta_0 = 0,\ \alpha_0 = 1$ and $U_0 = \sigma = 1.\ B = 0.01$, except in the last section in which $B = 0.001$ in order to tune the domain size. The total A-monomer ratio is fixed to $f_0 = 0.5$ for the symmetric lamella case, while $f_0 = 0.4$ for cylindrical morphologies. Particle's friction constant is $\gamma = 25.0$, except for the last subsection in which $\gamma = 10.0$ accordingly to colloid's radius. The grid size is defined as $\delta x = 1/4$, except for the hexagonal packing simulations in which we used $\delta x = 1/\sqrt{7}$ in order to have smaller BCP domains. The time step is changed accordingly as $\delta t = 0.05$ and $\delta t = 0.2$, while $M = 0.1$ for all our simulations. We disregard random fluxes in the BCP setting $\eta = 0$, for simplicity's sake.

Unless otherwise specified we will analyze our model on a 2D system of size 256×256 grid spacings. We will explore the collective behavior of BCP/colloid composites changing the colloidal area fraction. From this value one can infer the number of colloidal particles used in different simulations. The volume fraction is calculated using the effective radius, rather than the hard core one. Contrary to that, figures show hard-core radius, as can be appreciated from the coating of BCP surrounding the hard-core.

Initially the order parameter is an uniformly random distribution while for the colloids we choose an initial non-overlapping random configuration.

In this section we will apply our model to study the effects that colloidal particles induce in the morphology of a BCP depending on the chemical properties of the NPs surface, which is described in our model as the affinity towards a value of order parameter. The role of size, chemical composition and compatibility of NPs will be analyzed with regard to its effect on the colloidal assembly in the BCP matrix.

4.3.1 Phase transition induced by colloids

The phase diagram of a purely A-B diblock copolymer system is well known [14] and for the most simple case we can differentiate between lamellar and cylindrical phases depending on whether the total concentration of A and B monomers is symmetrical or not. For the second case the shortest block (referred here as the minority phase) forms domains which are hexagonally organized. In this subsection we analyze the ability of the colloids to distort the underlying BCP morphology, promoting a phase transition as we vary both their concentration and affinity

Several theoretical and experimental works have come across the change in the morphology of the BCP induced by the presence of colloids. In this section we apply our model in an attempt to reproduce these results. In contrast with previous works, our model also covers the time evolution towards the equilibrium and is able to reach larger system sizes.

From lamellae to cylinders

We start analyzing the effect of relatively large ($R_i^0 = 2.5$) colloids that have a strong affinity towards one of the blocks ($\psi_i^0 = 0.5$).

Figure 4.1 illustrates the morphological changes induced in a BCP lamellar matrix as the NP concentration increases . Figure 4.1 top-left shows a typical lamella morphology without colloids. In the low density regime (Figure 4.1 top-right, $\phi_p = 0.15$) the domains are shorter and drop-like domains appear as a result of colloids breaking lamella domains. The transition is not complete in Figure 4.1 bottom-left for $\phi_p = 0.35$ but coexistence of lamella and cylindrical phase is observed. At larger colloidal concentration, NPs are closely packed in the BCP domain they are more miscible in, and favor a distortion of the BCP domains, inducing a phase transition. This process is due to the influence of colloids in their preferred copolymer, which effectively increases the fraction of the domain in which they are soluble. Our model reflects the mechanism by which one type of copolymer is excluded from the volume occupied by the NP. This process of phase transition from lamella to ordered cylindrical morphology is in agreement with the experimental results by Kim *et al* [93] and Halevi *et al* [6] for which our model reproduces particularly well the coexistence of lamella and cylindrical domains, as shown in Figure 4.1 top-right.

Intermediate stages of the phase transition kinetics exhibit interesting features. Figure 4.2 shows snapshots of the time evolution. Initially, small cylindrical domains are formed. These domains can coalesce leading, at longer times, to larger cylindrical domains that coexist with long lamella domains formed by cylinder coalescence.

For very high filling fraction, the particles attempt to minimize the occupied area by packing closely. This leads to an hexagonal packing if we decrease the colloidal temperature, thus reducing the random component of the colloid's motion. Figure 4.3 shows the same system as in Figure 4.1 bottom-right with an slightly lower number of particles $\phi_p = 0.5\%$ and $T = 0.1$ reducing the thermal component of the colloidal velocity. This phenomena will appear again when we reach high concentrations and can be regarded as a transition from disordered to

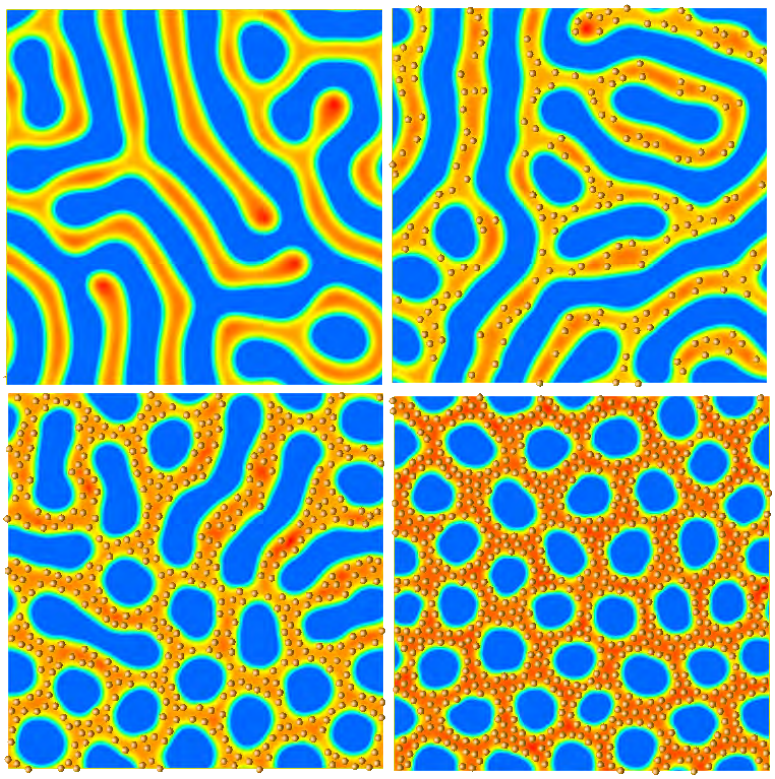

Figure 4.1: Phase transition-lamella to ordered cylindrical- induced by NPs as we increase their volume fraction with values $\phi_p = 0, 0.15, 0.35$ and 0.55 for top-left, top-right, bottom-left and bottom-right respectively.

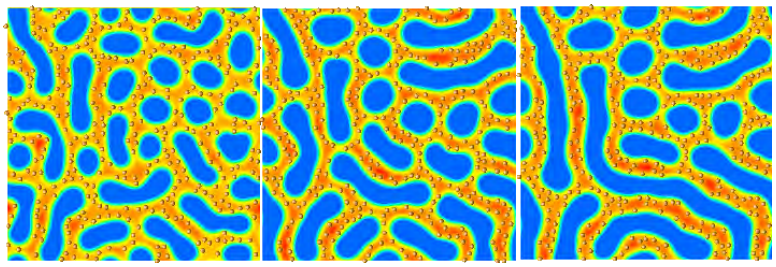

Figure 4.2: Time evolution of a lamella BCP/colloid with volume fraction $\phi_p = 0.25$ for different stage of the simulation. From left to right: $t = 0.5 \times 10^6$ steps, $t = 5.0 \times 10^6$ steps and $t = 14.2 \times 10^6$ steps.

ordered phase for the colloids, guided by the interplay between temperature and concentration. Further analysis is needed to obtain a clearer picture of the coupling between NP and BCP phase transitions.

From cylinders to lamellae

Contrary to the previous process, if we now begin with a cylindrical BCP morphology, such as in Figure 4.4 top-left, and we increase the particle concentration ($R_0 = 2.5$) with a strong affinity towards the minority phase ($\psi_i^0 = -0.8$) and $T = 0.1$, the effective total concentration of the minority phase is increased. In Figure 4.4 top-right this process is clear as colloids distort the drop-like domains due to the repulsive interaction between particles leading to elongated domains up to a point in which phase transition is achieved and BCP morphology changes to lamella (Figure 4.4 center-left). For an even further value of the filling fraction, closely packed

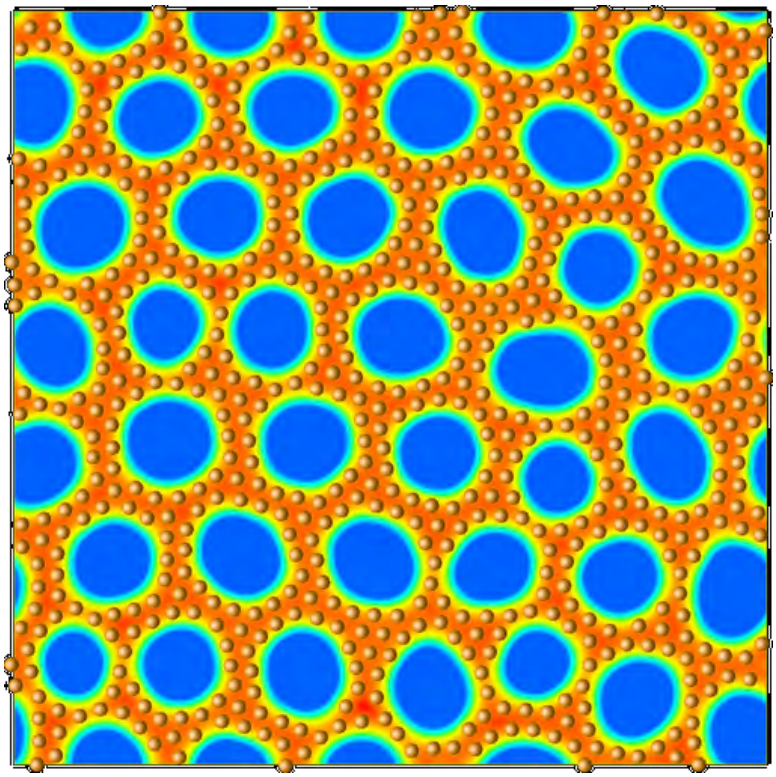

Figure 4.3: A system with a similarly high volume fraction of NPs as in Figure 4.1 bottom-right but with a temperature $T = 0.1$ for colloids.

NPs increase their occupied area. It triggers an additional phase transition from lamella to disordered cylindrical (the previously minority phase being the dominant now) which can be seen in different stages for an increasing number of NPs in Figures 4.4 cente-right and bottom , in which drop-like domains become the majority.

The phase transition from cylindrical to lamella can be prevented if we include colloids with the opposite affinity ($\psi_i^0 = +0.5$). This situation can be simulated using the same BCP morphology as in the previous study and a fixed number of colloids with radius $R = 2.5$ and volume fraction $\phi_{p,0} = 0.22$ with affinity towards the minority phase, while changing the number of identically sized NPs in the other BCP domain. Figure 4.5 shows this effect as in the left picture a low volume fraction of colloids in the majority phase ($\phi_{p,2} = 0.15$) allows the formation of a majority of lamella domains, while in the right hand side Figure the growth in the effective volume fraction of the majority copolymer due to a higher colloids volume fraction ($\phi_{p,2} = 0.50$) compensates for the presence of colloids in the cylindrical domains.

The study of the phase transition induced by the change in NPs volume fraction is in accordance with the phase diagram obtained by Lee *et al* [9] using SCFT/DFT. Our model allows us also to follow the kinetic relaxation to equilibrium.

4.3.2 Colloid radius influence on NP placement

The effect of the colloidal size in the particle position in the lamella domain has been studied both experimentally [32, 27] and theoretically [60] . It has been found that large particles - relative to the lamella domain- segregate to the lamella center while smaller particles are found preferentially in the lamella interface. This is due to the cost of the copolymer brush to encircle larger colloids. For small particles the decrease in their entropic contribution is not

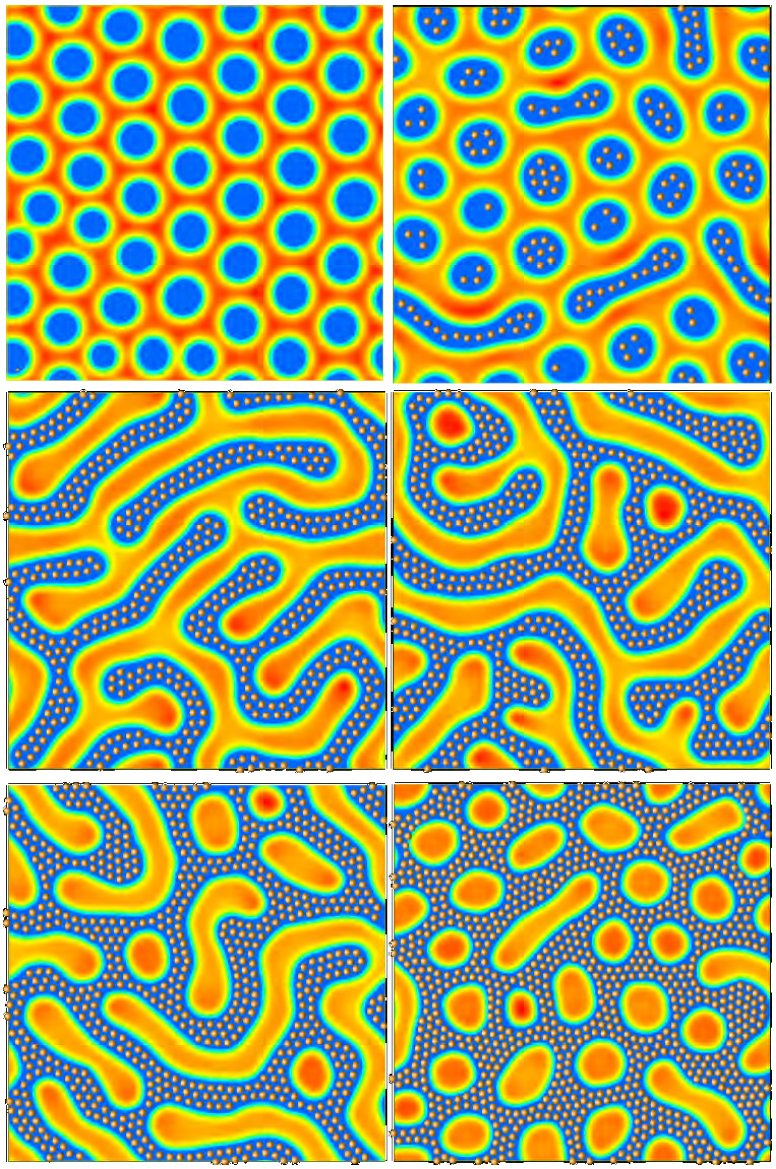

Figure 4.4: Phase transition-cylindrical to lamella,then to disordered cylindrical- induced by NPs as we increase their volume fraction with values $\phi_p = 0.0, 0.12, 0.32, 0.38, 0.46$ and 0.65 from top-left to bottom-right, respectively.

negligible with respect to the particle's translational entropy. This behavior has been proved computationally by means of a combination of SCFT for the copolymer and DFT for colloids [60] and the phase diagram was successfully obtained.

Since our model allows for two different sized kinds of particles we can reproduce the experimental result by Bockstaller *et al*[32] by assigning NPs with a weak affinity towards one block. In this regime, the particle size determines the position within the lamella domain. Size-selective segregation occurs if we simulate two kinds of particles with a size ratio $R_b/R_s = 6.0$ as shown in In Figure 4.6 where small particles remain mostly in the interface while big particles are detached towards the center.

In order to quantify the effect of colloidal size in the particle's position in the lamella domain we can calculate the relative average position inside of the BCP for different values of the hard core radius R_0 as shown in Figure 4.7. For a small value of $R_i^0 = 1.0$ and $N = 200$ (Figure 4.7-left) particles simply place themselves in the interface roughly in the same value of the

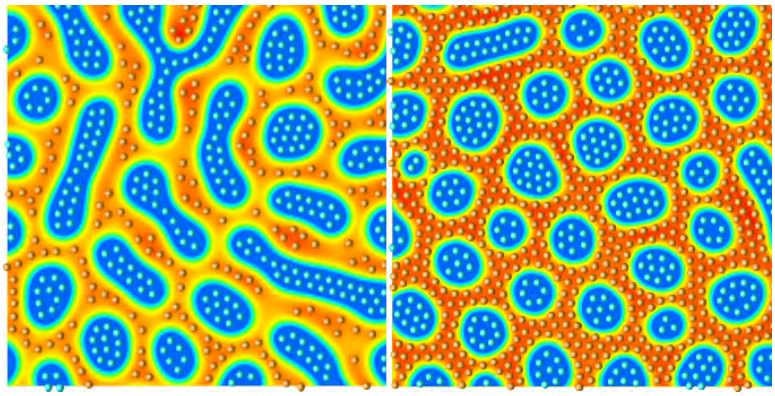

Figure 4.5: Effect of the inclusion of NPs with opposite affinity to a fixed number of colloids with affinity towards the center of the drop-like domains. On the left there are a colloids in the yellow phase with volume fraction $\phi_{p,2} = 0.15$ and $\phi_{p,2} = 0.50$ on the right picture.

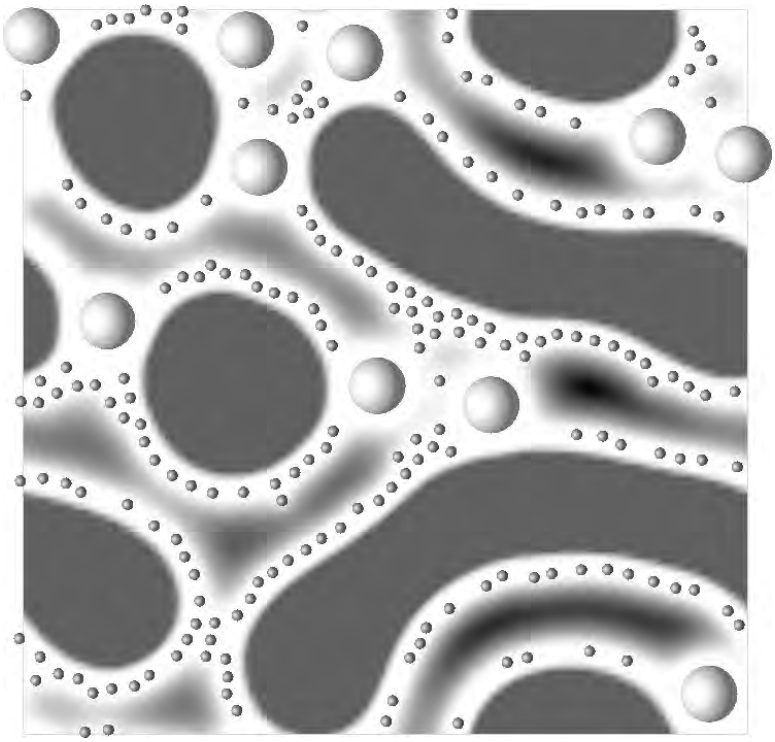

Figure 4.6: $N_s = 200$ small ($R_0^s = 1.0$) particles and $N_b = 10$ big ($R_0^b = 6.0$) particles with an assigned affinity $\psi_i^0 = 0.3$. System size is 128×128.

assigned affinity. For a larger value $R_i^0 = 3.0$ and while keeping the filling fraction constant, NPs are slighly detached from the interface, as depicted in Figure 4.7-center . For a comparable domain-particle size, particles are completely placed in the center of the domain, as shown in Figure 4.7-right .

The results are summarized in Figure 4.8, where we can observe the drift towards the center of the lamella as we increase the radius of the particles. The small lack of agreement for $R = 1.0$ is due to the fact that colloids create two layers in the interface due to a considerably high number of particles. Particles in the second layer contribute as if they had a preference for an slightly out-of-the-interface order parameter value. Although our model does not take into account the microscopic structure of the BCP, the qualitative effect is properly accounted for due to the distortion that big particles create in the order parameter. If the distortion is small,

the NP can easily fit the interface, but for a larger one the particles need a more homogeneous BCP environment .

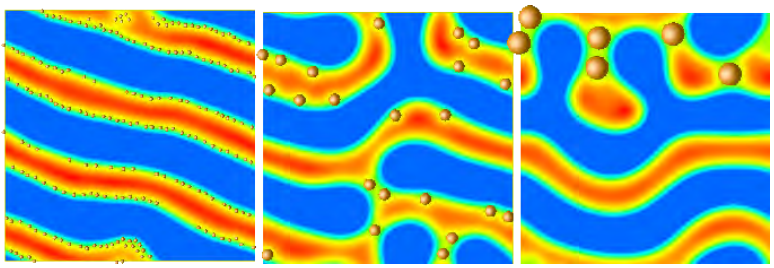

Figure 4.7: Effect of particle's size ($R_0 = 1.0, 3.0, 6.0$ from left to right) in its position for a fixed filling fraction and affinity $\psi_i^0 = 0.3$. System size is 128×128 in all cases.

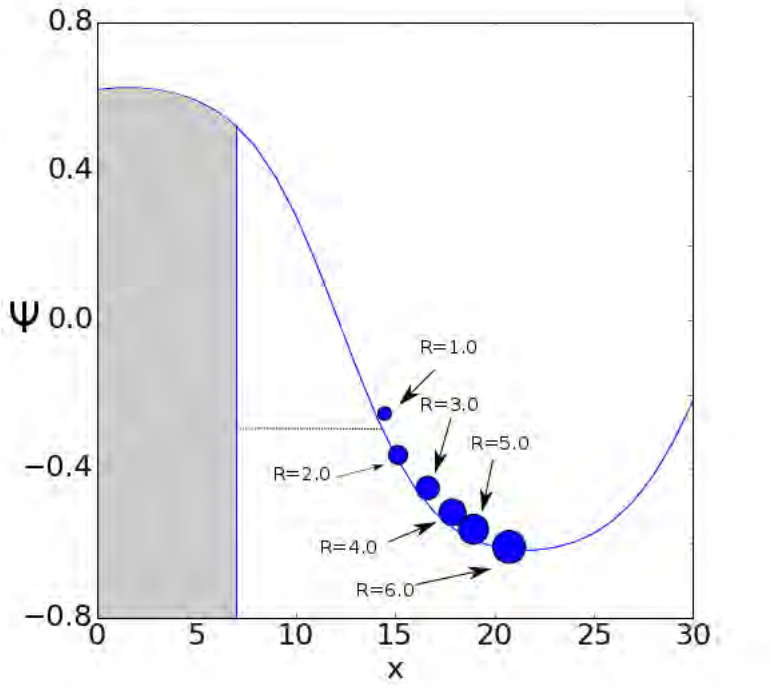

Figure 4.8: Relative average position of nanoparticles in an undistorted lamella profile. The gray area is taken as the reference of center of the domain. The horizontal line shows the affinity that is assigned to all particles. Positive-negative ψ values are inverted in this scheme and particles' sizes are not in scale.

4.3.3 Hexagonal packing of colloids

So far we have studied the effect of colloids in the BCP morphology when particles are compatible with one of the copolymers or they are equally soluble in both domains. Contrary to that, Ploshnik *et al* [85] performed experiments in the case in which nanoparticles are coated to be incompatible with both blocks, but to different extends, thus triggering a hierarchical structure of the BCP/colloid composite material and self-assembly of NP into hexagonal packing. In Figure 4.9 we reproduce a high resolution scanning electron microscopy image of Reference [85] where gold NPs are segregated at the black domains (PMMA) and form close packed aggregates.

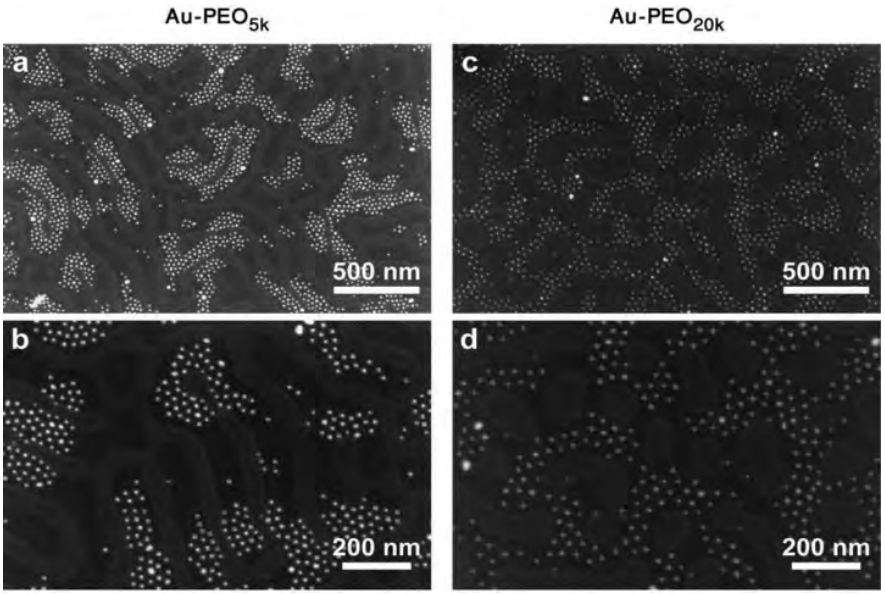

Figure 4.9: High resolution Scanning electron microscopy images, at two magnifications, of ultrathin PS-*b*-PMMA/Au-PEO films. Black and gray domains correspond to PMMA and PS domains, respectively. Reprinted with permissions from Ploshnik, E. , Langner, K. M., Halevi, A. , Ben-Lulu, M. , Müller, A. H., Fraaije, J. G., Agur Sevink, G. J. and Shenhar, R. (2013), Adv. Funct. Mater., 23: 4215-4226. Copyright 2013 Wiley. .

In our CDS/Brownian model we reproduce the incompatibility by assigning an affinity towards one of the copolymers, but larger in magnitude than the maximum value of the order parameter present in the simulation. By doing so we create a distortion in the BCP profile, leading to a penalty in the free energy that can only be minimized by a strong packing of the colloids.

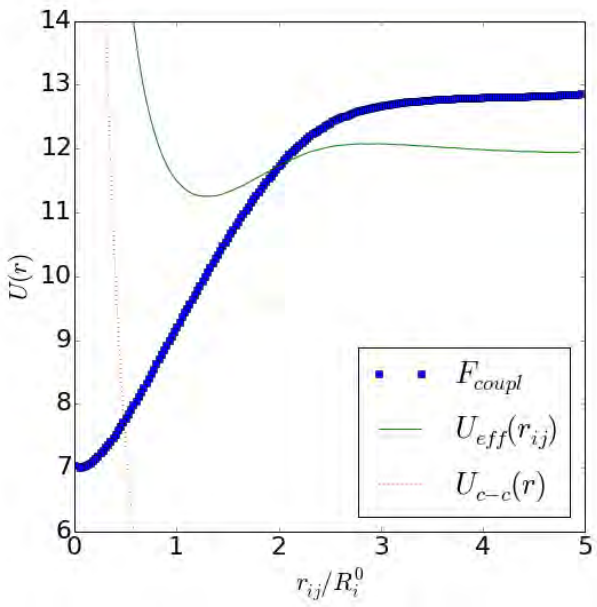

Figure 4.10: Effective potential between particles and colloid-colloid repulsive potential. The coupling free energy and the effective potential can be obtained by separating two NPs by a distance r and using equation 2.23 to calculate the coupling free energy after equilibrating the system.

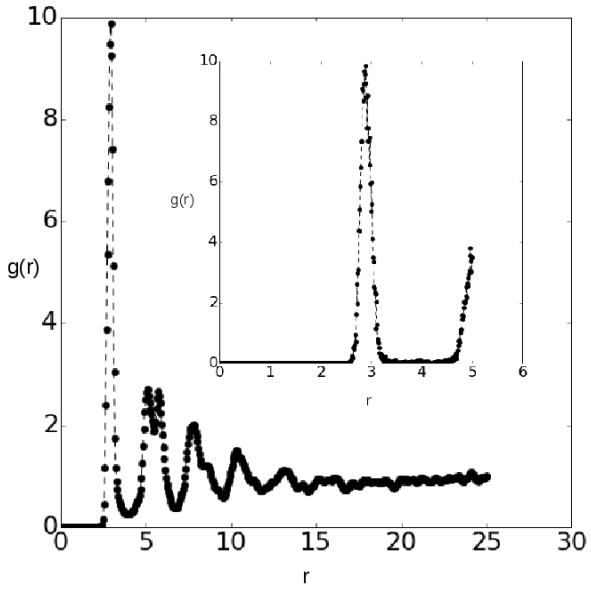

Figure 4.11: Radial distribution function for Figure 4.12 bottom-right. The inset of the first peak is calculated from a subdomain of the system in order to have the right coordination number for the first neighbor, thus removing edge-related effects.

We find that the overlapping of the distortion of two colloids creates an effective potential as in Figure 4.10. The clear minimum we observe leads to a Lennard-Jones-like potential that in result creates a hexagonal packing, as we can see in Figure 4.12.

Initially we can simulate a system for a small number of NPs at a volume fraction $\phi_p = 0.05$, for which the BCP lamella morphology is not significantly affected, as shown in Figure 4.12 top-left.The hexagonal packing already occurs at this low concentration by the formation of clusters of NPs,which resembles particularly correctly the experimental STEM image in Figure 2-I in Ploshnik *et al* work[85] . In this case, we use $\gamma = 1.0$ while in the next simulations we have used $\gamma = 10.0$ because a lower density of particles needs for considerably longer simulation times for particles to create clusters. For a larger number of particles ($\phi_p = 0.10$, Figure 4.12 top-right) the BCP morphology is distorted leading to a coexistence lamella/cylinder because of the presence of elongated clusters of hexagonally packed colloids. For an even higher volume fraction ($\phi_p = 0.20$,Figure 4.12 bottom-left) the phase transition is almost complete and BCP domains are distorted into irregular disks. Increasing the NP concentration leads to an almost complete filling of colloids into their least unfavorable phase, while the drop-like domains are considerably shrinked, as shown in $\phi_p = 0.50$, Figure 4.12 bottom-right.

This phase transition is fundamentally different from the one observed in Figure 4.1 since the resulting morphology now is disordered instead of hexagonally cylindrical, which is in accordance with experimental results [85] as phase transition from lamella to disordered occurs. Additionally, it is important to note that the hexagonal packing observed here is due to a different nature than the one appearing in the previous sections (see Figure 4.4) where packing was a result exclusively of the local high concentration limit (whether it is due to total high concentration value or a local constraint that forces close packing). In this case, hexagonal packing is present even for low concentration of colloids (see Figure 4.12 top-left) since colloids minimize the coupling free energy forming clusters.

Using the results from the $\phi_p = 0.50$ simulation (Figure 4.12 bottom-right) we can calculate

the radial distribution function (Figure 4.11) as well as the NP coordination number. The main curve represents $g(r)$ using the whole system which is correct qualitatively. The number of particles associated with the first peak does not result in the expected coordination value $N = 6.0$ due to the boundaries created by the inaccessible BCP domains. If we select a small subsystem in which colloids are homogeneously distributed and $g(r)$ is computed again (as shown in the inset in Figure 4.11) we obtain a value $N = 5.97$ for the coordination number after the integration over the first peak as in $N = 2\pi\phi_p \int_0^{r_0} dr\ r\ g(r)$ which acts as a further proof of the hexagonal packing of NPs.

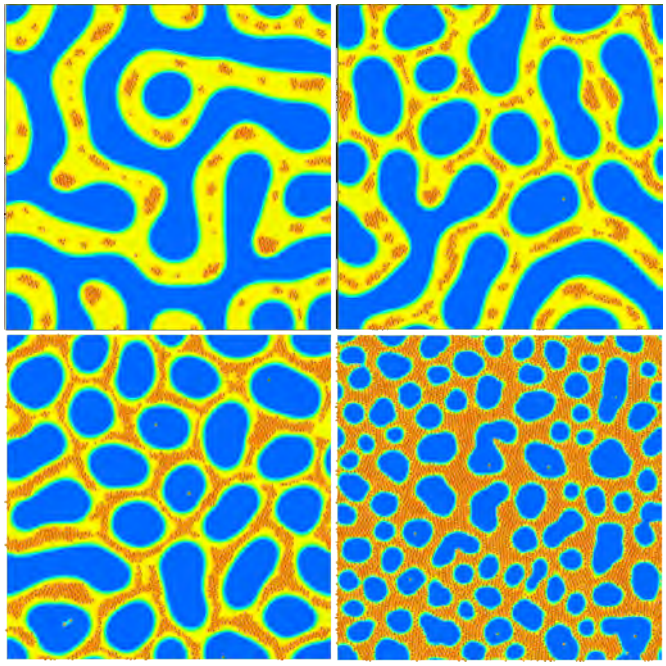

Figure 4.12: Phase transition for a lamella BCP morphology and N NPs with $R_0 = 1.0$ with increasing volume fraction $\phi_p = 0.05, 0.1, 0.2$ and 0.5 from top-left to bottom-right. Affinity is $\psi_i^0 = 1.2 > \max(|\psi|)$, larger value that the order parameter takes in the absence of colloids

Additional corroboration with the experiments is obtained if we calculate the fraction of colloids present in the interface with respect of the total number. As in the experiment in Figure 8 c in in Ploshnik *et al* [85] , the fraction of NPs in the interface decays with time, but it does it slower as the filling fraction is increased. In Figure 4.13 we can see the dependence for $\phi_p = 0.05$ and 0.2 fulfills the qualitative behavior of the experimental work. We consider interface values those than fulfill $\psi \in [-0.4, 0.4]$. This broad definition of the region is necessary since in our model NPs have a very strong affinity with the center of the domain, resulting in very high penalty for particles outside that region. Nonetheless, Figure 4.13 supports the notion proposed in the experimental work [85] that NPs create clusters in a slower timescale than BCP's self assembly.

4.4 Conclusions

Cell Dynamics Simulations along with Brownian motion dynamics have been used to simulate the governing equation of a mixture of diblock copolymer and colloids. Our model has proved to be successful when capturing the self assembly of colloids in a BCP matrix and reproducing the phase transition that the morphology of the BCP undergoes as we increase colloid's concentration. The relatively fast nature of the CDS scheme has proved to be crucial to obtain

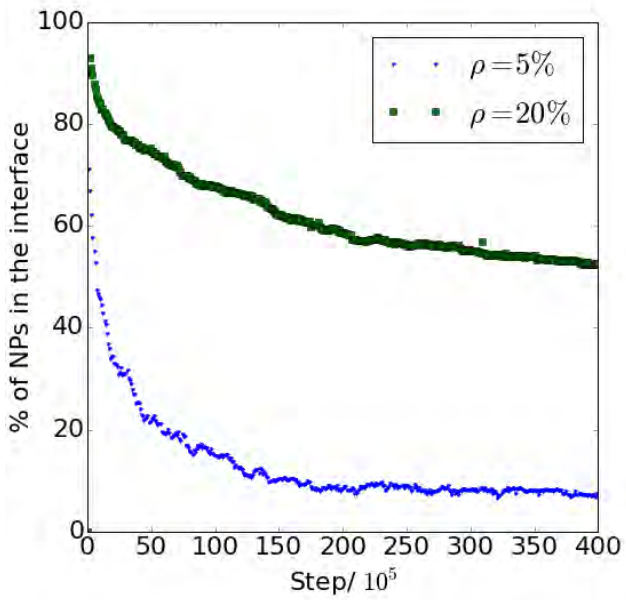

Figure 4.13: Fraction of NPs that lie in the interface as a function of time.

the time evolution of large systems over long times.

The inclusion of two-sized particles has allowed us to reproduce experiments[32, 27] in which the size of the particle is the main property determining the position of colloids inside of a BCP domain. Hence, our model is able to qualitatively reproduce size-related effects.

Further in our attempt to check the validity of our model, we reproduced the experimental setup in which colloids are incompatible with both blocks in the BCP provided that the affinity is not symmetric towards the blocks. We successfully achieved a clear hexagonal packing, reproducing properties (phase transition and fraction of NPs in the interface) that were present in the experiment[85] .

In summary, we have presented a model that is able to simulate the effects of size, concentration and chemical properties of NPs immersed in a BCP melt. Order-to-order phase transitions have been observed, depending on the compatibility of the NPs with each block and NPs volume fraction. The successful comparison with experimental results motivate us to study additional systems in the following chapters.

CHAPTER 5

Diblock Copolymer Nanocomposites: Morphology

Abstract

Nanocomposite materials made of block copolymer (BCP) and nanoparticles display properties which can be different from the purely polymeric matrix. The resulting material is a crossover of the original properties of the BCP and the presence of the assembled nanoparticles. A mesoscopic study using cell dynamic simulations is reported, to quantitatively describe the structural properties of such hybrid materials. The most relevant parameters are identified to be the fraction of nanoparticles in the system and its chemical affinity, while the nanoparticle size with respect to the BCP length scales plays a role in the assembly. The morphological phase diagram of the BCP is constructed for nanoparticles with chemical affinity ranging from A-compatible to B-compatible for a symmetric A-B diblock copolymer. Block-compatible nanoparticles are found to induce a phase transition due to changes in the effective concentration of the hosting phase, while interface-compatible particles induce the appearance of two new phases due to the saturation of the diblock copolymer interface. [1]

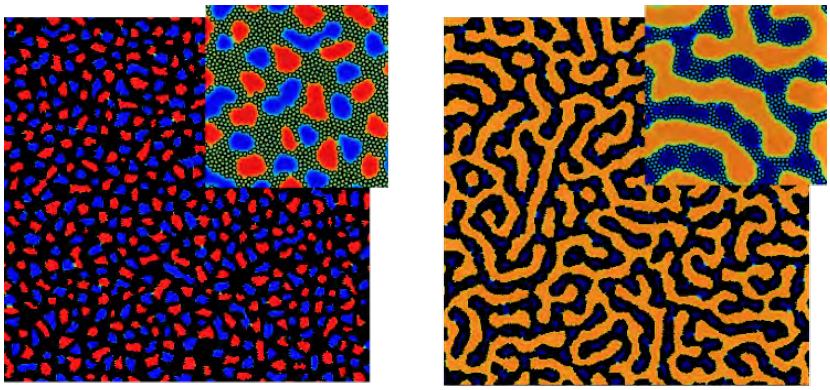

[1] The content of this chapter has appeared in the publication Diaz, J., Pinna, M., Zvelindovsky, A.V. and Pagonabarraga, I., **2018**. Phase Behavior of Block Copolymer Nanocomposite Systems. *Advanced Theory and Simulations*, 1(9), p.1800066.

5.1 Introduction

Block copolymer (BCP) materials are strongly periodic, serving as perfect templates for controlled placement of colloids[27, 28], resulting in highly ordered materials. In order to achieve a detailed control of the NP assembly within the BCP matrix it is necessary to be able to predict the phase behavior of the overall system once nanoparticles are added, as the distribution of nanoparticles critically depends on the morphology of the BCP, and the morphology itself is modified by the presence of NPs. We aim to provide a clear picture of the phase behavior of diblock copolymer systems in the presence of nanoparticles.

Modifying the surface of the nanoparticles to make them compatible with one of the blocks can lead to a precise localization of the NPs within BCP domains [1, 29, 30] or the interface between them[28, 94]. Since the presence of nanoparticles can induce a phase transition of the BCP, it is crucial to determine the overall morphology of the polymer nanocomposite system. We explore the phase diagram of several parameters (both polymeric and colloidal) in order to establish a clear picture of the interplay between the pure BCP matrix and the colloidal fillers depending on the BCP architecture, the nanoparticle shape and interactions, both between colloids and with respect to the BCP.

Simulation techniques such as Monte Carlo have been used [53, 54] to assert the assembly of BCP/NP systems on chemically nanopatterned substrates. In close resemblance with experiments, this method allowed to obtain well-ordered assembled nanoparticles. Furthermore, Huh et al[55] reported the changes in the diblock copolymer morphologies due to the presence of A-compatible nanoparticles in a diblock copolymer of arbitrary morphology (that is, exploring the composition ratio) using 3D simulations. This provided a phase diagram with only a few points. Molecular Dynamics [15] was used to study the phase behavior of BCP/NP systems for different Flory–Huggins parameter values using fixed symmetric diblock copolymers. It was also reported that nanoparticle localisation is increased with nanoparticle size, as was experimentally found by Bockstaller et al [32].

While many works mentioned in section 1.4 have addressed diblock copolymer nanocomposites, only Huh et al [55] has provided a quantitative study of the phase behavior of the diblock copolymer in the presence of a concentration ϕ_p of nanoparticles, with a limited amount of points. Furthermore, we aim to make use of computationally inexpensive methods to study such systems in detail and being able to tackle a large variety of parameters. For instance, we do not restrict our study to A-compatible colloids. By doing so, we are considering a more general approach than previous works, focusing on the morphologies of the resulting nanocomposite system, while a future work will tackle the assembly of colloids, under the same principles. Similarly, we do not restrict to a particular BCP matrix, i.e. we study a range of values of composition ratio f_0. This allows to predict with generality the resulting phase of a diblock copolymer nanocomposite.

In this Chapter we aim to systematically study the morphological transitions that have been found in Figures 4.1 and 4.4 . We aim to obtain a quantitative picture of the morphological behavior of BCP/NP systems. The coarse grained nature of the Cahn-Hillard equation suits this approach, as relatively large systems (in terms of several domain periods) are not numerically expensive. Throughout this Chapter we are restricted to 2D simulations which allow to perform a large number of simulations with considerable system sizes.

5.2 Model

The model that will be used here introduces no changes from the one described in chapter 2.

5.3 Results

The aim of this chapter is to study the phase behaviour of a diblock copolymer mixture in the presence of nanoparticles. For that purpose we restrict our study to a series of parameters which will be presented in the form of phase diagrams. The overall concentration of particles is the fundamental variable that will be considered, hence the purely polymeric properties can be retrieved at $\phi_p = 0$. Exploring a vast range of ϕ_p allows to consider several regimes, as we will consider both low-concentration and high concentration regimes of nanoparticles.

Since our objective is to assert composite systems, the purely polymeric parameters such as χN are not explicitly explored. Instead, we will tune f_0 to study different morphologies and therefore we are approximately covering horizontal lines in the well-known $\chi N - f_0$ phase diagram[23]. Similarly, domain size is explored in comparison with the nanoparticle size. Then, we use fixed values for the BCP parameters, which are standard in the literature[42, 49]: $A = 1.5, D = 0.5, \tau_0 = 0.35, v = 1.5, u = 0.5$. When used, the noise in the Cahn-Hillard equation has a strength of $\xi = 0.1$. Box sizes are 256^2, unless otherwise specified.

5.3.1 Nanoparticle coating

We firstly propose to study the effect that a varying affinity ψ_0 of nanoparticles have on a given block copolymer morphology. In Figure 5.1 we can see four final snapshots of a relatively low concentration of nanoparticles (5.6% of surface) dispersed in a symmetric lamellar-forming diblock copolymer. NPs are sized $R/L \approx 0.09$ with respect to the lamellar domain size (half of the period). In a) the affinity is $\psi_0 = -1$ meaning that the particles are totally compatible with the blue phase, therefore all colloids are well dispersed within its preferred phase. If the NPs are almost neutral they segregate to the interface (b), but they do only symmetrically when its affinity is $\psi_0 = 0$ (c). At $\psi_0 = 0.67$ (d), they are again dispersed within the yellow phase, but fewer NPs are found in the center of the domain, as the affinity is not identically 1.

The simulation results shown in Figure 5.1 can be compared with experimental distribution of gold NPs with different fractions of PS homopolymer grafted to the surface of the NP F_{PS} in a PS-*b*-P2VP lamellar-forming melt. Different values of F_{PS} lead to localisation of NPs within the phase-separated BCP.

Figure 5.1 clearly displays the importance of the affinity ψ_0 in the localization of NPs. As experiments have shown[31], the surface of NPs can be coated to be compatible with a part of the A-B diblock copolymer. In practice, typical ligands will be an A-copolymer or B-copolymer brush, or a mixed one, resulting into A-selective, B-selective or neutral nanoparticles, respectively. In theoretical works[61] this enthalpic interaction is introduced via two parameters χ_{AP} and χ_{BP}. In our model ψ_0 plays the role of the difference in enthalpic interaction and σ the NP/BCP interaction strength.

Furthermore, we can explore a range of concentrations of colloids so that the presence of nanoparticles can be quantified. In Figure 5.3 we have simulated a range of NP concentrations ϕ_p and several values of colloidal affinity ψ_0. At low concentration $\phi_p < 0.1$ nanoparticles are simply placed within the preferred region, therefore the morphology of the BCP remains

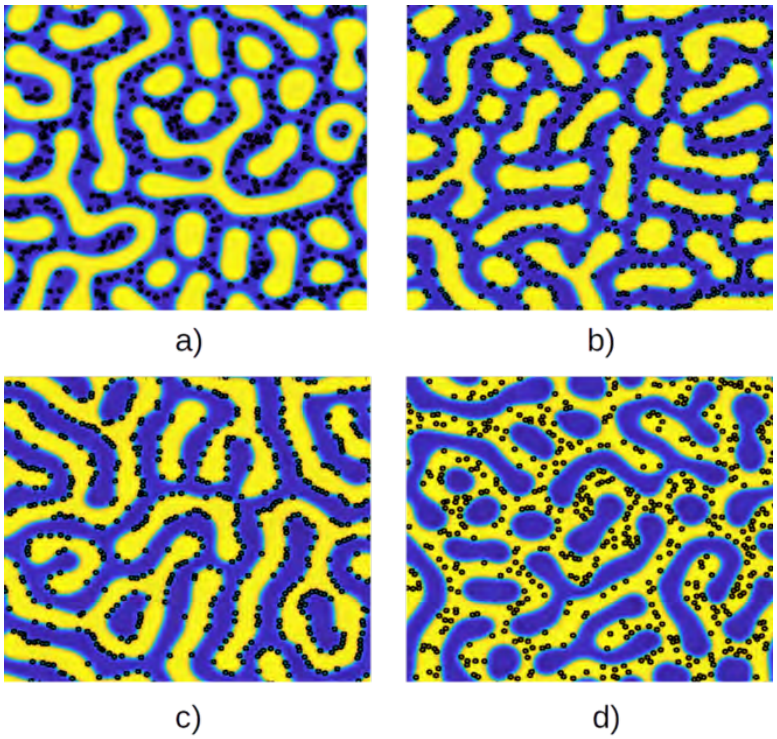

Figure 5.1: Low volume fraction ($\phi_p \approx 0.056$) segregation of NPs for $\psi_0 = -1$ (a), $\psi_0 = -0.33$ (b), $\psi_0 = 0$ (c) and $\psi_0 = 0.67$ (d), in a symmetrical lamellar matrix. Yellow and blue regions stand for A-rich and B-rich monomer, respectively. Nanoparticles are shown as black circles.

lamellar, represented by squares in the yellow region.

We observe that selective particles ($|\psi_0| = 1$) induce a phase transition from lamellar to cylindrical due to the effective increase in the composition ratio of the hosting domain. These two regions are symmetrically placed around the $\psi_0 = 0$ line, as blue and red regions.Contrary to that, in the $\psi_0 \approx 0$ regime NPs segregate to the interface until a saturation volume fraction ϕ_p^* is reached (similarly to what we described in Figures 5.1 b) and c)). At higher number of particles the domains are broken to create more interface. Eventually the lamella structure is destroyed to find alternating irregular domains surrounded by a continuous region of nanoparticles.

Intermediate values of the affinity result in particles that are neither totally compatible with one of the domains nor symmetrically placed in the interface. Therefore a larger number of particles is needed to induce the lamella-to-cylindrical phase transition. This accounts for the shape of the blue and red regions and can be quantitatively described by the expression,

$$f_{eff} = \psi_0 \phi_p + (1 - \psi_0 \phi_p) f_0 \tag{5.1}$$

which derives from the one introduced by Huh [55] after the simple substitution $\phi_p \to \phi_p \psi_0$. In Figure 5.3 this equation is showed by the dashed line which approximately describes the behavior of the phase transition.

Figure 5.3 explores several values of the affinity ψ_0 in a lamellar-forming BCP and two regimes have arisen: Compatible particles induce an order-to-order phase transition based on an increase of the effective concentration of the hosting phase. On the other hand, neutral nanoparticles break the BCP domain up by saturation of the interface. It can be noted that 3 different morphologies can be induced from a single lamellar-forming BCP matrix by a combination of NP loading and chemical coating of the NP's surface. We can now focus on these two

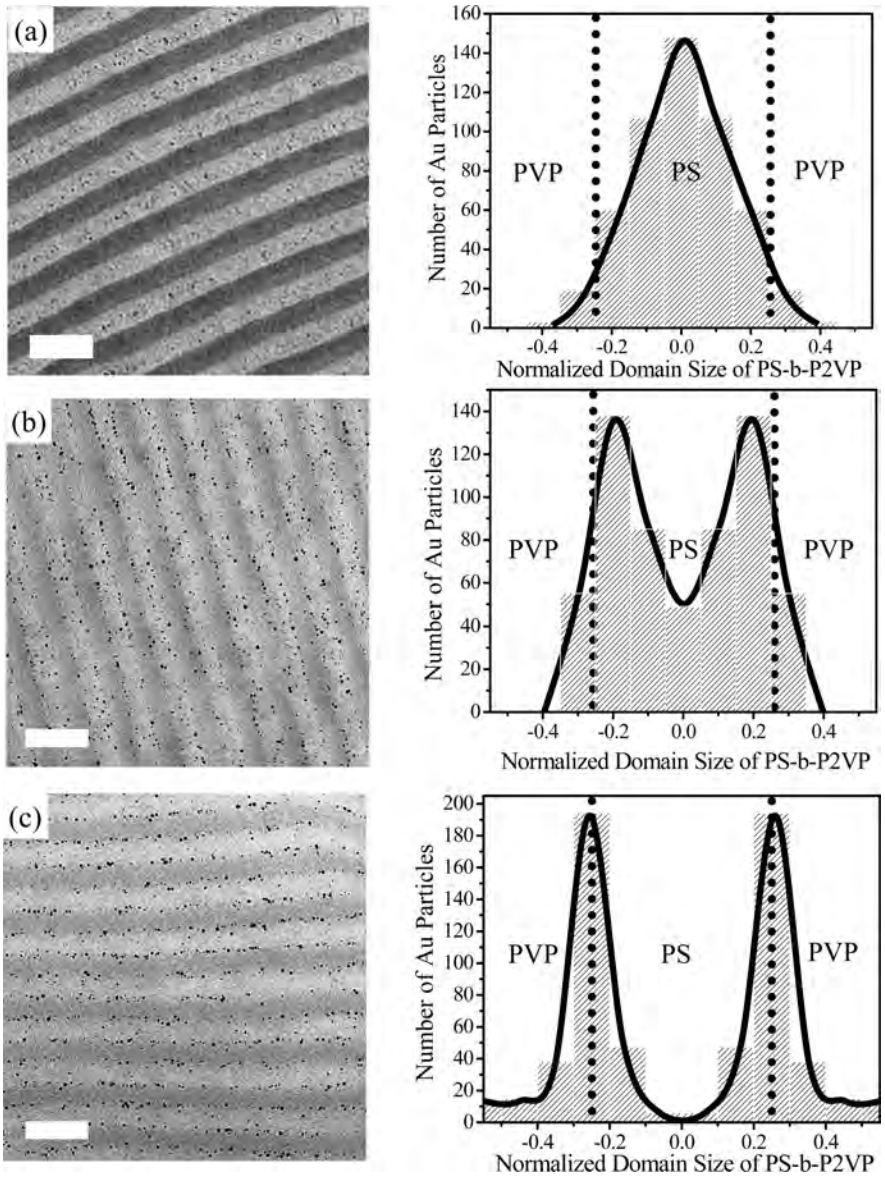

Figure 5.2: Cross-sectional TEM images showing the distribution of gold NPs at different fraction of PS homopolymer grafted to the NP surface . Reprinted with permission from *Langmuir* 2007,23,25,2512693-12703. Copyright 2007 American Chemical Society.

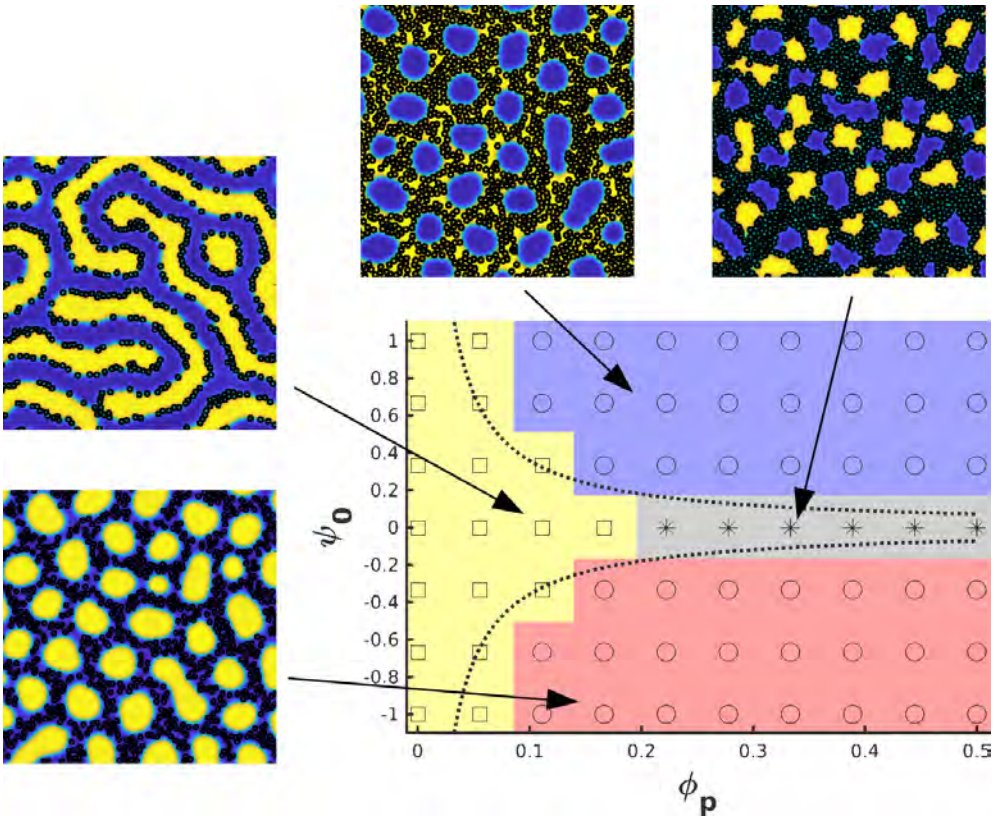

Figure 5.3: Phase diagram of a symmetric BCP with a volume fraction ϕ_p of NPs with different affinity, given by ψ_0. Squares represent lamellar, circles stand for cylindrical phase while asterisk for broken-lamellar phase. The dashed curve represents Equation 5.1.

regimes by fixing ψ_0 but explore the different morphologies of the BCP by changing f_0.

5.3.2 A-compatible NPs

Firstly, we consider a volume fraction of NPs that are strongly compatible with one of the blocks by choosing $\psi_0 = -1$. Various values of f_0 are considered so that we can observe the effect that NPs have on different BCP morphologies. NPs which are compatible with the majority phase will simply segregate within its hosting phase, which already percolates the system, therefore we are more interested in the case in which the hosting domain is the minority phase. For that reason in Figure 5.4 we explore $0.35 < f_0 < 0.6$, that is, in the absence of nanoparticles we observe the well-known phases: cylindrical (red and blue circles) and lamellar(yellow squares). A transition region is labeled as mixed phase (dots) .

At low ϕ_p we simply observe segregation of NPs towards the preferred domain. As the concentration is increased, the nanoparticles induce an increase in the effective volume fraction of the hosting phase, which can be tracked by Equation 5.1. Indeed, in Figure 5.4 we observe the NP-induced phase transition, which is found to qualitatively agree with Equation 5.1. Selective-NP-induced phase transitions have been observed both experimentally[6, 93, 95, 96, 97] and theoretically[98]. We have obtained a phase diagram with considerably more number of points than previous works[55], which allows us to confine the regions for each morphology more precisely. For completion, it should be straight-forward to revert Figure 5.4 for affinities $\psi_0 = +1$, that is, nanoparticles with an affinity towards the other domain: the phase space would be symmetrical with respect to the $f_0 = 1/2$ line.

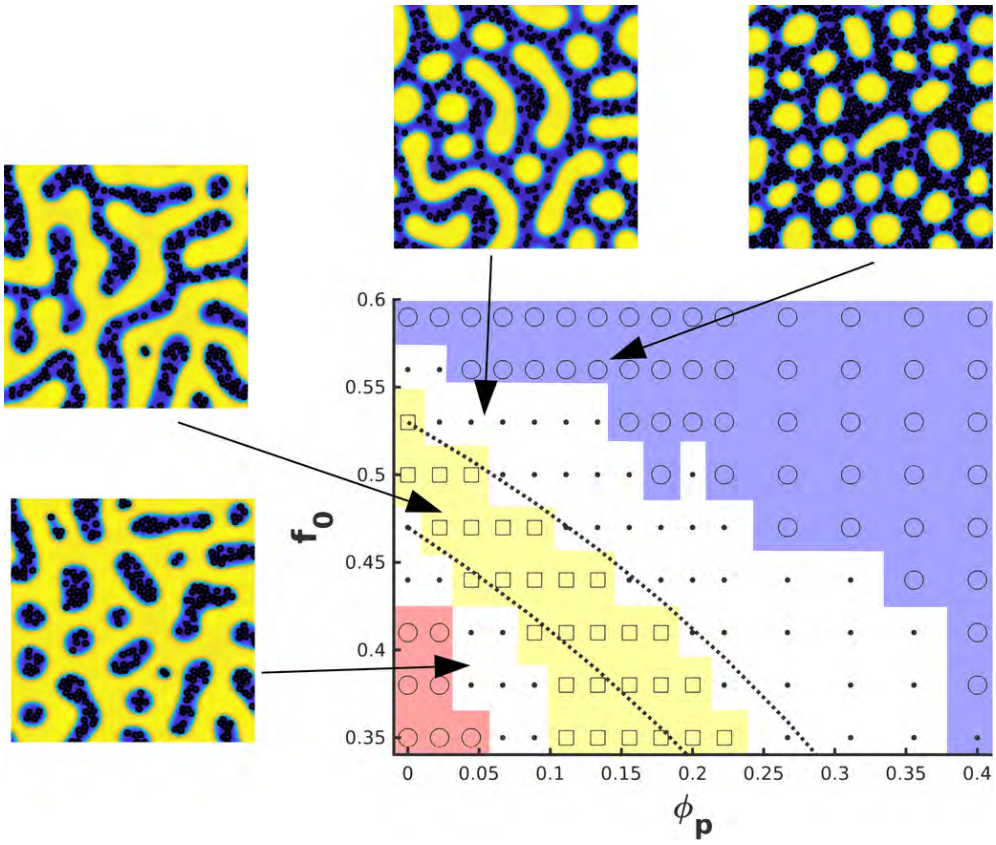

Figure 5.4: Morphology of a BCP/NP system with a f_0 ratio and ϕ_p nanoparticles which are strongly compatible towards one of the phases. Shown phases are: Circular phase(Circles),Mixed phase (dots) and lamellar (squares).

While Figure 5.4 explores a vast range of number of particles in the system, we can focus on $\phi_p < 0.16$ to study in detail the boundaries of the phase regions. To quantitatively determine the phase of the system with precision we ran 5 simulations with the same parameters but different initial condition. Then the number of domains in the system was averaged to determine the phase of the system with considerable precision. The results are shown in Figure 5.5, where again NP-induced transitions are observed. The quantitative agreement between the simulations and Equation 5.1 is noticeable for small ϕ_p. In fact, the disagreement between the phase diagram and the simple f_{eff} expression can be easily tracked as follows: at low volume fraction nanoparticles are relatively isolated within their preferred domain, that is, they rarely interact with each other. As the nanoparticles start to fill the domains collective behavior between nanoparticles appears, inducing an effective volume fraction that is larger than the ideal, described by Equation 5.1. Since the available volume for nanoparticles depend on the morphology of the system we can define an effective volume fraction $\phi_p^{eff} \equiv \phi_p / f_{eff}$ that explains why disagreeing regions appear at higher NP concentration as f_0 grows.

From these simulations and Equation 5.1 it is clear that ϕ_p is the most important control parameter in play when NPs are compatible with one phase. We aim to get a better insight of the phase behavior of BCP/NP systems by using a different interparticle potential. We repeated the procedure described for Figure 5.4 using colloids that interact through a Lennard-Jones potential and tuned the cut-off radius to set attractive and repulsive potentials. A large number of simulations were performed and its result can be seen in Fig. C.1 in Appendix C with no difference found between attractive or repulsive particles. Therefore, we can conclude

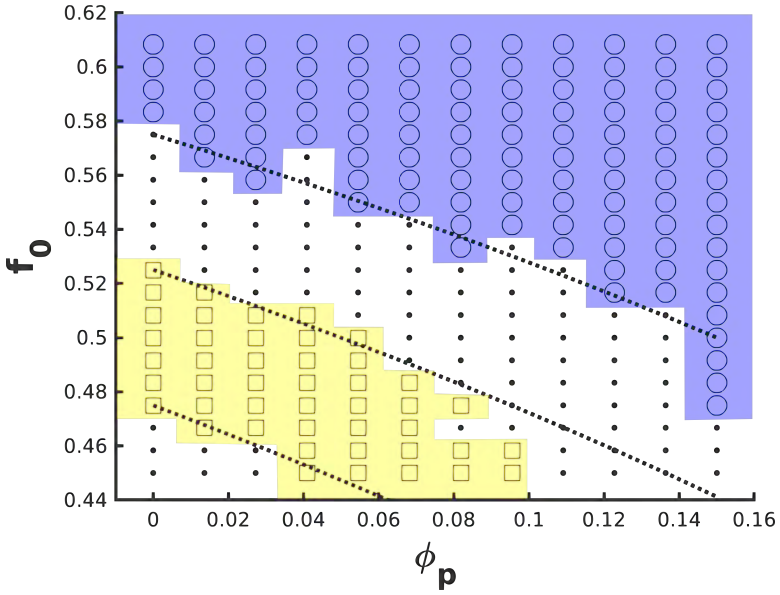

Figure 5.5: Morphology of a BCP/NP system with a f_0 ratio and ϕ_p nanoparticles which are strongly compatible towards one of the phases. Shown phases are: Circular phase(Circles),Mixed phase (dots) and lamellar (squares).

that the interparticle potential does not play a role in the NP-induced phase transition with our level of precision. Nonetheless, the assembly of nanoparticles within their preferred phase is totally different depending on the kind of potential we use, having no consequence over the BCP morphology.

Similarly to the interparticle potential, the size of the nanoparticles is determinant in the assembly of nanoparticles but at first sight it is not expected to be influencial in the BCP morphology. To assert it we performed simulations of different volume fractions of compatible particles $\psi_0 = -1$ for differently sized NPs. Small and large nanoparticles disturb the surrounding polymer in different ways, in fact, Figure 5.6 shows that smaller nanoparticles with respect to the domain size are more effective at inducing phase transitions. This behavior can be explained within our model as the characteristic length of the interface $\xi = 2\sqrt{D/\tau}$ relates to the size of the nanoparticle: a large number of closely separated nanoparticles with a typical interparticle distance $d < \xi$ does not allow for the order parameter to restore small disturbances in the otherwise flat profile. Since no attractive interaction is present, this result in groups of NPs that are only loosely together. In terms of polymeric chains we can conclude that NPs can create NP-rich regions that result in an effective higher concentration of NPs.

5.3.3 Neutral nanoparticles

In Figure 5.3 we found that neutral nanoparticles segregate at the interface and induce a phase transition which is essentially different to the one described in Figure 5.4. Since that analysis was performed for a given BCP morphology we now aim to study the case of changing f_0. Again, we now fix the affinity of nanoparticles and study the phase of a block copolymer with a morphology given by f_0, in the presence of a number of particle ϕ_p- using neutral nanoparticles instead. Therefore $\psi_0 = 0$, that is, nanoparticles always have a preference towards being symmetrically placed at the interface.

At low volume fraction, in figure 5.7 we simply observe segregation of nanoparticles to the interface. If we keep increasing the number of particles, a competition between NP-BCP

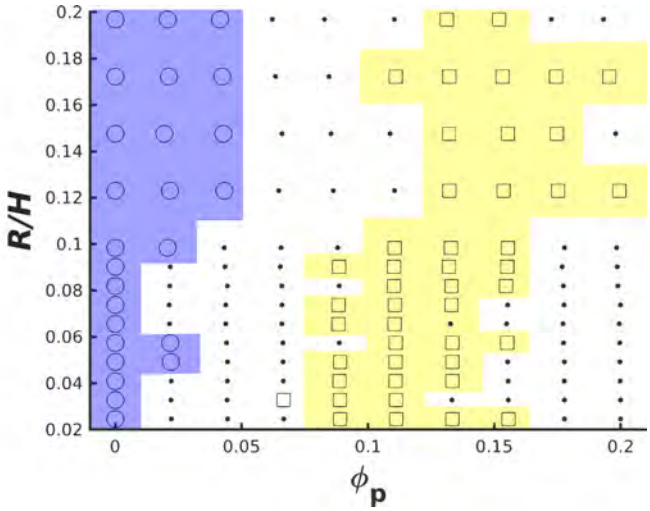

Figure 5.6: Phase diagram of an asymmetrical BCP matrix ($f_0 = 0.4$) with different NP fraction ϕ_p of different sizes R, reduced with the size of the periodicity H of the BCP morphology. The phases shown are: Cylindrical (Circles), Mixed (dots) and lamellar (Squares)

coupling free energy and the $(\nabla\psi)^2$ term in Equation 2.8 comes into action when the interface is filled with colloids. Therefore, new interface can be created when sufficient particles are present in the system. When the BCP's architecture is asymmetrical the presence of nanoparticles induces a transition from hexagonally-ordered circular domains to elongated, which explains the presence of mixed-to-lamellar (dots to squares) and circular-to-mixed (circles to dots) phase transitions in Figure 5.7. Symmetrical BCP (ie, lamellar, represented by squares) displays more interface in the absence of nanoparticles and therefore can accommodate a larger number of neutral nanoparticles than any other morphology. At sufficiently large number of particles lamellar domains are broken into smaller domains (asterisk). Figure 5.8 a) shows a large simulation of such a regime, in which the disordered overall structure can be seen.

At intermediate ϕ_p values we observe an interesting new phase (crosses) in the case of asymmetrical BCP ((×) in Figure 5.7): in the presence of a minority/majority BCP phase the NPs surround the minority domains and a particular balance $\phi_{majority} = \phi_{minority} + \phi_P$ can be reached, leading to the formation of a quasi-lamella phase for the majority phase and NP-enclosed minority domains, as can be also seen in Figure 5.8 b), where a considerably large system (512×512 grid points) are simulated. The overall orange phase percolates the surface, while blue domains are enclosed, as shown in the detail.

This behavior is not present any more when higher concentrations are reached ((∗) in Figure 5.7). At this point the particular architecture of the BCP becomes less important, with alternating A-B domains dispersed into a NP-rich matrix.

The surfactant-like nature of neutral nanoparticles results in the volume fraction ϕ_p not being the most relevant parameter to account for the phase behavior . The fraction of the block copolymer interface that is occupied by nanoparticles is more relevant instead. This magnitude is not easily accessible as it is strongly dependent on the dynamical evolution of the system, therefore we consider the ratio between nanoparticles' linear dimension and interface size in the absence of colloids $\gamma_p = 2RN_p/\Gamma_0(f_0)$. Ideally, in the symmetric BCP case the interface length only depends on the number of lamella periods that the system size can accommodate. Scaling with the size of the system $\Gamma_0(1/2)/V \sim 2/H$, with H being the periodicity of the lamella.

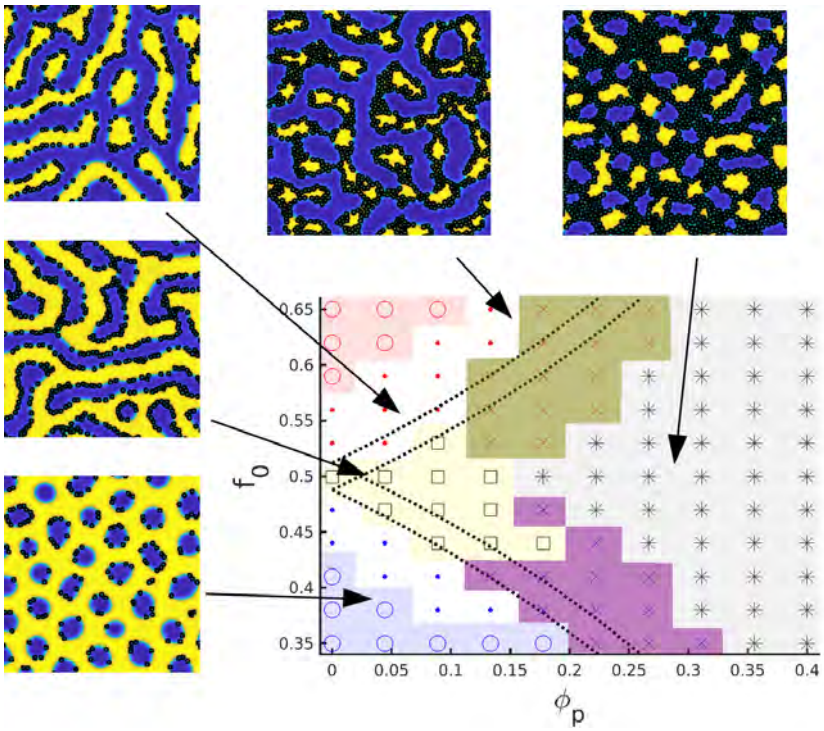

Figure 5.7: Mophological phase diagram of neutral nanoparticles ($\psi_0 = 0$) in several diblock copolymer matrices given by f_0. Shown phases are: Circular phase(Circles),Mixed phase (dots), lamellar (squares), broken lamella ($*$) and balanced lamella+circles ($\times$)

Therefore we can express the occupied interface fraction as

$$\gamma_p \sim \frac{\phi_p}{\pi R/H} \tag{5.2}$$

from which we can expect that the transition from lamella to broken-lamella phase will occur at $\phi_p^* \sim \pi\gamma_p^* \frac{R}{H}$ with $\gamma_p^* > 1$ meaning that we are over the saturation point. Hence, smaller-sized lamellar can accomodate a larger number of particles and therefore a larger number of particles are needed to induce the breaking of the domains into smaller ones. We can confirm this by running simulations in which the size of the lamella domains is changed at different volume fractions and record the overall phase. In Figure 5.9 we can observe the different phases and conclude that Equation 5.2 approximately captures the trend of the two phases, although it is far from a quantitative agreement. This is firstly due to the interface length being a complicated parameter to predict, even when we only consider a pure polymeric system: the interface size is always larger than $2/H$, as the system will often be trapped in metastable states. Furthermore, colloids do not simply assemble side-by-side in the interface, instead colloids often form small local clusters.

5.4 Conclusions

The phase behavior of BCP/NP composite systems has been studied in terms of the BCP composition and the nanoparticle loading, chemical affinity and size. The NP segregation within the BCP is determined by the affinity of the particle, that is, the coating of the surface of each NP in a typical experimental setup. At low concentrations nanoparticles can either segregate to the interface between domains or be dispersed within its preferred phase. We have presented

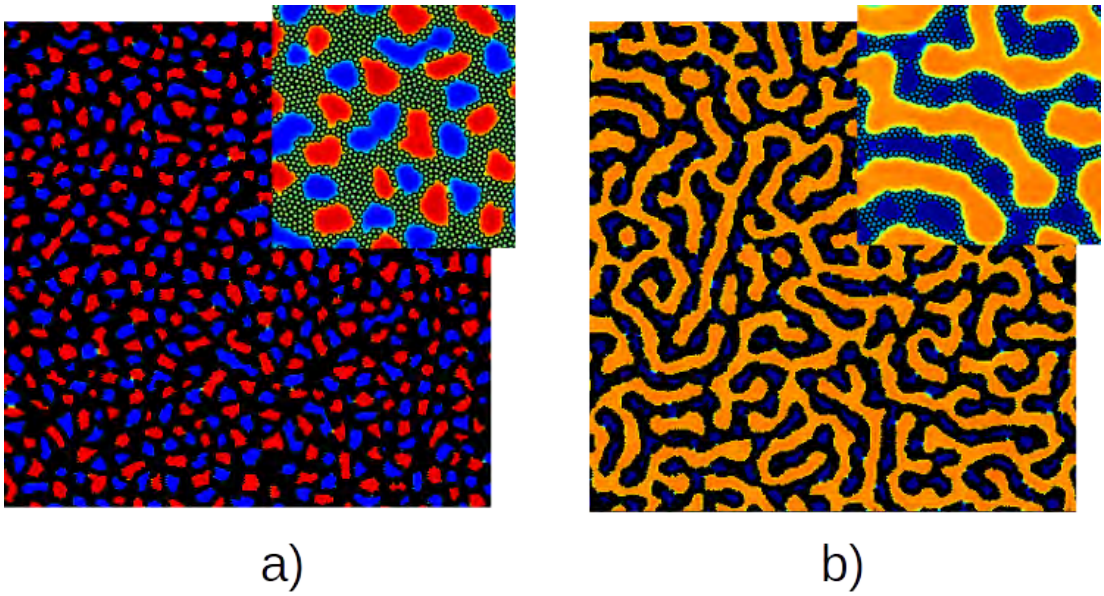

Figure 5.8: Final snapshots of 512×512 simulations with insets showing a 128×128 subregion. In a) $\phi_p = 0.4$ and $f_0 = 0.5$ while in b) $\phi_p = 0.22$ and $f_0 = 0.35$

a phase diagram of the morphology of the diblock copolymer in terms of different values of the affinity. To our knowledge, this is the first time that the chemical affinity of the colloids has been studied, exploring totally different regimes ranging from A-compatible to B-compatible coating.

In order to study high concentration cases with more generality we focus firstly on totally compatible particles, which segregate to one of the domains. Considering several BCP compositions we have found the expected order-to-order phase transition, and a phase diagram is constructed. This phase transition is due to an increase in the effective monomer fraction f_{eff} of the hosting domain. The ability to tune the effective composition of a diblock copolymer with a given f_0 by adding compatible nanoparticles is an advantage, as one single BCP sample can lead to a variety of morphologies[97].

The relatively fast CDS scheme has allowed to perform a large number of simulations to obtain a more precise phase diagram, in contrast with previous works using Monte Carlo methods [55]. Furthermore, we can compare the hybrid CDS/BD method with MC by plotting the transition curves given by Equation 5.1 as described by Huh [55]. This confirms a good agreement with previous works. This $f_0 - \phi_p$ phase diagram can be compared with experimental results via f_{eff}, as Lo et al.[95] directly mapped the morphology of a BCP/NP system with an effective composition ratio, obtaining a good agreement.

The size of the nanoparticles with respect to the block copolymer lengths has been examined to find that the R/ξ ratio plays a role in the morphological changes: smaller nanoparticles with respect to the interface size induces phase-transition more effectively. The interparticle potential has been shown not to affect the block copolymer, that is, the assembly of the nanoparticles does not influence the BCP morphology.

Secondly, neutral nanoparticles induce phase transitions in the BCP at concentrations higher than the saturation. In this regime NPs induce an increase in the BCP interface length, resulting in transitions towards elongated domains. The saturation process is strongly dependent on the size of the interface without colloids $\Gamma_0(f_0)$ which is larger for lamellar morphologies and smaller periodicity. The characteristic parameter is no longer the volume fraction of nanoparticles

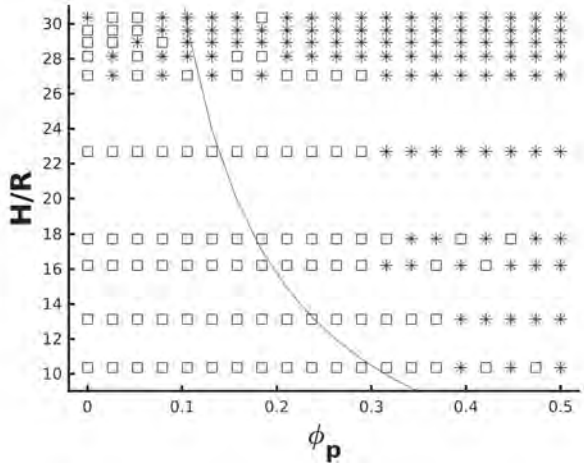

Figure 5.9: Phase diagram of neutral nanoparticles in a lamellar BCP matrix of different domain periodicity (H) and at different NP radius (R). Square represent lamellar while asterisk stand for broken lamella. The blue curve shows a constant saturation line in accordance to Equation 5.2

$\propto N_p R^2$ but an estimation of the fraction of nanoparticles in the interface $\propto N_p R$. In the case of lamellar morphology, the saturation of the interface leads to domains being broken into shorter ones, again to induce higher interface length. At sufficiently large saturation rate the nanoparticles percolate the system, with alternating block copolymer domains dispersed within a colloid-rich matrix. We have been able to construct a phase diagram which states the various regimes that emerge when adding neutral nanoparticles to a diblock copolymer characterised by a composition ratio f_0. This new phase diagram allows to predict the morphologies of a diblock copolymer in the presence of neutral nanoparticles.

Lamellar to bicontinuous morphological transitions have been reported in experiments using surfactant particles [99]. This behavior agrees qualitatively with our results involving a high concentration (above the saturation of the interface). Despite the simplicity of our model we are able to capture the same physical behavior as experiments. A future work will involve the precise comparison with experiments and theoretical prediction[51].

Asymmetrical diblock copolymers in the presence of moderate fractions of particles adopt a NP-induced phase based on the balance of the majority phase with respect to the combination of minority phase and NP-rich regions. Given this balance, the majority block displays a lamella-like morphology while minority domains are enclosed by the nanoparticles.

CHAPTER 6

Diblock Copolymer Nanocomposites: Colloidal Assembly

Abstract

The assembly of colloids suspended in a block copolymer melt can be considerably different from their organisation in a simple solvent. The mesoscale ordering of the block copolymer can help achieve highly ordered configurations depending on chemical properties and nanoparticle size. The formation of colloidal clusters is studied both for the case of selective and non-selective nanoparticles. Furthermore, the regions of parameter space in which hexagonal close-packed ordering occurs are delimited. The macrophase separation between neutral nanoparticles and the block copolymer melt can lead to the formation of interesting polymer morphologies which can be related to block copolymer/homopolymer blends and block copolymer nanoshells.

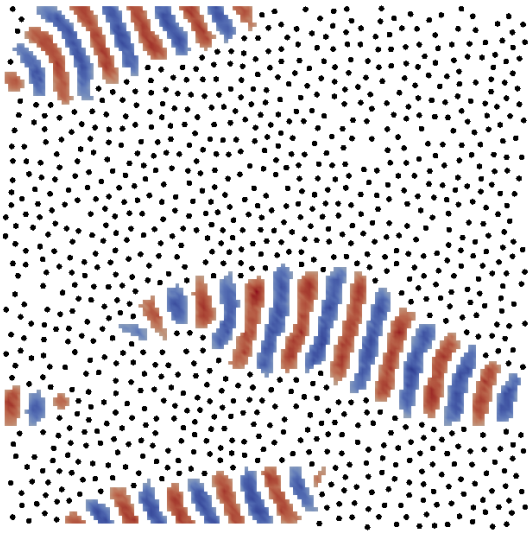

6.1 Introduction

In the previous Chapter we have performed a systematic study of the morphological changes induced by colloids in the resulting block copolymer (BCP) nanocomposite system. We have explored the morphologies of the BCP for a variety of nanoparticles (NPs) concentrations, sizes and chemical properties. Nonetheless, the aim of this thesis is to explore both the polymeric properties as well as the colloidal assembly. As we saw in Chapter 4, colloids can behave diffusively in a disordered manner at low concentrations when NPs are perfectly solvable in one of the phases of the BCP. On the other hand, we have also found instances of colloidal ordering into a crystal phase, as well as clustering, driven by NPs being insolvable or by constrained effects.

In this chapter we continue making use of the CDS/BD scheme and will cover the study assembly of colloids under several different conditions. Firstly, we can study selective NPs with a preference towards either A or B copolymers. After that, we can also study the colloidal behaviour of neutral, interface-compatible NPs. Neutral NPs have been comparatively devoted less experimental previous work, while results from previous Chapter indicates that interesting new phases can be found resulting from the mixture of neutral NPs and BCP.

6.2 Model

This model used in this chapter introduces no significant changes over the one described in Chapter 2

Hexatic bond order parameter

The hexagonal close-packed configuration in two dimensions is frequently found in colloidal physics at high packing densities. In order to characterise this structure it is common to use the hexatic order parameter

$$\psi_6 = \left\langle \frac{1}{6} \sum_{j=1}^{n} \exp\left(6i\theta_{ij}\right) \right\rangle \tag{6.1}$$

with n being the number of first neighbours to a particle α and $\langle * \rangle$ representing an average over all particles. The parameter ψ_6 is thus related to the angles between neighbouring particles θ_{ij}.

6.3 Results

In this section we will study the assembly of colloid mixed with a block copolymer melt. Unless otherwise specified, we will use the same parameters as in Chapter 5.

6.3.1 Ordering of colloids within A-phase

In Fig 4.3 in Chapter 4 we found a transition in the colloidal ordering from liquid-like diffusive motion to a colloidal arrangement in a hexagonal lattice configuration due the the local high concentration. This is clearly due to the presence of the BCP which reduces the available space for the colloids to diffuse. In Fig. 5.3 and Fig. 5.4 we have explored the morphology of the BCP in the presence of nanoparticles and made use of an effective parameter f_{eff}, defined in Eq. 5.1. This effective A monomer ratio takes into account the effective change in the overall monomer ratio due to the presence of a concentration ϕ_p of A-compatible colloids. The effective

available volume (surface in 2D) for a concentration ϕ_p can be written as $V_{avail} = f_{eff} V_{tot}$ which results in an effective NP concentration that can be written as

$$\phi_p^{eff} = \frac{\phi_p}{f_{eff}} \tag{6.2}$$

which results from assuming that a NP which is compatible with the A copolymer has access to a subregion of the whole system that can be written as $V_{avail} = V[\phi_p + (1 - \phi_p) f_0]$.

In order to validate the effective concentration we can explore the colloidal transition from a liquid-like disordered state to a solid-like hexagonal configuration. The colloidal ordering can be tracked by the orientational bond order parameter Ψ_6, as defined in eq. 6.1. In Fig. 6.1 we study the concentration of NPs ranging $0 < \phi_p < 0.9$ and the BCP composition $0.35 < f_0 < 0.6$ for $\psi = -1$ affinity NPs. At low concentrations these particles have no considerable order, and Ψ_6 grows monotonically with ϕ_p^{eff}, except for the very high ϕ_p^{eff} regime. It can be noted that a single parameter captures the ordering of colloids considerably well, with all curves approximately fitting into a single trend, regardless of the choice of f_0.

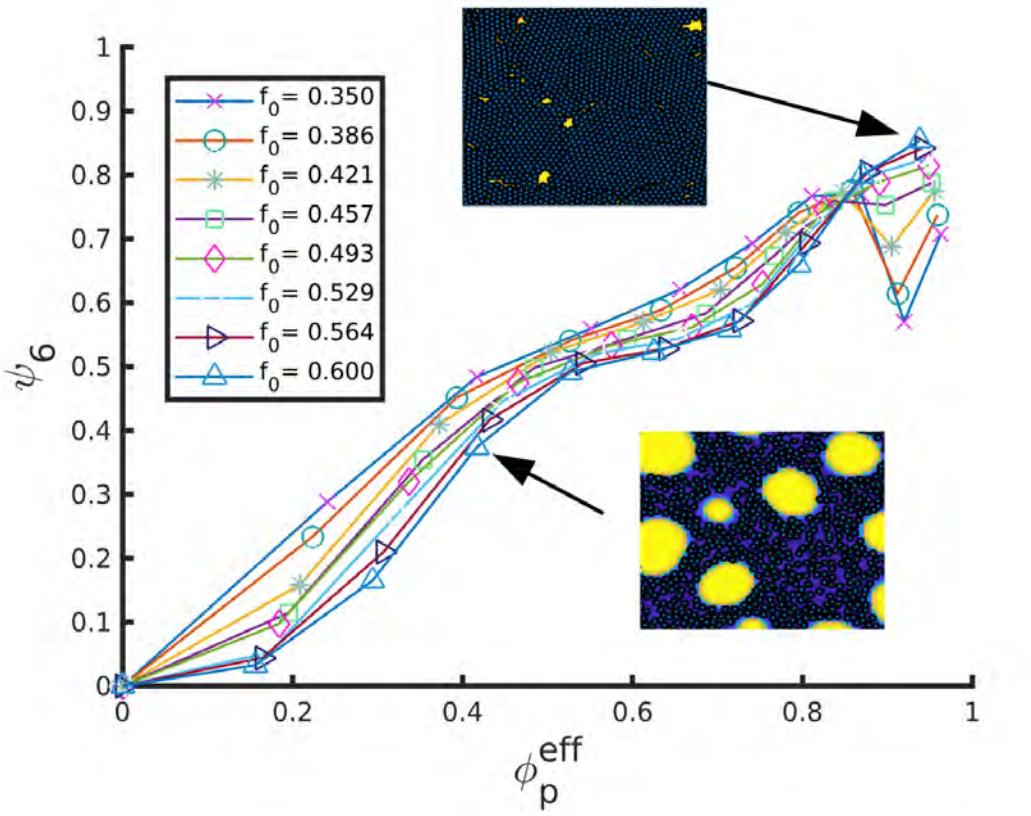

Figure 6.1: Curve of colloidal ordering represented by the hexatic order parameter Ψ_6 in function of the effective concentration for a range of concentrations and composition parameters f_0, which can be found in the legend.

While the curve in Fig. 6.1 approximately captures the trend of all values of f_0 into a single curve depending on ϕ_p^{eff}, a closer look can draw two different regimes in which a finer analysis of the system needs to be made. Firstly, the morphology of the BCP plays a role in the colloidal assembly. In the $f_0 < 1/2$ regime, colloids are segregated within the minority, circular domains. Thus the level of constrain is higher than NPs which can freely diffuse in a single majority domain. This explains why smaller values of f_0 lead to higher values of Ψ_6. This behaviour is not relevant any more in the high concentration regime. Here, the NPs are occupying the

majority of the system with only a few irregular B domains which are placed at the defects of the colloidal crystal structure. For this reason, a high f_0 value leads to high ϕ_p^{eff} values, that is, higher ordering, as it is correlated with less and smaller defects. A transition region occurs at $\phi_p^{eff} \sim 0.8$ where the two regimes approximately cross each other.

6.3.2 Aggregation of incompatible NPs

Asymmetrically incompatible NPs have been found to segregate to the least incompatible phase of an A-*b*-B BCP. In experiments[85], gold NPs mixed with PS-*b*-PMMA displaying lamellar morphology have been used to study the assembly of colloids which are not solvable with neither of the blocks of a BCP. NPs were found to segregate to the PMMA domains driven by a lower incompatibility between the poly(ethylene oxide) (PEO) coating the Au NP surface and the PMMA copolymer. Furthermore, a phase-separation occurs, where NPs form hexagonally ordered clusters. This is, in summary a hierarchical assembly of block copolymer nanocomposite systems.

In order to gain insight over this mechanism, we can make use of the Cahn-Hilliard approach to study the range of parameters for which such aggregation occurs. The perturbation created by a single NP in an otherwise flat BCP profile can be estimated by free energy minimisation. The approximate solution is semi analytic and is fully described in Appendix B. In summary, the profile of the order parameter $\psi(r)$ around a NP can be expressed as

$$\psi(r) \approx 1 + \beta(\sigma, R_{eff})\Delta\psi_0\psi_c(r/\rho) \tag{6.3}$$

in which the value of 1 represents the unperturbed BCP bulk value (should be -1 for a B' compatible NP inmersed in the B phase). The differential affinity $\Delta\psi_0 = |\psi_0 - 1|$ represents the difference between the bulk value of ψ and the affinity of the NP, ie, represents the incompatibility of each NP with its hosting phase. Parameter $\beta(\sigma, R_{eff})$ is a function of the strength and size of the particle and can be calculated numerically and serves as a weighing function that represents the amplitude of the distortion. The range of this perturbation is ρ which is always similar and larger than R_{eff}.

From what is described above, it is clear that a particle which is incompatible with its medium introduces a penalty which can be minimised but not eliminated. For this reason, two NPs separated will minimise the overall perturbation by aggregating. This suggests the existence of an effective interaction mediated by the surrounding block copolymer. This behaviour can be estimated by calculating the energy gap of this effective interaction, as follows: two nanoparticles separated by a distance $r_p >> 2\rho \sim 2R_{eff}$ are sufficiently far away that no influence is exerted between them. In such a regime, the total coupling free energy of the system is

$$F_\infty \equiv F_{cpl}(r_p \to \infty) = 2F_{cpl}^{(1)} \tag{6.4}$$

where $F_{cpl}^{(1)}$ is the coupling free energy of an isolated particle. Thus, the total coupling free energy is simply the sum of two contributions. To estimate the minimum of the $F_{cpl}(r_p)$ curve, the coupling free energy of two overlapping particles can be estimated, that is, when their relative distance is zero. In such case, the distortion created by the particle should be doubled, which can be controlled via the parameter σ. For this reason, we can approximate the effect that two particles introduce by considering a single particle with doubled distortion effect. Therefore,

$$F_0 \equiv F_{cpl}(r_p = 0) = 2 \cdot (2\pi R_{eff}^2 \sigma \Delta\psi_0^2) \int_0^1 dr\ r\psi_c(r)\left[1 - \beta(2\sigma, R)\psi_c(r/\alpha)\right]^2 \tag{6.5}$$

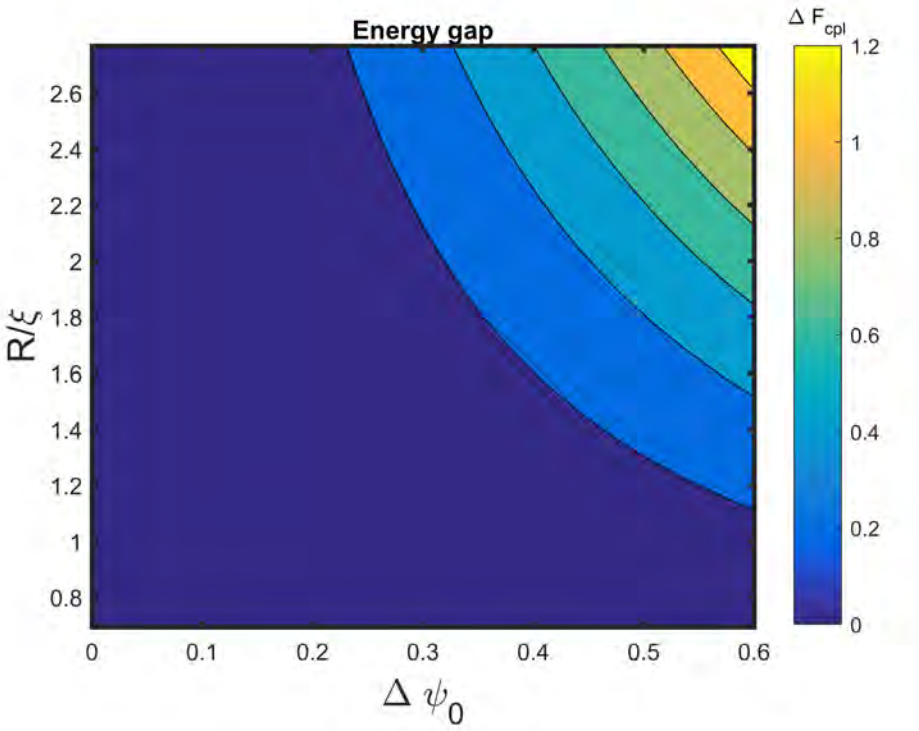

Figure 6.2: Colourmap of the energetic gap ΔF_{cpl} for $\sigma = 1$ and several values of the ratio R/ξ and the affinity difference with respect to the BCP equilibrium value $\Delta\psi_0 = \psi_0 - \psi_{eq}$. The colourbar represents the energetic gap scaled with k_BT .

the resulting effective $F_{cpl}(r_p)$ displays an energetic gap of size $\Delta F_{cpl} = F_\infty - F_0$ which can be evaluated numerically, as in figure 6.2, where we can observe the regions in which the energetic gap becomes noticeable with respect to k_BT.

This effective interaction translates into an attractive extra term in the dynamical behaviour of colloids, which in turn results in clusterisation and close-packed hexagonal assembly. We have already seen this behaviour in simulations -as shown in Chapter 4- and we can further study this by performing a large number of simulations exploring parameters R-ψ_0, the size of the particle versus its affinity. We can then let the system evolve and calculate the 2D bond order parameter which is 0 in a disordered state and 1 in a hexagonal configuration. The results are shown in figure 6.3 where we can observe the simulation points such that the bond order parameter is above a certain value. The behaviour is clearly consistent with our semi-analytical approximation.

6.3.3 Ternary mixture: BCP/NP$_A$/NP$_B$

So far we have focused on a single species of nanoparticles. In Chapter 4 we reported on NPs with different sizes and chemical affinities, mostly regarding their localisation within the BCP micro structure. We can extend this study to two species of NPs which interact differently with each other while maintaining an equal coupling with the BCP.

Using a Lennard-Jones interaction potential we can tune the attractive/repulsive interaction between the two species by introducing a pairwise additive potential with the interaction between two pairs of NPs i, j written as

$$V_{ij}(r_{ij}) = V_{Yuk}(r) + 4\epsilon_{ij}\left[\left(\frac{R_{12}}{r}\right)^{12} - \left(\frac{R_{12}}{r}\right)^{6}\right] \tag{6.6}$$

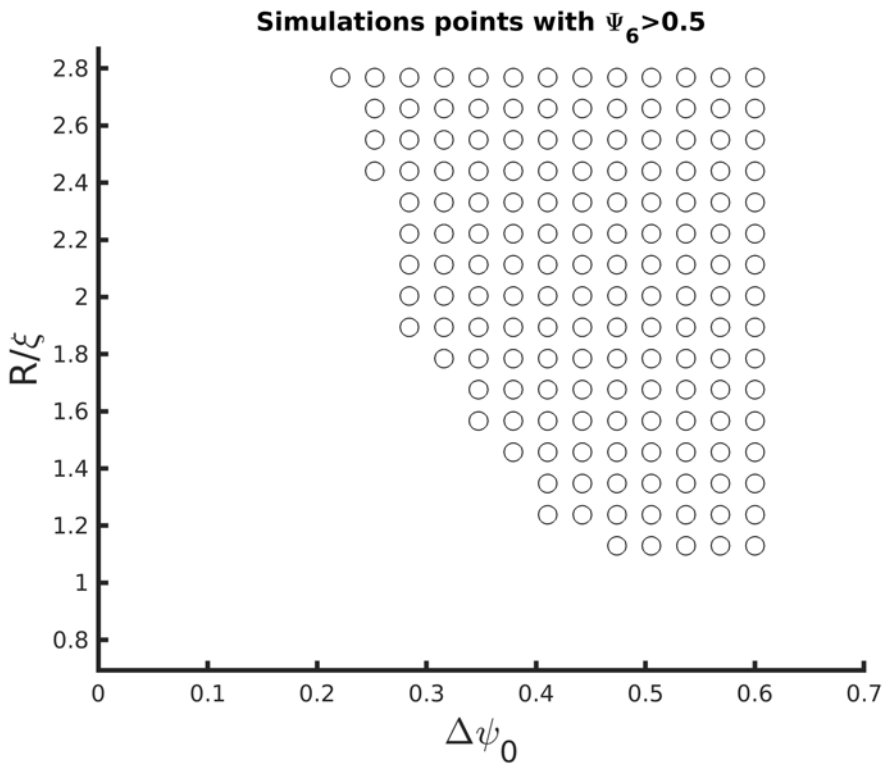

Figure 6.3: The simulation points for which the bond order parameter is above $\Psi_6 > 0.5$, thus indicating the region in which hexagonal order occurs.

where $R_{12} = 2R_0$ is the NP diameter and $\epsilon_{ij} = 0$ if i, j are particles of different species and $\epsilon_{ij} = U_0$ if they belong to the same species. A repulsive Yukawa potential is added in order to provide a numerically highly stable repulsion in all cases.

In Fig. 6.4 we show the time evolution of a system of two NP species which are compatible with the A-block (minority) in an slightly asymmetric BCP ($f_0 = 0.45$, chosen to prevent lamellar-to-cylindrical transition). Fig 6.4 (a) shows the initially disordered state after just 1000 simulation steps, while (b) and (c) show the formation of BCP morphology at steps $t_n = 10^5$ and 10^6, respectively. NPs are found to form aggregates of the same type of NPs. At only a much later stage ($t_n = 90 \cdot 10^6$) we can find the formation of considerably large, alternating NP clusters within the lamellar domains. It must be noted that the process of phase-separation between different colloidal species occurs only in the very late stages of the simulation. The final stages require a reduced time $t/\tau_{col} \sim 10^4$ using the colloidal diffusive time as a reference. These aggregation mechanism with phase-separated colloidal domains is in accordance with Dissipative Particle Dynamics simulations [57].

6.3.4 Phase behaviour of neutral nanoparticles

Nanoparticles can be coated to be compatible with the interface between BCP domains, for instance, by grafting a mixed brush of homopolymers into its surface[94, 31, 93]. Neutral NPs can greatly modify the BCP morphology after the inclusion of a considerable concentration[100, 94] of NPs. There are a multitude of sources for such morphological transitions. Using Strong Segregation Theory[51] it has been predicted that surfactant-like NPs can lead to layer instabilities of the symmetric BCP interface.

At high concentrations the interface can be saturated with NPs, which can lead to a pref-

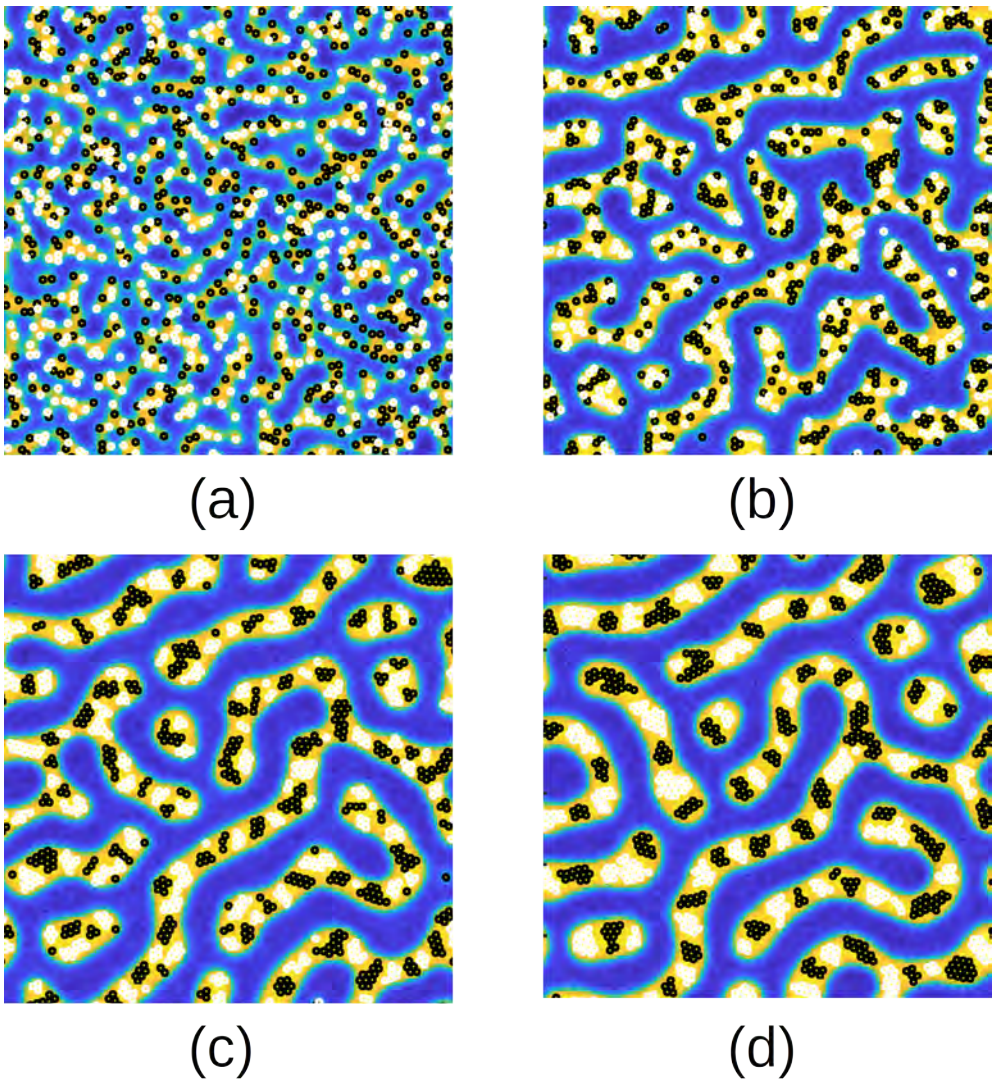

Figure 6.4: Time evolution of a ternary mixture of BCP and two types of NPs. Black and white colloids interact equally with the BCP but experience attractive NP-NP interactions only with same-colour NPs. Snapshots represent time steps 10^3, 10^5, 10^6 and 90×10^6, respectively for (a), (b), (c) and (d)

erence for curved interfaces that maximise the interface length. On top of that, each NP is introducing a small distortion in the surrounding BCP profile, both in the normal and parallel direction of the interface. In our coarse grained model this distortion is different from a typical capillary-interaction mechanism and is instead driven by the finite size of the interface. Each NP is introducing a small $\psi(\mathbf{r}) \sim \psi_0 = 0$ region with a length scale ξ of the order of the interface size. In Appendix B.3 we justify the origin of this intrinsic distortion created by a single neutral NP.

In Fig. 6.5 we explore a fixed concentration of NPs $\phi_p = 0.4$ for a range of values of the interface width 2ξ and the lamellar periodicity H. In this parameter space, the relative size ξ/H becomes extremely relevant. Fig. 6.5 shows the disordered phase of BCP (asterisk) in which A and B monomers are not undergoing microphase separation. A dotted line with a constant ξ/H ratio is shown to capture the ODT line. Fig. 6.6 bottom right shows this disordered state.

Contrary to that, in the left-most part of Fig. 6.5 we can observe a region of blue dots representing high hexagonal colloidal ordering. In this region the colloids are forming an almost unique percolating cluster. In this region the BCP domains (originally lamellar for $N_p = 0$) are broken down into smaller, irregularly shaped domains. For higher values of R/H we can observe an important morphological transition in the BCP from irregularly-shaped domains to elongated BCP-rich domains with alternating black/white domains. In this region the NPs are expelled from the interface between domains in order to create a NP-rich areas which are macrophase-separating from the BCP. This is represented by squares in Fig. 6.5. It is important to differentiate between BCP domains (black or white) and BCP-rich domains. In BCP-rich domains the density of colloids is low and microphase-separation of the block copolymer domains is occurring. In the squares region, the number of BCP-rich domains becomes low, while the number of NP-rich domains is higher.

NP phase separation from the BCP melt suggests a strong incompatibility between these two elements of the mixture. This region is clearly occurring with larger values of R/ξ. As mentioned before, the extend of the NP distortion is controlled by the size of ξ. On top of that, a higher value of R/H leads to an enhanced distortion which is longer ranged. It depends not only on the short range interfacial term in the free energy but also on the long range B term. The orientation of the BCP domains is normal to the NP-rich areas, as expected for an non-selective hard wall [43]. Furthermore, our results are considerably comparable with BCP/Homopolymer blends, as described by a two order parameter model using CDS[101]. We are, in essence, describing a ternary mixture of A-b-B/C component blend. A further morphological change occurs as the ratio R/H is again increased: the BCP-rich number of domains continues to lower and the NPs undergo order to disorder transition, in which they are now diffusively moving in a disordered BCP background. In this regime the ξ/H indicates the system is closer to the ODT and thus the BCP can easily find local disorder near NP-rich areas (NPs induce mixing in its surroundings). The higher available space leads to a disordered phase for the NPs, which behave as liquids. Finally, in this regime the BCP tends to form a single BCP-rich domain which is elongated as it tends to maximise the number of perpendicular black/white domain boundaries with the NP-rich domains.

6.3.5 Aggregation of large neutral nanoparticles

Neutral nanoparticles can be found to segregate at the interface between domains in order to minimise the interfacial tension with both BCP phases. Within the Landau-Ginzburg model we have presented, neutral NPs have an affinity towards the interface driven by the coupling

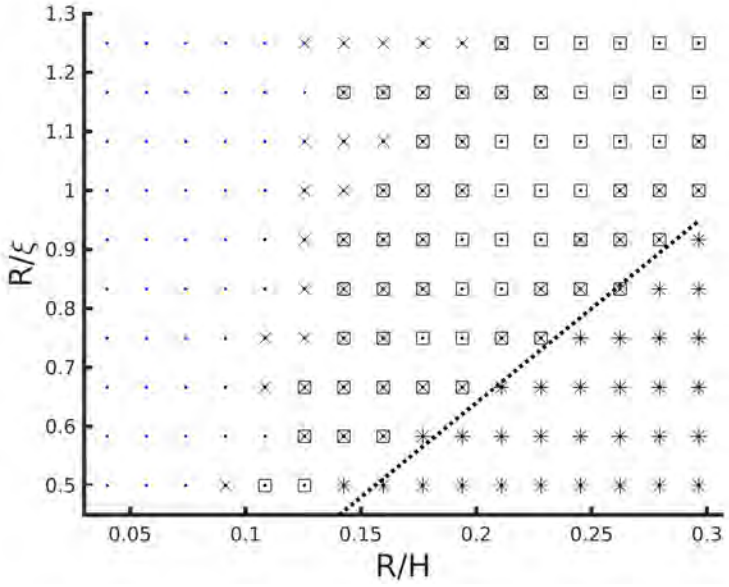

Figure 6.5: Phase behaviour of a mixture of lamellar-forming BCP with a fixed concentration $\phi_p = 0.4$ of interface-compatible nanoparticles. Symbols represent the following: A single black point represents a simulation point. On top of that, a blue dot marks values such that colloidal hexagonal order parameter $\Psi_6 > 0.4$, ie, when the colloids are hexagonally arranged. If the number of BCP-rich areas is smaller than 20, a square is used. An additional cross indicates a number of colloidal clusters larger than 7. Asterisks stand for disordered BCP phase along with a fluid-like arrangement of colloids.

term in the free energy. Nonetheless, relatively large nanoparticles compared to the interface are not easily accommodated between two BCP domains, thus a process of aggregation between nanoparticles can be triggered. We note that this is not driven by an explicit attractive NP-NP term in the interparticle potential energy. Instead, it is mediated by the BCP in order to minimise the global free energy. Indeed, the free energy is minimised by creating large areas with $\psi \approx 0$ where phase-separated NPs are localised. Examples of this behaviour can be found in Figure 6.7 where we simulate a BCP mixture in the weak-segregation limit $2\xi/H \approx 0.34$. We choose this regime as it allows us to simulate a large number of BCP domains, which we will show it essential in asserting the phases that we want to explore. Furthermore, NP incompatibilities are reinforced by having large NPs compared to the lamellar period.

For a fixed nanoparticle surface fraction $\phi_p = 0.1$ we tune the NP size as shown in figure 6.7. While a tendency to aggregate is present in all three cases, the aggregation in clusters can be found to grow with the particle size. In Fig. 6.8 we can plot the fraction of NPs that belong to the largest cluster, as an estimate to the aggregation. Globally, we observe the formation of NP-rich areas which are phase-separated from the surrounding block copolymer. As expected for neutral nanoparticles, the BCP lamellar domains are oriented normal to the NP-rich domains. We note that this behaviour is recovered from simulations of a single large NP surrounded by a BCP film (ie, nanoshell)[43]. This orientational condition determines also the shape of the NP clusters and their localisation.

In Fig. 6.9 we plot three possible assembly configurations of the NP clusters (gray areas) within the microphase-separated lamellar BCP (red and blue domains). In Fig. 6.9 (a), the system tries to maximise normal contacts between the lamellar direction of change (Y in Fig. 6.9) and the wall with the NP-rich gray area. For this reason, several instances of elongated, ellipse-like domains are present in snapshots in Fig. 6.7. This is preferred over a more isotropic

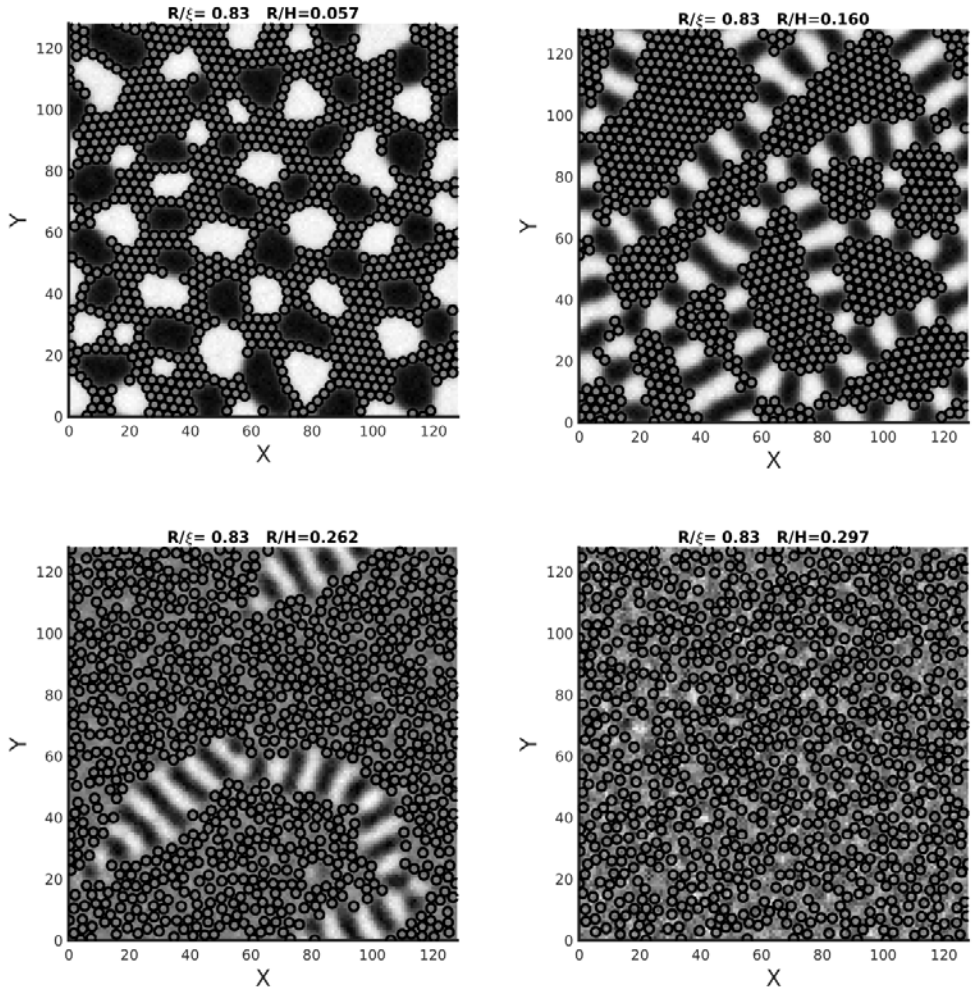

Figure 6.6: Four instances of lamellar-forming BCP mixed with a fixed concentration of interface-compatible nanoparticles. The size of the lamellar periodicity H is tuned with respect to the NP size.

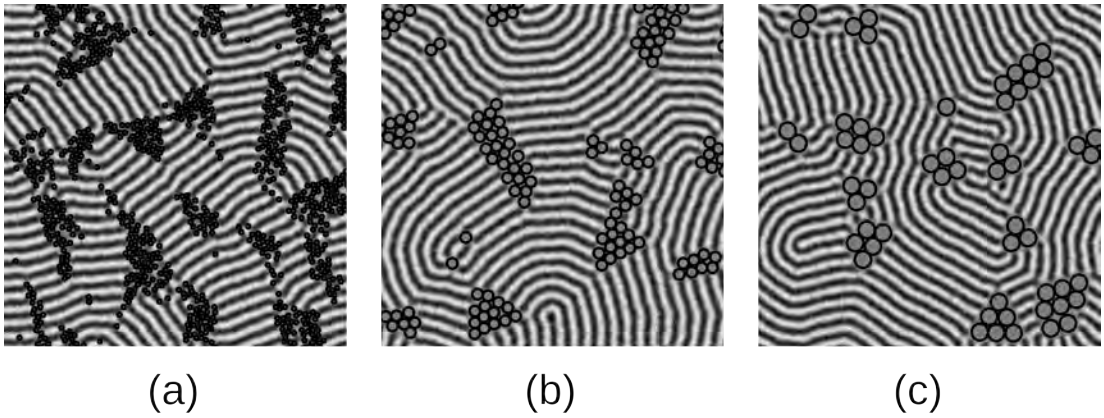

Figure 6.7: Aggregation of neutral NPs in a symmetric diblock copolymer with periodicity $H \approx 9.85$ for NP sizes $R_0 = 1.46, 3.77$ and 6.08 for (a), (b) and (c), respectively.

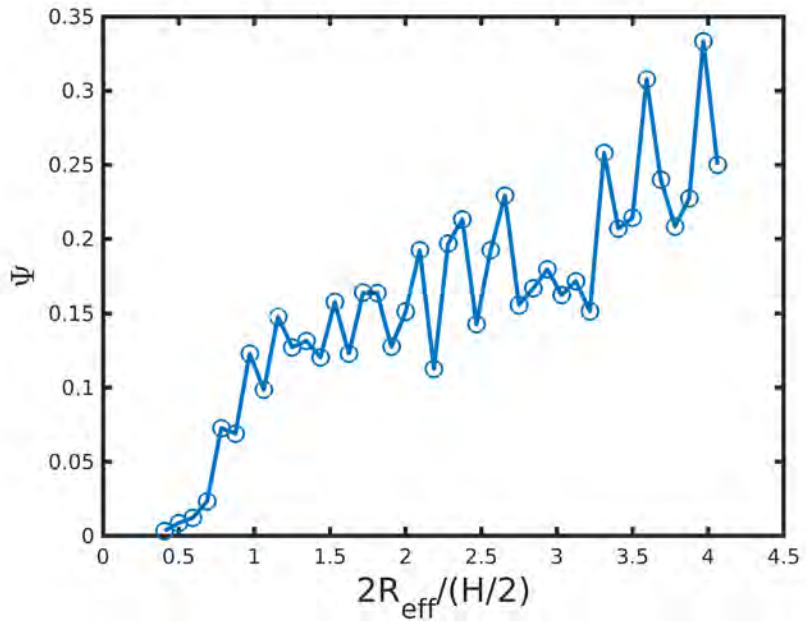

Figure 6.8: Fraction of neutral NPs that belong to the largest colloidal cluster for the same simulation set as shown in Fig. 6.7. In the X axis we show the reduced effective particle diameter with the lamellar spacing (half a lamellar period).

cluster shape. Another plausible assembly configuration is for the NP cluster to form a square-like domain with 4 different lamellar orientation, as in Fig. 6.9 (b). In this way, the cluster is placing itself in a BCP defect while maximising the number of normal contacts between the lamellar domain and the gray wall. Nonetheless, a north-south-east-west lamellar is difficult to achieve, as it would be highly unstable due to the perpendicular contacts between different grains of lamellar orientation. A more common type of defect is a triangular one, where three different lamellar orientations coexist. In Fig. 6.9 (c) we show an example of such a triangular-shaped cluster with the surrounding BCP. In Fig. 6.7 it is possible to see several instances of these two types of co-assembly: elongated NP cluster within a well-ordered lamellar region and triangular clusters in the defect formed by three cohesive lamellar grain.

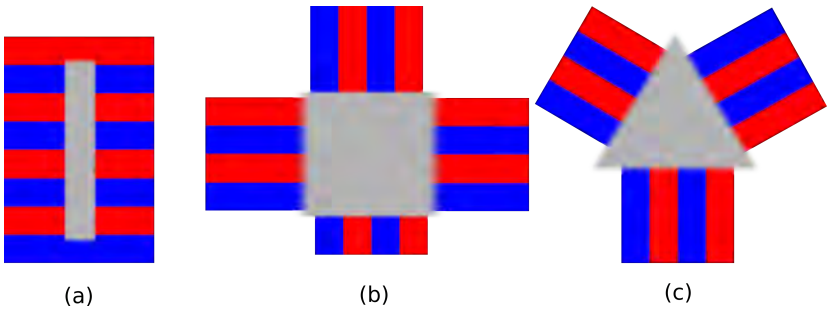

Figure 6.9: Examples of colloidal cluster (gray areas) shapes in BCP microphase separation (alternating red and blue domains).

6.4 Conclusions

In this chapter we have focused the attention on the assembly of colloids within a block copolymer melt. Firstly, we have studied the simple case of BCP-induced solidification in

the colloidal assembly for A-compatible colloids in a A-b-B BCP . We have found enhanced confinement effect due to the unavailable regions of space in which colloids are not solvable. A simple single effective concentration parameters broadly captures this mechanism in the same spirit as a single effective composition captured BCP transitions in Chapter 5. These effective parameters can be useful in further works involving block copolymer nanocomposites and it is not limited to continuous Ginzburg-Landau models.

The parameter space of the hexagonal close packing of B' compatible NPs in an A-b-B BCP has been studied to determine the regions in which the NPs form aggregates. It is confirmed with a semi analytical approximation to the effect of B' compatible NPs in a Ginzburg-Landau model.

Neutral NPs have been shown to exhibit a fascinating variety of ordered configurations when mixed with block copolymers. At low concentrations, neutral NPs can form aggregates when the incompatibility with the polymeric matrix is strong. This tendency grows with NP size, leading to a hexagonal close-packed organisation of large NPs. Furthermore, the shape of the colloidal clusters can be related to BCP/hard walls contact angles. Colloidal clusters have been shown to preferentially segregate to BCP defects to alleviate the cost of lamellar orientational grains in the overall free energy. Additionally, NP clusters can also be found within lamellar grains, with an orientation and shape that is again dictated by contact angles.

At high concentrations, neutral NPs can completely phase separate from the block copolymer matrix. In this regime, the colloid/BCP mixture behaves as a block copolymer/homopolymer blend in the continuous limit, in connection with previous simulation works. Moreover, the shape of polymer-rich domains can again be related to contact angles between block copolymers and hard walls.

CHAPTER 7

Chemically Inhomogeneous Colloids: Block Copolymer/Janus Nanoparticles

Abstract

Block copolymer are ideal matrices to control the localisation of colloids. Furthermore, anisotropic nanoparticles such as Janus nanoparticles possess an additional orientational degree of freedom that can play a crucial role in the formation of highly ordered materials made of block copolymers. This chapter presents a mesoscopic simulation method to assert the co-assembly of Janus nanoparticles in a block copolymer mixture, finding numerous instances of aggregation and formation of ordered configurations. Comparison with chemically homogeneous neutral nanoparticles shows that Janus nanoparticles are less prone to induce bridging along lamellar domains, thus being a less destructive way to segregate nanoparticles at interfaces. The combination of asymmetric block copolymer and asymmetric Janus nanoparticles can result in assembly of colloids with an even number of layers within the minority domain. [1]

[1] The content of this chapter has appeared in the publication Diaz, J., Pinna, M., Zvelindovsky, A.V. and Pagonabarraga, I., **2019**. Co-assembly of Janus nanoparticles in block copolymer systems. *Soft matter*, 15(31), pp.6400-6410.

7.1 Introduction

Colloids with patchy surfaces have attracted considerable attention in the last decades[102, 103, 104, 105] given their complex self-assembly processes. In particular, *Janus* -named after the Roman god of duality and transition- nanoparticles (JNPs) are colloids with two chemically distinct *faces* or sides. The self-assembly of a system of JNPs is rich in morphologies[106]. For instance, recent experiments [107] found different types of aggregation, along with alternating sheets of JNPs, which internally are organised in zigzag. Simulations have also explored the self-assembly of JNPs, finding several ordered phases such as lamellar-like structures using Brownian Dynamics [108, 109], Monte Carlo [110] and Molecular Dynamics [111].

JNPs have been mixed with binary mixtures such as homopolymer blends, to find that domain growth is slowed by the segregation of JNP at the interface between domains[112, 113, 114]. Similar results have been found using Dissipative Particle Dynamics (DPD) [115, 116]. The interfacial tension in the presence of Janus colloids[117] was studied by C. Zhou et al .

Experiments involving JNP and BCP are comparatively rare. Recently, Yang et al [13] synthesized JNP such that each side has an affinity towards one of the blocks of a PS-b-P2VP block copolymer, in order to segregate them at the interface between domains. Janus nanoparticles in block copolymers have been shown to posses a higher interfacial absorption energy compared to evenly coated nanoparticles[118].

Similarly to JNP in binary mixtures, JNP in BCP have also been studied using DPD[119, 120]. The combination of chemical-anisotropy and non-spherical shapes was studied by Yan et al [121], finding slowed-down timescale in the lamellar ordering. Using Self Consistent Field Theory (SCFT), random copolymer and mixed brush coated colloids at block copolymer interfaces were compared, finding that nanoparticles coeated with a mixed brush were more effectively segregated at interfaces [122]. SCFT/Density Functional Theory (DFT) simulations were used to study JNP orientation at block copolymer interfaces. The ordering and positioning of JNP in a lamellar-forming BCP have been investigated considering symmetric and asymmetric JNP made of two spheres[123, 124].

In this chapter we make use of a hybrid Cell Dynamic Simulation(CDS)/Brownian Dynamics approach to study JNPs dispersed in BCP mixtures. This in-grid/off-grid method combines a continuous description of the block copolymer with a discrete description of nanoparticles. This allows to simulate a considerably large number of BCP periods along with a large number of particles. Each JNP is considered as an individual object with inhomogeneous chemical behaviour.

The flexibility of the CDS/Brownian Dynamics scheme allows us to study a large parameter space in a relative short time We will attempt to consider nanoparticles with very different surface chemistry, in contrast with previous works in which JNP were mainly compatible with either of the blocks of the BCP. We aim to provide a full description of the JNP co-assembly in diblock copolymer, making the connection with their chemically homogeneous counterparts. While the model is valid both in two (2D) and three dimensions (3D), we will restrict our simulations to 2D. This will allow to study considerably large systems over long time scales. While some degree of richness in the assembly of JNP aggregates is partially lost in two dimensions, the basic features of the JNP/BCP assembly are captured in 2D, namely, the combination of phase-separated domains with a given periodicity in the block copolymer, along with the orientational degree of freedom of each JNP.

7.2 Model

The treatment of the BCP-colloidal coupling differs from previous chapters: while the two-face character of the JNP is introduced in a way that is different from previous approaches [125, 126], mainly because our coupling free energy will be shown to involve a volume (surface, in 2D) integral, as opposed to a surface (line, in 2D) integral. A suspension of N_p circular colloidal nanoparticles is identified by their particle positions $\mathbf{R}_p$. The interaction between the colloids and the BCP is determined by the coupling term in the free energy, which takes a simple functional form

$$F_{cpl}[\psi, \{\mathbf{R}_i, \phi_i\}] = \sum_{j=1}^{N_p} \sigma \int d\mathbf{r}\ \psi_c\left(\mathbf{r} - \mathbf{R}_j\right) \left[\psi(\mathbf{r}, t) - \psi_0(\phi_j)\right]^2 \tag{7.1}$$

with σ being a parameter that controls the strength of the interaction between the JNP and the BCP and ψ_c described in equation 2.17.

The function $\psi_c(\mathbf{r})$ is attached to each colloid accounting for the size and shape of the Janus nanoparticle. We will use

$$\psi_c(\mathbf{r}) = \exp\left[1 - \frac{1}{1 - \left(\frac{|\mathbf{r}|}{R_{eff}}\right)^{\alpha}}\right] \tag{7.2}$$

with $\psi_c(r > R_{eff}) = 0$ because it provides a monotonically decreasing function with a vanishing derivative at the cut-off R_{eff}. Furthermore, R_{eff} serves as the soft-core radius of the particle, while a hard-core radius can be defined as the distance from the center at which $\psi_c(R_0) = 1/2$, identifying the particle size, which results in $R^{\text{eff}} = R_0\left(1 + 1/\ln 2\right)^{1/\alpha}$. Therefore, α controls the sharpness of the decay of $\psi_c(r)$.

The affinity parameter $\psi_0(\phi_i)$ in Eq. 7.1 represents the chemical properties of the NP. Contrary to chemically homogeneous nanoparticles, the coating of a JNP is anisotropic, taking two distinct values $\psi_0 = \psi_+$ or $\psi_0 = \psi_-$ for the negative and positive side of the JNP. Each Janus nanoparticle has a unit vector $\mathbf{n}_i$ that controls the spatial distribution of its chemical anisotropy, as shown in Fig. 7.1, pointing into the positive side of the JNP. In order to characterize the JNP it is useful to introduce two parameters

$$\Delta\psi_0 = \psi_+ - \psi_-, \quad \bar{\psi}_0 = \frac{1}{2}\left(\psi_+ + \psi_-\right) \tag{7.3}$$

where $\Delta\psi_0$ quantifies the chemical inhomogeneity of the particle, such that $\Delta\psi_0 = 0$ describes an homogeneous nanoparticle, while $\bar{\psi}_0$ describes the mean of the affinity of each side of the JNP, which would be the affinity of an equivalent colloid characterized by a homogeneous affinity. These two parameters will help to characterize the JNP, while at the same time are useful to draw comparisons with homogeneous counterparts to JNPs.

The colloid-colloid interaction is introduced as an additional contribution to the total free energy F_{tot} in Eq. 2.1,

$$F_{cc} = \sum_{i,j} V(\mathbf{r}_i - \mathbf{r}_j) \tag{7.4}$$

where $V(r)$ describes the intercolloidal, pairwise potential. In this chapter we will focus on purely repulsive colloidal interactions, and will consider for specificity a Yukawa-like potential,

$$V(r) = U_0\left[\frac{\exp\left(1 - r/R_{12}\right)}{r/R_{12}} - 1\right] \tag{7.5}$$

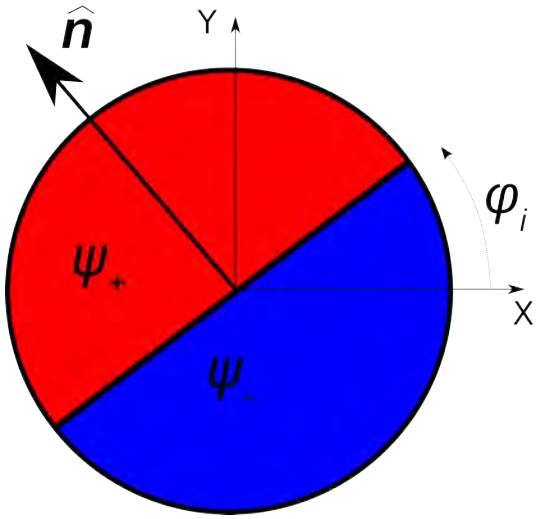

Figure 7.1: Model of a Janus nanoparticle with two chemically distinct sides. Unit vector **n** points into the positive half of the anisotropic nanoparticle.

with $R_{12} = 2R_0$ and r being the center-to-center distance.

Colloids dynamics is diffusive and governed by the Langevin equation in the over-damped regime. The center of mass of each colloid $\mathbf{R}_i$ is considered to follow Brownian Dynamics, that is,

$$\mathbf{v}_i = \frac{1}{\gamma}\left(\mathbf{f}_i^{cc} + \mathbf{f}_i^{cpl} + \sqrt{2k_BT\gamma}\xi\right) \tag{7.6}$$

with γ the friction coefficient, k_BT is the JNP thermal energy and ξ is a random Gaussian term satisfying Fluctuation-Dissipation theorem. The coupling force $\mathbf{f}_i^{cpl} = -\nabla_i F_{cpl}$ accounts for the interaction between the nanoparticle and the BCPs, while the colloid-colloid force arises due to the F_{cc} contribution as in $\mathbf{f}_i^{cc} = -\nabla_i F_{cc}$.

Initially, $\psi(\mathbf{r}, t = 0)$ is randomly distributed, corresponding to a disordered phase. In addition, the initial state for the colloidal center of masses is a non-overlapping random distribution with a random distribution of orientations. The system evolves from this initial condition until a stationary state is reached. The approach to equilibrium can be tracked[42] through $\langle|\psi(\mathbf{r}, t)|\rangle$.

In summary, we use a CDS scheme coupled with a Brownian Dynamics model for the JNPs. Each JNP interacts with the surrounding block copolymer via a shape function and a inhomogeneous affinity, which is split into two parts along the diagonal of the JNP. Each side posses a different affinity value ψ_+ and ψ_- which we will explore in the following sections.

7.2.1 Estimating the energetic coupling of a JNP at the interface

If we consider a flat interface in a diblock copolymer, and a JNP with two faces such as $\psi_+ = -\psi_-$, that is, it is a antisymmetric two-faced particle, we expect that as long as $\bar{\psi_0} > 0$ the nanoparticle will segregate at the interface. Furthermore, the JNP will orient in such a way that the positive face will be completely situated in the positive region of the flat interface. Let's consider a flat vertical interlace such that $\psi(x)$ and a nanoparticle that is assumed to be in $x = 0$ with an orientation given by the normal vector **n**. This vector points into the positive part of the JNP and in the equilibrium it should point also into the positive part of the phase-separared BCP. Nonetheless, we can expect that if the random fluctuations due to the brownian motion are dominant over the anisotropy of the particle, then we would observe

a low degree of orientational order.

Let's estimate the energy that is needed to undergo a flip, that is, for a particle to go from a $\mathbf{n}$ to a $-\mathbf{n}$. Let's begin by calculating the equilibrium coupling free energy

$$F_{cpl}(\mathbf{n}) = \sigma \int d\mathbf{r}\psi_c(r/R)\left[\psi(\mathbf{r}) - \psi_0(x)\right]^2 \tag{7.7}$$

we can't analytically predict the form of the flat interface in the presence of a nanoparticle, nonetheless, let's assume that particle weakly distorts the interface, therefore

$$\psi(x) \sim \psi_{eq} \tanh\left(\frac{x}{\sqrt{2}\xi}\right) \tag{7.8}$$

for an interface characterized by a size ξ.

$$F_{cpl}(\mathbf{n}) = \sigma \int_0^R dr\ r\ \psi_c(r/R) \int_0^{2\pi} d\phi \left[\psi(x) - \psi_0(x)\right]^2 \tag{7.9}$$

we can make the obvious non-dimensional changes such as $\psi \to \psi_{eq}\psi$, $r \to rR$ and

$$\bar{\xi} \equiv \xi/R \tag{7.10}$$

we can also observe that we can break the angular integral into the two semicircles. Both integrals are equal, then

$$F_{cpl}(\mathbf{n}) = 2\sigma R^2 \psi_{eq}^2 \int_0^1 dr\ r\psi_c(r/R) \int_{\pi/2}^{3\pi/2} d\phi \left[\tanh\left(\frac{r\cos(\phi)}{\sqrt{2}\bar{\xi}}\right) - \psi_0\right]^2 \tag{7.11}$$

let's also take the limit $\bar{\xi} \to \infty$ which means that we are in a regime in which the particle size is small compared with the interface size.

$$F_{cpl}(\mathbf{n}) = 2\sigma R^2 \psi_{eq}^2 \int_0^1 dr\ r\psi_c(r/R) \int_{\pi/2}^{3\pi/2} d\phi \left[\frac{r\cos(\phi)}{\sqrt{2}\bar{\xi}} - \psi_0\right]^2 \tag{7.12}$$

which result in

$$F_{cpl}(\mathbf{n}) = 2\sigma R^2 \psi_{eq}^2 \left[\frac{1}{4}\pi A_3 \bar{\xi}^{-2} + \frac{4A_2}{\sqrt{2}}\psi_0 \bar{\xi}^{-1} + \pi A_1 \psi_0^2\right] \tag{7.13}$$

where

$$A_n = \int dr\ r^n \psi_c(r) \tag{7.14}$$

Now, if we want to obtain the energetic difference needed to induce a flip, we need to calculate $\Delta F = F(\mathbf{n}) - F(-\mathbf{n})$, for which we have to calculate the coupling energy of a flipped state. But we can also notice that changing $\mathbf{n} \to -\mathbf{n}$ is equivalent to change $\psi_0 \to -\psi_0$. Therefore, as we subtract in the energetic difference, only the odd powers of ψ_0 remain, then

$$\Delta F_{cpl} = \frac{16\ A_2}{\sqrt{2}} \sigma R^2 \psi_{eq}^2 \frac{\psi_0}{\bar{\xi}} \tag{7.15}$$

This equation, although is the result of many strong approximations, maintains the reasonable idea that the energetic cost of a flip is proportional to ψ_0, which means that if we have an isotropic particle $\psi_0 = 0$, the cost is zero. Similarly, larger particles are more difficult to flip, which again is expected.

We can compare this with the thermal energy scale, such that

$$\chi_{orient} = \frac{\Delta F_{cpl}}{k_B T} = \frac{16\ A_2}{\sqrt{2}} \sigma R^2 \psi_{eq}^2 \frac{\psi_0}{\bar{\xi}\ k_B T} \tag{7.16}$$

7.2.2 Relevant order parameters

In order to quantify the different morphologies JNP and BCP give rise to, we will require to monitor the evolutuon of the magnitudes of several order parameters.

Nematic order parameter.

In order to characterize the local orientation of each colloid with respect to the BCP, we consider the scalar product between the JNP orientation vector and the vector that is locally pointing normal to the interface of the BCP.

$$S =< 2(\mathbf{P} \cdot \mathbf{n})^2 - 1 > \tag{7.17}$$

with $\mathbf{P} \propto \nabla\psi$, that is, a normal vector that is normal to the interface between BCP domains. $S = 1$ corresponds to a JNP oriented normal to the interface and $S = -1$ when the particle is oriented along it. In the absence of net orientation, $S = 0$.

Inter-particle nematic order parameter.

Similarly to the orientation between the BCP and the JNP, it is useful to consider the relative orientation between JNPs, for example, when they form lamellar-like arrangements. To this end, we introduce

$$S_{inter-col} = \langle S^i_{inter-col} \rangle_{i=1...N_p}; S^i = \sum_{r_{ij}<R^*} \left[2\left(\mathbf{n}_i \cdot \mathbf{n}_j\right)^2 - 1 \right] \tag{7.18}$$

in which we draw the same order parameter as in Eq. 7.17 into the orientation of the ith particle with its closest neighbors given by a cut-off distance that we can typically set as $R^* = 2.5R_0$.

In-cluster particle-to-center orientational order.

Clusters of aggregating JNPs can be identified as a set of particles connected with a distance $r < d^*$ with d^* determined from the radial distribution function. For a given cluster formed by several nanoparticles, we can calculate the orientation of each particle with the centre of the cluster. This is different from analyzing the interparticle orientation as here we are interested on the scalar product of the orientation of a particle with the particle-to-center unit vector. To this end, we introduce

$$Y_{orient} = \langle \mathbf{n}_i \cdot (\mathbf{r}_i - \mathbf{r}_{centre}) \rangle \tag{7.19}$$

with $\langle * \rangle$ meaning an average over all particles in a cluster, and then averaging over all clusters (excluding single-particle clusters). Vector $\mathbf{r}_i$ represents the position of a particle in a given cluster while $\mathbf{n}_i$ stands for its orientation and $\mathbf{r}_{center}$ is the geometric center of the cluster (which is calculated taking into account the periodic boundary conditions).

7.3 Results

We will subsequently analyse in detail the co-assembly of Janus nanoparticles in block copolymer mixtures. In the simplest case, we expect the particles to simply be segregated towards their preferred region of the microphase-separated block copolymer. Nonetheless, simulations[55] and experiments[6, 9] have demonstrated that, at high concentrations, the presence of nanoparticles can induce transitions in the block copolymer morphology. In the rest of

this chapter, unless otherwise stated, we will use the standard set of parameters for the BCP $\tau_0 = 0.35, u = 0.5.v = 1.5, A = 1.5, D = 1.0, B = 0.002$ while a radius $R_0 = 2.0$ will be used for the NP, in grid points. The lattice spacing is unity $\delta x = 1$. The choose a value of $\alpha = 2$ that tunes the cut-off distance of the BCP-NP interaction to be $R_0 = 3.12$. Furthermore, the temperature and the friction constant is generally fixed to be $k_B T = 1.0$ and $\eta_0 = 0.1$.

Firstly, we can assert the segregation and ordering of JNPs in a simple symmetric diblock copolymer mixture with $f_0 = 1/2$. In Fig. 7.2 we can see the time evolution of a system of $N_p = 300$ JNPs with two antisymmetric sides, $\Delta\psi_0 = 1$ and $\bar{\psi}_0 = 0$, where the positive side has an affinity towards the white phase, and the negative has an exact same affinity towards the black phase. At time step $t_n = 10^3$ (top snapshot) an early stage of BCP phase separation occurs, especially near a nanoparticle, which triggers phase separation in its vicinity. At $t_n = 10^6$ (right snapshot) the lamella structure is well formed, while the JNPs are all anchored at the interface between white and black domains. The orientation is always normal to the interface, as expected, and can be tracked in time with the curve of $S(t)$, where we can appreciate the orientational order parameter $S > 0$ in the late stages of the simulation. Visually, we can observe that the ψ_+ red side of the JNP is facing the white domains.

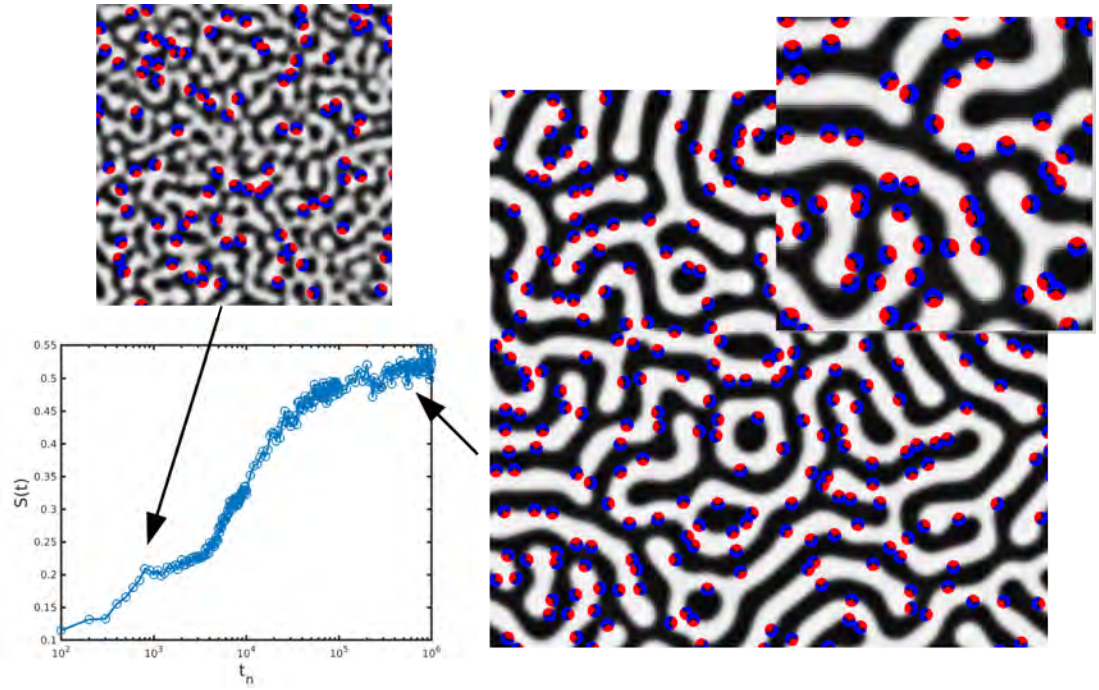

Figure 7.2: Time evolution of a JNP suspension in a symmetric diblok copolymer mixture. The orientation of the Janus particles, $S(t)$, is plotted against time, with two snapshots of early and late stages of the system.

A cylinder-forming (circle-forming in 2D) asymmetric BCP ($f_0 = 0.35$) can be mixed with $N_p = 800$ Janus nanoparticles to analyze the assembly of patchy particles at curved interfaces. The time evolution of an asymmetric BCP ($f_0 = 0.35$) /JNPs mixture can be found in Fig. 7.3, displaying the decrease in the number of domains with time for the cases of pure BCP ($N_p = 0$), homogeneous NPs and JNPs, as expected for a cylinder-forming BCP. The JNPs are segregated at the interface and orient normal to it. We observe a coexistence of circular-shaped BCP domains, with several black domains joined due to the presence of the JNP, resulting in elongated domains.

Figure 7.3 shows the number of black domains as a function of time, in the case of pure BCP

($N_p = 0$) and homogeneous nanoparticles ($\Delta\psi_0 = 0$, $\bar{\psi}_0 = 0$). We can observe that the the number of black domains is reduced by the presence of JNP, but to a lesser extend than in the case of homogeneous nanoparticles. In future sections we will study this behaviour in detail, but it serves as an introduction on the morphological changes induced by particles at interfaces, and the differences in the behaviour of Janus and chemically homogeneous nanoparticles.

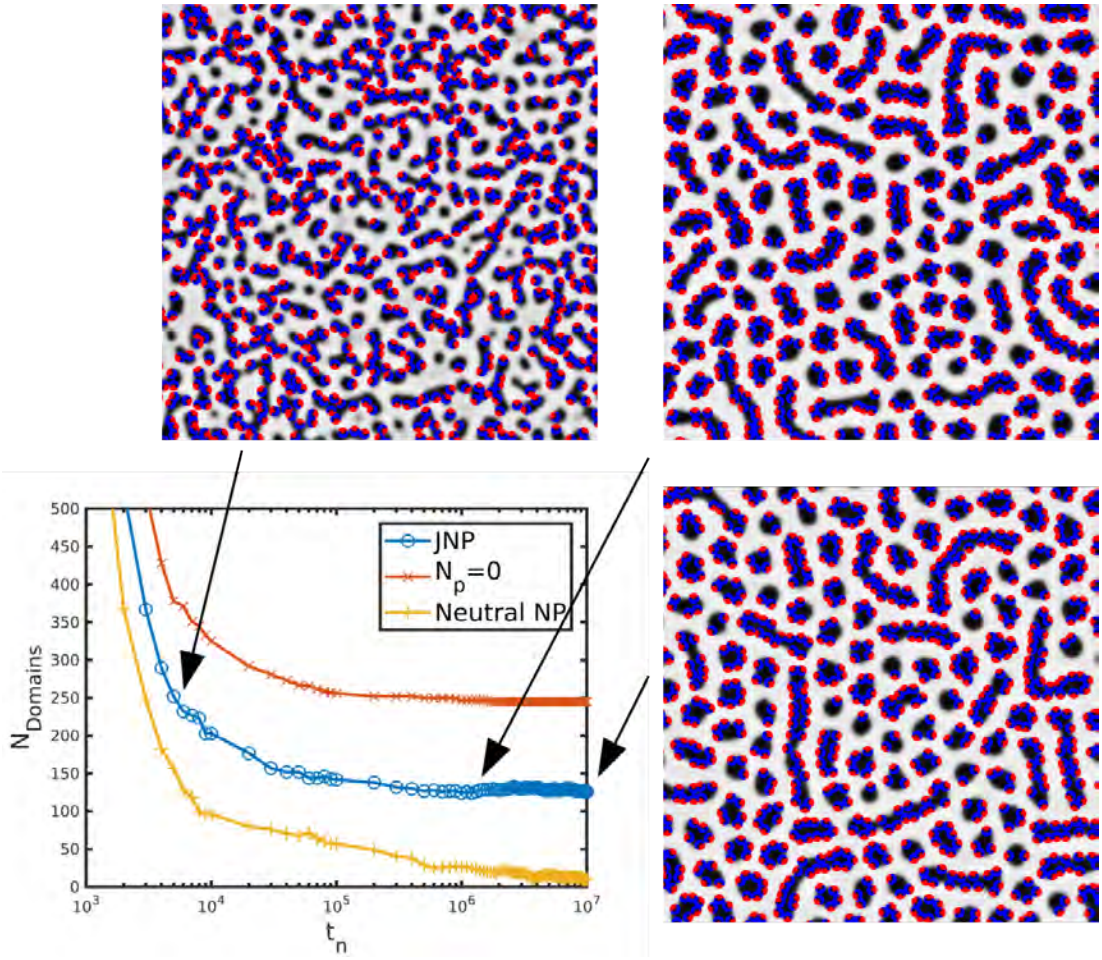

Figure 7.3: Time evolution of the number of BCP domains, along with several images of the simulation results. The pure BCP is cylinder-forming ($f_0 = 0.35$) while the presence of the JNP favours domain merging. The curves for pure BCP ($N_p = 0$) and homogeneous neutral nanoparticles are also shown for comparison.

7.3.1 Phase diagram of BCP-JNP composites

A Janus nanoparticle can be weakly attractive with one of the blocks while neutral to the other. This behaviour can be captured by the two affinities of the JNP, or, more suitably, by the differences and mean values of those affinities, $\Delta\psi_0$ and $\bar{\psi}_0$, respectively, as introduced in equation 7.3. For example, $\Delta\psi_0 = 0$ describes a homogeneously coated nanoparticle, while $\bar{\psi}_0$ describes the overall affinity of the colloid. We will analyze the parameter space in which the JNPs properties are dominant.

Figure 7.4 shows the JNP assembled phases in a low colloidal concentration,$\phi_p = 0.05$, such that the block copolymer assembly is weakly influenced by the presence of colloids. We will control the relative affinity of JNPs to BCP domains varying the mean affinity $\bar{\psi}_0$ and the inhomogeneity parameter $\Delta\psi_0$.

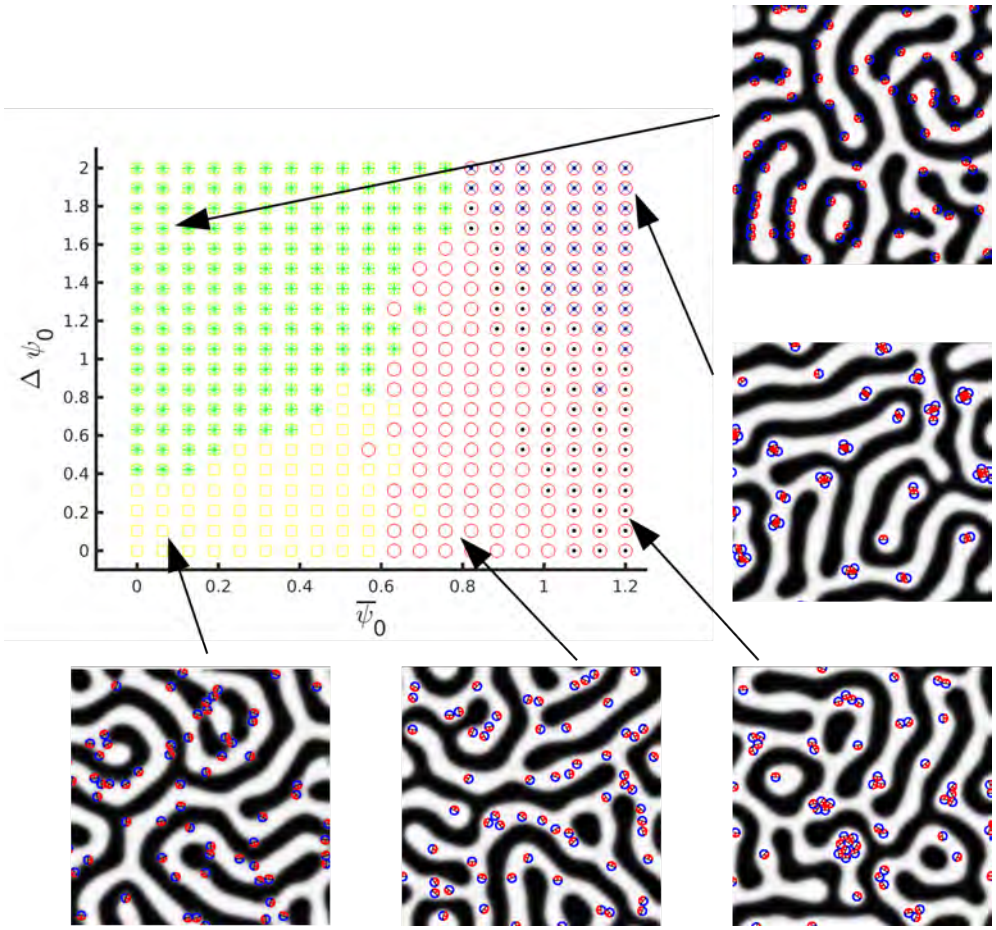

Figure 7.4: Phase diagram of a small concentration of JNPs for different values of $\Delta\psi$ vs $\bar{\psi}_0$, as defined in equation 7.3. The Y axis determines the Janus-like property of the colloid (smaller values meaning weakly Janus) while the X axis determines the interface-compatible or A-compatible overall compatibility of the particle. Yellow squares indicate nanoparticles which are anchored at the interface while red circles stand for NPs segregated within the domains. Yellow asterisks indicate orientational order of the colloids in the interface while black dots stand for nanoparticle aggregation. Finally, crosses indicate internal orientational order in the NP clusters.

At the bottom of the phase diagram in Fig. 7.4, we observe the expected behaviour, as values of the affinity which are close to zero lead to segregation of nanoparticles at the interface between domains (squares). As $\bar{\psi}_0 > 0$ increases, colloids are asymmetrically placed at the interface, up to a point when the colloids detach from it and segregate towards the centre of the positive, white domains (circles). We calculate the distance d from the JNP center of mass to the closest black domain to determine whether a particle is detached from the interface ($d > d_0 = 3.3$) or not. d_0 is chosen following analysis the behaviour of d for several simulations which agrees with the most relevant length scale in play: 2ξ, the width of the BCP interface. For values $\bar{\psi}_0 > 1$ the JNPs are not perfectly compatible with their hosting domains and thus free energy minimization leads to aggregation of colloids (circles + dots). Specifically, certain degree of aggregation takes place whenever the number of first neighbors is larger than 1. Negative values of $\bar{\psi}_0$ would show an equivalent behaviour in which colloids would segregate to the negative (black) BCP domains.

As we increase $\Delta\psi_0 > 0$ in Fig. 7.4, the Janus-like nature of the particles becomes more dominant. When JNPs have an antisymmetric positive/negative anisotropy (that is,when the

two-fold affinity follows $\psi_+ = -\psi_- \rightarrow \bar{\psi}_0 = 0$), they segregate at the interface (left-most part of the phase diagram), and the torque orients them normal to the interface. The combination of segregation at the interface and orientational order is marked in the phase diagram with an asterisk. Orientational order is characterised by the nematic-like order parameter, $S > 0.5$, defined in equation 7.17.

JNP ($\Delta\psi_0 > 0$) with $\bar{\psi}_0 > 0$ are not symmetrically placed at the interface. Instead, we can expect that a small positive value in $\bar{\psi}_0$ results in a small displacement of the center of mass of the JNP into the white phase, therefore, an asymmetrical placement in the interface while maintaining an orientational order. This regime is denoted by asterisks in the left-most part of the phase diagram.

As the displacement to the A domain becomes more prominent, the particle will lose the orientational order (yellow squares) and eventually detach from the interface into the white phase of the BCP. Nonetheless, the assembly of anisotropic nanoparticles in the positive, white phase of the block copolymer is distinct from their homogeneous counterparts. Here, even if the overall coupling energy favours detachment from the interface, one of the sides of the JNP can be incompatible with the hosting BCP domain. In turn, this leads to close-packed clusters of JNPs even at relatively lower values of $\bar{\psi}_0$, which explains the shape of the dotted circle regime in the right part of the phase diagram.

In contrast to homogeneously coated nanoparticles, in Fig. 7.4 top-right snapshot, JNPs form orientationally-ordered clusters. We exploit the order parameter introduced in Eq 7.19 to quantify the in-cluster orientation. We consider that clusters with $Y_{\text{orient}} > 0.7$ have an internal orientational order, as the normal vectors $\mathbf{n}_i$ point into the center of the cluster. These clusters acquire internal orientational order on top of a close-packed spatial organization. For instance, in Fig. 7.4 the positive (red) side of the JNPs is facing the interior of the cluster, which can be related to aggregation in self-assembly of patchy particles in solvents [107, 106]

7.3.2 Comparison between Janus and chemically homogeneous (neutral) nanoparticles

As we have seen in the previous section, JNPs have a strong tendency to segregate at the interface because each side of the particle is compatible with a different block. Chemically homogeneous($\Delta\psi_0 = 0$) neutral ($\bar{\psi}_0 = 0$) NPs also tend to segregate at the interface between domains as they are equally compatible with both blocks. Nonetheless, both types of assembly differ considerably, as JNP orient with $\mathbf{n}$ normal to the interface, while neutral NPs are randomly oriented. We can compare neutral and Janus nanoparticles, as in Fig. 7.5, where we simulate colloids in a symmetric BCP. Here, we find that at low concentration, both types of particles behave similarly, with neutral NPs segregating at the interface while only JNPs also orient normal to the interface. The BCP is barely changed by the presence of a small fraction of particles, which can be tracked by the number of domains in the system. A low number of lamellar domains is indicative of a well-ordered periodic structure. Nonetheless, we know from simulations and experiments that interface-segregated nanoparticles may form bridges across domains. This is a process of aggregation that may be undesirable if we want to have a well dispersed set of nanoparticles, to have an array of colloids, or even if destroying the lamella structure is inconvenient.

We can measure the degree of destruction of the lamella structure by calculating the number of different BCP domains present in the system. The lamella structure is characterized by having fewer domains than any other morphology. We can observe that neutral NPs form clusters that

lead to the formation of many small BCP domains. This does not occur with JNPs, which remain in the interface forming arrays.

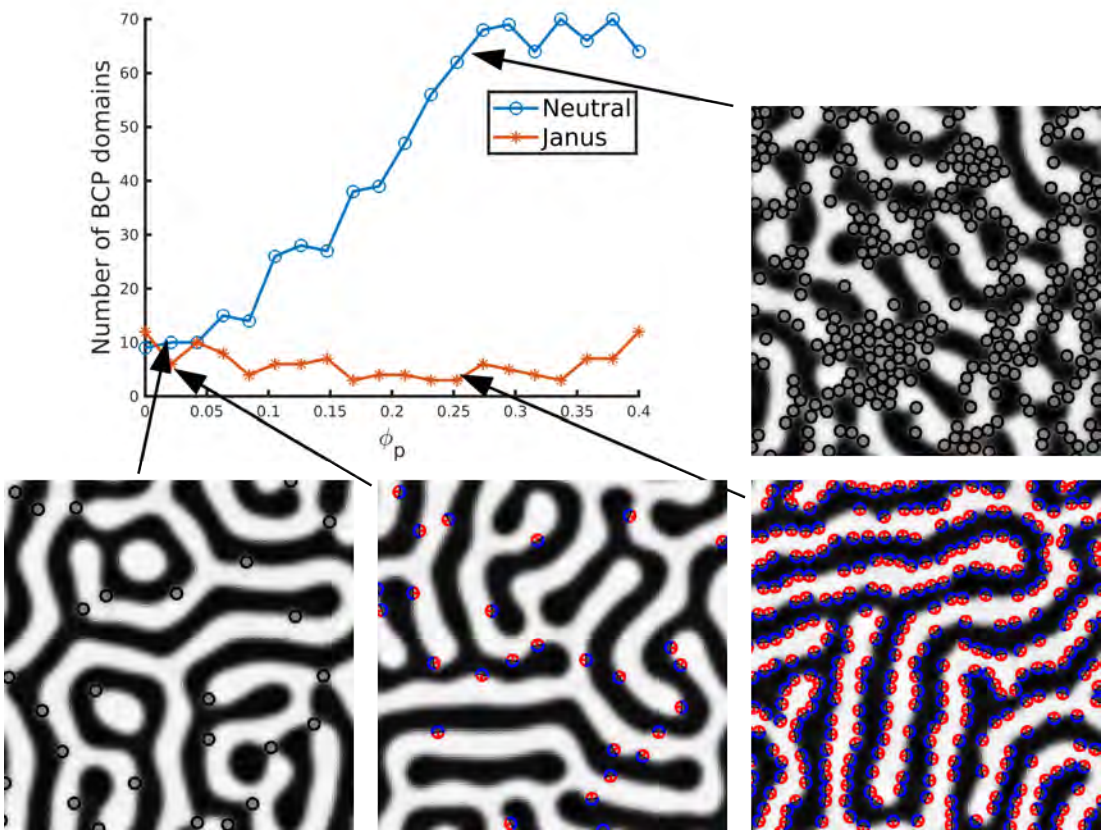

Figure 7.5: Number of BCP domains as a function of the colloidal concentration. The block copolymer is symmetric $f_0 = 1/2$. Homogeneous (neutral) and Janus nanoparticles are shown in different curves.

Similarly to what is done in Figure 7.5 for lamellar-forming BCP in the presence of JNP/Homogeneous neutral NPs, we can study the effect of JNPs on the morphology of a cylinder-forming BCP with $f_0 = 0.35$. In order to characterise the effect of JNP, we explore the fraction ϕ_p of particles in the system. Moreover, neutral isotropic NPs are also simulated in order to compare the behaviour of two different types of particles. In order to track the effect of NPs at interfaces, we compute the number of BCP domains (positive + negative domains). This is a broad measurement of the morphology of the system, with lamellar BCPs having the lower number of domains (ideally, two).

In figure 7.6 we can observe the number of domains in dependence of the fraction of particles in the system. While at low concentrations both types of particles disturb the BCP morphology, they do so in different rates. Neutral (isotropic) nanoparticles are segregated at the interface but during the phase separation process easily create elongated domains, in contrast to the circular domains that would be found in the pure block copolymer case. This leads to less domains (several small circular domains are now joined in one larger domain). While JNPs are also segregated at the interface, and also disturb the phase separation process, its effect is more moderate. We can compare the left-most and second left-most snapshots corresponding to the same ϕ_p. JNP are well dispersed within the system and are less prone to induce larger elongated BCP domains. For this reason, the number of domains is always larger in the JNP case, as compared with the neutral case. In both cases the curve is decreasing for the initial

range of ϕ_p.

Both curves reach a minimum at a different ϕ_p^* which represents the point in which the BCP resembles a lamellar-forming BCP the most. As explained in figure 7, symmetrical JNP and neutral JNP tend to create new interface in which to anchor. Previous work [100] have described how neutral particles in a highly asymmetrical BCP results in a lamellar-like morphology for the majority phase of the BCP (white domains in this figure), while the minority blocks are confined to smaller domains surrounded by NPs. JNP do not tend to aggregate as much, due to their two-face nature there is a preference to form elongated domains (see bottom, right-most snapshot).

Finally, at very high concentrations of particles the global behaviour depends less on the initial condition,with the NPs dominating the morphology of the system. Again, the JNP are more prone to form elongated domains with zero curvature, as their preference is to form side-to-side configurations within the monolayers of nanoparticles.

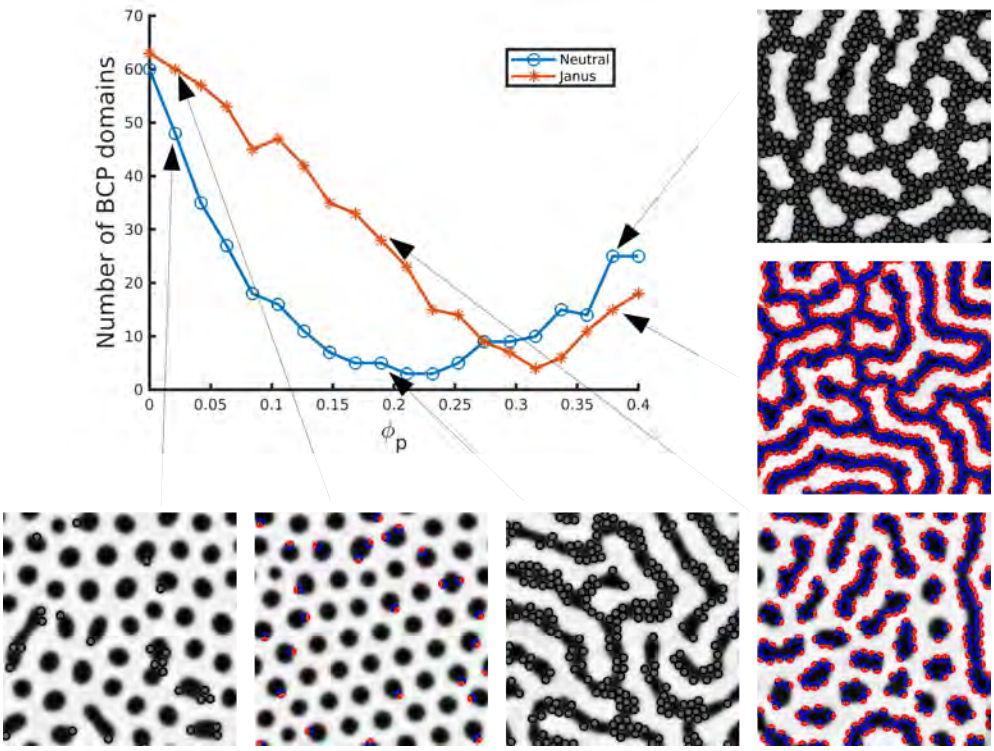

Figure 7.6: Number of BCP domains ($N_A + N_B$) in the presence of JNP and isotropic neutral nanoparticles. Snapshots of representative simulations are related with an arrow. Please refer to the colour version to see the positive/negative face of the Janus nanoparticles.

7.3.3 Orientational order vs thermal motion

A JNP with two antisymmetric sides ($\bar{\psi_0} = 0$) is expected to segregate at the interface and, if $\Delta\psi_0 > 0$, to orient with $\mathbf{n}$ pointing normal to the interface, into the positive region of the BCP, as was found in Fig. 7.4. This is clearly not true for homogeneous neutral particles, for which no orientational degree of freedom exists. We can also expect to find a regime of chemically inhomogeneous particles in which the Janus-like nature is weak, therefore the Brownian noise dominates. We have estimated this in section 7.2.1, and obtained a parameter that controls the

ratio between energetic coupling and thermal motion

$$\chi = \frac{\Delta F_{cpl}}{k_B T} = \frac{16\ A_2}{\sqrt{2}} \sigma R^2 \psi_{bulk}^2 \frac{\psi_0}{\bar{\xi}\ k_B T} \tag{7.20}$$

where ψ_0 stands for the value of the affinity in the positive side of the JNP, given that the two-face JNP has $\psi_+ = \psi_0$ and $\psi_- = -\psi_0$. ψ_{bulk} is the value of ψ that minimizes the local free energy in equation 2.9, that is, the (absolute) value of the BCP profile in the bulk. A_2 is a parameter related to the shape of the tagged function ψ_c that is defined in Eq. 7.14.

We can compare this theoretical prediction with simulations, exploring different values of the temperature ($0.1 < k_B T < 5$) and different degrees of anisotropy ($0.01 < \Delta\psi_0 < 5$). Fig. 7.7 shows the curve of the orientational order parameter S with an effective parameter χ. We can see that the points approximately align into a single curve. The lack of total order at $\chi >> 1$ is explained as the assembly can lead to imperfections such as curved domains and defects in the BCP. The behavior clearly shows that for $\chi < 1$ the thermal component of the Brownian motion is dominant, and so we find that disorder dominates $S \sim 0$. In the opposite regime, the coupling is much stronger than the random fluctuation ($S > 0$). These results can be related to SCFT/DFT simulations by Wang et al [123], who reported a monotonic growth of the order parameter S with the JNP size.

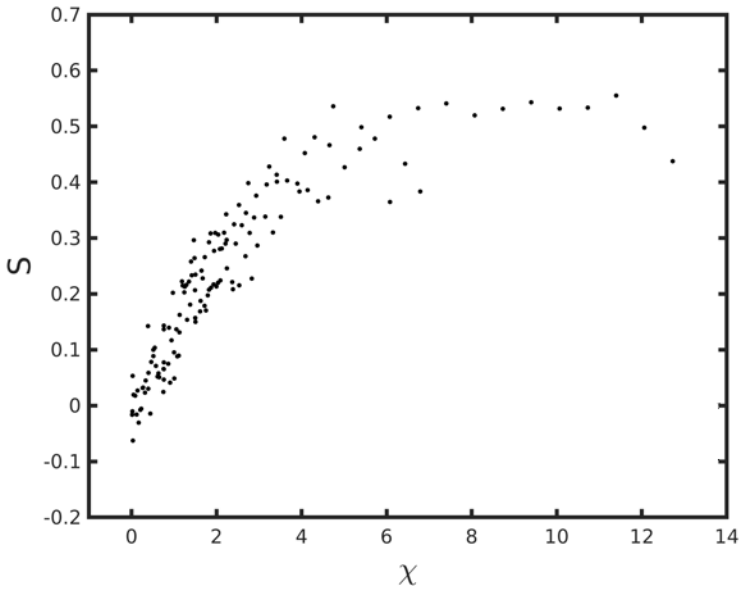

Figure 7.7: Orientational order parameter S of the JNP with respect to the BCP interface. Each point represents a different value of ψ_0 and $k_B T$ resulting in an ordered ($S > 0$) or disordered ($S \sim 0$) configuration.

7.3.4 Co-assembly of JNP in BCP

In previous sections we have mostly considered a lamellar-forming symmetric block copolymer by fixing $f_0 = 1/2$. Nonetheless, we can address the effect of JNPs for other morphologies, exploring the composition parameter f_0 to study the effect that JNPs a fixed chemistry will have on the equilibrium profile of a BCP/JNP system. Hence, we approach the complementary scenario to the one displayed in Fig. 7.4, where we fixed the BCP composition and varied the JNP affinity to the BCP domains.

Fig 7.8 displays the morphology of the composite system as we vary f_0 -which quantifies the relative amout of A monomers in the BCP- and ϕ_p, which controls the concentration of JNPs in the system. For the parameters chosen for Fig. 7.8, BCPs can display either circular domains (marked by circles) or lamellar (squares) morphology. We have performed additional simulations without particles to establish the reference phase-behaviour of the BCP. At low ϕ_p the colloids are simply segregated to the interface, as we have seen previously. The phase behaviour of the BCP is in this case dictated by the polymeric properties of the system.

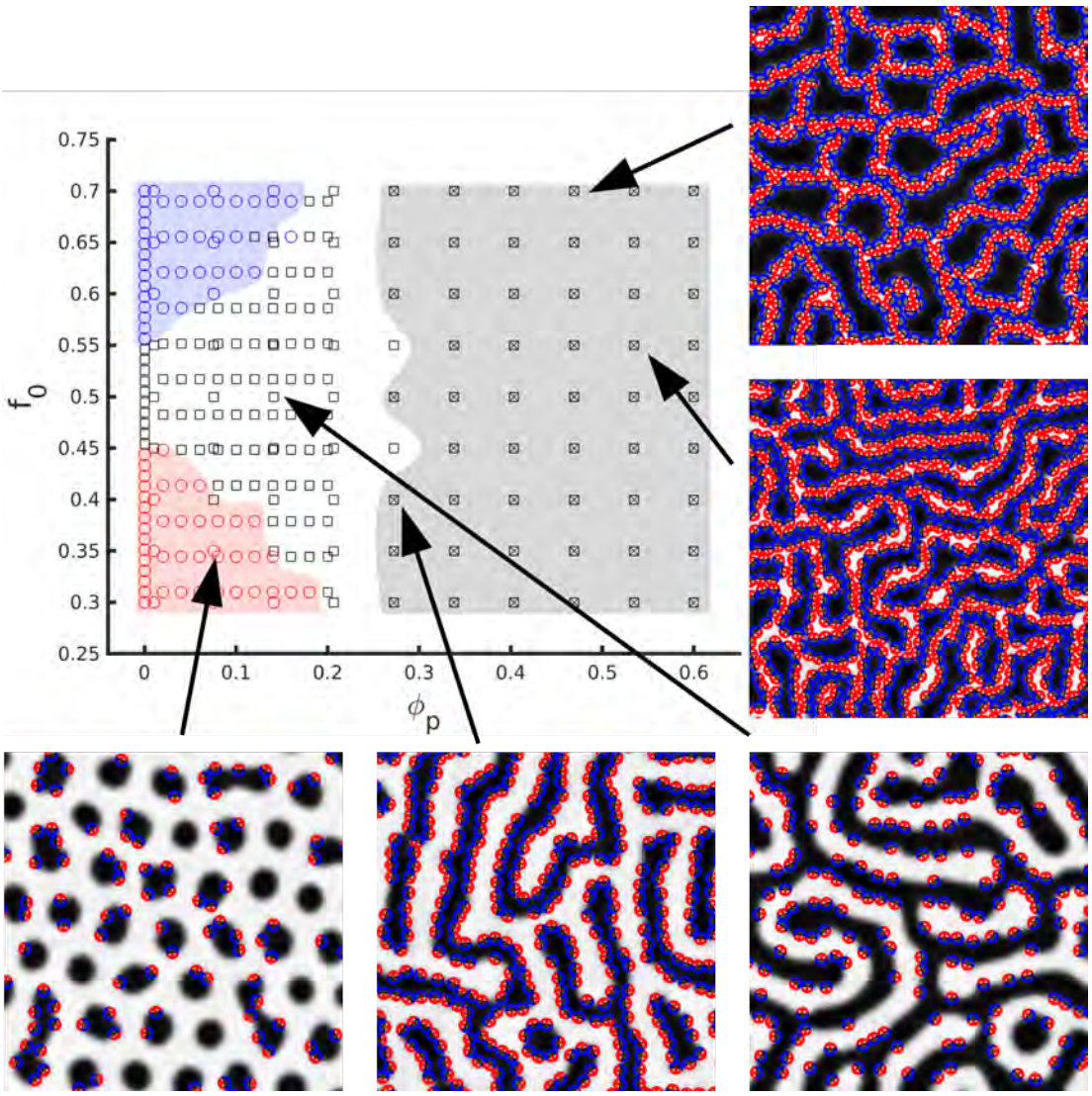

Figure 7.8: Phase behaviour of the BCP as a function of a JNP concentration ϕ_p. The morphology of the BCP is changed along the Y axis through the composition ratio of the chain f_0. The JNP here are symmetrical $\bar{\psi}_0 = 0$. Symbols describe the BCP morphology as: blue circles $\circ$ for cylindrical phase with white block as minority phase; red circles $\circ$ for cylindrical phase with black block as minority phase; black squares for lamellar phase. Furthermore, a black cross $\times$ represents points in which the interparticle orientational order parameter is larger than 0.1.

At high JNP concentrations, the presence of particles in the interface leads to the union of different circular BCP domains if the BCP is indeed in the cylindrical phase ($|f_0 - 1/2| > 0.05$). Due to this increase in the interface, a circular-to-lamellar phase transition is observed. At even higher surface fraction of JNP, the lamellar domains are broken to accommodate a larger number of colloids into newly created interfaces. If the number of particles is increased, the

BCP intrinsic order is strongly distorted, thus the system becomes totally occupied by a single percolating array of JNP. Due to the effective interaction mediated by the surrounding BCP, the JNPs tend to orient side-to-side, with vectors $\mathbf{n}_i \cdot \mathbf{n}_j \approx 1$ for two neighboring particles.

Figure 7.8 has shown the effect that perfectly antisymmetric ($\bar{\psi}_0 = 0$) JNPs produce on an arbitrary morphology of BCP. Nonetheless, we can extend this study to JNPs with stronger affinities towards one of the BCP domains. As we have seen in Fig. 7.4, such colloids can be detached from the interface or form orientationally-ordered clusters, when the affinity towards one of the domains is large enough. We can consider a rather extreme case $\Delta\psi_0 = 1.0$ and $\bar{\psi}_0 = 1.0$. Each side of the JNP has an affinity $\psi_- = 0.5$ and $\psi_+ = 1.5$. The $\psi_- = 0.5$ side is weakly compatible with the interface, while the larger affinity side is strongly incompatible with all phases, but still preferentially compatible with the positive phase (because $\psi_+ > 1$). Earlier simulations[69] have shown that this incompatibility is resolved by NP clustering, which reproduced experimental results [85].

In Fig. 7.9 we study a range of f_0 values of the polymeric chain ratio and the fraction of particles in the system. Initially, at low particles concentrations, JNPs are simply segregated within the BCP. In the bottom-left snapshot we can observe that JNP are weakly attached to the interface, with most particles dispersed in the positive BCP phase. Similarly, the ψ_+ side of the JNP minimises the coupling free energy by creating clusters, but the ψ_+ value is not high enough to create more than a few weakly linked coupled particles. In both cases the thermal motion dominates.

In the region $f_0 < 0.45$, at high concentrations the nanoparticles are always occupying the majority phase. For this reason no phase transition is observed and the morphology of the BCP is always cylindrical (red circles). Nonetheless, JNPs do undergo a disorder-to-order transition as the concentration is higher. A lamellar-like arrangement of JNPs occurs, which is explained as JNPs minimize the free energy by self-organizing as in Fig. 7.9 bottom-right snapshot. Again, the thermal motion is also strong enough to avoid the formation of any long-range order of JNPs.

Contrary to that, in the top-half of the phase diagram ($f_0 > 0.5$) JNPs are compatible with the minority phase. As a result, JNPs are segregated to the minority, white domains induding a cylinder-to-lamellar transition (see the circle to square transition and the enhanced square region in the phase diagram). Additionally, the geometric constraint induced by the minority-phase domain leads to a string organization of JNPs, in order to maximize alike side-to-side contacts between JNPs. Because of this constrain, JNPs are highly organized forming sheets or bilayers (snapshot top-right) or 4-layers (snapshot center-right). In both cases defects in the JNP array-like assembly are strongly correlated with BCP defects.

Starting from a lamellar-forming ordered BCP, Fig. 7.10 (a) displays the long range JNP order that develops in the absence of curved interfaces. JNPs self-assemble in a triangular lattice, which suggests a close-packed arrangement of colloids within the minority phase. In 3D, we would expect to observe a bilayer of JNPs in a 2D sheet with a thickness roughly corresponding to $4R_0$. Fig. 7.10 displays (b) a simple scheme of the used JNP, while Fig. 7.10 (c) shows the configuration. This colloidal configuration is mediated by the block copolymer coupling that leads to highly ordered colloidal assembly. In summary, we have found a translational and orientationally ordered JNP configuration which is a consequence of BCP asymmetry ($f_0 \neq 1/2$) and a precise choice in the JNP inhomogeneity. Indeed, the BCP undergoes a phase transition towards a lamellar morphology, while the JNPs self-organize into lamellar-like arrangement.

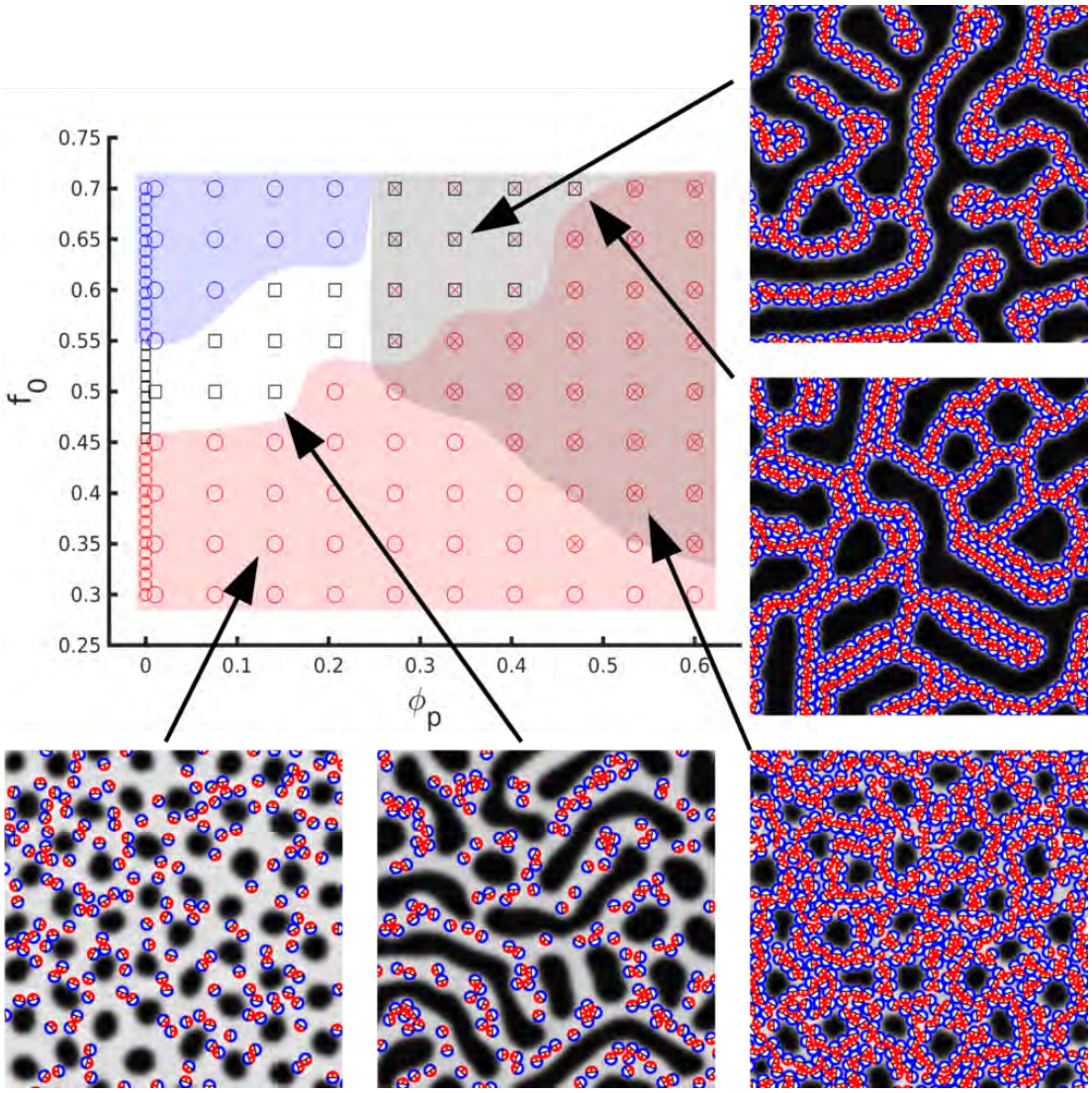

Figure 7.9: Phase behaviour of the BCP in the presence of a concentration ϕ_p of Janus Nanoparticles with $\bar{\psi}_0 = 1.0$ and $\Delta\psi_0 = 1.0$. Symbols are as follows: Circles stand for cylindrical phase with color determining the majority (red circles indicate white monomer as the majority and blue circles indicate the opposite); lamellar phase is denoted by black squares; A further cross indicates a high degree of particle-to-particle orientational order.

7.4 Conclusions

We have used a hybrid Cell Dynamic Simulation/Brownian Dynamics method to study the dynamics and equilibrium properties of a system of Janus Nanoparticles in a diblock copolymer mixture. A combination of segregation, orientation and aggregation of particles within the mixture leads to a rich variety of assemblies, ranging from the expected interface-compatible antisymmetrical JNPs, to aggregation of colloids within one phase, in close resemblance with JNP suspended in a single solvent. In our study the Janus-like character of the particles has been explored ranging from completely Homogeneous particles, to particles with a clear two-face behaviour.

JNPs have been shown to anchor at interfaces for a wider range of parameters than their homogeneous counterparts, in accordance to previous results[122]. The particles are found to orient normal to the interface between domains, with each face pointing into the preferred domain. Furthermore, JNPs are less prone to form bridges along BCP domains. These two

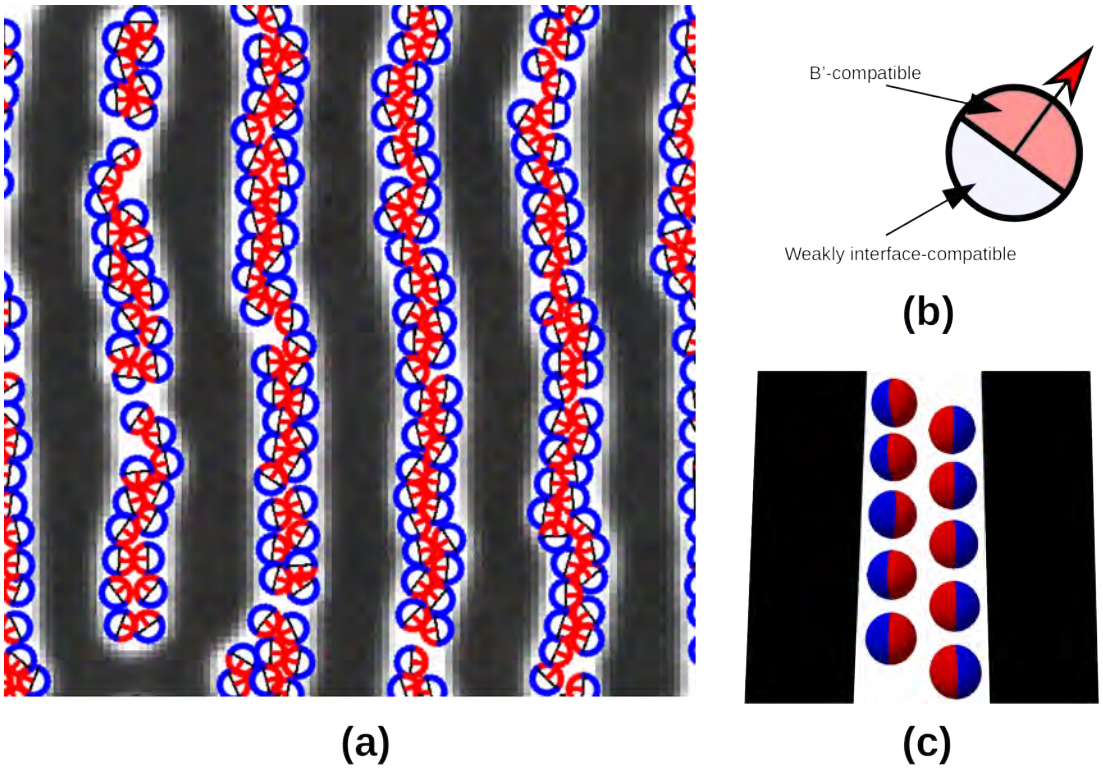

Figure 7.10: Co-assembly of an asymmetric diblock copolymer / asymmetric JNP mixture. The BCP undergoes a JNP-driven phase transition towards lamella due to the presence of the JNP in the interior of the white domains. The JNP form a bilayer due to their directional aggregation. Highly ordered simulation (a); scheme of the JNP (b) ; and scheme of the configuration (c).

properties are related, as JNPs are less likely to escape the interface and connect with other JNPs to create a broad, NP-rich area. This also means that the BCP structure is less affected by the presence of JNPs than with neutral nanoparticles. Therefore, using JNPs can be an effective way to segregate colloids at block copolymer interfaces, without inducing a break-up of lamellar-domains.

For interface-compatible JNPs, the degree of orientation with respect to the block copolymer interface can be tracked and compared with the thermal fluctuations present in the Brownian motion. We have characterised the role of the temperature in the colloidal orientational order, to establish under which conditions the JNP orientation is dominated by its thermal random motion. This opens a way to control the properties of the JNP by tuning their thermal motion. As has been shown, the BCP lamellar texture is also strongly dependent on the anisotropy of the JNPs.

Away from the interface, JNP are found to easily aggregate into clusters, as compared to homogeneously-coated colloids. This is due to one of the sides of JNP always being incompatible with its hosting phase. The BCP-induced aggregation can be related to instances of clusterisation of homogeneous nanoparticles within a incompatible environment [85], while the organization is in close resemblance with several experiments and simulations of JNP in suspensions. It is worth noing that we have not included any explicit attractive interaction between colloids, nor does the interparticle potential include any angular dependence. Thus, this orientational aggregation is solely induced by the presence of the block copolymer.

Exploring the surface fraction of JNPs in BCP mixtures with arbitrary f_0 we have been able to determine different phase regions, as the presence of JNPs leads to transitions in the

morphology of the BCP. Moreover, the morphology of the BCP also depends on the chemical properties of the JNP. While antisymmetric JNPs are segregated to the interface, a large amount of them can induce a transition in order to create a larger amount of interface in which they can anchor. Once this lamellar-to-cylindrical transition is completed, the JNPs dominate the morphology of the overall system, with JNP forming an almost totally connected network of colloids in an attempt to form maximize the interface.

Asymmetric JNP in BCP display a richer phase diagram. When one of the sides is compatible with the interface (neutral) and the other is strongly incompatible with one of the phases, the JNP have a weak tendency to form clusters within the less incompatible domain. When the fraction of particles is large the NPs form a bilayer in order to minimize the BCP-JNP coupling. The parameter space of this type of assembly is given not only by the fraction of particles in the system, but also by the block copolymer morphology, as this assembly is driven by the level of constrain induced by the BCP. At even higher fraction of particles, the JNP are again dominating the co-assembly, and tend to form larger even number of layers, with $(1-3-5-..)$-layers being prohibited by the JNP two-face nature, along with the presence of the block copolymer. This lamellar-like organisation of JNP can be easily compared with sheet-forming assembly of Janus particles in solvents. At the same time, the organisation within the BCP (all nanoparticles are oriented normal to the interface) is similar to shape-anisotropic particles such as nanorods [127].

In summary, the co-assembly of JNP within block copolymer has been found to result in a large variety of highly-ordered configurations, both for the BCP and the colloids, in contrast to a mixture of chemically homogeneous colloids/BCP or a simple suspension of JNP in a fluid. The combination of JNP anisotropy and the inherent periodic morphologies of the diblock copolymer has proved to be essential to create new structures in which a precise control over the JNPs position and orientation can be achieved.

CHAPTER 8

Shape Anisotropic Colloids I: Block Copolymer/Ellipsoids

Abstract

Simulations and experiments of anisotropic nanoparticles (NPs) show that co-assembly with block copolymer (BCP) melts leads to the formation of a superstructure of side-to-side NPs perpendicular to the lamellar axis. A mesoscopic model is validated against experimental scanning electron microscopy (SEM) images of CdSe nanorods (NRs) mixed with polystyrene-block-poly(methyl methacrylate). It is then used to study the co-assembly of anisotropic NPs with a major size in the same order of magnitude as the lamellar spacing. The phase diagram of BCP/NP is explored as well as the time evolution of the NP configuration. Anisotropic NPs which are slightly larger than the lamellar spacing are found to rotate and organise side-to-side with a tilted orientation with respect to the interface. Strongly interacting NPs are found to dominate the co-assembly while weakly interacting nanoparticles are less prone to form aggregates and tend to form well-ordered configurations. [1]

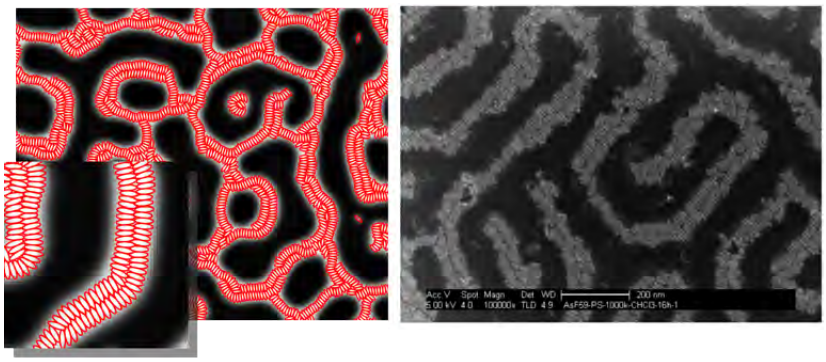

(a) (b)

[1] The experimental images that appear in Figures 8.4 and 8.7 are part of the experimental work done by Prof. Shenhar.

8.1 Introduction

Nanorods (NR) have attracted considerable attention as constituents of functional polymer nanocomposite materials[10]. The orientational degree of freedom of non-spherical colloids introduces new possibilities of BCP/NP co-assembly, thanks to the intrinsic ordered structures of the neat BCP (lamellar, cylindrical, etc). For instance, gold NRs have been found to orient along the lamellar domain axis when confined in one of the symmetrical phases[11, 128]. Similarly, gold NRs template the direction of the cylindrical domains in an asymmetrical diblock copolymer mixture[129]. Ordered arrays of aligned NRs were achieved by Thorkelsson [130, 131] in the co-assembly of BCP and anisotropic particles, where NRs were organised in an end-to-end configuration. Nanoplates alignment in a lamellar-forming BCP has been recently studied[8].

Experiments have reported the existence of an ordered phase when NRs are mixed with asymmetric diblock copolymer [127, 12] in thin films. Shenhar et al studied polystyrene-*block*-poly(methyl methacrylate) (PS-b-PMMA) copolymers mixed with PS-modified CdSe NRs, and found that NRs preferentially organized in a side-to-side configuration, forming long rows of particles in the PS domains, with an orientation normal to the interface between BCP domains, ie, perpendicular to the direction of the lamella domain. Furthermore, the number of rows and degree of order could be related to the size of the NRs and copolymer spacing.

Theoretical and computational works have studied the self-assembly of BCP and anisotropic NPs. Dissipative Particle Dynamics (DPD) has been largely used, thanks to the ability to combine several beads into rod-like sequences. Zhang et al studied the phase behavior of such systems and the orientation of nanoparticles [132, 133, 134] as well as the effect of shear in the global orientation has also been quantified [135]. Osipov et al [136, 137, 138] used Strong and Weak Segregation Limit Theory to determine the distribution of anisotropic particles in a diblock copolymer, with a low fraction of NPs present in the system.

Here, we make use of the considerably fast Cell Dynamic Simulation (CDS) method to simulate the BCP dynamics while Brownian Dynamics describes the assembly of ellipsoidal colloids. These simulations are compared with experiments involving CdSe NRs, in order to study the co-assembly of colloids within BCP domains. Simulations are used to gain insight over the behavior and occurrence of the orientational order of anisotropic colloids. Ellipses are used to mimic the shape of NRs, which is expected to be valid as the NP's anisotropy becomes larger.

We aim to systematically study the phase behaviour of a polymer composite system made of diblock copolymer and anisotropic NPs, restricting to the case of NPs which are compatible with one of the copolymers. Size, shape and number of particles were explored, to address its effect on both the diblock copolymer morphology and especially the colloidal assembly. Several length scales are present in polymer nanocomposite systems[139], specially in the case of NRs or elliptical particles. This richness in sizes has been shown to result in interesting effects of confinement, and presents a challenge for its study. Simulations are compared with experimental results, to first assess its validity and then explore several parameters and configurations which are experimentally difficult to achieve.

8.2 Model

8.2.1 Polymer/colloid interaction

Contrary to the polymeric matrix, a suspension of N_p nanoparticles describes each colloidal NP individually through the center of mass and orientation degrees of freedom $\mathbf{R}_i, \phi_i$. The interaction between the polymer and colloids is introduced through a contribution to the free energy $\mathcal{F}_{cpl}$, which must take into account the fact that colloids may have a preference for one of the components of the BCP. The simplest free energy that satisfies that is

$$\mathcal{F}_{cpl} = \sum_{i=1}^{N_p} \sigma \int d\mathbf{r}\ \psi_c(\mathbf{r}, \mathbf{R}_i, \phi_i) \left[\psi(\mathbf{r}) - \psi_0\right]^2 \tag{8.1}$$

where σ defines the strength of the interaction between polymer and colloids, and ψ_0 describes the affinity of NPs with the BCP.

In previous chapters, the size, shape and core/shell properties of the NP are described through the tagged function[80] $\psi_c(\mathbf{r})$. In order to account for non-spherical colloids, we generalise the spherical shape into an non-rotated ellipse placed at $\mathbf{R}_i = (0, 0)$ as

$$\psi_c(x, y) = \exp\left[1 - \frac{1}{1 - \left(\frac{x}{a}\right)^2 - \left(\frac{y}{b}\right)^2}\right] \tag{8.2}$$

which can be trivially extended for an arbitrary rotation ϕ_i[2] . The particle shape and size is characterised by a major semiaxis a, and hard-core major semiaxis $a_0 = a/\sqrt{1 + 1/\ln 2}$, and the same relationship holds for the minor semiaxis b. The ratio $e = b/a$ accounts for anisotropy of the ellipse. The tagged function is $\psi_c(\mathbf{r}) = 0$ outside of the ellipsoids, that is, for $(x/a)^2 + (y/b)^2 > 1$.

8.2.2 Interparticle potential

In order to introduce colloid-colloid interactions we require an orientational-dependent pairwise additive potential. The potential we use is the standard Gay-Berne (GB) potential [140, 141] which derives from a Gaussian overlap study of ellipsoids, making it suitable to our interactions. The GB potential has been widely used to describe liquid crystals[142, 143]. The interparticle potential can be written as

$$V(\hat{\mathbf{u}}_1, \hat{\mathbf{u}}_2, \mathbf{r}) = \epsilon(\hat{\mathbf{u}}_1, \hat{\mathbf{u}}_2, \hat{\mathbf{r}}) \left[\left(\frac{1}{r - \sigma(\hat{\mathbf{u}}_1, \hat{\mathbf{u}}_2, \mathbf{r})}\right)^{12} - \left(\frac{1}{r - \sigma(\hat{\mathbf{u}}_1, \hat{\mathbf{u}}_2, \mathbf{r})}\right)^{6}\right] \tag{8.3}$$

which is a modified Lennard-Jones interaction with anisotropic length and energy scales, $\sigma(\hat{\mathbf{u}}_1, \hat{\mathbf{u}}_2, \hat{\mathbf{r}})$ and $\epsilon(\hat{\mathbf{u}}_1, \hat{\mathbf{u}}_2, \hat{\mathbf{r}})$, respectively. The centre-to-centre distance is r while $\hat{\mathbf{u}}_i$ stands for the orientation of the major axis of particle i. This potential provides a length scale that describes the anisotropy of the ellipsoid

$$\sigma(\hat{\mathbf{u}}_1, \hat{\mathbf{u}}_2, \hat{\mathbf{r}}) = 2b \left\{1 - \frac{1}{2}\chi \left[\frac{(\mathbf{r} \cdot \hat{\mathbf{u}}_1 + \mathbf{r} \cdot \hat{\mathbf{u}}_2)^2}{1 + \chi(\hat{\mathbf{u}}_1 \cdot \hat{\mathbf{u}}_2)} + \frac{(\mathbf{r} \cdot \hat{\mathbf{u}}_1 - \mathbf{r} \cdot \hat{\mathbf{u}}_2)^2}{1 - \chi(\hat{\mathbf{u}}_1 \cdot \hat{\mathbf{u}}_2)}\right]\right\}^{-1/2} \tag{8.4}$$

and takes a value $2b$ at the side-to-side configuration. The energetic anisotropy is described with two parameters: U_0 describes the strength of the interaction while $\epsilon_r = \frac{\epsilon_e}{\epsilon_s}$ is an expression

[2]Even though in section 2.2.2 we have presented a general ψ_c curve depending on a parameter α controlling the sharpness of the decay, we have made use of a fixed parameter $\alpha = 2$ throughout this thesis.

of the anisotropy of the wells. The depth of the well is given by

$$\epsilon(\hat{\mathbf{u}}_1, \hat{\mathbf{u}}_2, \hat{\mathbf{r}}) = \epsilon(\hat{\mathbf{u}}_1, \hat{\mathbf{u}}_2)\epsilon'^2(\hat{\mathbf{u}}_1, \hat{\mathbf{u}}_2, \hat{\mathbf{r}}) \tag{8.5}$$

with

$$\epsilon(\hat{\mathbf{u}}_1, \hat{\mathbf{u}}_2) = U_0 \left[1 - \chi^2(\hat{\mathbf{u}}_1 \cdot \hat{\mathbf{u}}_2)^2)\right]^{-1/2} \tag{8.6}$$

and

$$\epsilon'(\hat{\mathbf{u}}_1, \hat{\mathbf{u}}_2, \hat{\mathbf{r}}) = 1 - \frac{1}{2}\chi' \left[\frac{(\mathbf{r}\cdot\hat{\mathbf{u}}_1 + \mathbf{r}\cdot\hat{\mathbf{u}}_2)^2}{1 + \chi'(\hat{\mathbf{u}}_1 \cdot \hat{\mathbf{u}}_2)} + \frac{(\mathbf{r}\cdot\hat{\mathbf{u}}_1 - \mathbf{r}\cdot\hat{\mathbf{u}}_2)^2}{1 - \chi'(\hat{\mathbf{u}}_1 \cdot \hat{\mathbf{u}}_2)}\right] \tag{8.7}$$

where two anisotropy parameters are introduced, regarding length and energy, respectively,

$$\chi = \frac{a^2 - b^2}{a^2 + b^2};\ \chi' = \frac{\epsilon_s^{1/2} - \epsilon_e^{1/2}}{\epsilon_s^{1/2} + \epsilon_e^{1/2}} \tag{8.8}$$

8.2.3 Colloid Dynamics: Brownian Dynamics

Since the NPs are anisotropic, the equation of motion does not involve only the friction constants but a diffusion tensor, $\mathcal{D}$. In general[144],

$$\frac{d\mathbf{r}}{dt} = \mathcal{D}_t \cdot \mathbf{f} \tag{8.9}$$

while the particle's orientational degree of freedom relates to the random (M_r) and exerted torques as

$$\frac{\partial \phi_i}{\partial t} = (M_i + M_r)/\gamma_\phi;\quad M_i = -\frac{\partial \mathcal{F}}{\partial \phi_i} \tag{8.10}$$

with [145]

$$\mathcal{D}_t = \bar{\mathcal{D}}\mathcal{I} + \frac{1}{2}\Delta\mathcal{D}\begin{pmatrix}\cos 2\phi & \sin 2\phi \\ \sin 2\phi & -\cos 2\phi\end{pmatrix} \tag{8.11}$$

and $\bar{\mathcal{D}} = \frac{1}{2}(D_a + D_b)$ and $\Delta\mathcal{D} = D_a - D_b$, D_a and D_b being the diffusion constants along each axis. The values of D_a, D_b and γ_ϕ are derived from the expressions obtained by Perrin [146, 147, 148]

8.2.4 Order parameter

To describe the orientation of the anisotropic NP, an order parameter can be used, which has been extensively employed in nematic liquid crystal systems,

$$S = \langle 2(\hat{\mathbf{u}} \cdot \mathbf{P})^2 - 1\rangle \tag{8.12}$$

which is an average over all particles of the scalar product of the orientation unit vector $\hat{\mathbf{u}}$ and a local unit vector $\mathbf{P}$ that is related to the gradient of the polymer order parameter $\psi(\mathbf{r}, t)$. This unit vector $\mathbf{P}$ is normal to the interface.

8.2.5 Simplified energetic analysis of the side-to-side configuration

Following the estimation of the interaction of a system of rods in Shenhar et al [12], we present a similar procedure for ellipses. In Figure 8.1 we show two ideal cases of side-to-side (left) and end-to-end configuration (right). We consider that two ellipses interacting side-to-side and end-to-end are separated by a distance which is the minimum in the Gay-Berne potential, ϵ_s

and ϵ_e, respectively. The spacing of the lamella domain is D while each ellipse is characterised by two dimensions $2a$ and $2b$ which lead to an anisotropy $e = b/a$. We assume $D \sim 2a$, and therefore the BCP can accommodate 1 row. On the other hand, if the configuration is end-to-end, the number of groups is n_1 that can be easily related to the magnitudes of the system as $(2b)n_1 = D \sim 2_a$, and therefore the number of groups that the BCP permits in the end-to-end configuration is

$$n_1 = \text{int}(e^{-1}) \tag{8.13}$$

the lowest integer of the inverse of the anisotropic factor.

In order to count the energetic interactions between ellipses we limit to the first neighbour and count only in groups of n_1 particles, as the internal interactions within one group is simply $-(n_1 - 1)\epsilon_s$

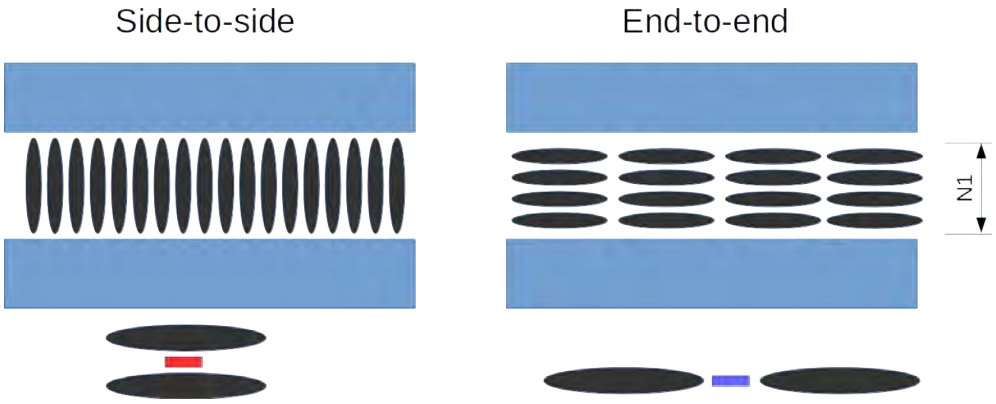

Figure 8.1: Scheme of the energetic interaction between ellipses for the side-to-side and end-to-end configurations. On the left, each ellipse interact with its first neighbor with a contribution ϵ_s to the potential energy, while on the right each particle interacts end-to-end with an energy ϵ_e with its horizontal neighbor and each vertical group adds a value $(n_1 - 1)\epsilon_s$ to the total energy.

We can calculate the energy of a system of N particles in these two configurations as

$$U_{ss} = -\frac{N}{n_1}\epsilon_s \tag{8.14a}$$

$$U_{ee} = -N\epsilon_e \tag{8.14b}$$

from which we conclude that in order for the side-to-side configuration to be energetically favorable we need to satisfy the condition

$$e \gg \epsilon_r \tag{8.15}$$

8.3 Results and discussion

In this section we explore the co-assembly of anisotropic NPs and BCP. As a first approach, we study the condition for the appearance of an ordered phase in a BCP with any composition value f_0, which gives rise to a variety of BCP morphologies. After that, the role of the NP size will be explored, in relation to the BCP periodicity. Finally, the role of the NP-NP interaction is assessed taking into account several initial conditions.

We introduce dimensionless parameters rescaling $D \to D/\delta x^2$ and $B \to B\delta x^2$. Lengths will expressed in terms of grid points. The standard values of CDS[42, 49, 68] will be used

$\tau_0 = 0.35, u = 0.5, v = 1.5, A = 1.5, D = 1.0$ while the BCP/NP interaction is set to $\sigma = 1.0$. A cell spacing $\delta x = 0.5$ and time discretisation $\delta t = 0.1$ are chosen. Unless otherwise specified, the NP size is set to $a_0 = 2$ and $e = 0.3$ while the BCP periodicity is determined by the CDS parameter $B = 0.002$. The box size of simulations is 128×128 except for larger systems which are explicitly stated in the text.

8.3.1 Phase diagram of A-compatible ellipsoidal colloids

The phase diagram of diblock copolymer/colloids has been widely studied both for nanospheres[55] and anisotropic NPs[128]. The presence of NPs which are compatible with one of the blocks increases the effective overall volume fraction of the hosting domain, which in turn results in a phase transition. As a first approach to a system of BCP and anisostropic NPs, we explore what is the effect that ellipse-shaped colloids have on the BCP morphology, by analysing the phase of BCP with arbitrary composition f_0 in the presence of a filling fraction ϕ_p of NPs.

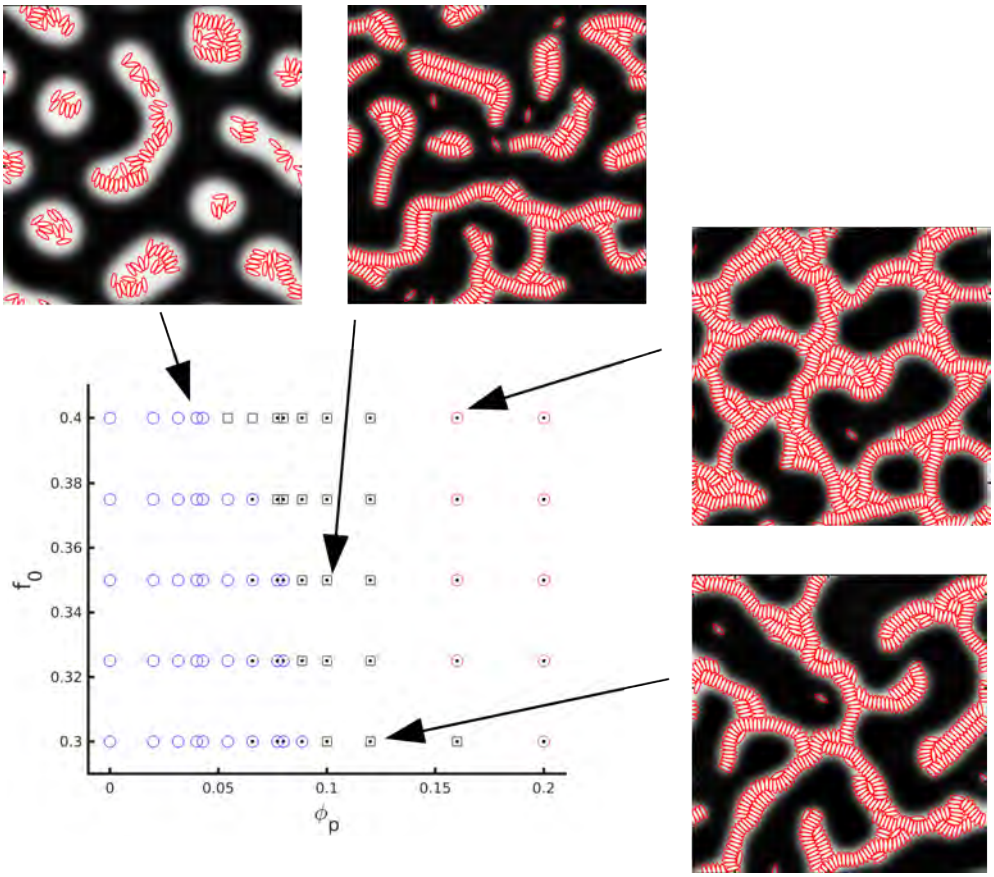

Figure 8.2: Phase diagram of a diblock copolymer nanocomposite system characterised by a filling fraction ϕ_p of ellipsoidal colloids and f_0 volume fraction of the A blocks in the neat BCP. Squares, blue circles and red circles stand for lamellar, cylindrical phase and inverted cylindrical phase, respectively. Dotted markers represent phase points in which $S > 0.3$ (eq. 8.12) ie, where ellipsoids are aligned normal to the interface.

In Figure 8.2 the filling fraction of ellipsoids is explored for different BCP A-ratios, f_0. The NP-NP interaction scale is set to $U_0/\sigma = 0.01$ so that the interparticle potential is not dominating over the BCP-NP interaction. As expected, at low filling fraction ϕ_p particles are simply segregated within their preferred phase (blue) which within the range of f_0 is always the minority phase. In the absence of constrains by the BCP (ie. a low local filling fraction)

ellipsoids display no orientational order. Furthermore, the BCP maintains a cylindrical phase (circular domains, in 2D).

At higher filling fraction, the ellipsoids enlarge the hosting domains to a point in which a cylinder-to-lamellae phase transition is induced. At the same time, higher filling fraction leads to a particular ordered phase in the colloids: ellipsoids prefer to orient normal to the interface and with a side-to-side interparticle configuration. This phase has been reported experimentally by Shenhar et al[127, 12], where ordering was reported to be driven by both attractive NP-NP interaction and minimisation of the repulsive interactions between the NRs and the B phase.

The orientation of the ellipsoids relative to the local interface is tracked by using the order parameter S defined in equation 8.12. In Figure 8.2 a black dot is added for phase points in which $S > 0.3$, that is, where orientational order is considerably high. Furthermore, we can define an effective filling fraction on the basis of A-compatible colloids having a reduced $V_A = f_0 V_{total}$ available space to occupy. [3] This effective filling fraction is [55]

$$\phi_p^{eff} = \frac{\phi_p}{f_{eff}} = \frac{\phi_p}{\phi_p + (1-\phi_p)f_0} \tag{8.16}$$

A plot of the orientational order parameter S against the defined effective filling fraction of ellipsoids is shown in Figure 8.3 where disorder ($S \sim 0$) is found for low effective filling fraction. The marker symbols again show blue circles for cylindrical phase. A rapid change in S occurs as a moderate effective filling fraction is reached, while at the same time the cylinders-to-lamellae transition is induced. This suggests that the orientational order is strongly dependent on high filling fraction of ellipsoids relative to the hosting domain, that is, ellipsoids need to be considerably constrained within their hosting domains. It can be noted that inverted cylindrical phase (ie, ellipsoids occupying the majority of the space) display slighly lower order than lamella ones, despite being at higher effective filling fraction. We can relate this to the higher local curvature of the interfaces which is characteristic of BCP cylindrical phases. This hypothesis will be corroborated by analysing the snapshots in detail in the next figures.

Figure 8.4 (a) shows an instance of ordering at a moderate filling fraction $\phi_p = 0.16$ and $f_0 = 0.4$ in a 256×256 grid system. One can notice that the side-to-side configuration is not homogeneous along the domains. Instead, we observe coexistence of both 1 and 2 rows, along with disordered states and even parallel (along the interface) orientation. Nonetheless, this behaviour appears more often near curved interfaces, as well as near defects of the lamellar structure. These features can be found in experiments involving CdSe NRs mixed with PS-*b*-PMMA at a filling fraction $\phi = 0.26$. This high resolution SEM images displays the side-to-side configuration of NRs within the PS domains. In Fig. 8.4 (b), 1 and 2 rows occur for the same NR size and instances for disorder of parallel configuration appear, specially at the end of domains or at intersections, that is, defects in the lamellar structure.

8.3.2 Relative size of hosting domain/nanoparticle

In Figure 8.4 (b) the size of the NR major axis is chosen to fit two rows into a BCP lamellar domain. Similarly, in Figure 8.4 experiments and simulations show coexistence of 1 and 2 rows of anisotropic NPs. The role of the relative $2a/(H/2)$ size can be explored for a higher number of rows by simulating a larger periodicity, given by the parameter B in the Ohta-Kawasaki free energy, which determines the value of the BCP periodicity H. Figure 8.5 shows simulations of

[3] This effective volume fraction has been studied in the context of circular NPs in BCP melts, as explained in Eq. 6.2. The curve of (orientational) ordering vs effective concentration in Fig. 8.3 can be related to translational ordering of isotropic NPs as in Fig. 6.1.

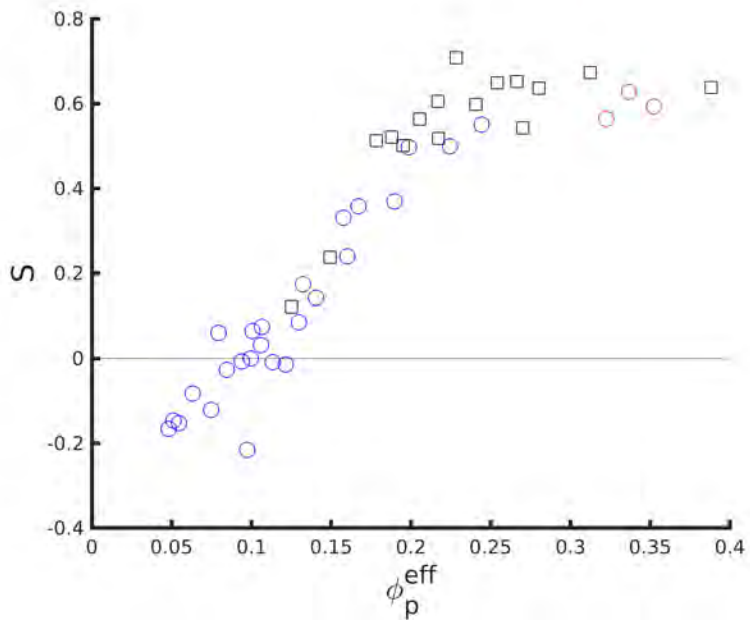

Figure 8.3: Values of the orientational order parameter S for different values of the effective volume fraction of ellipsoids ϕ_p^{eff} as of eq. 8.16. Squares, blue circles and red circles stand for lamellar, cylindrical phase and inverted cylindrical phase, respectively.

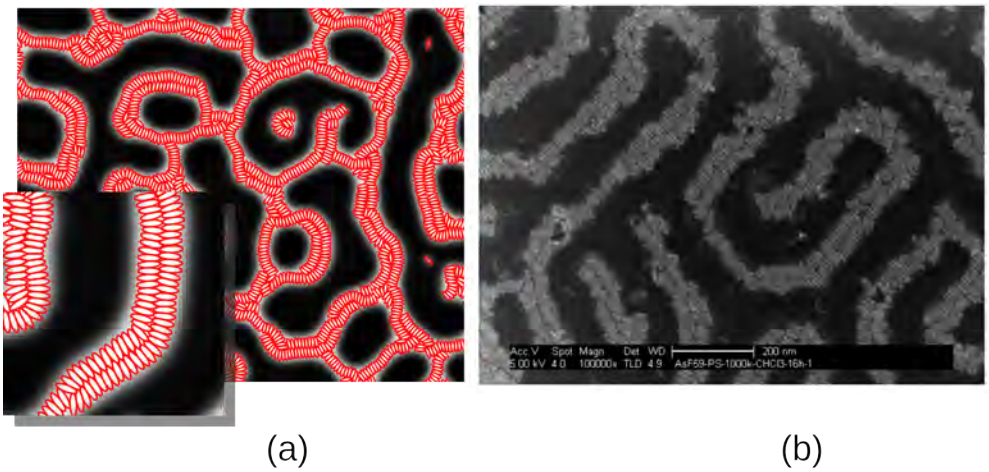

Figure 8.4: Moderate filling fraction of anisotropic NPs in diblock copolymer mixture. Comparison between (a) simulations with inset and (b) experiments using CdSe NR in PS-b-PMMA BCP.

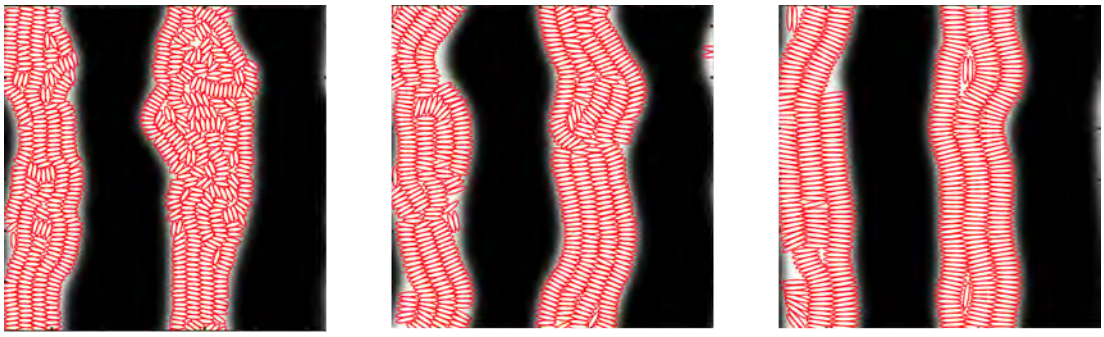

Figure 8.5: Final step of a system of ellipsoids with $b = 0.6$ minor axis and three values of major axis. The BCP constant $B = 0.0002$ is used to result in a large lamella domain.

3 different sizes (see captions). The values are chosen to fit 3, 4 and 5 rows. While the larger sizes in Figure 8.5 (b) and (c) show a well ordered configuration, the global order of the $a = 2$ case is low (a). This is in accordance with experiments [127] in which smaller NRs displayed lower ordering.

Composto et al [11] proved that when the major dimension of NRs is larger than the lamella domain width, colloids tend to orient along the domain axis. While experiments have shown that smaller nanonords orient normal to the domain direction, intermediate sizes can be explored using simulations. In Figure 8.6 we explored the role of the ratio $2a/L$ with $2a$ being the effective major length of the ellipsoid and $L = H/2 - 2\xi$, which is a measure of the available horizontal spacing for NPs. We should note that inspection of the ψ profile shows a clear weak segregation regime for the BCP, which makes difficult to delimiter an interface/bulk region. In any case, the curve of S along with the snapshots in Figure 8.6 clearly shows a $S \sim 1$ regime when the ellipsoids can easily fit into the domains and normal to the interface. As the size of the NPs is increased, a slight rotation appears, which results in a decrease in S. In conclusion, we observe a tilted configuration when the ratio between the major dimension of the ellipsoid and the BCP spacing is slighly larger than 1.

8.3.3 Low volume fraction of nanoparticles

The side-to-side, perpendicular-to-domain-axis colloid configuration is shown to appear when the anisotropic NP occupies most of the hosting domain, thus the surrounding B-block boundary inflects a pressure. In Figure 8.7 we show that even at low filling fraction the normal configuration holds. This is due to the attractive interaction between colloids, which minimizes the free energy even at relatively low filing fractions. The simulations (a) show a resemblance with the experiments in (b), where NPs indeed form aggregates within their preferred domain. Defects (perpendicular and disordered orientation) are present both in simulations and experiments.

8.3.4 Role of the initial condition

The hierarchical co-assembly displayed by NRs in experiments was dependent on the initial arrangement of particles within the BCP before annealing[127, 12]. In particular, the BCP was unable to break already-formed NP clusters. For that reason, simulations can be used to study the co-assembly starting from different initial conditions. A competition between the

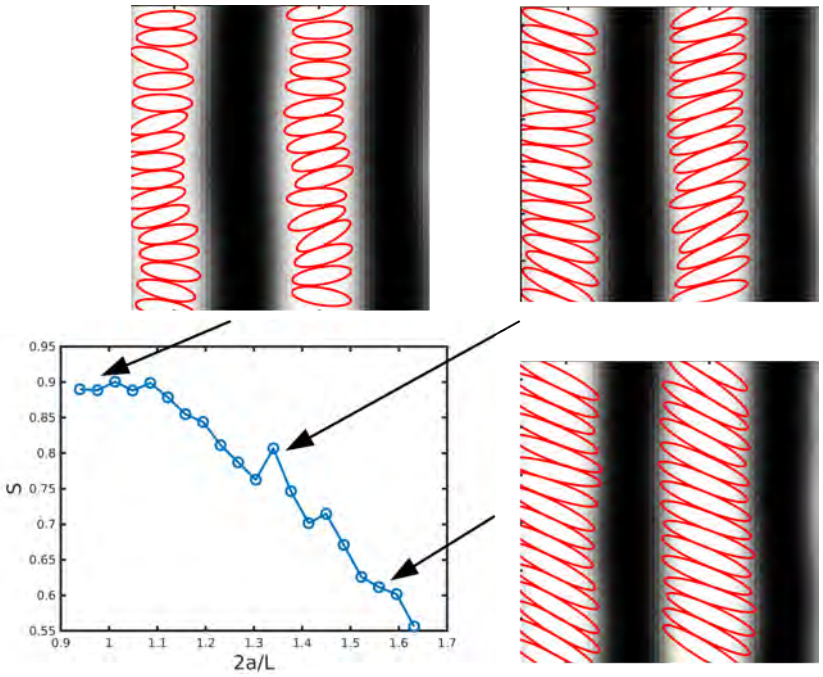

Figure 8.6: Decrease of orientational ordering of ellipsoids when the size of the major axis $2a$ is larger than the available normal spacing $H/2 - 2\xi$ with H the lamella periodicity and ξ the interface semi-size

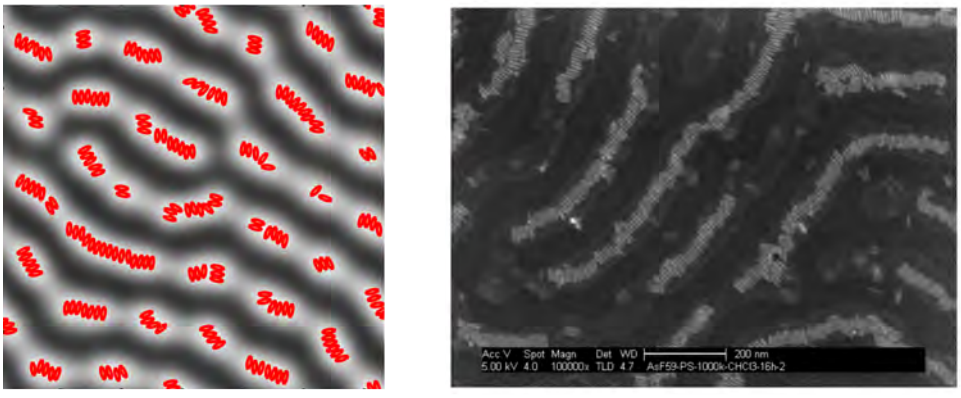

Figure 8.7: Low filling fraction of anisotropic NPs in BCP, comparing simulations (a) and experiments(b). Unoccupied lamellar domain which is available for NPs is shown in light gray/white in (a) and as gray areas in (b).

tendency of attractive NPs to form aggregates on the one hand, and the equilibrium periodic morphology of the BCP on the other hand needs to be studied in detail. For that reason two limiting regimes are selected: weakly and strongly interacting NPs with $U_0 = 0.001$ and 1.0, respectively.

Weakly interacting nanoparticles

Figure 8.8 shows five instances of the evolution of a system of relatively small particles with respect to lamellar spacing in a diblock copolymer. The initial and final states are shown, while the order parameter $S(t)$ plot over time can be found in the right-most column. In all cases a dotted line marks the horizontal line $S = 0$, so that instances of ordering $S > 0$ are clear. In this figure, the BCP is initialised as a sinusoidal, therefore, it is initially ordered. In (a), the NPs are randomly oriented and placed within the blue domains. The system is then evolved into a final, ordered configuration of side-to-side ellipses. The system also alternates one and two rows of ellipses. (b), (c) and (d) show three different initial conditions regarding the orientation of the ellipses at $t = 0$, respectively, $\phi_i = 0, \pi/2$ and $\pi/4$. Regardless of the initial condition, the final configuration is similar, meaning that this configuration is energetically favourable. It can be observed that in (a), (c) and (d) the order parameter S reaches a final (approximately steady) state only in the very long stages of the simulation. Instead, the already-horizontal ordering of the ellipses in (b) barely changes S over time. Finally, (e) shows ellipses which are initially forming clusters in their preferred BCP domains. The final BCP morphology lacks the global orientation of the previous instances, since the NPs are initially forming clusters. Nonetheless, the orientation and ordering of ellipses is equally normal to the interface, which can be checked visually and by the positive $S > 0$ value of the orientational order parameter.

Figure 8.9 shows four instances of NR initial configuration in an initially disordered BCP. While the position of the particles is randomly chosen, the orientation is random for (a) and $\phi_i = 0, 0.35\pi$ for (b) and (c), respectively. The final state is shown in the central column while the evolution of the order parameter is displayed in the right column. In (d) the NPs are initially forming clusters without a collective orientation (disordered). In all of these cases the final state is a side-to-side configuration with ellipses oriented normal to the interface, that is, $S > 0$. Observing the evolution of $S(t)$ one can notice that the (b) and (c) cases reach the final S value at a much shorter timescale than angularly-disordered cases (a) and (d).

Figure 8.10 shows an initially ordered diblock copolymer, with NPs forming clusters with a low internal order (contrary to Figure 8.8 (e)) in which the internal orientation was random) . The time evolution suggests that the NPs are dispersed within the BCP, which is modified to accommodate the long-ordered sequences of ellipses. NPs form ordered arrays of side-to-side orientation within the white domains.

Strongly interacting nanoparticles

In all of the above described cases, the BCP is able to acquire a stripe-like morphology, while NPs tend to appear relatively dispersed within the A domains, regardless of the initial condition. This was valid for particles which interact weakly between each other, which can be applied to metal NPs that lack a fixed dipole moment. Nonetheless, experiments involving semiconductor NRs, such as CdSe, report a strong interparticle attractive interaction that led to particle aggregation dominating over the BCP assembly[12].

A strong interparticle potential scale parameter $U_0 = 1$ can be used to understand the co-assembly behavior in the strong interparticle potential limit, as in figures 8.11,8.12 and 8.13.

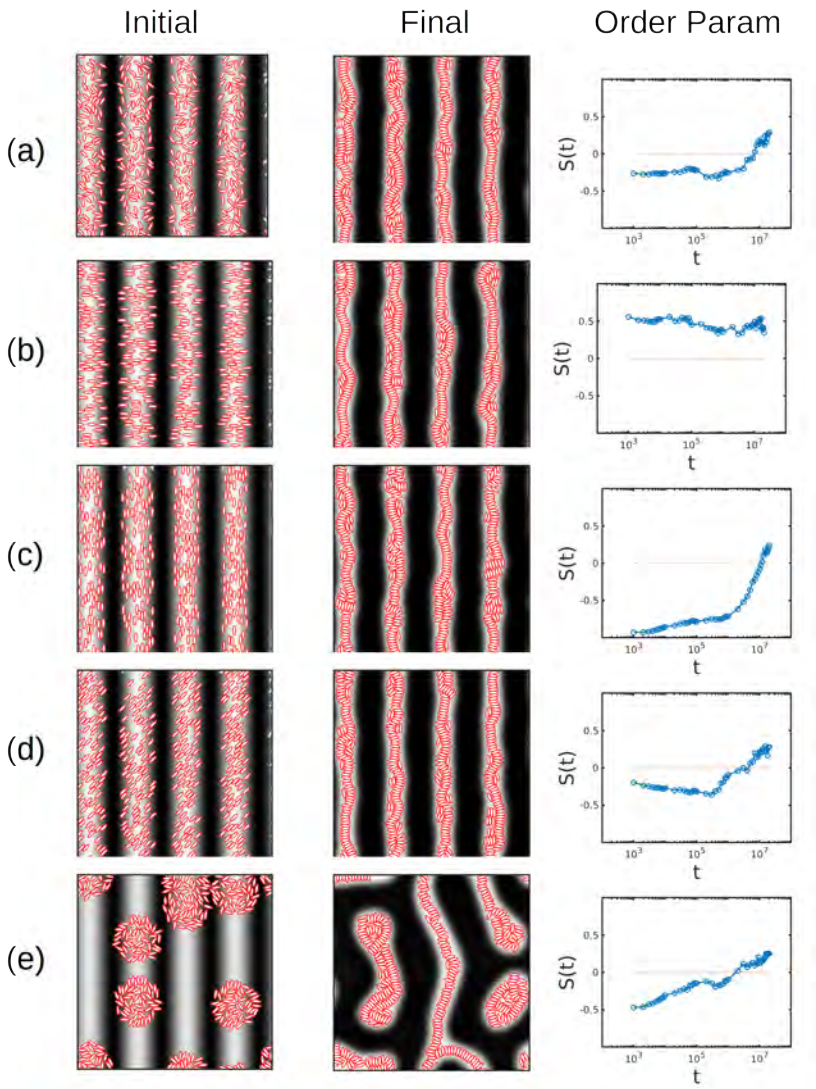

Figure 8.8: Initial and final snapshot of several systems with different initial conditions. The time evolution of the orientational order parameter $S(t)$ is also shown for each case. In all cases the BCP is initially fixed to a sinusoidal concentration profile. In (a), NPs are randomly oriented and the position is random, within the white domain. In (b),(c) and (d), positions are again randomly chosen, while the orientation is $\phi_i = 0, \pi/2, \pi/4$, respectively. In (e), the ellipses are placed randomly within small clusters

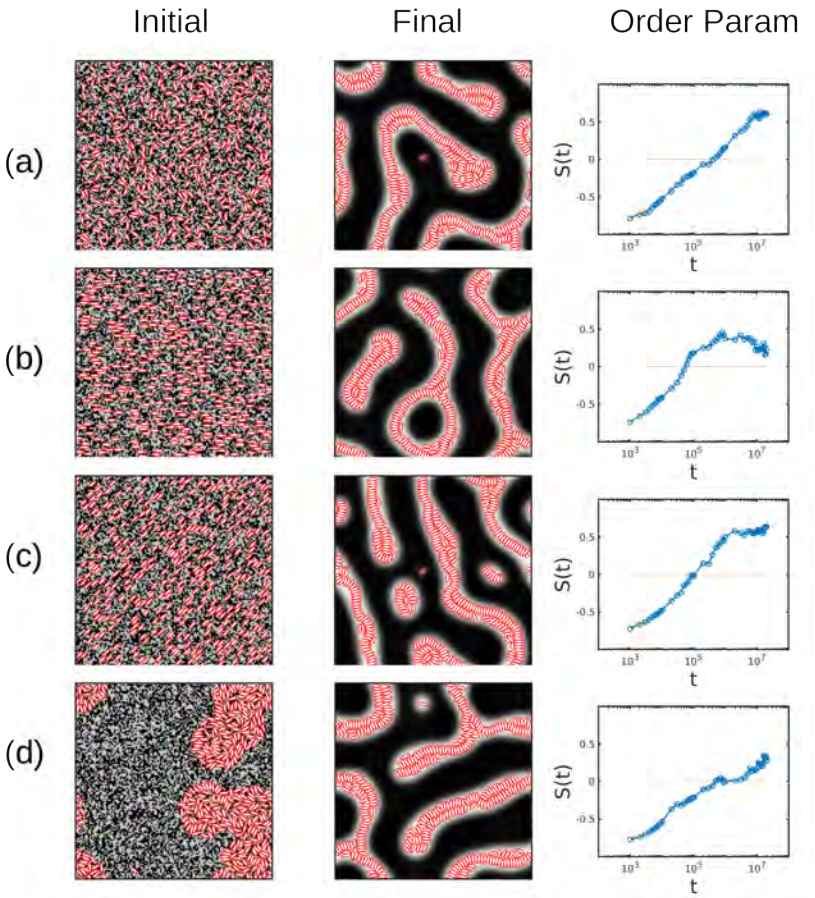

Figure 8.9: Initial and final snapshot of several systems with different initial conditions. The time evolution of the orientational order parameter $S(t)$ is also shown for each case. In all cases the BCP is initially random(disordered). In (a) the orientation and position of all particles is chosen randomly. In (b) and (c), the position is chosen randomly, while the orientation with respect to the horizontal axis is $\phi_i = 0, 0.35\pi$, respectively. In (d) the particles are initially forming clusters.

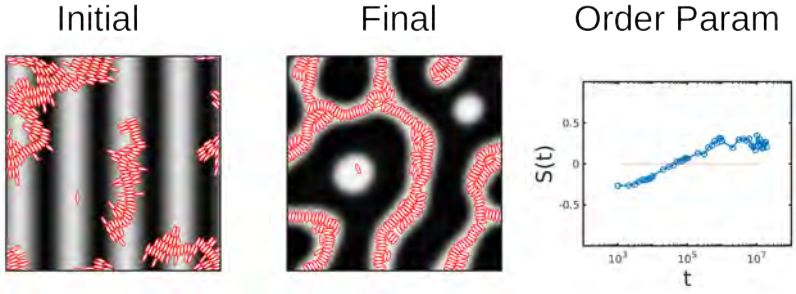

Figure 8.10: Initially ordered BCP with NP forming ordered clusters at $t = 0$. Initial and final snapshots are shown in the left and center figures while the order parameter $S(t)$ is displayed in the right-most figure.

These are directly related to figures 8.8, 8.9 and 8.10 by selecting the same initial conditions.

Comparing figures 8.8 (weakly interacting) and 8.11 (strongly interacting) we can clearly draw the conclusion that at $U_0 = 1$ the NPs are driving the co-asembly, with the BCP domains being formed around aggregates of colloids (except for (b), as compared with the weakly interacting case, in which the BCP tended to form elongated lamellar-like domains. Ordering in the NPs is also strongly dominated by the initial configuration in the $U_0 = 1$ regime, with $S > 0$ only in (b) and (e) cases. A comparison between the curve of $S(t)$ in Figure 8.8 (c) and 8.11 (c) leads to the conclusion that in the weakly interacting NPs regime the NPs undergo first a dispersion within the BCP domains, while in a slower time scale the NPs achieve global normal orientation with the BCP interface. This global ordering is not present at $U_0 = 1$, where the strong interparticle potential rapidly assembles the NPs into vertically oriented groups of particles in aggregates. Similarly, in (e) the aggregated particles at $t = 0$ tend to form clusters also after the time evolution, with the BCP clearly being forced to form less elongated domains.

The initial orientation of NPs when the BCP is initially disordered also affects the co-assembly in the strong interacting NP regime. In Figure 8.12, compared to its equivalent 8.9, clearly displays less elongated domains, with NPs more prone to form well-ordered structures, while at the same time forming more aggregates that enhance the local size of the hosting domains. Again, this suggests that the BCP is unable to complete its assembly by disassembling the aggregates, instead, it merely forms domains around aggregates of ellipses.

Similarly, in Figure 8.13 the initial NP aggregates cannot be broken into elongated domains to the same degree as occurred in Figure 8.10. Instead, the BCP forms domains around clusters of particles. Since the initial aggregates were already made of considerably well-ordered NPs, the final S value is particularly high, meaning that a high ordering is achieved.

In summary, the role of the initial condition is crucial when the NPs interact strongly with each other. This strong interaction leads to the formation of aggregates in the early stages of the time evolution of the system that are not broken by the BCP evolution (whether it is from disorder to order, or an already phase-separated BCP). Weakly interacting NPs, on the other hand, undergo a co-assembly on a similar time scale as the BCP, therefore, the side-to-side along with the normal-to-interface configuration is easily obtained under any initial condition.

8.3.5 Role of energetic parameters

Simulations can be used to gain insight on the effect that the interaction parameters have on the formation of the side-to-side configuration normal to the interface between domains. A simple energetic analysis for NRs suggests that this configuration is energetically preferential both for the inter-colloidal potential and the NP-polymer coupling [127, 12].

The interparticle Gay-Berne potential described in the Model section sets the interaction between two ellipses with two energetic parameters: U_0 sets the scale of the interaction, while ϵ_r describes the anisotropy in the depth of the potential minima. For that reason, in Figure 8.14 we explore these two parameters via the orientational order parameter S. It is clear that the anisotropy value ϵ_r is key on the formation of the side-to-side configuration as we find $S \sim 0$ as the anisotropy of the potential is closer to 1. This leads to more tip-to-tip configurations, which in turn are better accommodated with the NPs oriented along the domains, as can be found in the two snapshots in the right hand-side of Figure 8.14. Contrary to that, high anisotropy leads to well-ordered side-to-side configuration. Because the lamella domain spacing is similar to the major size of the ellipses, the BCP accommodates only one row of ellipses.

Figure 8.14 shows that the energetic scale U_0 plays a less relevant role than the anisotropy

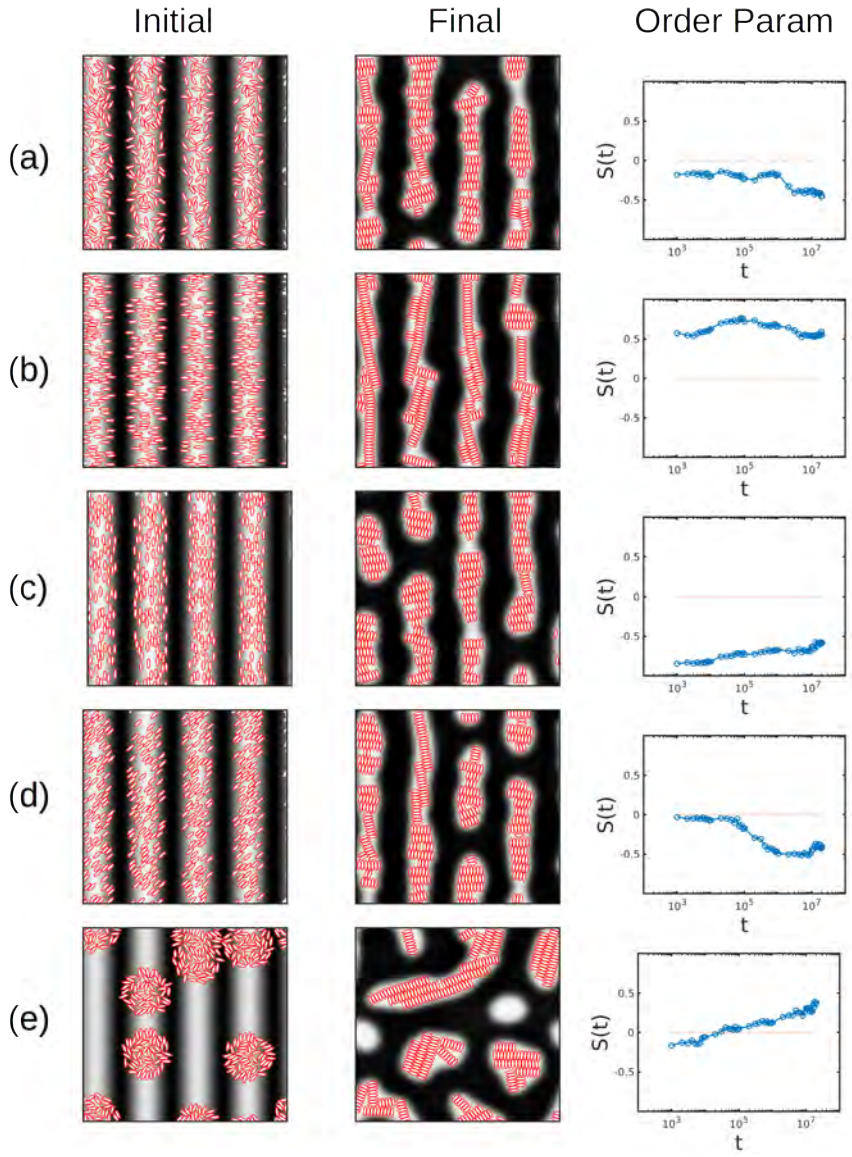

Figure 8.11: Initial and final snapshot with different initial conditions (same as Figure 8.8) in the strong interaction regime $U_0 = 1$. The time evolution of the orientational order parameter $S(t)$ is also shown for each case. In all cases the BCP is initially fixed to a sinusoidal concentration profile. In (a), NPs have initial random orientation and their position is random and confined to the white domains. In (b),(c) and (d), positions are again randomly chosen, while the orientation is $\phi_i = 0, \pi/2, \pi/4$, respectively. In (e), the ellipses are placed randomly within small clusters

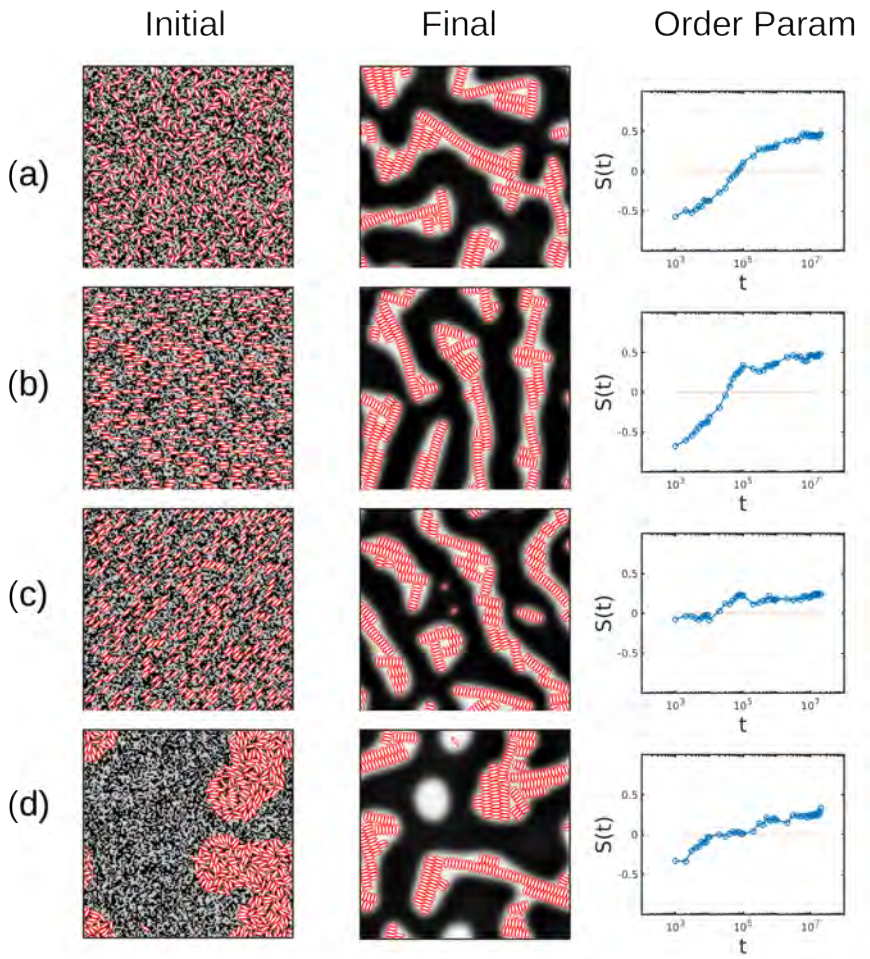

Figure 8.12: Initial and final snapshot with different initial conditions (same as Figure 8.9) in the strong interaction regime $U_0 = 1$. The time evolution of the orientational order parameter $S(t)$ is also shown for each case. In all cases the BCP is initially random(disordered). In (a) the orientations and positions of all particles are chosen randomly. In (b) and (c), the position is chosen randomly, while the orientation with respect to the horizontal axis is $\phi_i = 0$ and 0.35π, respectively. In (d) the particles are initially forming clusters.

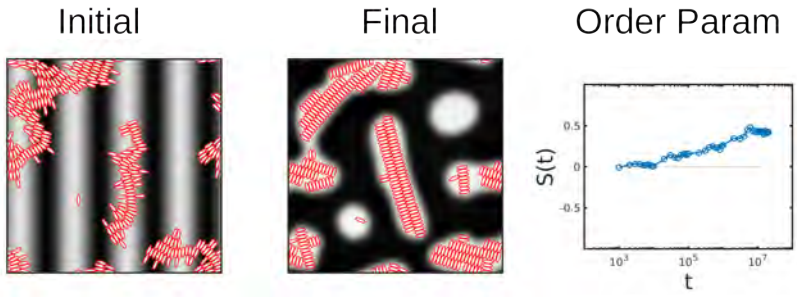

Figure 8.13: Initially ordered BCP with NP forming ordered clusters at $t = 0$. Initial and final snapshots are shown in the left and center figures while the order parameter $S(t)$ is displayed in the right-most figure. The NP-NP interaction parameter is $U_0 = 1$.

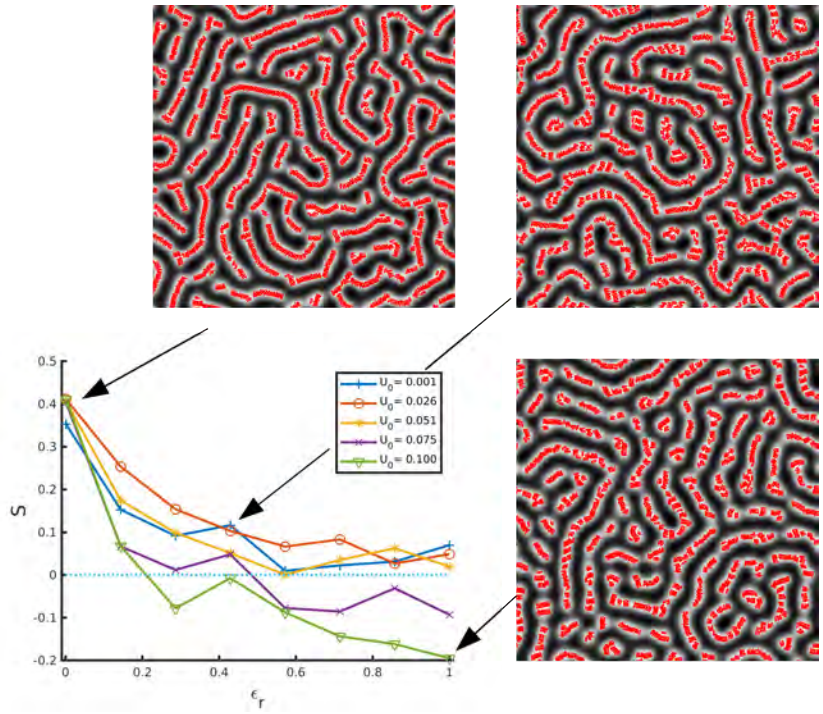

Figure 8.14: Orientational order parameter S for different final stages tuning the interparticle potential parameters: U_0 and ϵ_r, the strength and anisotropy of the Gay-Berne potential, respectively. Three snapshots of the representative parameters are shown.

factor ϵ_r. We observe that even at low values of U_0 the ordering is kept $S > 0.4$ which is indicative that the configuration is stable even at low interparticle potential strengths. These results are in accordance with a simple energetic analysis shown in section 8.1 , where we conclude that in order to have an energetic minimum in the side-to-side configuration, we need to satisfy $e >> \epsilon_r$.

Such energetic analysis is considered only in the case of relatively high filling fraction of NPs in the system, a regime in which the particles-to-polymer coupling is considerably strong, as the contacts between the colloids and the interfaces become important. In Figure 8.15 we explore both the number of particles via the fraction of particles in the system ϕ_p, and the strength of the potential U_0, from a very small $U_0 = 0.001$ up to $U_0 = 1$. The cylinder-forming neat BCP is chosen by setting $f_0 = 0.3$. The orientational order is characterised by the order parameter S. In the low filling fraction regime we can find ellipsoids segregated within the minority white domains without a particular orientation with respect to the BCP interface. On the other hand, at high filling fraction the nanoparticles can induce a transition into elongated BCP domains. In this regime, a lower value of the U_0 NP-NP energetic scaling leads to a higher ordering. Contrary to that, a large interaction strength leads to the interparticle potential driving the time evolution of the system. In this regime the NPs are less prone to minimise the contacts with the yellow domains, and minimisation of the interparticle potential is dominant enough. This result is in agreement with what we described in figures 8.8-8.10 when compared with 8.11-8.13 when a lower interaction strength led to a higher degree of ordering.

We can therefore conclude that at low volume fraction, a strong interparticle interaction is necessary to have ordered NPs. This is not the case at higher filling fraction, in which merely the NP-BCP interaction is enough to assure that the NP will assemble in the described configuration.

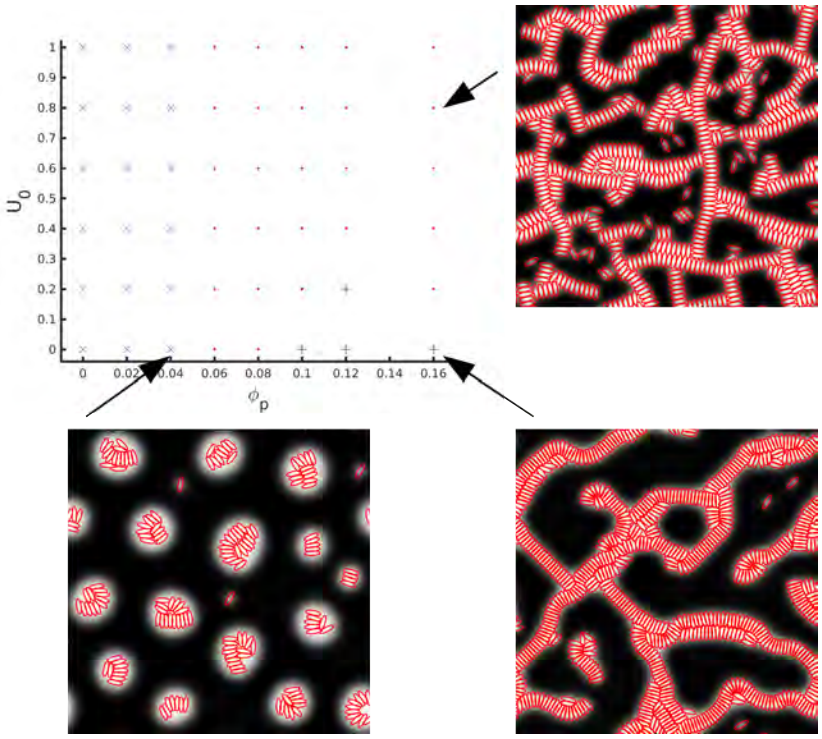

Figure 8.15: Phase diagram of the assembly of ellipses in a diblock copolymer with $f_0 = 0.3$. The number of particles is explored in the X axis ϕ_p and the strength of the interparticle potential is tuned via U_0. Markers relate to the value of the orientational order parameter as: blue cross x for $S < 0.01$; red dots · for $0.01 < S < 0.3$; and black plus sign + for $S > 0.3$

8.4 Conclusions

The co-assembly of anisotropic nanoparticles in BCPs has been studied by means of mesoscopic simulations in the case of A-modified NPs with elliptical shape. Ellipsoidal nanoparticles have been shown to induce phase transitions in the block copolymer matrix due to the enhancement of the hosting domains. In turn, the combination of BCP-NP coupling and intercolloidal attractive forces leads to a well-ordered configuration of anisotropic colloids which reproduces experimental results [127, 12]. When confined within one of the BCP phases, ellipsoids are found to orient normal to the domain axis in order to minimise the contacts with the surrounding incompatible phase while minimising the angle-dependent intercolloidal potential. Ellipsoidal colloids are used to mimic CdSe nanorods mixed with PS-*b*-PMMA used in experiments. Direct comparison between experimental SEM images and simulations can be performed, finding a considerable similarity between simulations and experiments. The size of the NP with respect to the BCP periodicity plays a crucial role in the assembly of anisotropic colloids. Smaller NPs tend to form fewer rows than larger ones, while the ordering increases with larger particles, which is in accordance with experiments. Furthermore, NPs which are slightly larger than the lamella spacing undergo a rotation with respect to the interface, while maintaining the side-to-side intercolloidal organisation.

A study of several different initial conditions (both initially ordered and disordered) has draw the conclusion that weakly interacting NPs organise side-to-side within a phase-separating BCP that achieve a lamellar morphology, regardless of the initial condition. In this regime the BCP can undergo the usual phase-separation even in the case of an initially-clustered NP configuration. On the contrary, the initial configuration of colloids is crucial in the case of strongly-interacting nanoparticles, which are trapped in a metastable state that does not allow

the system to reach a side-to-side organisation. This occurs, for example, if NPs are initially forming aggregates, which the BCP is unable to break-up. Finally, a high energetic anisotropy in the colloid-colloid potential has been shown to be crucial at determining the final side-to-side/normal to domain axis configuration.

In summary, we have presented a computational method that mimics a complex co-assembly process of anisotropic NPs in BCPs. We have been able to gain insight over the role of several parameters which are experimentally difficult to explore. We have identified the importance of the relative size between the NP main axis and the lamellar spacing, which dictates the relative orientation and the number of rows in the assembly. Two different energetic regimes have been identified: weakly and strongly interacting NPs undergo different types of co-assembly with the BCP, which corresponds to semiconductor and metallic NPs. Weakly-interacting NPs with a high energetic anisotropy have been shown to display the highest level of side-to-side configuration while allowing the BCP lamellar morphology to fully develop.

CHAPTER 9

Shape Anisotropic Colloids II: Block Copolymer/Super Ellipses

Abstract

A hybrid block copolymer(BCP) nanocomposite model is used to study nanoparticles(NPs) with a generalised shape including rectangles and rhombus. Simulations are used to study the role of anisotropy in the assembly of colloids within BCPs, ranging from NPs that are compatible with one phase, to interface-compatible NPs. We investigated the ordering of square-like NPs into grid configurations within a minority BCP domain, as well as the alignment of nanorods in a lamellar-forming BCP, comparing with experiments. Furthermore, the assembly of rectangular NPs at the interface between domains resulted in alignment along the interface. The aspect ratio is found to play a key role on the aggregation of colloids at the interface, with leads to a distinct co-assembly behaviour for low and high aspect ratio NPs

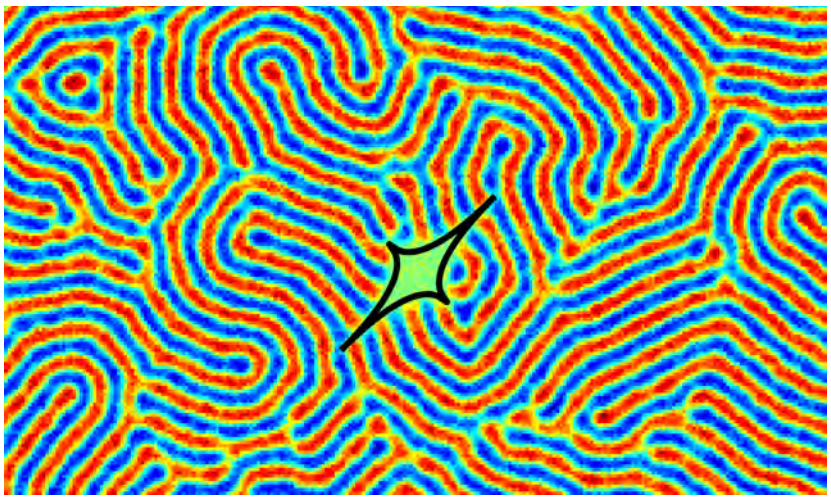

9.1 Introduction

Polymer nanocomposite materials containing anisotropic nanoparticles have attracted a lot of attention due to their ability to create functional materials with enhanced properties[10]. Fillers have been added to polymeric materials to improve its properties, such as in the well-known case of carbon black [26]. In particular, block copolymers can serve as perfect matrices to produce highly ordered polymer nanocomposite materials due to the well-defined, periodic structures that block copolymer melts has. This periodicity makes block copolymers excellent matrices to host nanoparticles (NPs), which can be localised in specific regions of the phase-separated block copolymer[27, 28].

While spherically shaped colloids have been widely studied -both experimentally and theoretically [139]- the additional difficulty of modelling anisotropy have resulted in comparably less work devoted to it. Nevertheless, the orientational degree of freedom of non-spherical colloids introduces new possibilities of BCP/NP co-assembly, given the intrinsic ordered structures of the neat block copolymer (lamellar, cylindrical, etc). Complex non-spherical nanoparticles such as nanorods(NR) have attracted a lot of attention as constituents of functional polymer nanocomposite materials[10]. For instance, gold nanorods orient along the lamellar domain when confined in one of the symmetrical phases[11, 128]. Similarly, gold nanorods template the direction of the cylindrical domains in an asymmetrical diblock copolymer mixture[129]. Ordered arrays of aligned nanorods were achieved experimentally [130, 131] in the co-assembly of BCP and highly anisotropic NPs, where NRs were organised in an end-to-end configuration.

In this chapter a generallisation of previous hybrid BCP/NP models[68] for a vast family of NP shapes is presented. The shape of the NPs is motivated by experiments. For example, considerable attention has been given to nanocubes[149, 150] as an example of faceted particles that can lead to the formation of crystals[151].

While in Chapter 8 we have studied the assembly of ellipsoidal-shaped particles in comparison with a particular experimental setup (A-compatible anisotropic NPs in a A-*b*-B BCP), in this chapter we aim to consider a more general approach, studying both A-compatible and neutral NPs, as well as paying a detailed attention to the role of anisotropy. In the following section a generalised model for anisotropic NPs will be presented.

9.2 Model

9.2.1 Coupling between the block copolymer and nanoparticles

In previous works[68], the presence of N_p nanoparticles has been introduced via an extra term in the free energy, given by

$$F_{cpl} = \sum_{p=1}^{N_p} \sigma \int d\mathbf{r}\ \psi_c(\mathbf{s}) \left[\psi(\mathbf{r}) - \psi_0\right]^2 \tag{9.1}$$

In the case of a simple circular particle, $\mathbf{s} = |\mathbf{s}|/R = (x/R)^2 + (y/R)^2$ and the tagged function is related to the core/shell nature of the particle. It is a smoothly monotonically decreasing function that takes values $\psi_c(0) = 1$ and $\psi_c(1) = 0$. In our choice,

$$\psi_c(s) = \exp\left[1 - \frac{1}{1-s}\right] \tag{9.2}$$

for $s < 1$ and $\psi_c(s > 1) = 0$. This expression allows us to design a nanoparticle that interacts softly with the surrounding block copolymer, and it avoids the need to explicitly consider the NP-BCP boundary.

To extend the colloidal shape from a circular particle to an elongated ellipse, one can trivially rescale the axis, such that $s = (x/a)^2 + (y/b)^2$ for an ellipse that is resting horizontally (vertically) if $a > b$ ($a < b$). Furthermore, we can consider a generalisation of this procedure, to represent a larger family of curves, namely, superellipses. Such closed curves are given by

$$s(\mathbf{r}) = \left[\left| \frac{x}{a} \right|^{2n} + \left| \frac{y}{b} \right|^{2n} \right]^{1/n} = 1 \tag{9.3}$$

where the exponent $1/n$ rescales the decay[152] of ψ_c. Again, x, y should be related to the rotated $x'(\phi), y'(\phi)$ versions of the variables. In Fig. 9.1 representative examples of superellipses are given for several values of n, for two values of the aspect ratio.

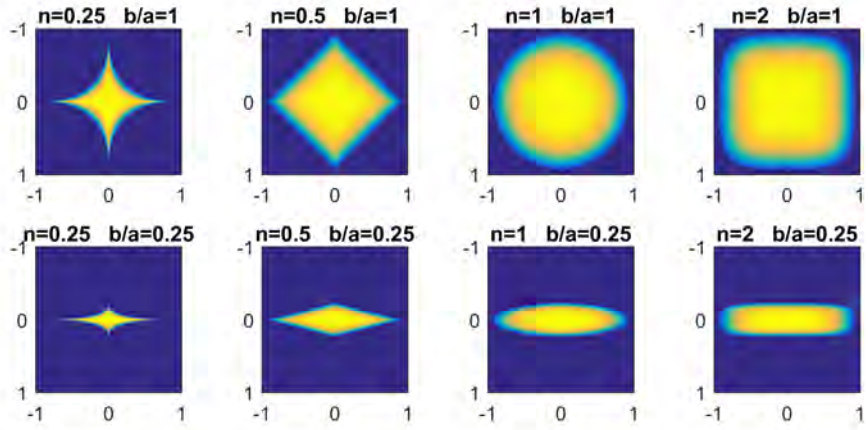

Figure 9.1: Colourmap of ψ_c as described in Eqs. 9.2 and 9.3 for several values of n and b/a. The particles are assumed to have no rotation $\phi = 0$ and larger semiaxis $a = 1$.

The simplicity of the coupling free energy allows us to simulate a vast range of NP shapes. The family of superellipses in two dimensions include ellipses, rectangles, rhombus and star-like particles. Many of these shapes can serve as a faithful representation of experimentally-motivated non-spherical colloids such as nanocubes, nanospheres or nanorods.

9.2.2 Interparticle potential

Once the BCP/NP coupling contribution to the free energy has been specified, it is important to introduce an intercolloidal pairwise additive potential from which forces and torques can be derived. In the particular case of ellipsoids ($n = 1$), a modified Lennard-Jones potential has been widely used[140]. Nonetheless, in this chapter we will study the particular case of rhomboid and rectangular shaped particles. To this end, we design a simplified repulsive potential that will assure non-overlapping between particles.

We introduce a colloid-colloid contribution to the free energy as

$$\mathcal{F}_{cc} = \sum_{i \neq j} U(\mathbf{r}_i, \mathbf{r}_j, \phi_i, \phi_j) \tag{9.4}$$

with $U(\mathbf{r}_i, \mathbf{r}_j, \phi_i, \phi_j)$ a potential that depends on the distance between two colloidal particles, as well as their orientations ϕ_i, ϕ_j. Specifically, we choose a potential that is proportional to

the overlapping area (volume in three dimensions) between two colloidal particles of arbitrary shape

$$U(\mathbf{r}_i, \mathbf{r}_j, \phi_i, \phi_j) = U_0 A_{\text{overlap}}(\mathbf{r}_i, \mathbf{r}_j, \phi_i, \phi_j) \tag{9.5}$$

which prevents overlapping between colloids. To our knowledge, there is no general analytic expression of the overlapping area between two parallelogram of arbitrary orientation and distance. Nonetheless, the Separating Axis Theorem (SAT) is widely used in computer science to test collisions between convex polygons[153].

In order to derive forces and torques between colloids, we require an expression of the overlapping area. To this end we numerically calculate the overlapping area between colloids and perform a fit of the results into simple analytical expressions. The details for different shapes, orientations and distances can be found in Appendix D.

9.2.3 Brownian Dynamics

Colloids undergo diffusive dynamics described by the Langevin equation in the overdamped regime. The centre of mass of each colloid follows Brownian Dynamics, that is,

$$\frac{d\mathbf{R}_i}{dt} = \frac{1}{\gamma_t}\left(\mathbf{f}_{cc} + \mathbf{f}_{cpl} + \sqrt{2k_BT\gamma_t}\xi\right) \tag{9.6}$$

where $\mathbf{f}_{cpl}$ is the coupling force derived from Eq. 9.1 and $\mathbf{f}_{cc}$ is the colloid-colloid force derived from Eq. 9.4 through the fitted expression of the overlapping area in Eq. 9.5. Similarly, the orientation of particle i follows

$$\frac{d\phi_i}{dt} = \frac{1}{\gamma_R}\left(M_{cc} + M_{cpl} + \sqrt{2k_BT\gamma_R}\xi\right) \tag{9.7}$$

where γ_t and γ_R are the translational and rotational friction coefficients. Generally speaking, the translational diffusivity is a tensor that accounts for the anisotropic diffusivity of arbitrary shaped particles [144] along the parallel and perpendicular main axis of the colloid. Nonetheless, we are interested on the equilibrium properties of the assembly of polyhedra shaped colloids. Thus, we can assume these γ_t to be a scalar[128]. The torques acting on the particle i are M_{cc} and M_{cpl}, respectively the colloid-colloid and coupling contributions.

9.3 Results

The standard values of CDS[42, 49, 68] will be used $\tau_0 = 0.35, u = 0.5, v = 1.5, A = 1.5, D = 2.0$ while the BCP/NP interaction is set to $\sigma = 1.0$. A cell spacing $\delta x = 1.0$ and time discretisation $\delta t = 0.1$ are chosen. Lengths will be presented in units of grid points.

9.3.1 A-compatible NPs

In order to study a minimal example of anisotropic colloids in BCP, we can firstly consider square-like NPs which are compatible with the minority phase of the BCP. By doing so, we are introducing a high effective volume fraction of colloids. We select a cylinder-forming BCP with $f_0 = 0.35$ and explore a concentration of colloids ϕ_p with a side length $2a_0$. At low concentrations, the NPs are confined within circular BCP domains. At higher concentration, the NPs are effectively increasing the fraction minority monomers, enough to induce a cylinder-to-lamellae transition in the BCP. [69, 100, 6, 93, 95, 98, 55]. A combination of the entropic NP-NP

interaction and the enthalpic effect of the surrounding block copolymer can lead to organisation of the square-shaped colloids into a defined side-to-side assembly. In order to quantify an eventual grid-like arrangement, we can define the interparticle orientational parameter

$$T_{22} \equiv \langle\langle \left[2(\mathbf{n}_1 \cdot \hat{\mathbf{r}})^2 - 1\right]^2 \left[2(\mathbf{n}_2 \cdot \hat{\mathbf{r}})^2 - 1\right]^2 \rangle\rangle \tag{9.8}$$

where the brackets indicate average over all particles' neighbours. This parameter is 1 for a grid-like arrangement of particles and it is clearly defined positive. It provides insight both on the orientational and translational order of the colloidal set of particles.

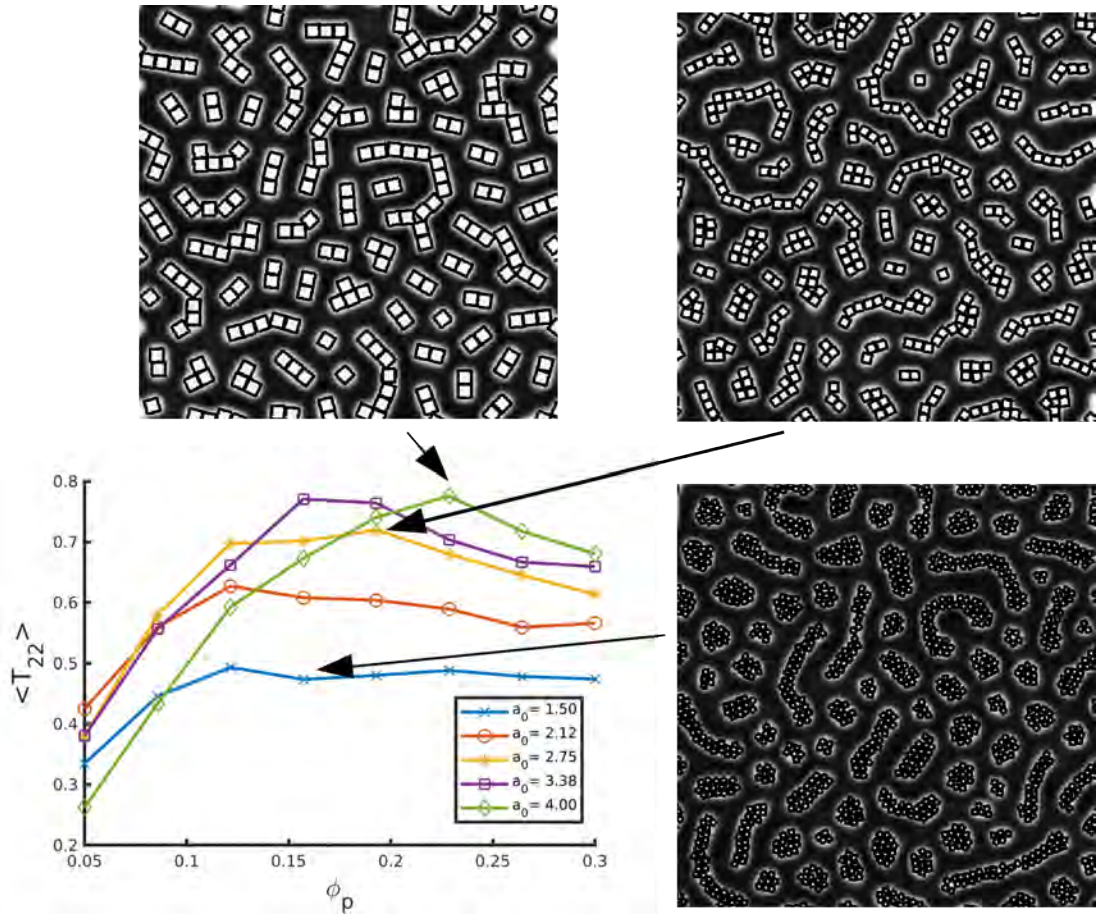

Figure 9.2: Interparticle orientation parameter for a concentration ϕ_p of square-shaped NPs for different sizes (squares with side $2a_0$). Snapshots show representative instances of the colloidal assembly.

We can explore the parameter space given by the fraction of particles in the system ϕ_p and the size of the particle a_0. By doing so we can explore the arrangement of particles for a given level of constrain for different sizes. In figure 9.2 we plot such curves. We can observe that small-sized particles are not well oriented within the block copolymer, with $T_{22} < 0.5$ for any fraction of particles when $a_0 = 1.5$. We can conclude that small particles tend to be dominated by thermal motion and neither the block copolymer, nor the entropy associate with the anisotropy of particles can induce an ordered phase. Larger particles, instead, can achieve ordered configurations with array-like organisation of squares. For a three-dimensional system, we can expect a monolayer of well-ordered cubes in a lamellar phase.

In Fig. 9.3 we study the assembly of rhombus-shaped NPs by selecting an exponent $n = 0.6$ from Eq. 9.3. Following the analysis described in Fig. 5.4, we can select a value $f_0 = 0.35$ and

$\phi_p = 0.2$ such that the BCP morphology is lamellar in the presence of a concentration of NPs. By doing so, rhomboid-shaped NPs segregate within the minority domains and experience a considerable local effective concentration, which leads to close-packed configuration for three different rhomboid sizes: $a_0 = \sqrt{2}, 2$ and $2\sqrt{2}$ for (a), (b) and (c), respectively. The NP aspect ratio is kept constant $b/a = 1/2$. Regardless of the size of the particles, the BCP lamellar morphology and its confinement effect leads to a highly ordered NP configuration.

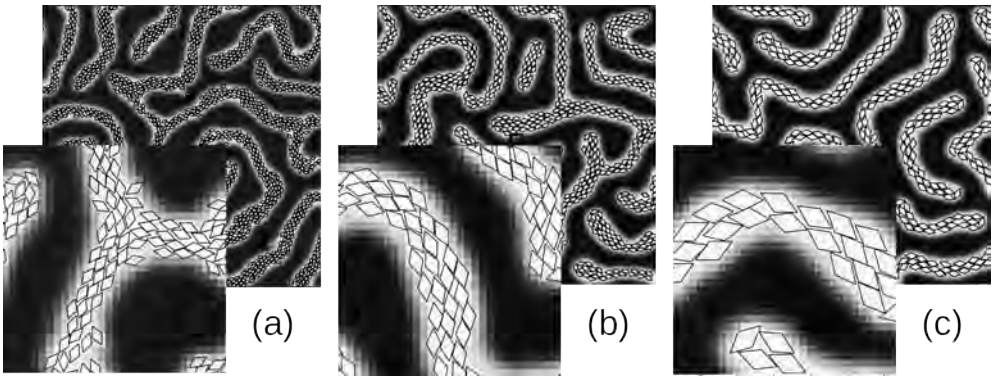

Figure 9.3: Rhomboid-shaped NPs compatible with the minority domain in a $f_0 = 0.35$ asymmetric BCP. A fixed concentration $\phi_p = 0.2$ is considered for NP sizes $a_0 = \sqrt{2}, 2$ and $2\sqrt{2}$ for (a), (b) and (c), respectively.

9.3.2 Comparison with experiments

Anisotropic nanoparticles possess an additional orientational degree of freedom which- when mixed with phase-separating block copolymers- can induce an orientational order. Experimentally, this has been widely studied. For instance, Composto et al found nanorods oriented along the lamellar domains [11] while end-to-end, in-lamella assembly has been found in thin films [131]. More recently, nanoplates have been found to align within a lamellar-forming PS-*b*-PMMA block copolymer. While this type of assembly is intrinsically three dimensional, we can aim to study the two-dimensional slice of a nanoplate into a rectangle with sizes d_1 and h, related to the larger diagonal and the thickness of a nanoplate. Along with the lamellar periodicity, we can simulate experimentally relevant parameters of such systems, as in figure 9.4 where we observe a clear alignment of rectangular nanoparticles along the lamellar domains.

Furthermore, we can simulate the horizontal cross-section of a nanoplate as a rhomboid particle using experimental relative sizes [8] to simulate realistic rhomboids (nanoplates in 3D) with sizes $b/a = 0.629$ (ratio of diagonals) and the relative size between the lamella thickness and larger diagonal tuned accordingly. In figure 9.5 top-left we can see how the rhomboids are placed within the circular domains, enlarging those in which more than one nanoparticle is placed. Furthermore, the rhomboids tend to assemble in a close-packed manner. If we increase the number of particles, this behaviour is even more clear, as in top-right. For a lamellar-forming BCP (bottom row), the nanoparticles are not totally confined , only within the stripe domains. Because the lamellar thickness cannot accommodate a single NP, they tend to aggregate in order to minimise the distortion induced by the presence of NPs.

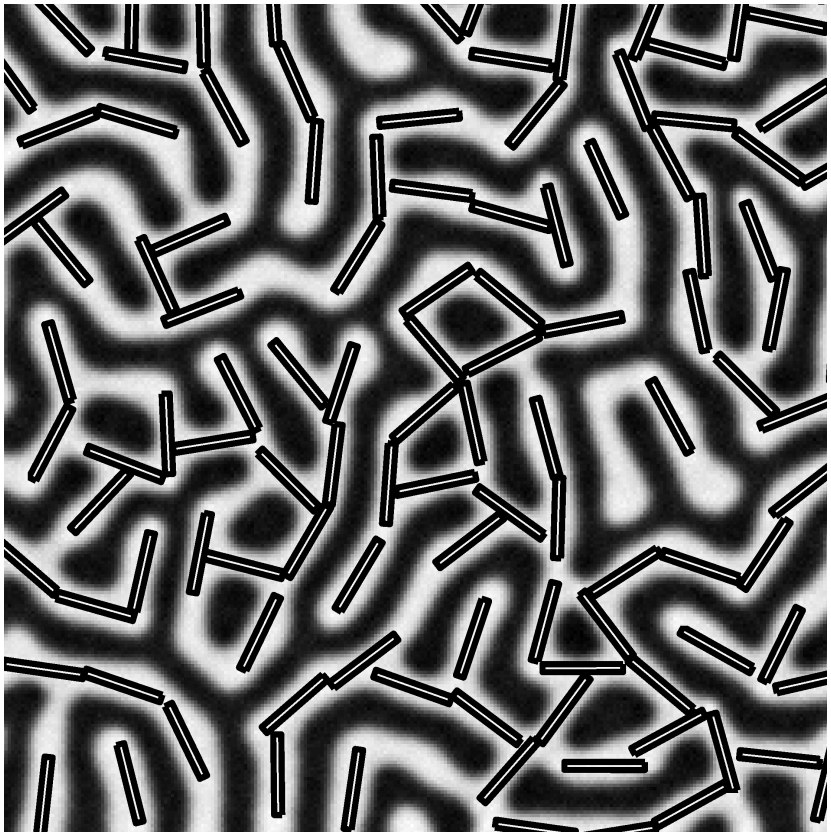

Figure 9.4: Alignment of rectangular nanoparticles in a symmetric block copolymer. Nanoparticle size is $a_0 = 12.11$ and $b_0 = 1.21$ for the major and minor semiaxis while the BCP lamellar spacing is $L \approx 8$.

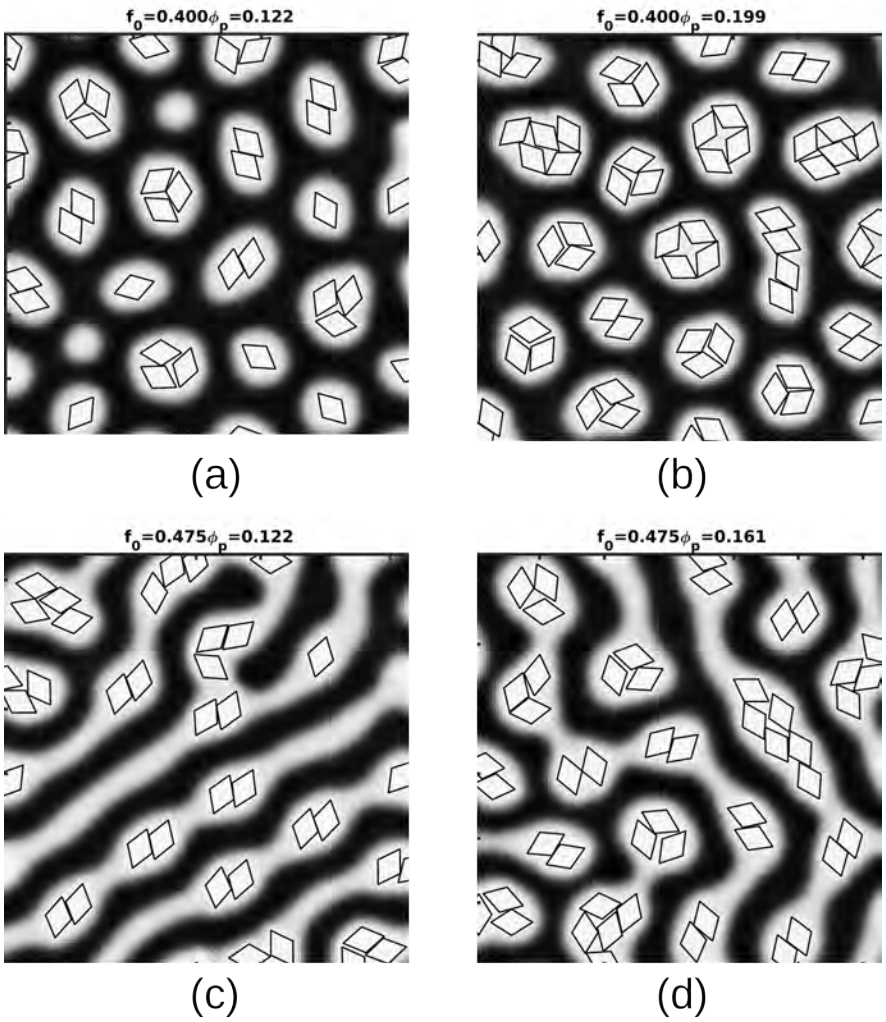

Figure 9.5: Examples of a concentration ϕ_p of minority-compatible rhomboid particles mixed with block copolymer with f_0 (see titles for values).

9.3.3 Neutral rectangles

Homopolymer chains can be grafted to the surface of NPs to create surfactant NPs that tend to segregate at the interface between BCP domains[31]. Setting a neutral affinity $\psi_0 = 0$, we can study the role of anisotropy in the assembly of rectangular NPs ($n = 2$). Because of the colloidal shape, rectangular nanoparticles tend to orient along the interface, as can be seen in Figures 9.6 (a) for an asymmetric, cylinder-forming BCP. In Figure 9.7 (a) we can see the orientation of colloids along the lamellar domains. In both cases, a large number of particles oriented in the interface leads to a transition induced by the saturation of the interface and by the formation of bridges along domains.

Figure 9.6 shows the transition from a cylinder-forming BCP with circular domains organised hexagonally (a) into a blue-domain lamellar with a combination of minority (red) phase with colloidal-rich region (b). This transition was already reported in simulations with circles in Fig. 5.9 in but one can notice how many colloids still prefer to assemble at the interface and oriented along it.

A lamellar, symmetric BCP mixed with rectangular particles can be seen in figure 9.7. In (a), a small concentration of particles is oriented along the interface. At larger concentrations the colloids form bridges along domains which break them into smaller, irregular domains. The

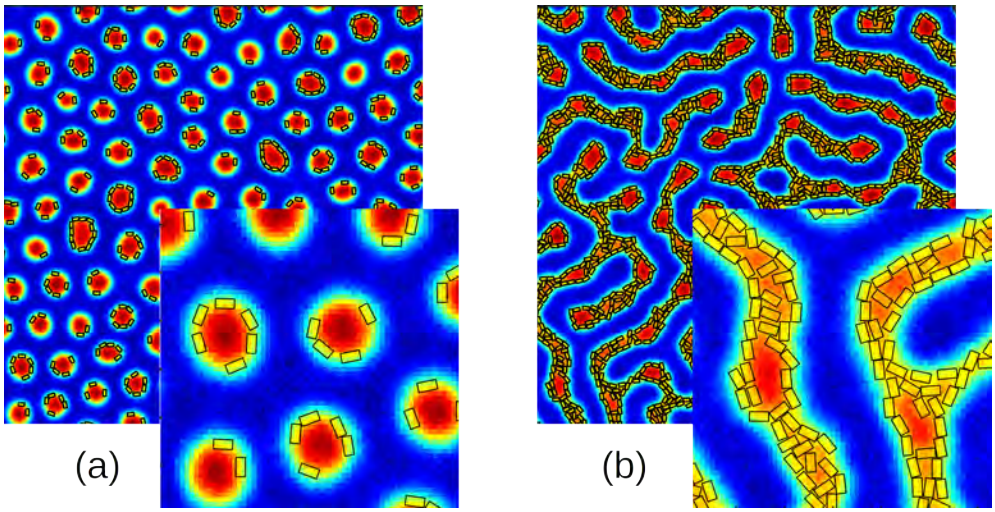

Figure 9.6: Morphological transition in an asymmetric block copolymer ($f_0 = 0.35$) induced by the presence of rectangular-shaped particles with size $a_0 = 2, b_0 = 1$ (grid point units). The particles have affinity $\psi_0 = 0$ (neutral) and the fraction of particles is $\phi_p = 0.05$ (a) , $\phi_p = 0.2$ (b).

chessboard-like arrangement of BCP domains can be noticed, which was not as clear in mixtures of circles/BCP in Fig. 5.9. This is clearly a consequence of the anisotropy of colloids, as can be noticed in the detail image in Figure 9.7 (b), where the rectangular particles tend to orient along interfaces which can enhance the formation of grid-like configuration of BCP.

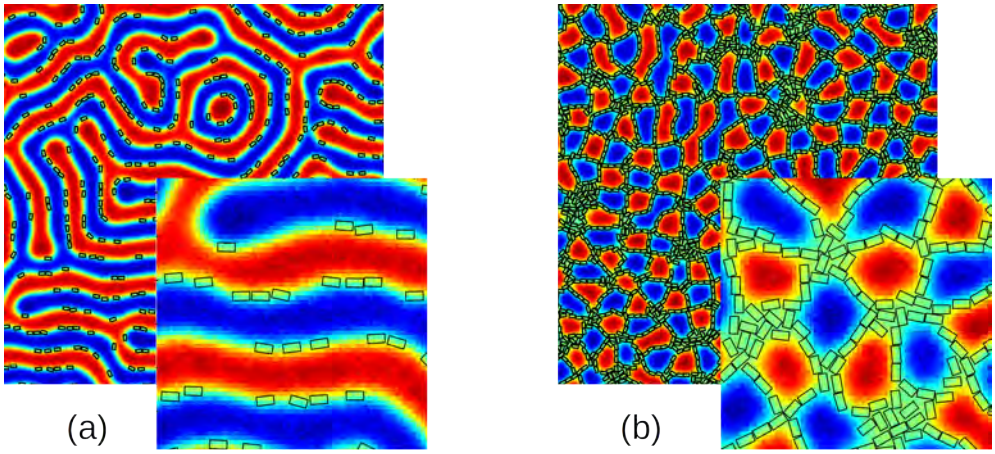

Figure 9.7: Morphological transition in a symmetric block copolymer ($f_0 = 0.5$) induced by the presence of rectangular-shaped particles with size $a_0 = 2, b_0 = 1$ (grid point units). The particles have affinity $\psi_0 = 0$ (neutral) and the fraction of particles is $\phi_p = 0.05$ (a) , $\phi_p = 0.25$ (b).

The anisotropy of neutral nanoparticles has been shown to result in alignment along the interface. The effect that the aspect ratio of rectangles have on the assembly of colloids and its effect on the overall co-assembly of the BCP composite system can be studied. In particular, we can consider a lamellar-forming BCP ($f_0 = 0.5$) mixed with a concentration ϕ_p of neutral nanoparticles with a larger semiaxis sized $a = 3$ and an aspect ratio $e = b/a$. At low concentration, we can expect NPs to be preferentially segregated towards the interface. Figure 9.8 shows that even at low concentration weakly anisotropic NPs ($e = 0.67$ and $e = 1.0$) display a radically distinct behaviour from strongly anisotropic NPs ($e = 0.33$). The latter are

mostly attached to the interface, leaving the BCP largely unmodified. This can be tracked by calculating the number of BCP domains in the system, which remains constant up to a high concentration value in which the interface is saturated and the lamellar domains are divided into shorter domains. Contrary to that, weakly anisotropic NPs are prone to form aggregates due to their comparatively lower trapping energy at the interface. For this reason we BCP morphology suffers a steady increase in the number of domains due to the break-up of domains following the formation of NP clusters.

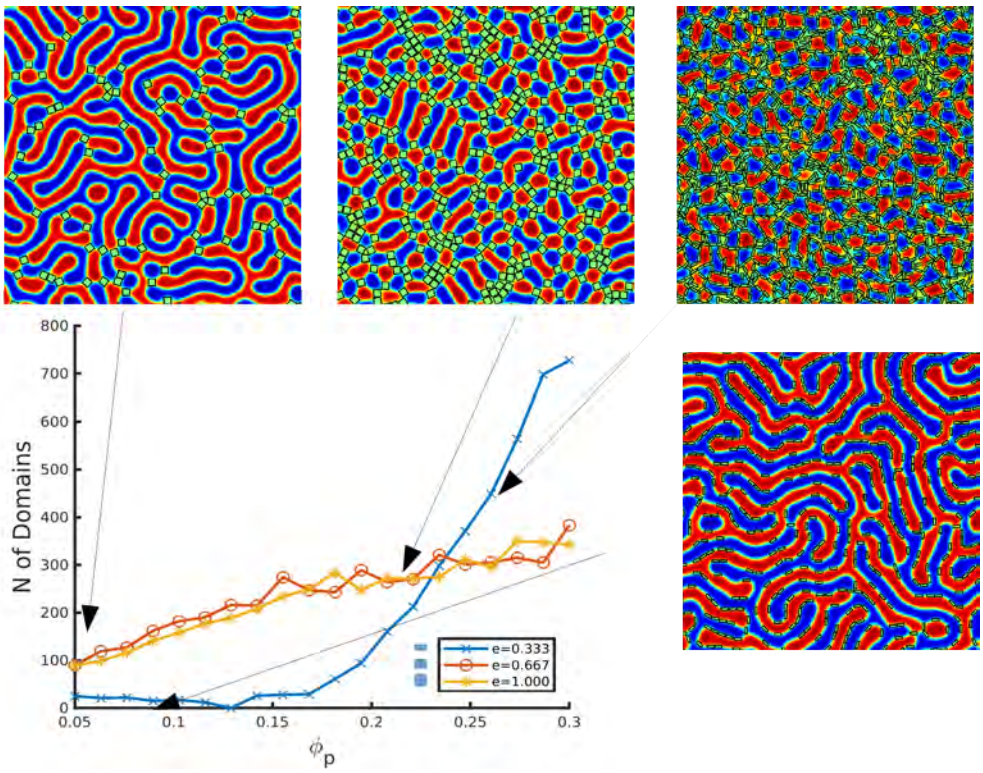

Figure 9.8: Number of BCP domains in terms of the fraction of particles in the system for several particle types. $b = 1, 2, 3$ represent 3 types of rectangular particles with $a = 3$ larger semiside and b being the shorter semiside.

9.4 Conclusions

A general model to simulate anisotropic nanoparticles immersed in block copolymer has been introduced. This flexible scheme can cover the family of curves known as super ellipses which include ellipsoids, rectangles and rhomboids. A colloid-colloid potential that is proportional to the overlapping area between two objects has been used. This analytical potential allows to calculate forces and torques and thus study the time evolution of anisotropic NPs. Due to the computational efficiency of the CDS/BD model, this hybrid method can be used to study the co-assembly of BCP/anisotropic nanoparticles, exploring a large parameter space.

The assembly of square-shaped in a minority phase of a BCP has been studied for different values of concentration and NP size, finding that the enthalpic interaction of the BCP coupling dominates over the assembly of colloids at large particle sizes, compared with the BCP period. At high concentrations colloids were able to organise into a side-to-side configuration thanks to the orientational-dependent NP-NP interaction. Similarly, minority-compatible rhomboid-shaped NPs where found to align along the domain axis when mixed with a lamellar-forming

BCP. This type of assembly is entirely different from the assembly of ellipsoidal NPs described in Chapter 8. This is originated both in the shape of NPs as well as the lack of an attractive NP-NP potential.

We have been able to compare experimental conditions by considering both rectangular NPs and rhomboid-shaped nanoparticles in order to mimic three-dimensional nanoplates. Using relative sizes from recent experiments [8], we have found alingment of anisotropic colloids within the lamella domains, reproducing experiments involving nanorods [131, 11].

Contrary to A-compatible NPs in a A/B BCP, we have studied the co-assembly of neutral, interface-compatible nanoparticles. We have found that neutral anisotropic NPs are preferentially aligned along the interface, which results in a saturation of the interface at high concentration. This behaviour is nonetheless dependent on the aspect ratio, as a consequence of the strong trapping that anisotropic particles undergo at the interface. Weakly anisotropic NPs, on the contrary, have shown a tendency to aggregate which results in a distortion of the lamellar morphology.

CHAPTER 10

Three Dimensional Study of Polymer Nanocomposites

Abstract

Block copolymers melts can self-assemble into a rich variety of morphologies in the bulk. This makes them perfect candidates to host and localise colloids within its phase separated domains. The morphological changes of block copolymers in the presence of a considerable filling fraction of colloids are studied, assessing the kinetic pathway towards a steady-state profile. Furthermore, colloids can be found to assemble into ordered hexagonally close-packed structures in a defined number of layers when softly confined within the phase-separated block copolymer. This behaviour is found to be non-monotonic with the concentration and strongly dependent on the periodicity-to-diameter ratio. A high concentration of interface-compatible nanoparticles leads to complex block copolymer morphologies depending on the polymeric composition. Macrophase separation between the colloids and the block copolymer can be induced if colloids are unsolvable within the matrix. This leads to the formation of ellipsoid-shaped polymer-rich domains elongated along the direction perpendicular to the interface between block copolymer domains

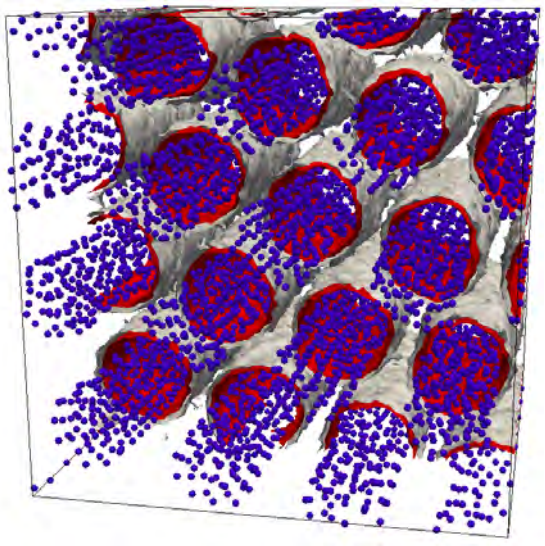

10.1 Introduction

Block Copolymers (BCP) are a fascinating class of materials due to their unique chain structure, made of several polymer subchains, joint covalently. This property translates into a rich phase behaviour in the bulk or in thin films. In particular, diblock copolymers have been found to self-assemble into a variety of periodic ordered structures such as lamellar, cylindrical or body-centered cubic spheres[23]. Colloidal particles sized a few nanoparticles are perfect candidates to be segregated within block copolymers, which, due to their periodic structure can lead to a highly organised nanocomposite material[139, 154].

Hybrid block copolymer/nanoparticle systems have been shown to co-assemble forming interesting collective behaviour that is both dependent on the polymeric properties and the number, size and chemical coating of the colloids[32, 2, 100]. Non-spherical nanoparticles such as nanorods [85, 127, 11] or nanoplates [8] can be found to posses a defined alignment within the block copolymer domains due to the competition between the several length scales that converge in a block copolymer nanocomposite. Many models have focused on the two-dimensional behaviour of such systems[65, 68], which is a physically reasonable approximation as many properties can be inferred from two (2D) to three dimensions (3D). Moreover, many experiments and simulations are devoted to the case of thin films[155, 156] and ultra-thin films[85, 157]. Nonetheless, the three-dimensional bulk assembly of block copolymers is considerably richer than the two-dimensional one. Similarly, the possibilities of colloidal assembly in 3D are less restricted, for instance, allowing the formation of two-dimensional layers with internal ordering.

The modification of the NP surface through, for example, grafted polymer chains, has led to a precise control of the localisation of colloids within the BCP phase-separated domain [1, 29, 30] or the interface between them [28, 94]. Since the presence of nanoparticles can induce a phase transition of the BCP, it is crucial to determine the overall morphology of the polymer nanocomposite system.

BCP/NP systems have been widely studied with theoretical and computational techniques. Strong segregation theory have been used to analytically study the viscoelastic properties of polymer nanocomposites [97, 51, 52] , finding a reduction of the lamella thickness when non-selective nanoparticles are present in the interface. A lamellar to bicontinuous transition was also reported, given by the vanishing of the bending modulus of the diblock copolymer, which is in accordance with experimental findings [31].

Simulation techniques such as Monte Carlo have been used [53, 54] to assess the assembly of BCP/NP systems on chemically nanopatterned substrates. In close resemblance with experiments, this method allowed to obtain well-ordered assembled nanoparticles. Furthermore, Huh et al[55] reported the changes in the diblock copolymer morphologies due to the presence of A-compatible nanoparticles in a diblock copolymer of arbitrary morphology (that is, exploring the composition ratio) using 3D simulations. This provided a phase diagram with only a few points. Molecular Dynamics [15] was used to study the phase behavior of BCP/NP systems for different Flory–Huggins parameter values using fixed symmetric diblock copolymers. It was also reported that nanoparticle localisation is increased with nanoparticle size, as was experimentally found by Bockstaller et al [32].

The aggregation of two kinds of nanoparticles within diblock copolymer was examined using Dissipative Particle Dynamics [56, 57, 58, 59], finding NP-assembly dependence on the lamella morphology, resulting in a transition to a complex phase. Self Consistent Field Theory (SCFT) [60, 61, 62, 9, 63] has been widely used to study the segregation of nanoparticles within the diblock copolymer domains, again reporting the size-selectivity of NP localisation found in

experiments[32]. While Lee et al[9] provided the phase diagrams of the diblock copolymer morphology in terms of the composition ratio and the affinity of the nanoparticle, the volume fraction of nanoparticles was not explored. The Cahn-Hillard equation [65, 66, 67] has been used to study the dynamical evolution of the phase separation, which is found to be slowed down by the presence of nanoparticles in the polymer blend. In these cases, a moderate volume fraction of nanoparticles that do not interact with each other is considered.

In this chapter we aim to make use of a computationally efficient simulation method to study the 3D co-assembly of block copolymers and nanoparticles. The subjects of this study are both the block copolymer morphological behaviour and the colloidal assembly. The relative speed of this computer program allows us to reach considerably large systems, along with a high number of particles. Thanks to this, we can explore a vast range of regimes, both when colloids are a mere additive and when the co-assembly of the system is driven by the dominating high concentration of colloids.

10.2 Model

The model that will be used in this chapter does not differ from the one presented in chapters 2 and 3.

10.3 Results

We aim to study the three dimensional phase behaviour of block copolymers in the presence of colloidal nanoparticles along with the assembly of colloids. Because a complete and rigorous description of all the phase space of such systems can be cumbersome, we will restrict to some particularly interesting instances in which 3D simulations can add interesting behaviours to the 2D description. We will refer to the 2D simulations and compare results in each case. In this chapter we use the standard parameters of CDS: $\tau_0 = 0.35$, $A = 1.5$, $u = 0.5$, $v = 1.5$. The size of the block copolymer period is controlled by $B = 0.002$. while the time and length discretisation are set to $\delta t = 0.1$ and $\delta x = 1.0$. Unless otherwise specified, simulations were performed in 64^3 box sizes.

10.3.1 NPs compatible with one copolymer

Phase transition induced by NPs

One of the most common instances of NP dispersion in BCP is the case of colloidal particles which are coated to be compatible with one of the blocks, for example, when coated with the same homopolymer A in a A-*b*-B diblock copolymer. Such particles have been found to segregate to their preferred domain, both experimentally[12] and in simulations[67]. Nonetheless, many works have shown that a considerable concentration of such particles can induce phase transition due to the swelling of hosting domains (in this case, A phase). A full phase diagram has been achieved using Monte Carlo[55] simulations and CDS in two dimensions [100]. In this section we will explore both the morphological transition as the number of particles is increased, as well as the time evolution starting from a disordered block copolymer.

Using particles with size $R_0 = 1.5$ and a symmetric block copolymer we begin by assigning a lamellar-like morphology at $t = 0$. We are utilising an initially-ordered block copolymer state, as opposed to starting from a random condition. Then, the system with a number of particles N_p is let to evolve for $N_{steps} = 1 \times 10^6$ time steps.

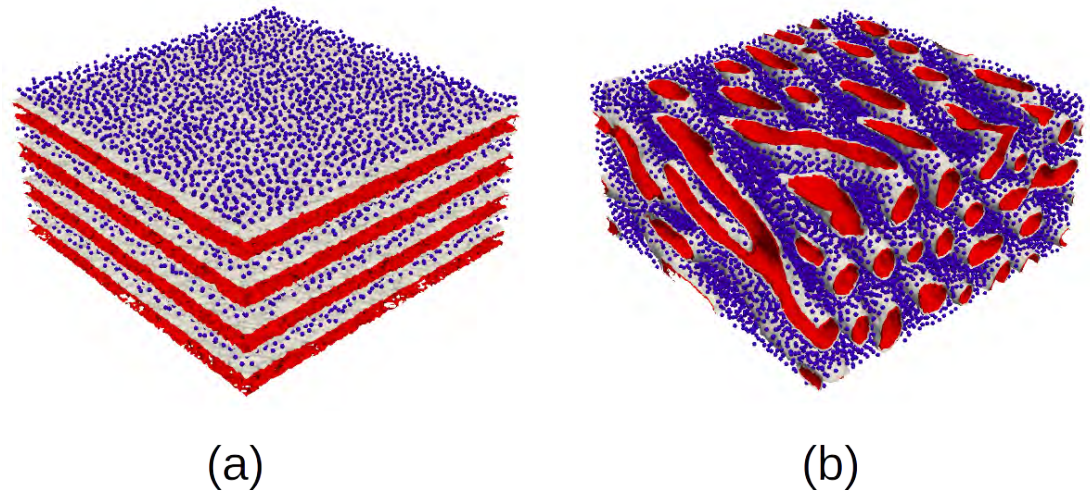

Figure 10.1: Transition in a symmetric diblock copolymer mixture ($f_0 = 1/2$) induced by the presence of a volume fraction of colloids ϕ_p. Nanoparticles are compatible with the grey phase. The block copolymer melt is initialised as a sinusoidal in the Z direction. Concentrations are $\phi_p = 0.15$ and $\phi_p = 0.47$ for (a) and (b), respectively. Simulation box is $128 \times 128 \times 64$ grid points. Colloids are shown as spheres in blue. The block copolymer is visualised through isosurfaces of $\psi(\mathbf{r})$ field, showing the A (red) and B (gray) domains.

At low concentrations of particles ϕ_p, colloids are simply located within their preferred domain, which in this case is a simple horizontal lamellar domain. This arrangement of colloids can be found in Figure 10.1, left. A larger number of particles results in a stronger confinement of colloids within their preferred phase, which eventually leads to a break-up of the lamellar structure into a cylindrical phase, as can be seen in Figure 10.1 (right) for a relatively high concentration of $\phi_p = 0.465$.

We can gain insight over both the dynamical evolution of such a transition, as well as the equilibrium transition for several values of the number of particles. Firstly, Figure 10.2 shows the number of block copolymer domains for different values of the colloidal concentration ϕ_p. A clear transition can be observed at $\phi_p^* \sim 0.35$ in which the number of BCP domains abruptly changes from a 8 domain (result of 4 periods with two domains each) to a very low number of domains, which hints of a bi-continuous morphology of well-connected domains. As the concentration of particles is again increased we observe how the block copolymer transitions again into cylindrically-shaped domains with hexagonal packing. The nanoparticles are effectively increasing the fraction of A monomers in the system, which is equivalent to exploring a horizontal deviation in the $f_0 - \chi N$ phase diagram for pure block copolymer melts[23].

Secondly, we can track the kinetic pathway to equilibrium following a quench from a disordered state, both for the block copolymer and the NPs. Figure 10.3 shows the Euler characteristic of the block copolymer in time, for the same parameters as Figure 10.2 and $\phi_p = 0.465$. The time evolution of χ is in fact equivalent of the reported one for a cylinder-forming pure BCP melt[158], thus confirming the role of nanoparticles as effectively increasing the hosting monomer fraction. In the inset of Figure 10.3 we can observe a late-stage behaviour $\chi \to 0$ from negative values of the Euler characteristic, which indicates the formation of isolated cylinders from a connected network of cylindrical domains. Bottom-right and right snapshots confirm this assertion.

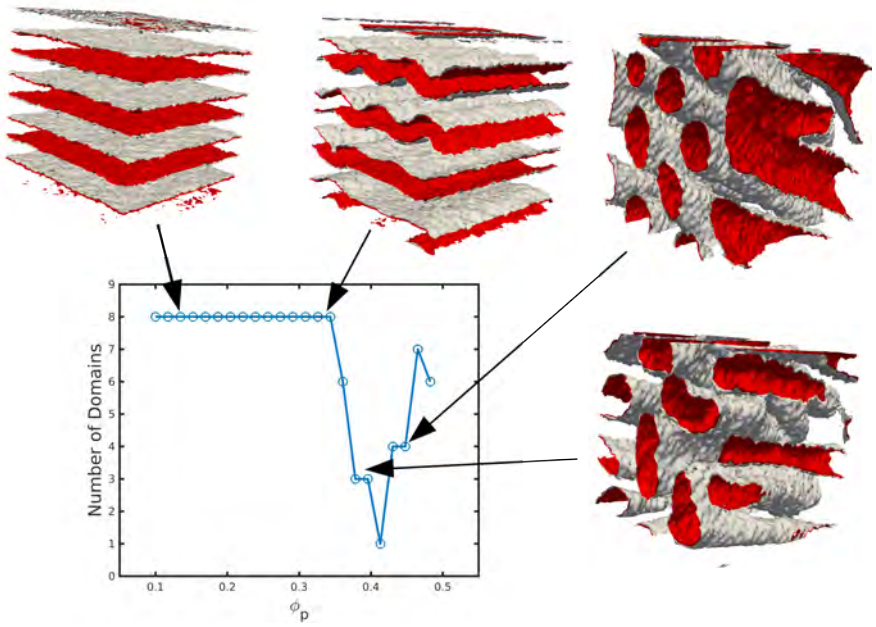

Figure 10.2: Number of domains of a symmetric ($f_0 = 1/2$) block copolymer as a function of the concentration of colloids ϕ_p. Snapshots of the final state of some representative simulations are shown, where the colloids are not shown for clarity.

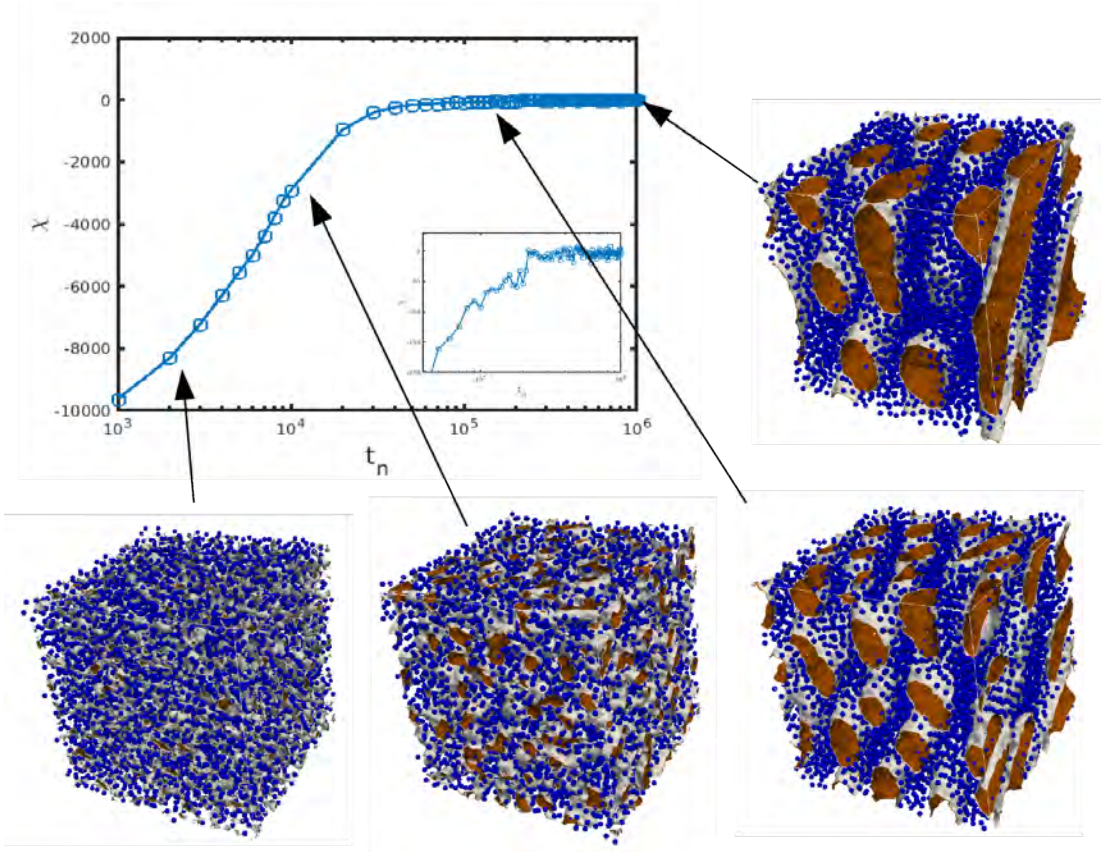

Figure 10.3: Time evolution of an initially-disordered symmetric BCP ($f_0 = 1/2$) mixed with a concentration $\phi_p = 0.465$ of colloids, tracked by the Euler characteristic χ. The inset shows a detail of the long-time curve while snapshots show specific simulation steps.

Assembly of colloids

In the previous section we have focused on the morphological behaviour of the block copolymer in the presence of colloids. Nonetheless, we can now assess how the confinement induced by

the phase-separating lamellar domains influences the configuration of colloids. Since the focus is on the colloidal assembly, we choose a value of $f_0 = 0.39$ such that phase transition from lamella to cylinders is prevented[100]. We consider an initially phase-separated block copolymer and initially disordered colloidal set of N_p particles with a radius R_0. Visualisation and analysis can be considerably easier using such initial condition. As an example, Figure 10.4 shows the soft confinement induced by three lamellar domains in the colloids. A layered organisation can be hinted in (a) while the hexagonal packing of the layers colloids within each layer can be observed in (b).

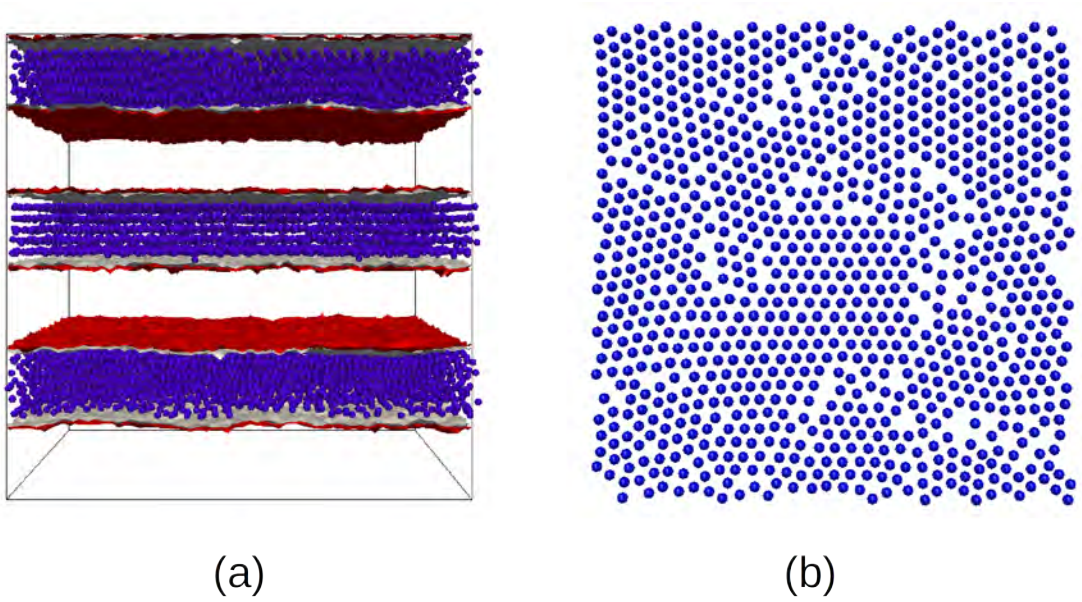

Figure 10.4: Example of colloidal ordering assembly in a soft confinement in the presence of block copolymer. In (a) the interface between A-B BCP is shown and a frontal view of the colloids is presented. In (b) we can observe a top view of a single layer of the hexagonal organisation of colloids where the block copolymer is not depicted for clarity.

A-compatible colloids in a lamellar-forming block copolymer are softly confined, as opposed to a hard confinement between parallel plates. In order to have an a priori estimation of the confinement effect, in Figure 10.5 we plot the reduced diameter of the particle $2R_{eff}/D_{eff}$ where R_{eff} is simply the soft-core radius of the particle(eg. the cut-off of the BCP-NP interaction), while $D_{eff} = H/2 - 2\xi$ serves as an estimate of the spacing available for the particle, where $H/2$ is half a lamellar period while 2ξ is the thickness of the interface.

In Figure 10.5 we can find the average number of first colloidal neighbours for each simulation in a color map (see colorbar in the right). In the X axis we explore the concentration of NPs while on the Y axis the particle size is tuned. Visual inspection of the simulation results confirms the assembly of colloids in different number of layers, growing with the concentration of particles present in the system. One can then conclude that an increasing number of particles forces a close-packed type of assembly with increasingly larger number of colloidal layers. Moreover, the relative size of particles and lamellar spacing dictates the rate of growth in the number of layers.

Detailed insight over the ordering of colloids within these layers can be obtained by using the 3D hexagonal close-packing (HCP) order parameter Q_6 which is 0.75 for a perfect HCP configuration[159]. Similarly, Q_4 characterizes the cubic structure. In Figure 10.5 points for which $Q_6 > 0.15$ are shown, that is, systems in which the ordering is above that of a disordered

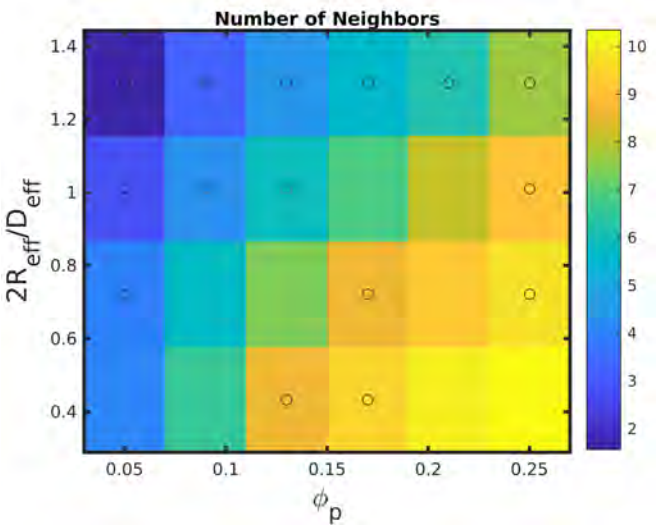

Figure 10.5: Color map of the average number of colloidal neighbors for each simulation of an asymmetric block copolymer mixed with minority-compatible nanoparticles. Circles represent simulation points such that $Q_6 > 0.15$.

liquid. At first sight, one could suspect that the behaviour of $Q_6(\phi_p)$ is non-monotonic, as for a fixed colloidal size it reaches higher values to then decreases.

In order to study the behaviour of Q_n and the assembly of colloids, we can focus on an specific particle size $R_0 = 2.33$ and calculate Q_n for a range of concentrations. In Figure 10.6 we can see the non-monotonic behaviour of both order parameters. At low concentration Q_6 approximately grows with ϕ_p while Q_4 remains constant. A considerable positive value of Q_6 indicates a degree of interparticle ordering, which is due to the particle size being large enough to induce an effective particle attraction. This is rather weak at low concentrations, but as the 2D monolayers are filled, a close-packing entropic interaction results in a broad peak in Q_6. The addition of higher number of particles, instead, does not produce increased ordering but destroys the monolayer structure. This results in a sharp decrease in Q_6 and Q_4 that is followed by a steady increase in Q_6, since a similar behaviour is occurring as in the case of a monolayer, only now we have close-packed hexagonal ordering in two layers of colloids. A sharp decrease is again followed by the formation of a three-layer with considerable colloidal ordering.

A similar behaviour can be found in a mixture of asymmetric($f_0 = 0.35$), cylinder-forming block copolymer and minority-compatible nanoparticles($\psi_0 = -1$). Figure 10.7 shows the BCP/NP co-assembly in cylinders at low concentration ($\phi_p = 0.12$, (a)) and large concentration ($\phi_p = 0.33$, (b)). While the cylindrical morphology is preserved in the BCP, the nanoparticles enhance the size of the cylinders without changing the number of domains. In fact, the nanoparticles are confined within the red, minority phase forming arrays of particles along the direction of the cylinders. Figure 10.7 (c) and (d) show the frontal view of such an arrangement corresponding to the top (a) and (b) snapshots. A radial assembly of colloids along the axis of the cylinders is equivalent to the layered configuration in Figure 10.4, in which we again observe an increased number of layers with higher concentration.

10.3.2 Interface-compatible NPs

Nanoparticles which are grafted with a mixed brush of homopolymer can be made compatible with the interface between block copolymer domains (neutral NPs)[31]. Experimentally, neutral

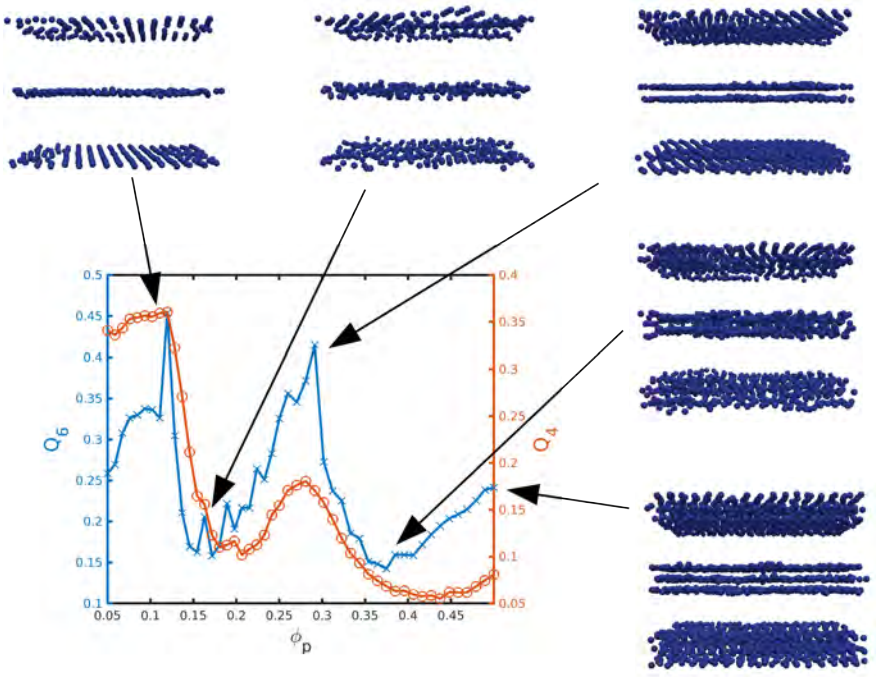

Figure 10.6: Q_6 (left axis, blue $\times$) and Q_4 (right axis, red $\circ$) order parameters of the colloidal assembly in terms of the fraction of particles in the system ϕ_p. Snapshots of the final configurations are shown with arrows indicating its respective simulation points in the Q_6 curve. Images of the block copolymer are missing in order to help the visualisation of the colloidal horizontal, in-domain, ordering.

nanoparticles have been found to segregate to the interface between block copolymer domains, as shown in chapter 5. At high concentration, a symmetric block copolymer can undergo lamellar-to-bicontinuous phase transition[94, 99].

We can study an initially-disordered BCP melt with a volume fraction ϕ_p of particles with a neutral affinity $\psi_0 = 0$. The nanoparticle size $R_0 = 1.5$ as well as the BCP length scales - $D = 0.503$ and $B = 0.02$- are chosen from Fig. 6.5 in Chapter 6. In Fig. 10.8 (a) we can observe the aggregation of NPs in a lamellar-forming BCP. The concentration of NPs is relatively low $\phi_p = 0.1$. This aggregation is driven by the minimisation of the total free energy by creating a NP-rich domain where the order parameter takes an almost zero $\psi \approx 0$ value. This is, in fact, a disordered area induced by the coating of the NP. In section 6.3.4 we have covered this type of aggregation both in the case of low and high concentration. Furthermore, in appendix B.3 we have provided additional support for the mechanism in which neutral NPs create a distortion in the free energy that is minimised by aggregation.

In Fig. 10.8 (b) a $\phi_p = 0.24$ concentration of NPs is shown. For this higher concentration the colloids are able to build an almost continuous network of NP-rich domains. Here, it is even more clear that the BCP and the NPs are macro-phase separating, forming two distinct domains. In Fig. 10.9 (a) we run a simulation in a small box $V = 32^3$ and $\phi_p = 0.27$ where the macrophase separation is clear. Additionally, the orientation of lamellar domains with respect to the NP-rich domain is clearly normal with a small tilted effect which can be due to the box size effect. In Fig. 10.8 (c) the concentration of NPs is high enough -$\phi_p = 0.45$- to create a single NP-rich matrix in which the BCP assembles into separated domains. The morphology of the BCP-rich domains (different from the A-rich or B-rich BCP domains themselves) can be directly related to the two dimensional counterparts as shown in Fig. 6.6: The isolated BCP-

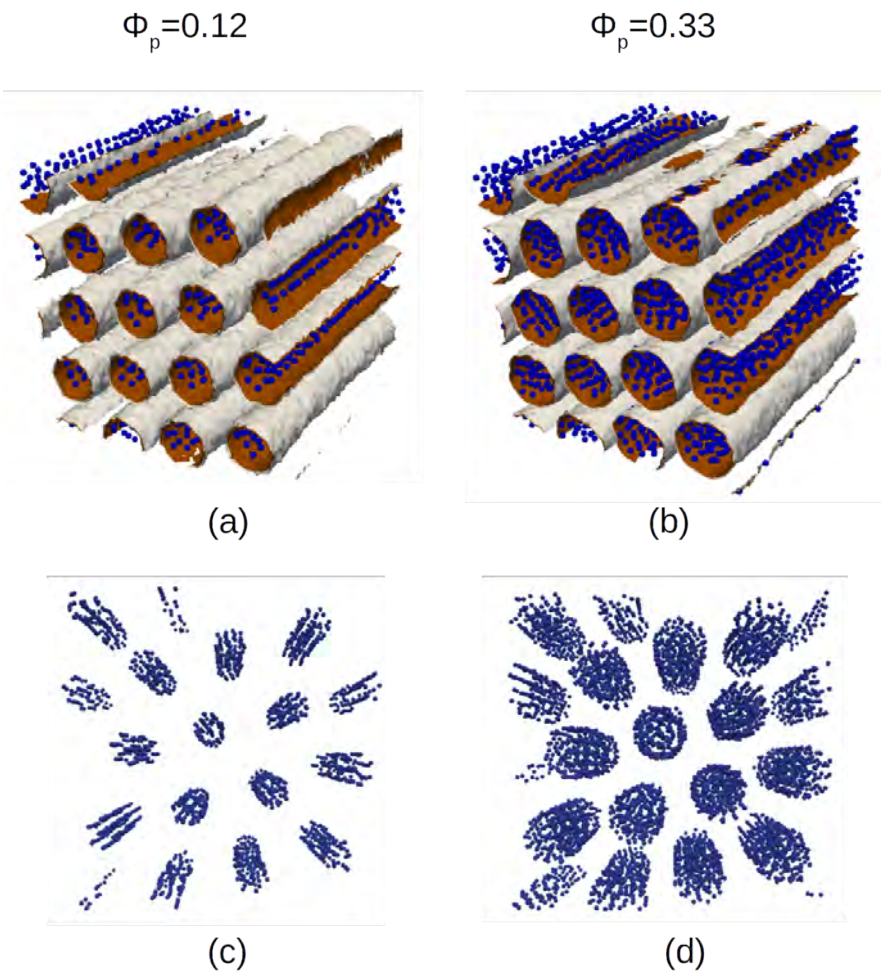

Figure 10.7: Mixture of cylinder-forming BCP ($f_0 = 0.35$) and minority compatible nanoparticles at two different concentrations (a) and (b). (c) and (d) correspond to the frontal view of (a) and (b), respectively, showing only the colloidal assembly.

rich domains take an ellipsoidal-like shape as the morphology of the neat BCP is lamellar. A detail of the simulation can be found in Fig. 10.9 (b), where the NPs are not shown in order to be able to clearly observe the polymer domain morphology. Therefore, the BCP chains privilege a layered structure alternating, parallel red and gray domains. On top of that, the contact angle between a wall and a BCP melt interface can be controlled by the chemical properties of the wall, which in this case are the affinity ψ_0 of the NP-rich matrix. This has been shown in Ref. [43] in the context of nanoshells. For these reasons, the BCP-rich domains minimises the free energy by maximising the contact surface between the alternating domains and the NP-rich matrix, and minimising the exposure of A-rich or B-rich only domains to the matrix. For these reasons, the BCP assembles into isolated, elongated domains which are growing in the direction normal to the interface between domains.

Through the same mechanism as described above, neutral NPs have been found to aggregate forming NP-rich areas in two dimensional simulations, as described in section 6.7. We can perform a long-time calculation up to $t_n = 10 \times 10^6$ CDS steps to obtain the morphology shown in Fig. 10.10. Here, we can observe a NP-rich area -coloured in transparent yellow- where all NPs are phase-separated from the microphase-separated BCP lamellar domains. In particular, due to periodic boundary conditions, we can identify a single NP-rich domain which has an elongated shape, in the direction of the lamellar interface. As in the case of 2D, this shape and orientation can be related to free energy minimisation. In particular, a lamellar-forming BCP near a neutral wall tries to orient its domains normal to the wall.

While the assembly of neutral nanoparticles at lamellar-forming has been experimentally studied , cylinder-forming (asymmetric) block copolymers/neutral nanoparticles have not been devoted experimental work. In Figure 10.11 we can observe the number of colloidal clusters in an asymmetrical ($f_0 = 0.35$), cylinder-forming BCP. At low concentrations colloids are found to simply be segregated within the interface of the cylinders. As the interface becomes saturated with nanoparticles, the colloids start to form bridges along neighbouring domains. Figure 10.12 (a) we can observe the segregation of nanoparticles at interfaces. If the concentration of particles is higher than $\phi_p^* \sim 0.213$, nanoparticles form a single percolating cluster. Visual inspection in Figure 10.12 (b), (c) and (d) can draw the conclusion that the block copolymer maintains a phase-separated microstructure even at high concentrations as in $\phi_p = 0.28$. This NP-induced morphology in the BCP can be related to that of a 2D asymmetric BCP mixed with neutral NPs, as in Figure 7 (a) in ref [100], where the majority-phase of the BCP forms a continuous, percolating lamellar-like domain, while the minority phase is enclosed by an NP-rich area which together with the minority BCP forms a lamellar-like percolating domain. Similarly, this bicontinuous BCP structure can be related to a lamellar-to-bicontinuous transition found in experiments [94].

10.3.3 Large nanoparticles

As an example on the ability of the presented model to scale up to considerably large systems, we can explore the regime in which the NP size is considerably larger than the BCP period. To this end we select parameters $R_0 = 8.5$ and $B = 0.02$ for $N_p = 100$ nanoparticles which have an affinity $\psi_0 = -1$ in a cylinder-forming BCP $f_0 = 0.4$. The system size is $V = 400^2 \times 300$ with $n_p = 4 \times 4 \times 3$ processors. In Fig. 10.13 (a) the cylinder-forming morphology of the BCP can be observed, along with NPs which create a local perturbation in the nearby BCP. A detail of the BCP assembly near a large NP can be observed in (b), where we can find a spherical shell of the compatible block to the NP, followed by a secondary shell made of the minority

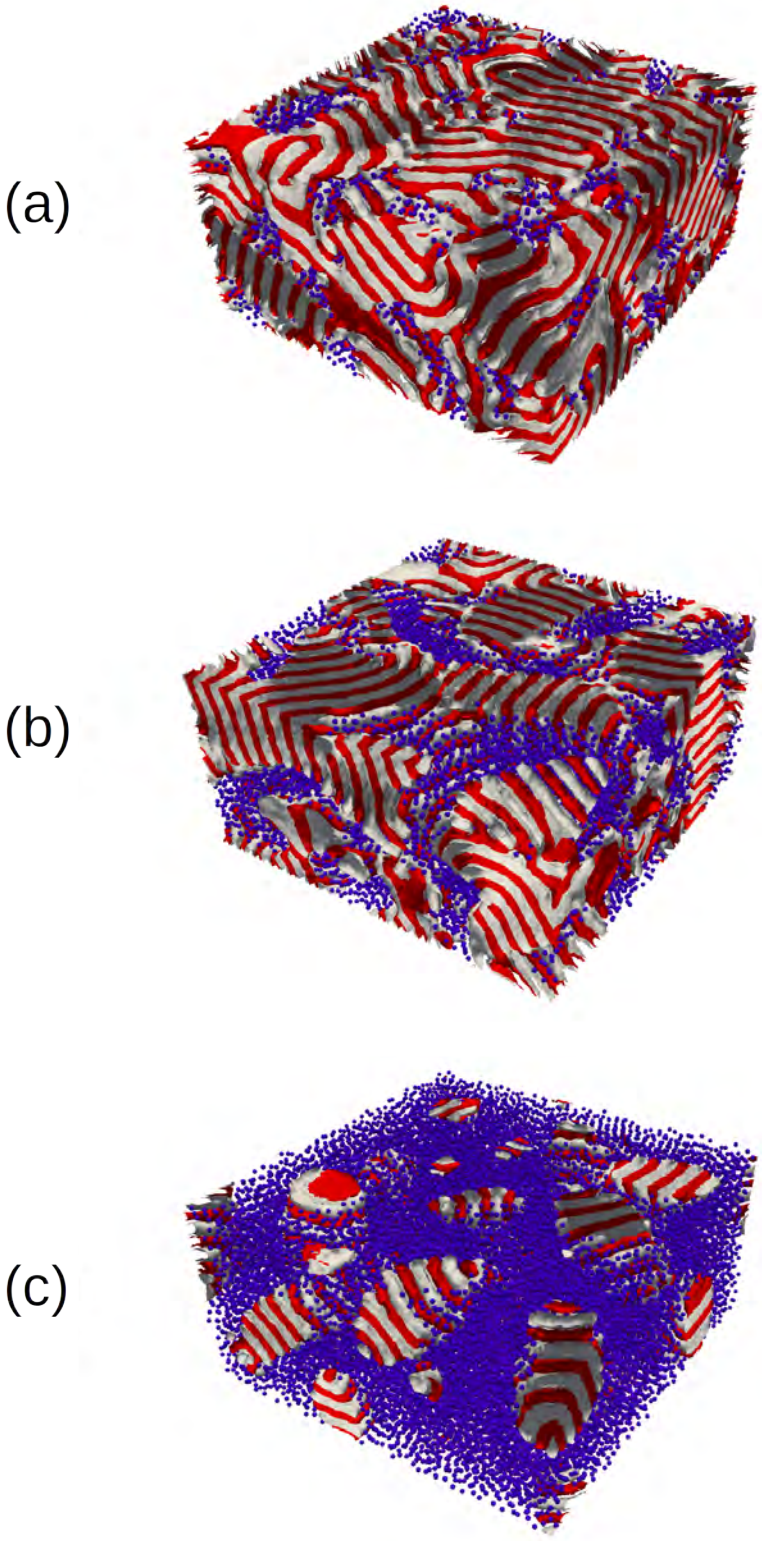

Figure 10.8: Phase transition of a symmetric ($f_0 = 0.5$) BCP induced by the presence of a concentration ϕ_p of neutral nanoparticles. The concentrations of NPs are $\phi_p = 0.1$, 0.24 and 0.45 for (a), (b) and (c), respectively. System size is $V = 128^2 \times 64$ using 8 processors.

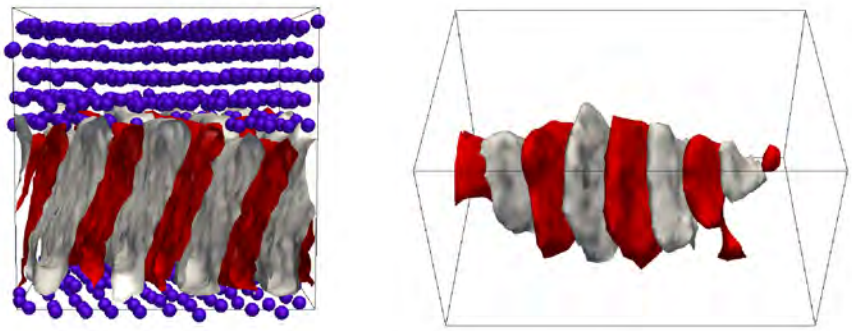

Figure 10.9: In (a) a simulation in a small box $V = 32^3$ with a concentration $\phi_p = 0.27$ and the same parameters as in Fig. 10.8. In (b) we show a detail of Fig. 10.8 (c) without showing nanoparticles.

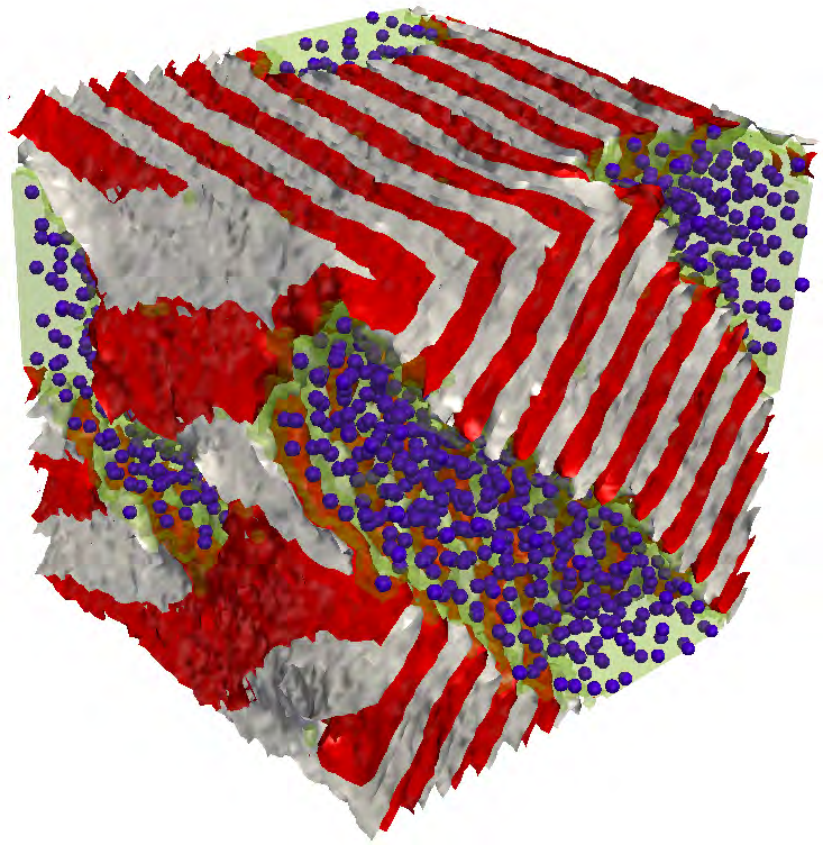

Figure 10.10: Simulation of a low concentration $\phi_p = 0.1$ of neutral NPs sized $R_0 = 1.7$ in a symmetric $B = 0.02$ BCP. NP-rich area -given by $-0.2 < \psi < 0.2$- is coloured transparent yellow.

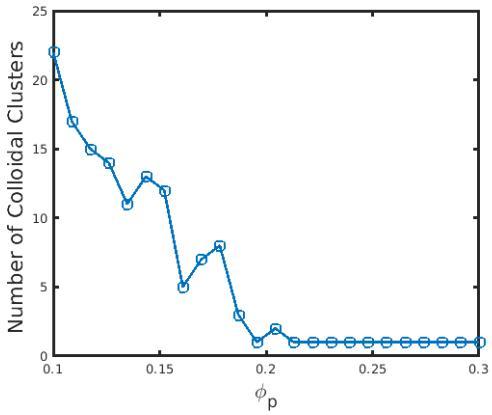

Figure 10.11: Number of colloidal clusters formed by neutral colloids in a cylinder forming block copolymer mixture as a function of the concentration of particles.

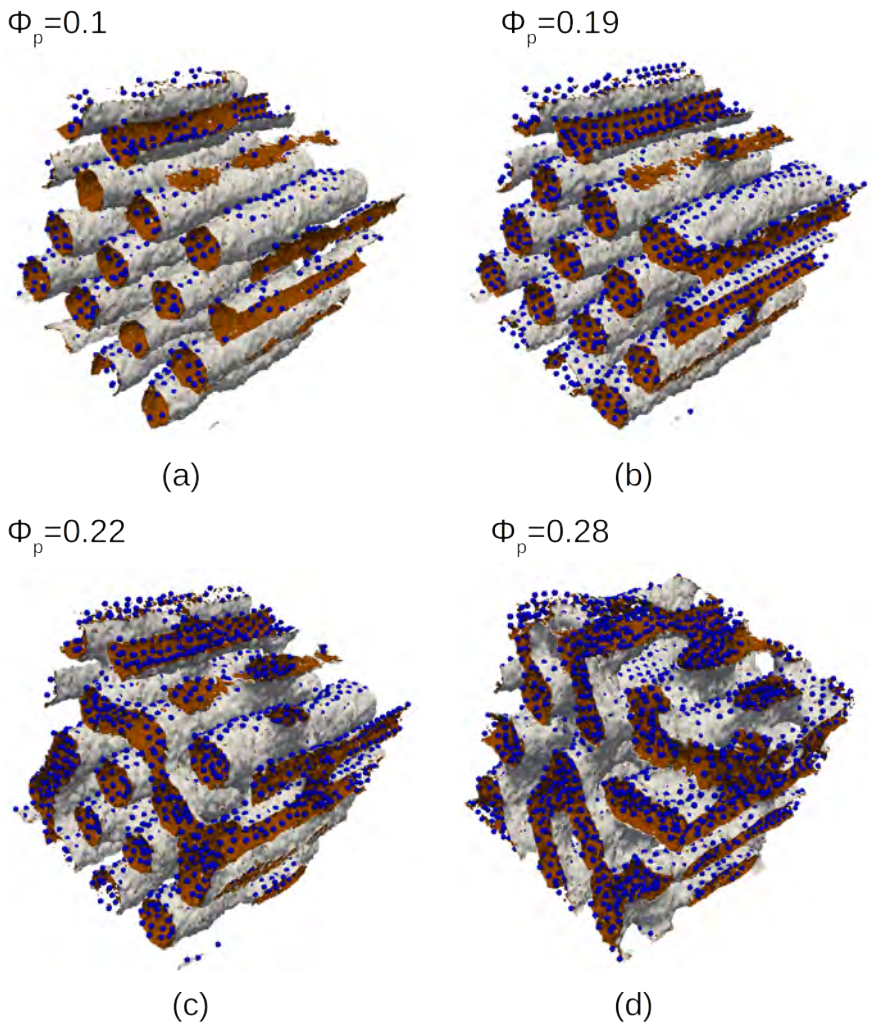

Figure 10.12: Snapshots of simulation results of neutral nanoparticles in a cylinder-forming block copolymer matrix corresponding to the curve in Figure 10.11. Nanoparticles are segregated to the interface between red and grey domains.

copolymer forming cylinders. This behaviour can be directly related to BCP nanoshells, as in Fig. 2 (f) in Reference [43].

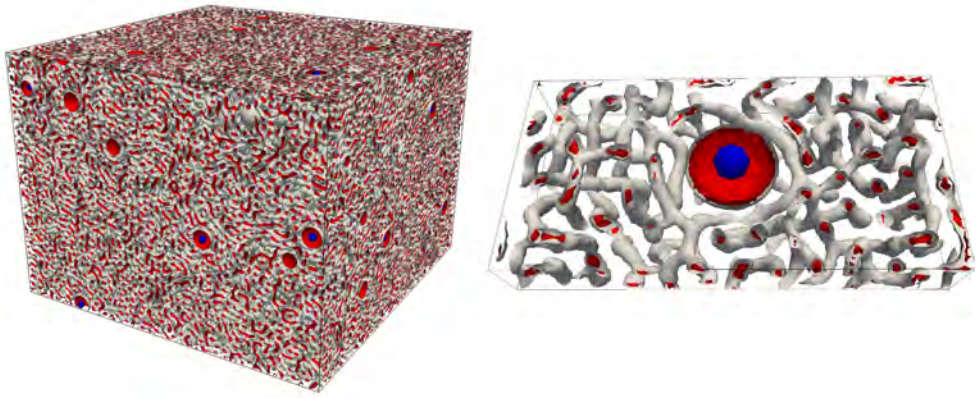

(a) (b)

Figure 10.13: Co-assembly of large NPs $R_0 = 8.5$ compatible with the minority block in a asymmetric $f_0 = 0.4$ BCP. System size is $V = 400^2 \times 300$ and 48 processors were used.

10.4 Conclusions

Three dimensional simulations of block copolymer/nanoparticle mixtures have been used to analyse the morphological changes induced by colloids in a block copolymer melt, as well as the assembly of colloids within the phase-separated block copolymer. The comparatively fast computational model has allowed us to achieve a vast range of number of particles, in turn making it possible to study the high concentration regime of particles.

The order-to-order phase transition due to the presence of A-compatible nanoparticles in a symmetric, lamellar-forming BCP has been studied in detail in terms of the particle loading. It has been shown that the lamellar-to-cylinder transition evolves through a bicontinuous intermediate state that concludes in the well-defined cylindrical morphology. The time evolution towards this final structure can be tracked with the Euler characteristic, finding intermediate stages of connected networks of elongated domains.

The assembly of colloids in the block copolymer has been studied both in the case of block-A compatible and interface-compatible colloids. In the first case, we have studied the soft-confinement case in which the NP's ability to diffuse is strongly influenced by the lamellar phase separation. In fact, a layered, hexagonally close-packed assembly of colloids can be found which is driven by the relative length scales between the nanoparticle size and the lamellar spacing. Colloid are found to organize in crystal-like structures forming layers due to the confinement exerted by the BCP. This behaviour is non-monotonic with the number of layers dictated by the NP concentration and intermediate disordered colloidal states between defined layers.

Neutral, interface-compatible nanoparticles have been found to segregate to the surface between A-*b*-B domains. A high concentration of nanoparticles at the interface tends to form NP-rich areas, which in the case of a symmetric lamellar-forming BCP results in macrophase separation of the BCP and NPs. At high concentration NPs tend to form bridges along cylindrical domains, eventually forming a continuous network of nanoparticles. These complex morphologies are due to the presence of colloids and cannot be related to pure BCP phases

(differently from lamellar to cylinders phase transitions). Comparisons can be drawn between the morphologies described in Fig. 10.8 and computer simulations of ternary blends made of BCP/homopolymer as described by Ref. [101]. This serves as a way to validate our description as it can cover regimes ranging from low concentration, almost passive NPs up to the high concentration regime, in which the NP are the dominant phase and BCP assembles forming independent domains. It should also be noted that our colloidal description is individual, while Ref. [101] made use of a continuous model comprising two order parameters in a Cahn-Hilliard description.

In conclusion, we have shown the variety of structures that can be achieved through the co-assembly of colloids and block copolymers. The enthalpic interaction between colloids and the block copolymer melt, along with the entropic constrains arising from the relative lengthscales of the system have resulted in several instances of colloidal ordering and morphological phase transitions in the block copolymer. The ability to explore vast regimes in terms of concentration of particles justifies the use of a hybrid BCP/NP model.

CHAPTER 11

Conclusions to the Thesis

In this work, a systematic study of systems comprising block copolymers and nanoparticles has been performed. The morphological properties of block copolymers in the presence of nanoparticles have been assessed, along with the assembly of colloids within block copolymers. Altogether, we have described a complex case of co-assembly between an ordered matrix (BCP) with a periodic structure and additives which greatly modify the hosting phase, leading to phase transitions and the appearance of new phases.

The model presented by Pinna et al [68] has been largely used to reproduce experiments and simulations, as well as predicting new behaviours. Cell Dynamic simulations has proved to be an efficient simulation method that can be validated against other computational methods, as demonstrated in Chapter 4. The presented hybrid CDS/Brownian Dynamic scheme has been shown to provide a flexible framework in which colloidal properties can be easily tuned, as shown for NP shape and chemical inhomogeneities.

The presence of NPs in the BCP has been shown to modify the morphology of the neat block copolymer, depending, on first approximation, on the concentration of NPs and the chemical properties of colloids. The coating of NPs dictate their localisation within the phase-separated BCP, while at high NP concentration, colloids can behave as an additional matrix inducing macro-phase separation, when NPs are considerably insolvable with the BCP melt. When NPs are easily solvable within one of the domains of the BCP, phase transitions are induced, which have been delimited in phase diagrams for arbitrary BCP compositions.

Mixtures of BCP melts and anisotropic NPs have been shown to form highly ordered configurations, reproducing experimental results using nanorods. A side-to-side configuration of ellipsoidal NPs segregated within one of the BCP domains and normal to it has been found. The conditions for its formation has been studied, finding limiting regimes where the co-assembly is hierarchical and the BCP morphology In experiments, anisotropic NPs have been shown to tilt relative to the domain axis in order to accommodate such particles. The model has also been used to reproduce results involving long nanorods relative to the lamellar spacing, leading to NP orientation along the domain axis. Moreover, the co-assembly of block copolymer and anisotropic particles of additional shapes (rectangles, squares, rhomboids) has been studied. Using a purely repulsive potential anisotropic NPs have been found to assemble into well-ordered configurations within one of the BCP domains, as well as leading to interesting new phases when segregated within the interface.

Janus particles have been studied as a simple example of an spherical particle with an orientational degree of freedom given by its anisotropic chemical properties. It has been shown that the Janus nanoparticles can display a complex variety of behaviours when mixed with block copolymers. Mainly, we have shown that Janus nanoparticles are generally more strongly trapped at interfaces between phases. Furthermore, the particular (directional and strong) type of anchoring at interfaces results in a lack of bridging along domains, as compared to neutral particles(which are also trapped at interfaces). We can conclude that Janus nanoparticles are better options to homogeneously disperse nanoparticles at interfaces, without destructing the hosting BCP structure. Furthermore, we have shown that the two-face nature of the JNP can result in complex assembled structured, such as lamellar-like configuration that is described in Chapter 7.

Motivated to reproduce experimental results, we have modelled systems comprising non-spherical particles. The implementation of the equation of motion, along with the coupling with the surrounding block copolymers have resulted in new computer programs which are more complex in the description of the behaviour if nanocomposite structures than was observed in previous models. Moreover, we have extended the existing code into three dimensional

simulations. All of these have resulted in new available models and programs that can help us study nanocomposite systems. Furthermore, great effort has been made produce efficient computer programs. This is essential in order to capture the physical behaviour of processes occurring in the large length scale or long time scales (or both). For instance, the aggregation of large particles in Chapters 6 and 10. For that purpose profiling has been used to identify the bottlenecks of the code and effort has been done to write most efficient possible programs.

As a general conclusion, this thesis has attempted to cover the physical behaviour of block copolymer nanocomposite systems using hybrid phase-field computational tools. A systematic study has been performed, which we believe can improve our understanding of such fascinating materials in the mesoscale. Interesting new morphologies have been found in the assembly of BCP due to the presence of colloids, while colloidal nanoparticles have been shown to organise in well-ordered configurations, due to their shape, size, chemical properties or simply due to a collective behaviour in which both nanoparticles and the block copolymer participates. Indeed, the relevance of the co-assembly of the nanocomposite system has been showed. We have validated our computational model against both previous simulations and experimental work. Furthermore, the present model has been used to gain insight over experimental findings which could be difficult to achieve in a lab (time tracking of magnitudes, systematic exploration of parameter space, etc). We believe our (although simple) model can be extremely helpful in collaboration with more microscopic approaches to complete a physical description over a wide range of length scales.

11.1 Future work

In this work we have tried to perform a systematic study of the most relevant properties and mechanism in play. Nonetheless, it is natural that many questions emerge as new simulations are produced and not all of them could be completed. For instance, the ability to produce a parallel code has open the door to achieve a more complete study of three-dimensional systems.

In fact, as mentioned in Chapter 3, it was not until the late stages of the PhD research that we developed the parallel code. This has open up new questions as now large system sizes are available at reasonable computational times. On a more technical note, many aspects of the parallel code could still be polished. A more sophisticated output saving algorithm, for example, could reduce the memory and saving time. A combination of Verlet List and Cell List algorithm could reduce even more the computational time for high number of NPs. In fact, in the low number of particles regime, a Cell List is not particularly efficient and limits the particle size. A separate code could deal with few, very large particles and produce results in the regime in which NPs are much larger than the BCP period.

Of course, the non-spherical, non-uniform properties of NPs shown in Chapters 8, 9 and 7 can be extended to three dimensions. We believe many of the results that have been shown in this work are largely valid and could be easily extrapolated into 3D. Nonetheless, a certain degree of complexity is missed, for instance, when considering complex BCP morphologies or complex assemblies. In any case, most of the model could be easily extended into three dimensions with minimal modification.

In Chapter 9 we have presented a considerably general model to describe a large family of colloidal shapes. To this end we have used a very simple non-overlapping potential. A more sophisticated approach could provide more realistic results and, furthermore, could help us consider a generalised model that can account for all colloidal shapes available.

In this work, we have focused on self-assembly in the bulk, considering periodic boundary

conditions at all times. Nonetheless, block copolymers can exhibit interesting properties also under confinement in thin films [155]. Our three-dimensional parallel code can be trivially extended to account for such a setup.

APPENDIX A

Dynamic equations

A.1 Dimensionless Cahn-Hilliard equation in the absence of colloids

We can write the Cahn-Hilliard equation (see Model Chapter for a complete derivation), in the absence of any nanoparticle present in the system. For simplicity, we can write the case of a symmetric, lamella-forming BCP melt ($f_0 = 1/2$)

$$\frac{\partial \psi}{\partial t} = M\left[\nabla^2\left(-\tau\psi + u\psi^3 - D\nabla^2\psi\right) - B\psi\right] \tag{A.1}$$

we can write time, length and BCP order parameter ψ in terms of dimensional magnitudes in order to obtain dimensionless equations. For that purpose, we can make the following changes,

$$\mathbf{r} \to L\mathbf{r}' \tag{A.2a}$$

$$t \to T_{pol}t' \tag{A.2b}$$

$$\psi \to \psi_{eq} = \sqrt{\tau/u} \tag{A.2c}$$

where ψ_{eq} is the (positive) minimum of the local free energy $H(\psi)$. Here we are assuming the local free energy per unit volume $H(\psi)$ possess two minima values ψ_+ and ψ_-. After this substitution we can obtain the following expression

$$\frac{\partial \psi'}{\partial t'} = \frac{T_{pol}M\tau}{L^2}\left[\nabla'^2\left(-\psi' + \psi'^3 - \frac{D}{\tau L^2}\nabla'^2\psi'\right) - \frac{BL^2}{\tau}\psi'\right] \tag{A.3}$$

we can choose length and time scales as

$$L = \sqrt{D/\tau} \tag{A.4a}$$

$$T_{pol} = \frac{L^2}{M\tau} \tag{A.4b}$$

this leads to a reduced equation

$$\frac{\partial \psi'}{\partial t'} = \nabla'^2\left(-\psi' + \psi'^3 - \nabla'^2\psi'\right) - \frac{BL^2}{\tau}\psi' \tag{A.5}$$

from which we can identify a second length scale H such that the last prefix can be written as a length ratio

$$\frac{BL^2}{\tau} = \left(\frac{L}{H}\right)^2 \to H = \sqrt{\frac{\tau}{B}} \tag{A.6}$$

we can define the interfacial-to-periodicity size ratio as

$$\chi_H = \frac{L}{H} = \frac{\sqrt{D/B}}{\tau} \tag{A.7}$$

Finally, a dimensionless Cahn-Hilliard equation is found to be

$$\frac{\partial \psi'}{\partial t'} = \nabla'^2\left(-\psi' + \psi'^3 - \nabla'^2\psi'\right) - \left(\chi_H\right)^2\psi' \tag{A.8}$$

It is widely known that the equilibrium profile of a binary mixture in the Cahn-Hilliard model satisfies $\psi(x) \propto \tanh\left(\frac{x}{2\xi}\right)$ with $\xi = \sqrt{D/\tau}$. Therefore, we can identify the length scale L with the microphase separation in a binary mixture. Therefore, the time scale given by

$T_{pol} = L^2/(M\tau)$ can be related to the microphase separation process. In a longer, slower time scale the diblock copolymer domains grow, up until a large length scale H is reached.

A.2 Dimensionless equations of a BCP/Nanoparticle mixture

In the case that colloids are present we need to introduce the coupling term of the free energy. We end up having the following non-dimensional equation

$$\frac{\partial \psi'}{\partial t'} = \nabla'^2 \left[-\psi' + \psi'^3 - \nabla'^2\psi' + 2\bar{\sigma}\psi_c(\mathbf{r})\left(\psi' - \bar{\psi}_0\right)\right] - \left(\frac{L}{H}\right)^2 \psi' \tag{A.9}$$

where $\bar{\sigma} = \sigma/\tau$ and $\bar{\psi}_0 = \psi/\psi_{eq}$ is the value of the affinity after scaling with the equilibrium value of ψ. We can use σ/τ as a parameter to set the importance of the coupling and set the particular regime in a simulation. In this document the $\tau_0 = 0.35$ value is taken, as it is standard in the literature. A unit value of σ leads to a reduced value $\bar{\sigma} \approx 2.9$.

Now, let's write the Brownian Dynamics equation that dictates the time evolution of a nanoparticle immersed in a fluid

$$\frac{d\mathbf{R}}{dt} = \frac{\mathbf{f}}{\gamma} + \sqrt{\frac{2k_BT}{\gamma}}\xi \tag{A.10}$$

let's assume that the force has a generic scaling as $\mathbf{f} = \mathbf{f}'U_0/R$ where we are setting up the energetic and length scale of the interaction. To be consistent with the dimensionless choice we did for the Cahn-Hilliard equation, let's use T_{pol} and L as our time and length scales to reduce $\mathbf{R}$ and t. We obtain that

$$\frac{d\mathbf{R}'}{dt'} = \frac{U_0}{R}\frac{1}{\gamma}\frac{T_{pol}}{L} + \frac{T_{pol}}{L}\sqrt{\frac{2K_BT}{\gamma}}\xi T_{pol}^{-1/2} \tag{A.11}$$

where we have to note that ξ has dimensions, as given by the Fluctuation-Dissipation theorem. The diffusive time scale of the colloid is given by $T_{col} = R^2/D$ with the diffusion $D = K_BT/\gamma$. Therefore, we can express the random part of the colloidal force as

$$\frac{R}{L}\sqrt{2\frac{T_{pol}}{T_{col}}} \tag{A.12}$$

while the non-stochastic (BCP-NP coupling, external or NP-NP pairwise interaction) is

$$\frac{U_0}{\tau}\frac{L}{R}\frac{M_{NP}}{M} \tag{A.13}$$

where $M_{NP} = 1/\gamma$ is the mobility of the particle.

We can also define a non-dimensional parameter that controls the energetic ratio between the coupling free energy and colloid-colloid potential. In the simplest case the colloid-colloid interaction is characterised by a single energetic parameter U_0 which can be the Lennard-Jones pre-factor or the Yukawa potential pre-factor. Then,

$$\epsilon^*_{cpl} = \frac{\sigma R^2_{eff}\psi^2_{eq}}{U_0} \tag{A.14}$$

APPENDIX B

Approximations to the effect of nanoparticles in the block copolymer

B.1 Introduction

Throughout this document the effect of NPs in the BCP is a key element that determines the co-assembly of the system. Often times the single-particle behaviour serves as a good approximation to the collective dynamics of a large number of colloids. For this reason, it is useful to explore some analytical or semi analytical effects that a single NP can create in the BCP.

It is beyond the scope of this work to perform a complete analytical study of the analytical aspects of BCP/NP systems in the context of Cahn-Hilliard equation coupling with Brownian Dynamics. Nonetheless, in this appendix we study some relevant cases in which the analysis of the dynamics equations and equilibrium properties can provide insight over the simulations, often helping to set the appropriate regimes to consider in simulations.

B.2 B'-compatible NPs

Diblock copolymer nanocomposite systems have been modelled using a hybrid method involving a continuous description of the block copolymer via an Ohta-Kawasaki free energy and a Brownian dynamics scheme for the colloids. In particular, simulations regarding incompatible particles have reproduced experiments in which nanoparticles formed hexagonally ordered clusters within the least incompratible copolymer phase. A method to estimate the distortion created by nanoparticles is presented and the effective interaction between colloids via the surrounding block copolymer is approximated.

B.2.1 Minimisation of the free energy

A diblock copolymer/nanoparticle (BCP/NP) mixture has been characterised by a simple free energy consisting on the standard Ohta-Kawasaki free energy, an intercolloidal potential energy and a coupling term that can be understood as the harmonic approximation of a more realistic NP-BCP interaction.

Locally, the phase separation of a symmetric diblock copolymer can be modelled with an order parameter

$$\psi(\mathbf{r},t) = \phi_A(\mathbf{r},t) - \phi_B(\mathbf{r},t) \tag{B.1}$$

and the local free energy describing a binary mixture can be expressed as

$$F_{local} = \int d\mathbf{r}\ H(\psi);\ H(\psi) = -\frac{1}{2}\tau\psi^2 + \frac{1}{4}u\psi^4 \tag{B.2}$$

which is minimised with $\psi = \psi^*$ taking values $\pm\sqrt{\tau/u}$. Hereafter we consider the nondimensional form in which $\psi^* = \pm 1$

Adding a colloidal nanoparticle, we model the total free energy as

$$F_{tot} = F_{sr} + F_{int} + F_{lr} + F_{cpl} \tag{B.3a}$$

$$F_{sr} = \int d\mathbf{r} \left(-\frac{1}{2}\psi^2 + \frac{1}{4}\psi^4\right) \tag{B.3b}$$

$$F_{int} = \frac{1}{2}D \int d\mathbf{r}\,(\nabla\psi)^2 \tag{B.3c}$$

$$F_{lr} = \frac{1}{2}B \int d\mathbf{r}_1 \int d\mathbf{r}_2 \psi(\mathbf{r}_1)\psi(\mathbf{r}_2)G(\mathbf{r}_1,\mathbf{r}_2) \tag{B.3d}$$

$$F_{cpl} = \sigma \int d\mathbf{r}\psi_c(r/R)\left[\psi(\mathbf{r}) - \psi_0\right]^2 \tag{B.3e}$$

where F_{lr} is the long-ranged term of the free energy, that accounts for the connectivity of the copolymers. F_{int} is the interface free energy and introduces a penalty on gradients of the local order parameter. We can neglect the intercolloidal free energy F_{cc} in order to study the distortion created by one nanoparticle in a diblock copolymer. Furthermore, we also consider that the size of our particle R is much smaller than the diblock copolymer periodicity. Therefore, the introduction of a nanoparticle is not expected to affect the long-ranged free energy of the system. Finally, we are reduced with a simplified free energy, which is equivalent of a single nanoparticle in a homopolymer/homopolymer binary mixture,

$$F_{tot} = F_{sr} + F_{int} + F_{cpl} \tag{B.4}$$

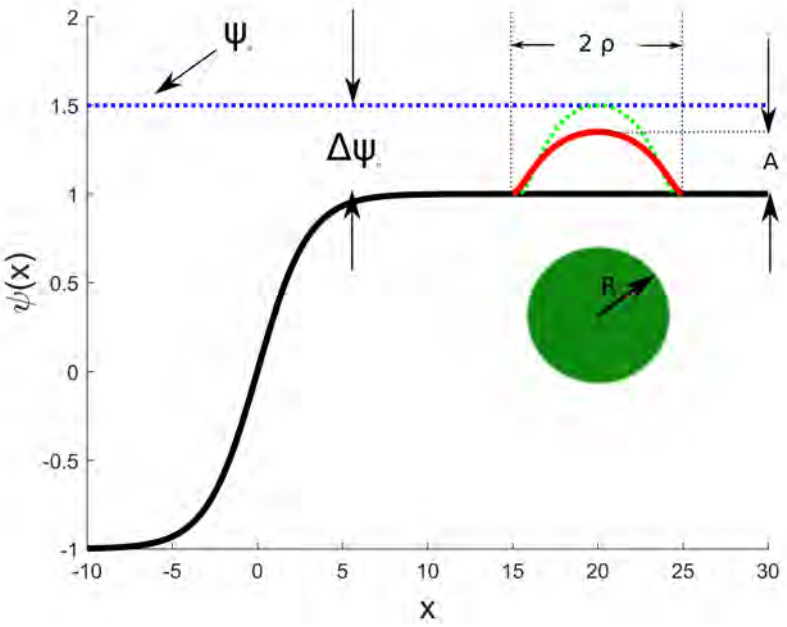

Figure B.1: The profile of an unperturbed order parameter $\psi(x)$ near an interfaced (solid black line) and a distortion created by the presence of one nanoparticle sized R. This distortion has an amplitude A and an extension 2ρ.

We assume that in the bulk (far away from the interface) the order parameter takes a value $\psi \sim 1$ and we introduce a particle at a point that we select as our origin of coordinates. The distortion that a single nanoparticle induces in the otherwise flat ψ profile is approximated by

$$\psi(r) \approx 1 + \phi(r; A, \rho) \tag{B.5}$$

meaning that the NP creates a distortion which is Gaussian-like shaped, with an amplitude $\phi(0) = A$ and a extension ρ such that $\phi(\rho)/A \approx 0$, that is, that at a distance given by ρ the distortion is negligible.

The free energy can be written in terms of A and ρ. The values that minimise this free energy are the ones that best accommodate a particle for a given set of parameters. Before doing so, it is clear that there is a competition: the nanoparticle (the coupling free energy) wants to create a 'perfect distortion', which would make the coupling free energy exactly zero, that would mean: $A = \psi_0 - 1$ and $\rho = R$. That is not possible because the polymeric part introduces

a penalty for $|\psi| \neq 1$, and therefore prefers to keep $A = 0$. Furthermore, the interfacial penalty given by the square of the gradient of the order parameter penalises gradients in the order parameter profile, and then would tend to keep $\rho >> R$.

The particular functional form of $\phi(x)$ affects the minimisation of the free energy. Nonetheless, we assume that we can use an ansatz given that it satisfies the conditions given in the previous paragraph. The function ψ_c introduced in the coupling free energy to account for the shape of the NP serves as an appropriative choice as it takes a zero value $\psi_c(x > 1) = 0$ outside of the particle's radius. Therefore,

$$\phi(x, A, \rho) = A\psi_c(r/\rho) \tag{B.6}$$

which satisfies all the properties required.

Firstly, let's introduce equation B.6 into the bulk free energy, which can be expanded around $\psi \sim 1$ as

$$F_{bulk} = \int d\mathbf{r} H(\psi) \approx -\frac{1}{4} + \phi^2 + \mathcal{O}(\phi^3) \tag{B.7}$$

where we can clearly ignore the additive factor and then

$$F_{local} \approx \int d\mathbf{r}\phi(r)^2 = 2\pi\rho A^2 \int_0^1 dr r\psi_c(r) = 2\pi\rho A^2 a_{1,1} \tag{B.8}$$

where we have introduced $a_{1,1}$ as a constant. At the end all the defined constant will be explicitly defined.

The interfacial free energy is

$$F_{int} = \frac{1}{2} D \int d\mathbf{r}(\nabla\phi)^2 = \pi D A^2 \int_0^1 dr\ r \left[\frac{\partial\psi_c(r)}{\partial r}\right]^2 \tag{B.9}$$

for which we can introduce a constant $C \equiv \int_0^1 dr\ r \left[\frac{\partial\psi_c(r)}{\partial r}\right]^2$

For the coupling free energy let's introduce a more relevant magnitude

$$\Delta\psi_0 = \psi_0 - 1 \tag{B.10}$$

that is, the deviation of the affinity from the bulk value. Then the coupling free energy can be written as

$$F_{cpl} = \sigma \int d\mathbf{r}\psi_c(r/R) \left[A\psi_c(r/\rho) - \Delta\psi_0\right]^2 \tag{B.11}$$

we can again ignore the global additive term and then

$$\begin{aligned} F_{cpl} =& \sigma \int d\mathbf{r}\psi_c(r/R) \left[A^2\psi_c(r/\rho)^2 - 2A\Delta\psi_0\psi_c(r/\rho)\right] = \\ & 2\pi\sigma \int_0^R dr\ r\ \psi_c(r/R) \left[A^2\psi_c(r/\rho) - 2A\Delta\psi_0\psi_c(r/\rho)\right] \end{aligned} \tag{B.12}$$

here we have to remember that $\psi_c(r > 1) = 0$ then, we need to distinguish to different cases

1. $R < \rho \rightarrow \alpha > 1$
2. $R > \rho \rightarrow \alpha < 1$

where we have defined the parameter that scales the 'reaction' of the block copolymer length with the size of the particle

$$\alpha \equiv \frac{\rho}{R} \tag{B.13}$$

I - $\alpha > 1$

When the particle radius is smaller than the distortion size we can truncate the integral up to R because anything else will be adding zeros.

$$F_{cpl} = 2\pi R^2 \sigma \int_0^1 dr\ r\ \psi_c(r) \left[A^2 \psi_c(r/\alpha)^2 - 2A\Delta\psi_0 \psi_c(r/\alpha)\right] \tag{B.14}$$

where we can introduce the following parameter that only depends on α

$$a'_n(\alpha) \equiv \int_0^1 dr\ r\ \psi_c(r)\psi(r/\alpha)^n \tag{B.15}$$

then

$$F_{cpl} = 2\pi R^2 \sigma A^2\ a'_2(\alpha) - 4\pi R^2 \sigma A \Delta\psi_0\ \alpha'_1(\alpha \tag{B.16}$$

II - $\alpha < 1$

We can do a similar proceding to obtain

$$F_{cpl} = 2\pi\sigma\rho^2 A^2 b(\alpha) - 4\pi\sigma\rho^2 A\Delta\psi_0 a'_1(\alpha^{-1}) \tag{B.17}$$

where we have defined

$$b(\alpha) = \int_0^1 dr\ r\ \psi_c(\alpha r)\psi_c(r)^2 \tag{B.18a}$$

$$a'_1(\alpha) = \int_0^1 dr\ r\ \psi_c(r)\psi(\alpha\ r)^n \tag{B.18b}$$

Total Free Energy

Therefore, putting all together, we can scale out factor $2\pi R^2$ to obtain

$$F_{tot} = \alpha^2 A_{11} A^2 + \frac{1}{2} C_1 \frac{\xi^2}{R^2} + \frac{F_{cpl}(\alpha, A)}{2\pi R^2} \tag{B.19}$$

here we have substituted $D = \xi^2$ with ξ being a length scale related to the size of the interface, that is, to the gradient of the order parameter.

After rescaling F_{cpl} too,

$$F_{cpl}(A, \alpha > 1) = \sigma A^2 a'_2(\alpha) - 2\sigma A\Delta\psi_0 a'_1(\alpha) \tag{B.20a}$$

$$F_{cpl}(A, \alpha < 1) = \sigma A^2 \alpha^2 b(\alpha) - 2\sigma A\Delta\psi_0 \alpha^2 a'_1(\alpha^{-1}) \tag{B.20b}$$

Minimisation

So now we can minimise the total free energy with respect to (A, α) for some values of $[\sigma, R, \Delta\psi_0]$. With have firther simplfiied by redefining $R = R/\xi$.

Firstly, let's derivate with respect to A

$$0 = \frac{\partial F_{tot}(\alpha, A)}{\partial A} \tag{B.21}$$

then we obtain

$$A(\alpha > 1) = \frac{\sigma\Delta\psi_0\ a'_1(\alpha)}{a_{11}\alpha^2 + \frac{1}{2}C_1 R^{-2} + \sigma a'_2(\alpha)} \tag{B.22a}$$

$$A(\alpha < 1) = \frac{\sigma \Delta\psi_0 \ \alpha^2 \ a_1'(\alpha^{-1})}{a_{11}\alpha^2 + \frac{1}{2}C_1 R^{-2} + \sigma\alpha^2 b(\alpha)} \tag{B.22b}$$

Minimisation with respect to α is not so straight forward as it requires the derivation of many of the functions we have defined, which do not have an analytic expression. Then, we do the following: we plug $A(\alpha)$ into the total free energy equation, and then minimise the free energy numerically, as it is easy to construct such a function given all the different cases and terms. In figure B.2 it is clear that the free energy has a minima at a point $\alpha \sim 1$. That is

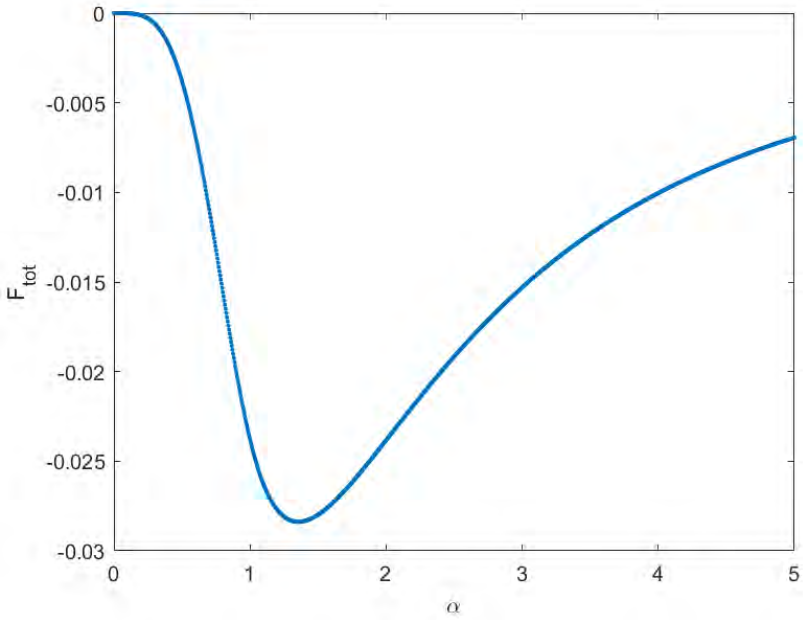

Figure B.2: Total free energy in terms of α before minimsation. Parameters are: $\sigma = R = \Delta\psi_0 = 1$

exactly what we expect: the free energy is minimsed when the BCP distortion has an extension that is similar to the NP tagged function (size).

Now we can find for each value of $\sigma, R, \Delta\psi_0$ the minimisation values for (α, A), meaning that we can construct the distortion function as

$$\psi(r) = 1 + A(\sigma, R, \Delta\psi_0)\psi_c(r/\rho) \tag{B.23}$$

. The semi-analytic approach allows us to write explicetly the dependance with some parameters,

$$\psi(r) = 1 + \beta(\sigma, R)\Delta\psi_0\psi_c(r/\rho) \tag{B.24}$$

with $\beta(\sigma, R) = A/\Delta\psi_0$ the scaled amplitude of the distortion. We can further reduce the number of parameters after inspection of the minimisation of the free energy with respect to α. We find that it does not depend on $\Delta\psi_0$ and therefore we can obtain the numerical solution of the minimisation problem for both α and β as in Figure B.3.

B.3 Interface-compatible nanoparticles

A perfectly neutral NP can be modelled via the affinity parameter $\psi_0 = 0$. As a first approximation, we can neglect the higher order, long range free energy terms and express the

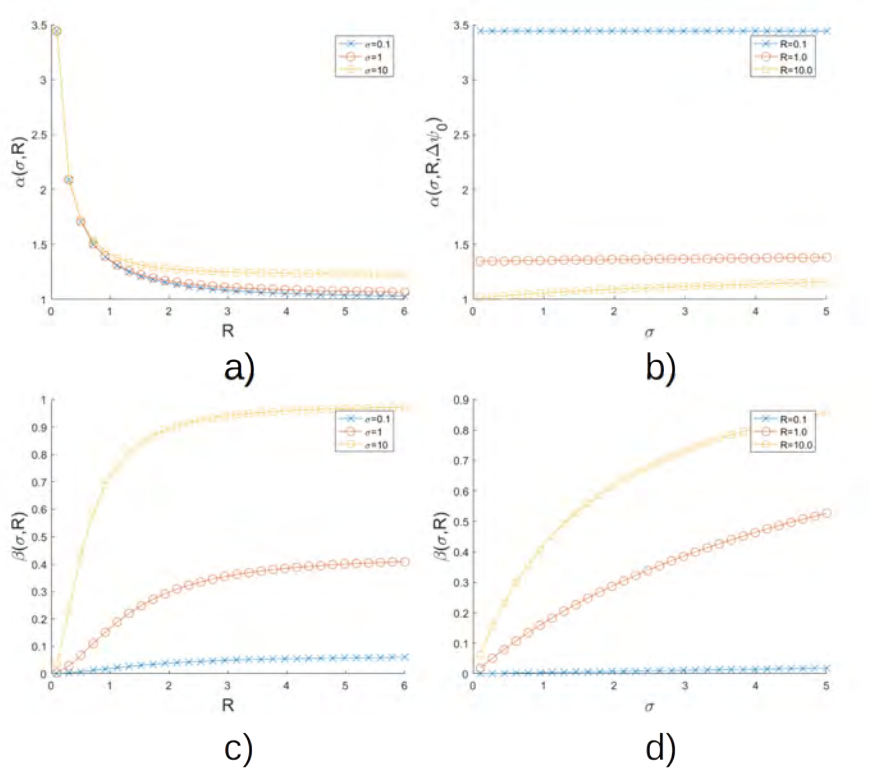

Figure B.3: Curves of α and β for several values of σ, R.

local free energy of a BCP/neutral NP mixture as

$$F = \int d\mathbf{r} \left[H_0(\psi) + \frac{1}{2} D(\nabla\psi)^2 + \sigma\psi_c(r/R_{eff})\psi^2 \right] \tag{B.25}$$

with $H_0(\psi) = -\frac{1}{2}\tau_0\psi^2 + \frac{1}{4}u\psi^4$. The size of the NP is controlled by the effective radius R_{eff} while the sharpness of the tagged function $\psi_c(r)$ depends on a parameter α as described in Chapter 2. In this section we will restrict to $\alpha = 2$, as it is the only value that we have used in this thesis.

Parameter τ is the coefficient of the second order expansion of $H_0(\psi)$ and thus its sign controls the order/disorder transition. We can introduce an effective τ parameter that captures the effect of the NP in the BCP.

$$\tau_{eff}(r/R)/\tau_0 = 1 - 2\bar{\sigma}\psi_c(r/R) \tag{B.26}$$

in which we introduce the dimensionless $\bar{\sigma}/\tau_0$ which is in accordance with the dimensionless parameters obtained in Eq. A.9. The distance to the center of mass of the NP is r.

The equilibrium profile of the order parameter nearby a NP with a radius R_{eff} is thus controlled by the minimisation of an effective local free energy per unit volume (surface)

$$H_{eff}(\psi, r) = -\frac{1}{2}\tau_{eff}\psi^2 + \frac{1}{4}u\psi^4 \tag{B.27}$$

from which we can conclude that for points such that $\tau_{eff} < 0$ the order parameter ψ takes zero (disordered) values. This occurs because the local free energy $H_{eff}(\psi, r)$ posses a single well at $\psi = 0$ in such a regime. We can therefore predict a $\psi = 0$ disordered value of the order parameter for distances $r < r_c$ while $\psi = 1$ values for $r > r_c$, with $\tau_{eff}(r_c) = 0$. The square

gradient term introduces a short length scale of decay of the order of $\xi \sim \sqrt{D/\tau_0}$ that connects the disorder values of ψ inside the particle with the bulk values of ψ in a smooth manner.

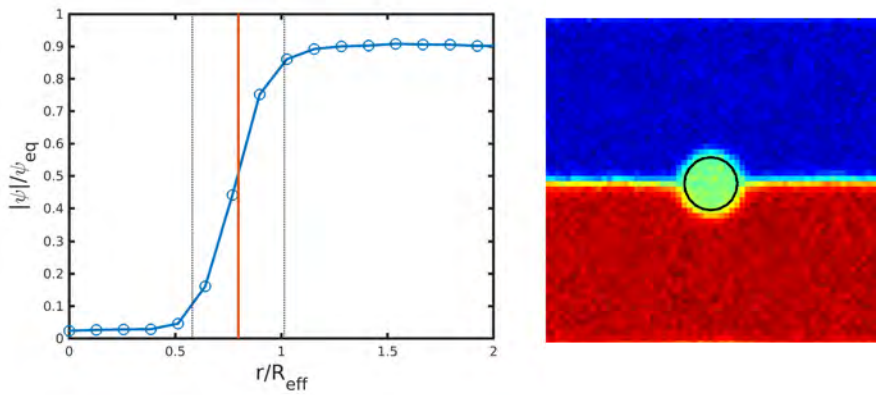

Figure B.4: (a) Profile of the averaged absolute value of the order parameter $|\psi|(r/R_{eff})|$ centred around the NP. The solid vertical line represent the value r_c while dotted lines represent $r_c - \xi$ and $r_c + \xi$. In (b) we show a snapshot of a the NP trapped at the interface.

In Fig. B.4 we can compare this simple analytical study with an actual simulation of a NP in a flat interface. In (b) we show the snapshot of the final configuration. The profile of ψ is plotted in (a) as a function of the distance to the center of mass of the particle. Distances are reduced with the NP effective radius while the order parameter is reduced with the equilibrium value $\psi_{eq} = \sqrt{\tau_0/u}$. Our study predicts a disorder state for $r < r_c$ which is shown as a vertical solid line. This line indeed approximately captures the transition from disorder to order. In fact, the smooth transition has been predicted to have a width 2ξ and additional dotted lines corroborates that the transition region falls approximately within these limits $r_c - \xi < r < r_c + \xi$.

In summary, the effect of a single NP in an interface that is governed by the the Ginzburg-Landau model can be controlled by a single effective parameter τ_{eff} equivalent to the τ_0 second order coefficient in the free energy power expansion of the local free energy. In fact, in the totally local approximation in which the square gradient term is neglected, the profile of ψ is exactly determined by the minimisation of $H_{eff}(\psi, r)$ as in

$$\psi(r) = \begin{cases} 0 & , r < r_c \\ \sqrt{\frac{\tau_{eff}(r)}{u}} & , r_c < r < R_{eff} \\ 1 & , r > R_{eff} \end{cases} \tag{B.28}$$

The effect of a single NP at the interface can be also studied in terms of the energetic difference compared with a flat interface in the absence of a colloidal nanoparticle. We can consider a flat interface in the binary mixture regime $B = 0$ and express the total free energy as

$$F_0 = \int_V d\mathbf{r} H_0(\psi_0) \tag{B.29}$$

in which $H_0(\psi_0)$ represent the free energy per unit volume (surface) in the absence of colloidal NPs and ψ_0 is the BCP profile without NPs. For simplicity, we are neglecting any non-local contributions to the free energy explicitly, that is, the interface size is considered $\xi = 0$ ($D = 0$), but we can implicitly introduce a transition length in the form of ψ (namely, a hyperbolic

tangent). The integral is extended over the whole volume V.

The total free energy of a system with a NP trapped at the interface can be expressed as

$$F_1 = \int_V d\mathbf{r} H_{eff}(\psi) \tag{B.30}$$

where H_{eff} is expressed in Eq. B.27 and ψ is the equilibrium profile of the order parameter as derived in Eq. B.28. Again, we are neglecting the square-gradient term in the free energy. Following Eq. B.28 we can separate the contributions as

$$F_1 = \int_{r<R_c} d\mathbf{r} H_{eff}(\psi) + \int_{r_c<r<R_{eff}} d\mathbf{r} H_{eff}(\psi) + \int_{r>R_{eff}} d\mathbf{r} H_{eff}(\psi) \tag{B.31}$$

where the first term can be made to zero as $\psi(r < r_c) = 0$ and in the last the integrand is a constant. The final expression is thus

$$F_1 = \int_{r_c<r<R_{eff}} d\mathbf{r} H_{eff}(\psi) + \int_{r>R_{eff}} d\mathbf{r} H_{eff}(\psi) \tag{B.32}$$

Terms can be cancelled out when the difference is taken between the free energy of a flat interface with and without NP

$$\Delta F = F_1 - F_0 = \int_{r_c<r<R_{eff}} d\mathbf{r} H_{eff}(\psi) - \int_{r<R_{eff}} d\mathbf{r} H_0(\psi_0) \tag{B.33}$$

in which the second term can be easily calculated as $\psi_0^2 = \tau_0/u$ and therefore $\int_{r<R_{eff}} d\mathbf{r} H_0(\psi_0) = -1/4\tau_0^2/uV_p$ with V_p being the volume or surface of the particle.

The first term in Eq. B.33 can be expressed as

$$\int_{r_c<r<R_{eff}} d\mathbf{r} H_{eff}(\psi) = -\frac{1}{4}\frac{\tau_0^2}{u}\int_{r_c<r<R} dr \left[1 - 2\bar{\sigma}\psi_c(r/R)\right]^2 \tag{B.34}$$

after introducing Eq. B.28. Moreover, we can express it depending on the number of dimensions

$$\text{2D: } \int_{r_c<r<R_{eff}} d\mathbf{r} H_{eff}(\psi) = -\frac{1}{4}\frac{\tau_0^2}{u}(2\pi)R^2 C_2(\bar{\sigma}, \bar{r}_c) \tag{B.35a}$$

$$\text{3D: } \int_{r_c<r<R_{eff}} d\mathbf{r} H_{eff}(\psi) = -\frac{1}{4}\frac{\tau_0^2}{u}(4\pi)R^3 C_3(\bar{\sigma}, \bar{r}_c) \tag{B.35b}$$

where $\bar{r}_c = r_c/R$ and $C_n(\bar{\sigma}, \bar{r}_c) = \int_{\bar{r}_c}^1 dt\ t^n[1 - 2\bar{\sigma}\psi_c(r)]^2$. The energetic difference ΔF can be found to be positive over a large range of $\bar{\sigma}$ values, as in Fig. B.5. A positive value indicates that $F_1 > F_0$, that is, the presence of a NP introduces a distortion in the profile leading to an increase in the overall free energy. This distortion can be minimised by an aggregation mechanism mediated by the surrounding mixture.

Further evidence of the effective NP-NP attractive interaction mediated by the mixture can be found in simulations. We can study a particular setup in a quasi-1D, long time simulation to compare initially aggregated and initially disordered systems, as in Fig B.6. Snapshots of the final systems can be found in Fig. B.7 for initially ordered and disordered colloids, (a) and (b), respectively. Comparing the time evolution of the free energy we can see that the free energy of a system with BCP/NP phase separation is lower than a system with small NP clusters.

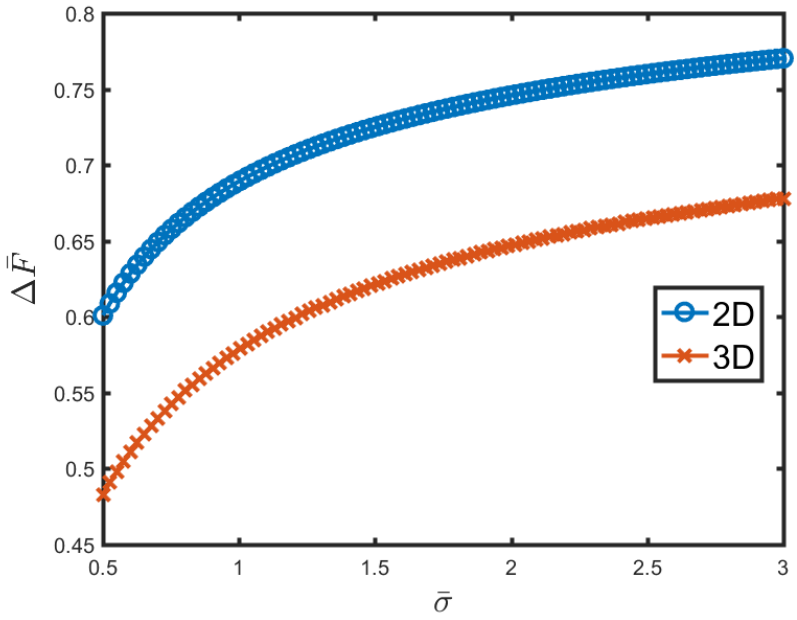

Figure B.5: Reduced energetic difference corresponding to equation B.33 $\Delta F/(\pi R^n \tau_0^2/4u)$.

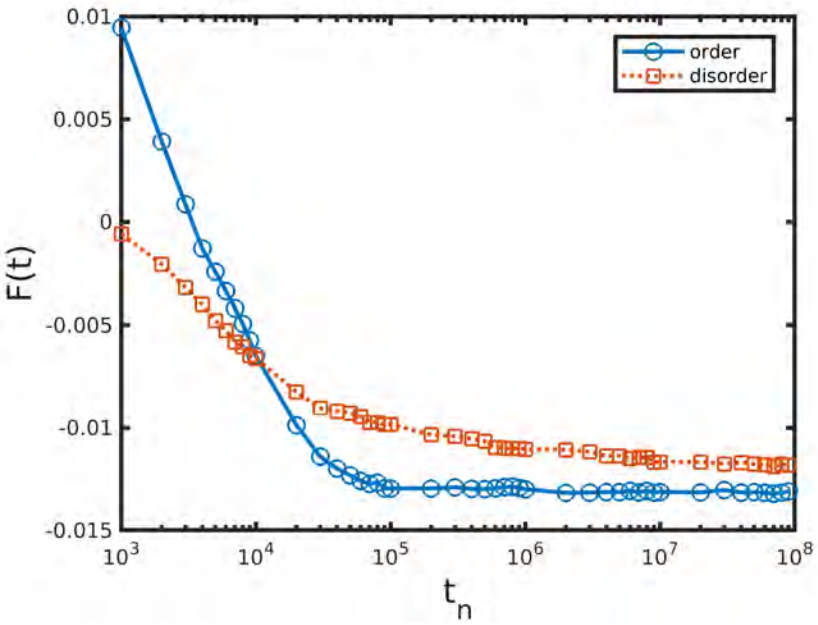

Figure B.6: Comparison of the free energy of a quasi 1D system starting from order (clusterised) or disorder (random initial condition) for (a) and (b), respectively. The free energy is calculated using [160].

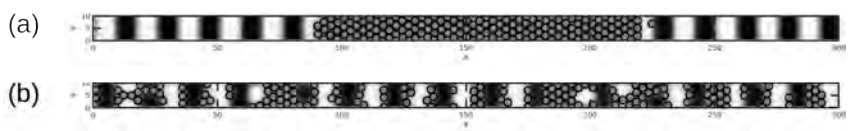

Figure B.7: Quasi 1D long time simulations with initially ordered, clusterised condition for the colloids (a), or disordered, random distribution (b).

APPENDIX C

Role of colloid-colloid interaction in BCP morphology

The role of the interparticle potential has been studied by introducing a standard Lennard-Jones potential with a tuned cut-off to determine a purely repulsive and an attractive-repulsive potential. We again reproduced the same phase diagram found in Figure C.1, a smaller upper limit for ϕ_p, as we expect that at higher concentrations the repulsive part of the potential will dominate. Also, keeping the number of particles lower allows us to perform a larger number of simulations at a reasonable computational time to have higher precision. Figure S1 clearly demonstrates that the interparticle potential plays a negligible role in the phase behaviour of BCP/NP systems.

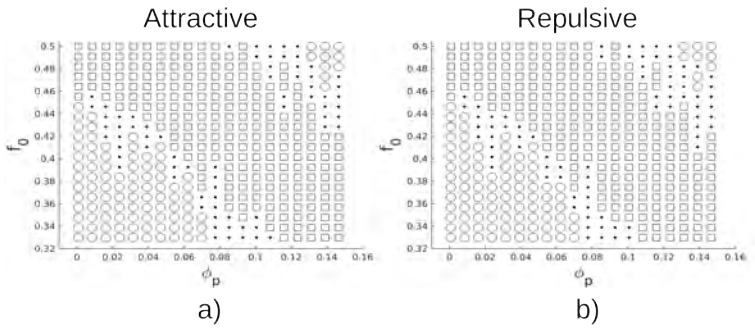

Figure C.1: : Phase behaviour of BCP/NP system for strongly compatible particles with the minority phase. Circle, dot and square stand for cylindrical, mixed and lamella phase, respectively. The cut-off radius is tuned to result in an attractive (a) interaction and repulsive (b).

APPENDIX D

Square-like nanoparticle potential

D.1 Introduction

In this document we derive fitted expressions for the interparticle potential in the case of arbitrary shapes described by the closed curve

$$\left[\left|\frac{x}{a}\right|^{2n} + \left|\frac{y}{b}\right|^{2n}\right]^{1/n} = 1 \tag{D.1}$$

known as the family of superellipses. In particular we will restrict to the case of $1/4 < n < 1$ and $n > 1$, respectively for rhombus and sharp-corner rectangles. We are motivated by recent experimental non-spherical shapes in colloidal suspensions. Moreover, we aim to derive simple expressions for the colloid-colloid potential.

We choose a pair-wise additive soft potential that is strictly repulsive. The colloid-colloid contribution to the free energy is then

$$\mathcal{F}_{cc} = \sum_{i \neq j} U(\mathbf{r}_i, \mathbf{r}_j, \phi_i, \phi_j) \tag{D.2}$$

where interparticle potential U is dependent on the particle positions but also on the orientations.

A simple, non-hard choice for the interparticle potential is proportional to the overlapping area between two arbitrary-shaped colloids. It assures non-overlapping and is expected to allow numerical stability. Relating interparticle potential and overlapping area has already been successfully used for the case of generalised ellipsoids [140, 141]. Therefore, the expression

$$U(\mathbf{r}_i, \mathbf{r}_j, \phi_i, \phi_j) = U_0 A_{\text{overlap}}(\mathbf{r}_i, \mathbf{r}_j, \phi_i, \phi_j) \tag{D.3}$$

where the particle-particle potential is proportional to the overlapping area. Since no analytic generalised expression exist for the overlapping area of two rotated objects given by Eq. D.1 we will study the numerical behaviour of the curves of overlapping and fit the results into simple elementary expressions.

D.2 Overlapping areas

We begin by considering the simplest possible case of two arbitrary oriented squares of the same size. We can firstly consider a square nanoparticle with a fixed orientation placed at the origin of the system of reference with a fixed orientation and a second particle at position $\mathbf{r}_2$ and orientation ϕ_2, as in Fig. D.1. The overlapping area is clearly proportional to $A \approx A_0(1 - r/X_{min})$. Although this expression clearly fails to capture the complexities of the overlapping behaviour, it should be noted that in a typical event of contact the actual overlapping area is considerably small, as deep overlap would be rather non-physical. Therefore, the force that the particle experiences when contact occurs is always repulsive, which is approximately correct. In summary, the force between two particles is simply considered to be repulsive. Complexities regarding the relative orientations are exactly captured by the condition of overlapping.

In order to calculate the torque that two particles experience it is necessary to have an approximate expression to the area of overlapping depending on the orientation of each colloid. The range of parameters can be difficult to analyse, as we need to consider both the orientation of the square 2, as well as the position $\mathbf{r}_2 = (x_2, y_2)$. Nonetheless, it is reasonable to explore the more relevant cases only, such as those in which overlapping is small. For this reason, we

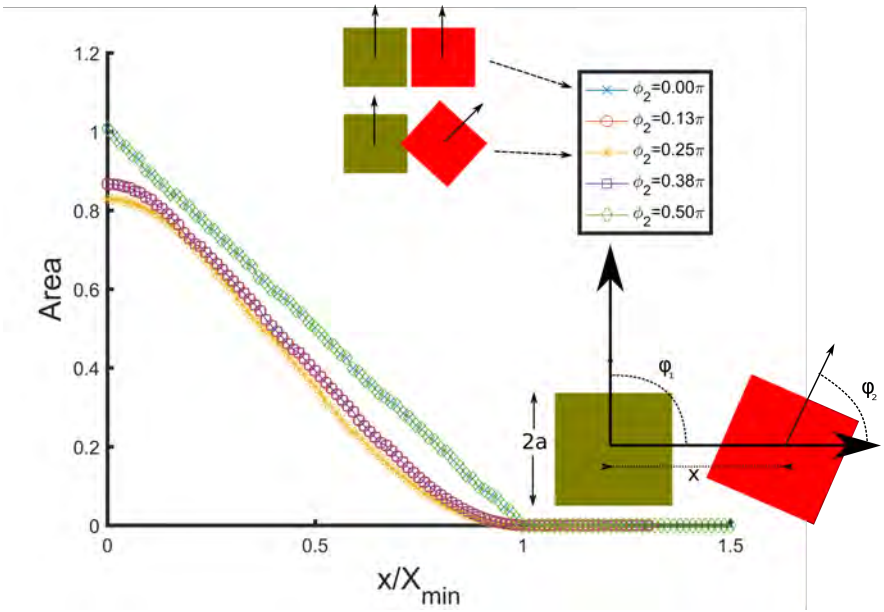

Figure D.1: Numerically calculated overlapping area between two squares. The horizontal distance is modified (X axis) for different NP orientations (different curves). The X axis is then rescaled so that the contact between two particles always occurs at $x/X_{min} = 1$. Particle 1 (left, green) is fixed and unrotated. particle 2 (red) is free to move in the $y_2 = 0$ line.

consider a particle 2 at a distance $x_2 = 2$ in the horizontal direction. Then, the orientation ϕ_2 is explored for different values of y_2. Figure D.2 shows three instances of this for heights $y_2 = 0, y_2 = 1.2$ and $y_2 = 1.5$, respectively (a), (b) and (c). In the simplest case (a), we observe a clear minimum at $\phi_2 = 0$ and $\phi_2 = \pi/2$, which can be easily pictured as in such cases the overlapping area is zero when two squares are 'parallel' , while it is larger than zero otherwise.

Figure D.2 (b) and (c) show two examples of overlapping area at different heights given by y_2. We can see that now that the area is no longer symmetric and in the case of (c) there are also cases of non-overlap.

In order to compare this overlapping area with an analytic function, let's consider the simplest case (a). Here, two particles are placed in such a way that the angle that $\mathbf{n}_1$ sustains with the center-to-center vector is $0, \pi/2, \pi....$ Due to the symmetry of the problem, the most reasonable choice in this case is to use

$$\text{Area} \propto 1 - \cos^2(2\Delta\phi) \tag{D.4}$$

with $\Delta\phi = \phi_1 - \phi_2$. The prefix 2 in the cosine assures that the right symmetry holds, and permits minimum of relative orientation at $\Delta\phi = 0, \pi/2, \pi, 3/2\pi$. This analytic expression is shown in figure D.2 (a) in which the Y axis has been rescaled. The similarity between the numerical and the two analytic expressions is clear.

Now let's consider case (b), where the second particle is displaced upwards. While the minimum is still at $0, \pi/2, \pi, 3/2\pi$, now the wells are not symmetric, instead, the left part of each minimum is much steeper. This is reasonable, as the particle will experience a much stronger repulsion when rotating negatively (clock-wise) rather than increasing ϕ (counter-clockwise). This behaviour is definitely not captured by the simple expression we describe in Eq. D.4. Let's propose a new functional form that is more complex:

$$\text{Area} \propto 1 - \left(2(\mathbf{n}_1 \cdot \hat{\mathbf{r}})^2 - 1\right)^2 \left(2(\mathbf{n}_2 \cdot \hat{\mathbf{r}})^2 - 1\right)^2 \tag{D.5}$$

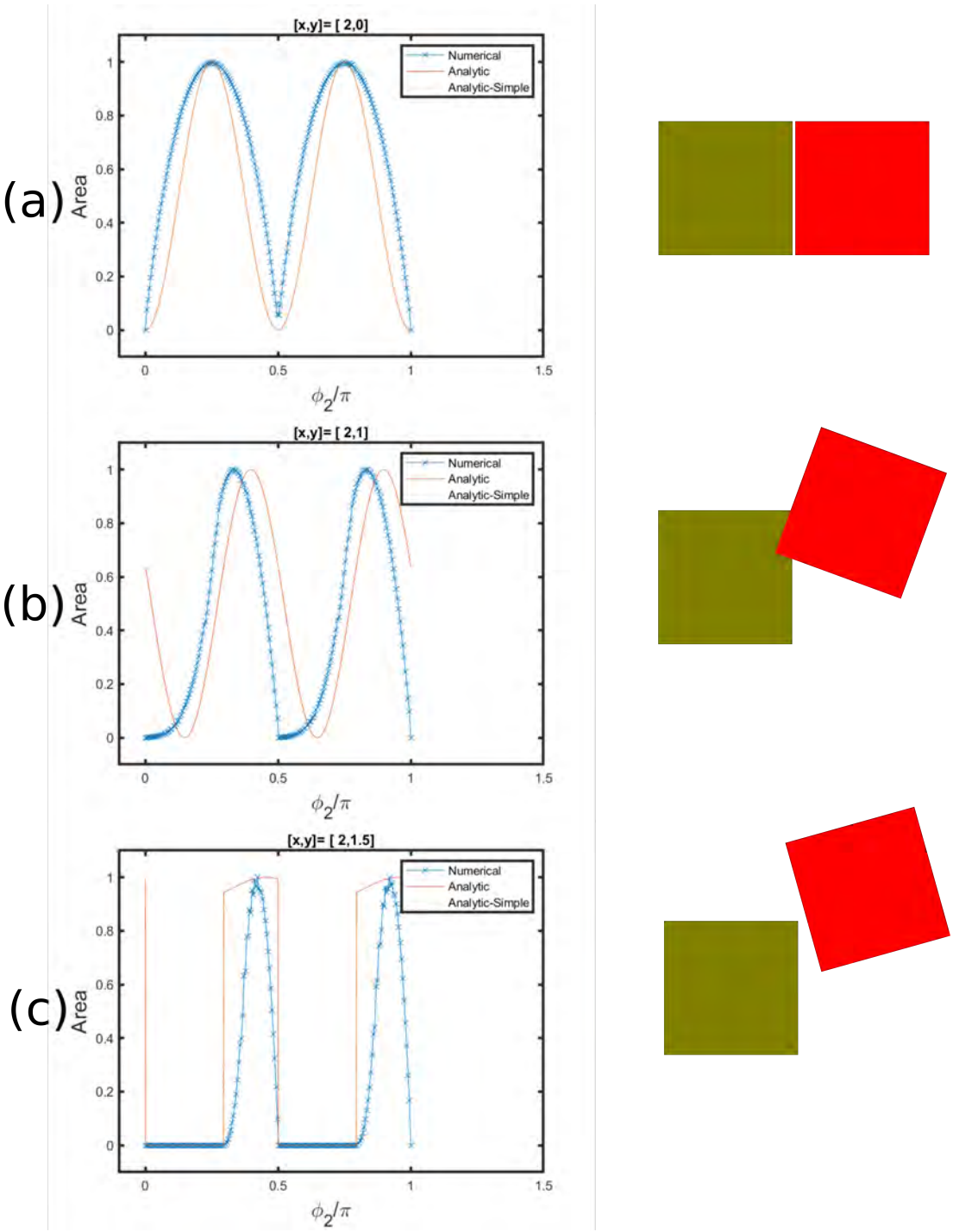

Figure D.2: Numerically calculated overlapping area between two squares for different orientations (ϕ_2). Particle 1 is fixed at the origin and unrotated while particle 2 is fixed at a horizontal distance $x_2 = 2$ (for numerical reasons $x_2 = 2 - \epsilon$ with $\epsilon << 1$ being a very small number, this assures that there is always contact). The height y_2 is different in (a) (b) and (c) (see title for each plot). Legend is : Numerical (-x) is the actual overlapping area calculated using a grid; Analytic is equation D.5 while Analytic-Simple is equation D.4 (which can be see that never changes).

This expression is what is described as **analytic** in Fig. D.2, while **Analytic-Simple** is also shown (this expression does not depend on y, therefore never changes when overlapping is true).

In figure D.2 (a) both analytic expressions capture the behavior of the numerical calculation correctly. This is important because in the case of close packing this configuration (side to side squares) is the most typical.

In Fig. D.2 (b) **Analytic** (equation D.5) captures the displacement of the minimum, although definitely not perfectly. Meanwhile Analytic-Simple remains showing a symmetric minimum. In a simulation, this means that two squares that are overlapping as in the picture in (b) will experience a torque which is different depending on the direction of rotation, even though the minimum energy state is in both cases two particles which are parallel.

In result, the total colloid-colloid potential can be written is a closed form as

$$U(\mathbf{r}_1, \mathbf{r}_2, \phi_1, \phi_2) \propto U_0 \left(1 - \frac{r}{2a}\right) \Phi(\hat{\mathbf{r}}, \phi_1\phi_2) \tag{D.6}$$

with $\Phi(\hat{\mathbf{r}}, \phi_1\phi_2) \propto \left(2(\mathbf{n}_1 \cdot \hat{\mathbf{r}})^2 - 1\right)^2 \left(2(\mathbf{n}_2 \cdot \hat{\mathbf{r}})^2 - 1\right)^2$ from which forces and torques can be easily derived. The force and torque is zero in the case of non-overlapping.

In this section we have presented the fitted potential in the simplest case of two squares with an arbitrary position and orientation. Extension to rectangles and rhomboids can be done similarly, while an expression for two star-like colloids has not been achieved. This is originated by a further difficulty derived from the concave sides.

Final Notes

List of Publications

The following publications have appeared in scientific journals involving work that also appears in this dissertation

- Diaz J, Pinna M, Zvelindovsky AV, Asta A, Pagonabarraga I. - Cell dynamic simulations of diblock copolymer/colloid systems. *Macromolecular Theory and Simulations.* **2017**
- Diaz J, Pinna M, Zvelindovsky AV, Pagonabarraga I. - Phase Behavior of Block Copolymer Nanocomposite Systems. *Advanced Theory and Simulations.* **2018**
- Diaz J, Pinna M, Zvelindovsky AV, Pagonabarraga I. - Co-assembly of Janus nanoparticles in block copolymer systems. *Soft Matter* **2019**
- Diaz J, Pinna M, Zvelindovsky AV, Pagonabarraga I. -Non-spherical nanoparticles in block copolymer composites: nanosquares, nanorods and diamonds *Macromolecules* [accepted]

Overview of computer programs

Throughout this PhD a number of computer programs have been written. This is a list of the programs that have been used, all of which have been written in FORTRAN (f90) programming language.

2D BCP(CDS) and circular colloids

- with Yukawa (non-overlapping, totally repulsive) potential. This code was written by Dr Marco Pinna and Dr Adelchi Asta.
- with Lennard-Jones potential.
  - Single-type colloids
  - Multispecies: different affinities, sizes, interparticle interactions.

2D BCP(CDS) and Ellipsoidal NPs (see Chapter 8).

2D BCP(CDS) and Super Ellipses (see Chapter 9).

2D BCP(CDS) and Janus NPs (see Chapter 7).

3D BCP (CDS) and Spherical NPs (serial code, see Chapter 10).

3D BCP (CDS) and Spherical NPs (parallel code, see Chapter 3).

Unless otherwise specified, these codes have been developed as part of the PhD thesis by the author of this thesis. Access has been granted to Archer -the UK supercomputer- and Mare Nostrum -Spanish Supercomputer.

Visualisation of 2D simulations has been performed using MATLAB except in Chapter 4 where Open DX was used instead. Paraview has been used for three dimensional simulations.

Bibliography

[1] J. J. Chiu, B. J. Kim, E. J. Kramer, D. J. Pine, *Journal of the American Chemical Society* **2005**, *127*, 5036.

[2] M. R. Bockstaller, R. A. Mickiewicz, E. L. Thomas, *Advanced Materials* **2005**, *17*, 1331.

[3] A. Haryono, W. Binder, *Small* **2006**, *2*, 600.

[4] V. Z. Chan, *Science* **1999**, *286*, 1716.

[5] C. Liedel, K. A. Schindler, M. J. Pavan, C. Lewin, C. W. Pester, M. Ruppel, V. S. Urban, R. Shenhar, A. Böker, *Small* **2013**, n/a.

[6] A. Halevi, S. Halivni, M. Oded, A. H. E. Müller, U. Banin, R. Shenhar, *Macromolecules* **2014**, *47*, 3022.

[7] M. Yoo, S. Kim, S. G. Jang, S.-H. Choi, H. Yang, E. J. Kramer, W. B. Lee, B. J. Kim, J. Bang, *Macromolecules* **2011**, *44*, 9356.

[8] N. M. Krook, J. Ford, M. Maréchal, P. Rannou, J. S. Meth, C. B. Murray, R. J. Composto, *ACS Macro Lett.* **2018**, 1400.

[9] J. Y. Lee, R. B. Thompson, D. Jasnow, A. C. Balazs, *Macromolecules* **2002**, *35*, 4855.

[10] M. J. A. Hore, R. J. Composto, *Macromolecules* **2014**, *47*, 875.

[11] R. D. Deshmukh, Y. Liu, R. J. Composto, *Nano Letters* **2007**, *7*, 3662.

[12] E. Ploshnik, A. Salant, U. Banin, R. Shenhar, *Advanced Materials* **2010**, *22*, 2774.

[13] Q. Yang, K. Loos, *Macromol. Chem. Phys.* **2017**, *218*, 1600451.

[14] M. W. Matsen, M. Schick, *Phys. Rev. Lett.* **1994**, *72*, 2660.

[15] A. J. Schultz, C. K. Hall, J. Genzer, *Macromolecules* **2005**, *38*, 3007.

[16] M. Doi, *Soft Matter Physics*, Oxford University Press, **2013**.

[17] T. Kawakatsu, *Statistical Physics of Polymers: An Introduction*, Advanced Texts in Physics, Springer-Verlag, Berlin Heidelberg, **2004**.

[18] H. Sai, K. W. Tan, K. Hur, E. Asenath-Smith, R. Hovden, Y. Jiang, M. Riccio, D. A. Muller, V. Elser, L. A. Estroff, S. M. Gruner, U. Wiesner, *Science* **2013**, *341*, 530.

[19] I. W. Hamley, *The Physics of Block Copolymers*, Oxford University Press, Oxford, New York, **1998**.

[20] C. Koning, M. Van Duin, C. Pagnoulle, R. Jerome, *Progress in Polymer Science* **1998**, *23*, 707.

[21] M. Pinna, L. Schreier, A. V. Zvelindovsky, *Soft Matter* **2009**, *5*, 970.

[22] M. W. Matsen, F. S. Bates, *Macromolecules* **1996**, *29*, 7641.

[23] M. W. Matsen, F. S. Bates, *Macromolecules* **1996**, *29*, 1091.

[24] P. J. Flory, *J. Chem. Phys.* **1941**, *9*, 660.

[25] M. L. Huggins, *J. Chem. Phys.* **1941**, *9*, 440.

[26] I. Chodák, M. Omastová, J. Pionteck, *Journal of Applied Polymer Science* **2001**, *82*, 1903.

[27] A. Okumura, K. Tsutsumi, T. Hashimoto, *Polymer Journal* **2000**, *32*, 520.

[28] B. J. Kim, J. Bang, C. J. Hawker, E. J. Kramer, *Macromolecules* **2006**, *39*, 4108.

[29] J. J. Chiu, B. J. Kim, G.-R. Yi, J. Bang, E. J. Kramer, D. J. Pine, *Macromolecules* **2007**, *40*, 3361.

[30] A. Horechyy, B. Nandan, N. E. Zafeiropoulos, D. Jehnichen, M. Göbel, M. Stamm, D. Pospiech, *Colloid and Polymer Science* **2014**, *292*, 2249.

[31] B. J. Kim, J. Bang, C. J. Hawker, J. J. Chiu, D. J. Pine, S. G. Jang, S.-M. Yang, E. J. Kramer, *Langmuir* **2007**, *23*, 12693.

[32] M. R. Bockstaller, Y. Lapetnikov, S. Margel, E. L. Thomas, *Journal of the American Chemical Society* **2003**, *125*, 5276.

[33] T. Ohta, K. Kawasaki, *Macromolecules* **1986**, *19*, 2621.

[34] T. Ohta, K. Kawasaki, *Macromolecules* **1990**, *23*, 2413.

[35] L. Leibler, *Macromolecules* **1980**, *13*, 1602.

[36] A. J. Bray, *Advances in Physics* **2002**, *51*, 481.

[37] J. D. Vavasour, M. D. Whitmore, *Macromolecules* **1992**, *25*, 5477.

[38] Y. Oono, Y. Shiwa, *Mod. Phys. Lett. B* **1987**, *01*, 49.

[39] S. Puri, Y. Oono, *Phys. Rev. A* **1988**, *38*, 1542.

[40] Y. Oono, S. Puri, *Physical Review A* **1988**, *38*, 434.

[41] M. Bahiana, Y. Oono, *Physical Review A* **1990**, *41*, 6763.

[42] S. R. Ren, I. W. Hamley, *Macromolecules* **2001**, *34*, 116.

[43] M. Pinna, X. Guo, A. V. Zvelindovsky, *Polymer* **2008**, *49*, 2797.

[44] M. Pinna, S. Hiltl, X. Guo, A. Böker, A. V. Zvelindovsky, *ACS Nano* **2010**, *4*, 2845.

[45] M. Pinna, A. V. Zvelindovsky, S. Todd, G. Goldbeck-Wood, *The Journal of Chemical Physics* **2006**, *125*, 154905.

[46] M. Pinna, X. Guo, A. V. Zvelindovsky, *The Journal of Chemical Physics* **2009**, *131*, 214902.

[47] M. Pinna, A. V. M. Zvelindovsky, X. Guo, C. L. Stokes, *Soft Matter* **2011**, *7*, 6991.

[48] M. Pinna, A. V. Zvelindovsky, *Soft Matter* **2008**, *4*, 316.

[49] M. Pinna, A. V. Zvelindovsky, *The European Physical Journal B* **2012**, *85*.

[50] J. U. Kim, B. O'Shaughnessy, *Physical Review Letters* **2002**, *89*.

[51] V. Pryamitsyn, V. Ganesan, *Macromolecules* **2006**, *39*, 8499.

[52] V. Pryamitsyn, V. Ganesan, *Macromolecules* **2006**, *39*, 844.

[53] F. A. Detcheverry, H. Kang, K. C. Daoulas, M. Müller, P. F. Nealey, J. J. de Pablo, *Macromolecules* **2008**, *41*, 4989.

[54] H. Kang, F. A. Detcheverry, A. N. Mangham, M. P. Stoykovich, K. C. Daoulas, R. J. Hamers, M. Müller, J. J. de Pablo, P. F. Nealey, *Physical Review Letters* **2008**, *100*.

[55] J. Huh, V. V. Ginzburg, A. C. Balazs, *Macromolecules* **2000**, *33*, 8085.

[56] D. Liu, C. Zhong, *Macromolecular Rapid Communications* **2006**, *27*, 458.

[57] H. Chen, E. Ruckenstein, *Polymer* **2010**, *51*, 5869.

[58] P. Posocco, Z. Posel, M. Fermeglia, M. Lísal, S. Pricl, *Journal of Materials Chemistry* **2010**, *20*, 10511.

[59] M. Maly, P. Posocco, S. Pricl, M. Fermeglia, *Industrial & Engineering Chemistry Research* **2008**, *47*, 5023.

[60] R. B. Thompson, *Science* **2001**, *292*, 2469.

[61] R. B. Thompson, V. V. Ginzburg, M. W. Matsen, A. C. Balazs, *Macromolecules* **2002**, *35*, 1060.

[62] M. W. Matsen, R. B. Thompson, *Macromolecules* **2008**, *41*, 1853.

[63] V. V. Ginzburg, *Macromolecules* **2005**, *38*, 2362.

[64] G. He, V. V. Ginzburg, A. C. Balazs, *Journal of Polymer Science Part B: Polymer Physics* **2006**, *44*, 2389.

[65] A. C. Balazs, V. V. Ginzburg, F. Qiu, G. Peng, D. Jasnow, *J. Phys. Chem. B* **2000**, *104*, 3411.

[66] V. V. Ginzburg, C. Gibbons, F. Qiu, G. Peng, A. C. Balazs, *Macromolecules* **2000**, *33*, 6140.

[67] V. V. Ginzburg, F. Qiu, A. C. Balazs, *Polymer* **2002**, *43*, 461.

[68] M. Pinna, I. Pagonabarraga, A. V. Zvelindovsky, *Macromolecular Theory and Simulations* **2011**, *20*, 769.

[69] J. Díaz, M. Pinna, A. V. Zvelindovsky, A. Asta, I. Pagonabarraga, *Macromolecular Theory and Simulations* **2017**, *26*, 1600050.

[70] J. W. Cahn, J. E. Hilliard, *The Journal of Chemical Physics* **1959**, *31*, 688.

[71] H. E. Cook, *Acta Metallurgica* **1970**, *18*, 297.

[72] R. C. Ball, R. L. H. Essery, *Journal of Physics: Condensed Matter* **1990**, *2*, 10303.

[73] I. W. Hamley, *Macromolecular Theory and Simulations* **2000**, *9*, 363.

[74] S. R. Ren, I. W. Hamley, G. J. A. Sevink, A. V. Zvelindovsky, J. G. E. M. Fraaije, *Macromolecular Theory and Simulations* **2002**, *11*, 123.

[75] G. J. A. Sevink, M. Pinna, K. M. Langner, A. V. Zvelindovsky, *Soft Matter* **2011**, *7*, 5161.

[76] J. Feng, E. Ruckenstein, *The Journal of Chemical Physics* **2004**, *121*, 1609.

[77] T. Ohta, Y. Enomoto, J. L. Harden, M. Doi, *Macromolecules* **1993**, *26*, 4928.

[78] L.-T. Yan, H. G. Schoberth, A. Böker, *Macromolecular Chemistry and Physics* **2009**, *210*, 1003.

[79] K. S. Lyakhova, A. V. Zvelindovsky, G. J. A. Sevink, *Macromolecules* **2006**, *39*, 3024.

[80] H. Tanaka, T. Araki, *Physical Review Letters* **2000**, *85*, 1338.

[81] X. Guo, M. Pinna, A. V. Zvelindovsky, *Macromolecular Theory and Simulations* **2007**, *16*, 779.

[82] A. K. Khandpur, S. Foerster, F. S. Bates, I. W. Hamley, A. J. Ryan, W. Bras, K. Almdal, K. Mortensen, *Macromolecules* **1995**, *28*, 8796.

[83] A. V. Zvelindovsky, G. J. A. Sevink, B. A. C. van Vlimmeren, N. M. Maurits, J. G. E. M. Fraaije, *Phys. Rev. E* **1998**, *57*, R4879.

[84] K. Tsuchiya, S. Nagayasu, S. Okamoto, T. Hayakawa, T. Hihara, K. Yamamoto, I. Takumi, S. Hara, H. Hasegawa, S. Akasaka, N. Kosikawa, *Opt. Express, OE* **2008**, *16*, 5362.

[85] E. Ploshnik, K. M. Langner, A. Halevi, M. Ben-Lulu, A. H. E. Müller, J. G. E. M. Fraaije, G. J. Agur Sevink, R. Shenhar, *Advanced Functional Materials* **2013**, *23*, 4215.

[86] M. Metcalf, J. Reid, M. Cohen, *Modern Fortran Explained*, Oxford University Press, Oxford ; New York, edición: 4 edition, **2011**.

[87] A. Fanfarillo, T. Burnus, V. Cardellini, S. Filippone, D. Nagle, D. Rouson, in *Proceedings of the 8th International Conference on Partitioned Global Address Space Programming Models*, PGAS '14, ACM, New York, NY, USA, 4:1–4:11.

[88] S. Garain, D. S. Balsara, J. Reid, *Journal of Computational Physics* **2015**, *297*, 237.

[89] M. P. Allen, D. J. Tildesley, *Computer Simulation of Liquids: Second Edition*, Oxford University Press, **2017**.

[90] F. S. Bates, G. H. Fredrickson, *Physics Today* **1999**, *52*, 32.

[91] M. Templin, A. Franck, A. Du Chesne, H. Leist, Y. Zhang, R. Ulrich, V. Schädler, U. Wiesner, *Science* **1997**, *278*, 1795.

[92] D. Zhao, *Science* **1998**, *279*, 548.

[93] B. J. Kim, J. J. Chiu, G.-R. Yi, D. J. Pine, E. J. Kramer, *Advanced Materials* **2005**, *17*, 2618.

[94] B. J. Kim, G. H. Fredrickson, C. J. Hawker, E. J. Kramer, *Langmuir* **2007**, *23*, 7804.

[95] C.-T. Lo, B. Lee, V. G. Pol, N. L. Dietz Rago, S. Seifert, R. E. Winans, P. Thiyagarajan, *Macromolecules* **2007**, *40*, 8302.

[96] C.-T. Lo, Y.-C. Chang, S.-C. Wu, C.-L. Lee, *Colloids and Surfaces A: Physicochemical and Engineering Aspects* **2010**, *368*, 6.

[97] G. Kim, S. Swier, H.-J. Lee, C. Wang, *Macromolecules* **2016**, *49*, 7370.

[98] S. W. Sides, B. J. Kim, E. J. Kramer, G. H. Fredrickson, *Physical Review Letters* **2006**, *96*.

[99] B. J. Kim, G. H. Fredrickson, J. Bang, C. J. Hawker, E. J. Kramer, *Macromolecules* **2009**, *42*, 6193.

[100] J. Diaz, M. Pinna, A. V. Zvelindovsky, I. Pagonabarraga, *Advanced Theory and Simulations* **2018**, *1*, 1800066.

[101] T. Ohta, A. Ito, *Physical Review E* **1995**, *52*, 5250.

[102] A. Walther, A. H. E. Müller, *Soft Matter* **2008**, *4*, 663.

[103] A. B. Pawar, I. Kretzschmar, *Macromolecular Rapid Communications* **2010**, *31*, 150.

[104] J. Du, R. K. O'Reilly, *Chem. Soc. Rev.* **2011**, *40*, 2402.

[105] A. Walther, A. H. E. Müller, *Chem. Rev.* **2013**, *113*, 5194.

[106] B. Ren, I. Kretzschmar, *Langmuir* **2013**, *29*, 14779.

[107] Y. Iwashita, Y. Kimura, *Soft Matter* **2017**, *13*, 4997.

[108] D. J. Beltran-Villegas, B. A. Schultz, N. H. P. Nguyen, S. C. Glotzer, R. G. Larson, *Soft Matter* **2014**, *10*, 4593.

[109] R. A. DeLaCruz-Araujo, D. J. Beltran-Villegas, R. G. Larson, U. M. Córdova-Figueroa, *Langmuir* **2018**, *34*, 1051.

[110] Z. Preisler, T. Vissers, F. Smallenburg, G. Munaò, F. Sciortino, *J. Phys. Chem. B* **2013**, *117*, 9540.

[111] W. L. Miller, A. Cacciuto, *Phys. Rev. E* **2009**, *80*, 021404.

[112] H. Nie, X. Liang, A. He, *Macromolecules* **2018**, *51*, 2615.

[113] H. Nie, C. Zhang, Y. Liu, A. He, *Macromolecules* **2016**, *49*, 2238.

[114] K. C. Bryson, T. I. Löbling, A. H. E. Müller, T. P. Russell, R. C. Hayward, *Macromolecules* **2015**, *48*, 4220.

[115] M. Huang, Z. Li, H. Guo, *Soft Matter* **2012**, *8*, 6834.

[116] Y. Zhou, M. Huang, T. Lu, H. Guo, *Macromolecules* **2018**, *51*, 3135.

[117] C. Zhou, S.-k. Luo, Y. Sun, Y. Zhou, W. Qian, *J. Appl. Polym. Sci.* **2016**, *133*, 44098.

[118] Q. Yang, K. Loos, *Polymer Chemistry* **2017**, *8*, 641.

[119] B. Dong, Z. Huang, H. Chen, L.-T. Yan, *Macromolecules* **2015**, *48*, 5385.

[120] P. Chen, Y. Yang, B. Dong, Z. Huang, G. Zhu, Y. Cao, L.-T. Yan, *Macromolecules* **2017**, *50*, 2078.

[121] L.-T. Yan, N. Popp, S.-K. Ghosh, A. Böker, *ACS Nano* **2010**, *4*, 913.

[122] J. U. Kim, M. W. Matsen, *Phys. Rev. Lett.* **2009**, *102*, 078303.

[123] L. Wang, J. Lin, X. Zhu, *RSC Advances* **2012**, *2*, 12870.

[124] M. A. Osipov, A. S. Ushakova, *Journal of Molecular Liquids* **2018**, *267*, 330.

[125] A. Krekhov, V. Weith, W. Zimmermann, *Phys. Rev. E* **2013**, *88*, 040302.

[126] Y.-q. Guo, J.-x. Pan, M.-n. Sun, J.-j. Zhang, *The Journal of Chemical Physics* **2017**, *146*, 024902.

[127] E. Ploshnik, A. Salant, U. Banin, R. Shenhar, *Physical Chemistry Chemical Physics* **2010**, *12*, 11885.

[128] Q.-y. Tang, Y.-q. Ma, *The Journal of Physical Chemistry B* **2009**, *113*, 10117.

[129] C. S. T. Laicer, T. Q. Chastek, T. P. Lodge, T. A. Taton, *Macromolecules* **2005**, *38*, 9749.

[130] K. Thorkelsson, A. J. Mastroianni, P. Ercius, T. Xu, *Nano Letters* **2012**, *12*, 498.

[131] K. Thorkelsson, J. H. Nelson, A. P. Alivisatos, T. Xu, *Nano Letters* **2013**, *13*, 4908.

[132] L. He, L. Zhang, A. Xia, H. Liang, *The Journal of Chemical Physics* **2009**, *130*, 144907.

[133] L. He, L. Zhang, H. Chen, H. Liang, *Polymer* **2009**, *50*, 3403.

[134] L. He, L. Zhang, H. Liang, *Polymer* **2010**, *51*, 3303.

[135] Z. Pan, L. He, L. Zhang, H. Liang, *Polymer* **2011**, *52*, 2711.

[136] M. A. Osipov, M. V. Gorkunov, *The European Physical Journal E* **2016**, *39*.

[137] M. A. Osipov, M. V. Gorkunov, Y. V. Kudryavtsev, *Molecular Crystals and Liquid Crystals* **2017**, *647*, 405.

[138] M. A. Osipov, M. V. Gorkunov, A. V. Berezkin, Y. V. Kudryavtsev, *Physical Review E* **2018**, *97*.

[139] K. M. Langner, G. J. A. Sevink, *Soft Matter* **2012**, *8*, 5102.

[140] J. G. Gay, B. J. Berne, *The Journal of Chemical Physics* **1981**, *74*, 3316.

[141] B. J. Berne, P. Pechukas, *J. Chem. Phys.* **1972**, *56*, 4213.

[142] E. De Miguel, L. F. Rull, M. K. Chalam, K. E. Gubbins, *Molecular Physics* **1991**, *74*, 405.

[143] R. Berardi, A. P. J. Emerson, C. Zannoni, *J. Chem. Soc., Faraday Trans.* **1993**, *89*, 4069.

[144] Y. Han, A. M. Alsayed, M. Nobili, J. Zhang, T. C. Lubensky, A. G. Yodh, *Science* **2006**, *314*, 626.

[145] B. t. Hagen, S. van Teeffelen, H. Löwen, *Journal of Physics: Condensed Matter* **2011**, *23*, 194119.

[146] Z. Zheng, Y. Han, *The Journal of Chemical Physics* **2010**, *133*, 124509.

[147] J. Happel, H. Brenner, *Low Reynolds number hydrodynamics: with special applications to particulate media*, number v. 1 in Mechanics of fluids and transport processes, M. Nijhoff ; Distributed by Kluwer Boston, The Hague ; Boston : Hingham, MA, USA, 1st pbk. ed edition, **1983**.

[148] F. Perrin, *J. Phys. Radium* **1934**, *5*, 497.

[149] J. Henzie, M. Grünwald, A. Widmer-Cooper, P. L. Geissler, P. Yang, *Nature Materials* **2012**, *11*, 131.

[150] B. Wang, X. Wang, J. Zou, Y. Yan, S. Xie, G. Hu, Y. Li, A. Dong, *Nano Lett.* **2017**, *17*, 2003.

[151] A. K. Sharma, F. A. Escobedo, *J. Phys. Chem. B* **2018**, *122*, 9264.

[152] A. Donev, J. Burton, F. H. Stillinger, S. Torquato, *Phys. Rev. B* **2006**, *73*, 054109.

[153] S. Gottschalk, M. C. Lin, D. Manocha, in *Proceedings of the 23rd Annual Conference on Computer Graphics and Interactive Techniques*, SIGGRAPH '96, ACM, New York, NY, USA, 171–180.

[154] V. Ganesan, A. Jayaraman, *Soft Matter* **2014**, *10*, 13.

[155] R. Dessí, M. Pinna, A. V. Zvelindovsky, *Macromolecules* **2013**, *46*, 1923.

[156] M. W. Matsen, *J. Chem. Phys.* **1997**, *106*, 7781.

[157] Y. Aviv, E. Altay, L. Fink, U. Raviv, J. Rzayev, R. Shenhar, *Macromolecules* **2019**, *52*, 196.

[158] G. J. A. Sevink, A. V. Zvelindovsky, *The Journal of Chemical Physics* **2004**, *121*, 3864.

[159] P. Rein ten Wolde, M. J. Ruiz-Montero, D. Frenkel, *J. Chem. Phys.* **1996**, *104*, 9932.

[160] M. Serral, M. Pinna, A. V. Zvelindovsky, J. B. Avalos, *Macromolecules* **2016**, *49*, 1079.